8-2012

Prediction of the Wear & Evolution of Cutting Tools in a Carbide / Ti-6Al-4V Machining Tribosystem by Volumetric Tool Wear Characterization & Modeling

Mathew Kuttolamadom
Clemson University, mathew23@gmail.com

PREDICTION OF THE WEAR & EVOLUTION OF CUTTING TOOLS IN A CARBIDE / TI-6AL-4V MACHINING TRIBOSYSTEM BY VOLUMETRIC TOOL WEAR CHARACTERIZATION & MODELING

A Dissertation
Presented to
the Graduate School of
Clemson University

In Partial Fulfillment
of the Requirements for the Degree
Doctor of Philosophy
Materials Science & Engineering

---

by
Mathew Abraham Kuttolamadom
August 2012

Accepted by:
Dr. M. Laine Mears, Committee Chair
Dr. Marian S. Kennedy
Dr. Vincent Y. Blouin
Dr. Eric C. Skaar

ABSTRACT

The objective of this research work is to create a comprehensive microstructural wear mechanism-based predictive model of tool wear in the tungsten carbide / Ti-6Al-4V machining tribosystem, and to develop a new topology characterization method for worn cutting tools in order to validate the model predictions. This is accomplished by blending first principle wear mechanism models using a weighting scheme derived from scanning electron microscopy (SEM) imaging and energy dispersive x-ray spectroscopy (EDS) analysis of tools worn under different operational conditions. In addition, the topology of worn tools is characterized through scanning by white light interferometry (WLI), and then application of an algorithm to stitch and solidify data sets to calculate the volume of the tool worn away.

The motivation for this work is two-fold. First, the evolving dominance of different wear mechanisms with time, as well as with significant tool and process factors has been characterized only in a limited fashion for this tribosystem. Traditional modeling of tool wear treats wear mechanisms individually. Hence, quantifying the mechanism-dominance at different operational conditions through a comprehensive approach of combining and weighting wear mechanisms is essential for understanding wear. Second is the critical need for better quantifying the wear itself. Wear is a 3D phenomenon. However, machining tool wear has historically been measured only in 1D which is inadequate to capture the true tool wear status, even with standardization.

The methodology was to first combine and weight dominant microstructural wear mechanism models, to be able to effectively predict the tool volume worn away. Then, by developing a new metrology method for accurately quantifying the bulk-3D wear, the model-predicted wear was validated against worn tool volumes obtained from corresponding machining experiments.

The changing dominance of different microstructural wear mechanisms was captured by formulating mechanism-weighting-factors from SEM imaging and EDS analysis. These were formulated for each of the three speed-regimes, which then fed into a multi-mechanistic volumetric wear rate model. On comparing this model-predicted wear to the actual tool volume worn away, prediction on the order of the observed wear was achieved, with better prediction at low and medium surface speeds – this was quantified by sum-of-squares computations.

On analyzing worn crater faces using SEM/EDS, adhesion was found dominant at lower surface speeds, while dissolution wear dominated with increasing speeds – this is in conformance with the lower relative surface speed requirement for micro welds to form and rupture, essentially defining the mechanical load limit of the tool material. It also conforms to the known dominance of high temperature-controlled wear mechanisms with increasing surface speed, which is known to exponentially increase temperatures especially when machining Ti-6Al-4V due to its low thermal conductivity. Thus, straight tungsten carbide wear when machining Ti-6Al-4V is mechanically-driven at low surface speeds and thermally-driven at high surface speeds.

Further, at high surface speeds, craters were formed due to carbon diffusing to the tool surface and being carried away by the rubbing action of the chips – this left behind a smooth crater surface predominantly of tungsten and cobalt as observed from EDS analysis. Also, at high surface speeds, carbon from the tool was found diffused into the adhered titanium layer to form a titanium carbide (TiC) boundary layer – this was observed as instances of TiC build-up on the tool edge from EDS analysis. A complex wear mechanism interaction was thus observed, i.e., titanium adhered on top of an earlier worn out crater trough, additional carbon diffused into this adhered titanium layer to create a more stable boundary layer (which could limit diffusion-rates on saturation), and then all were further worn away by dissolution wear as temperatures increased. At low and medium feeds, notch discoloration was observed – this was detected to be carbon from EDS analysis, suggesting that it was deposited from the edges of the passing chips. Mapping the dominant wear mechanisms showed the increasing dominance of dissolution wear relative to adhesion, with increasing grain size – this is because a 13% larger sub-micron grain results in a larger surface area of cobalt exposed to chemical action.

On the macro-scale, wear quantification through topology characterization elevated wear from a 1D to 3D concept. From investigation, a second order dependence of volumetric tool wear (VTW) and VTW rate with the material removal rate (MRR) emerged, suggesting that MRR is a more consistent wear-controlling factor instead of the traditionally used cutting speed. A predictive model for VTW was developed which

showed its exponential dependence with workpiece stock volume removed. Also, both VTW and VTW rate were found to be dependent on the accumulated cumulative wear on the tool. Further, a ratio metric of stock material removed to tool volume lost is now possible as a tool efficiency quantifier and energy-based productivity parameter, which was found to inversely depend on MRR - this led to a more comprehensive tool wear definition based on cutting tool efficiency.

DEDICATION

To my wife Leah, & mom & dad, for their never-failing love, support & prayers…

ACKNOWLEDGMENTS

First and foremost, I would like to express my sincere gratitude to Dr. Laine Mears for taking me under his wing for the last 4 years. I am simply a much better person both professionally and personally solely due to his support and mentorship. Today, I start an academic career both because of his guidance, and due to the desire to be like him. Above all, I thank him for having faith in me; I am forever indebted.

Next, I want to thank Dr. Marian Kennedy for her invaluable guidance, not just in research, but on how to present, write, and communicate research effectively. Also, my sincere thanks go out to Dr. Vincent Blouin and Dr. Eric Skaar for keeping me rooted in the reality of models, materials, and probabilities.

I would also like to thank Dr. Thomas Kurfess for his guidance and support all along and beyond, as well as the staff at CU-ICAR, especially Gary Mathis. My peers here have contributed in more ways than just professionally to keep me afloat through the years – thank you Josh, Wes, Perry, Kavit, Numair, Yujie, and many more.

Last but not least, I want to thank my wife Leah for her love and prayers all along, as well as mom and dad for their support and encouragement.

TABLE OF CONTENTS

Page

ABSTRACT ii

DEDICATION vi

ACKNOWLEDGMENTS vii

LIST OF ABBREVIATIONS xii

LIST OF SYMBOLS xiii

LIST OF TABLES xvii

LIST OF FIGURES xviii

Chapter

1. INTRODUCTION 1

    1.1 Objective 1
    1.2 The Problem 1
    1.3 Motivation #1 – Evolving Dominance of Different Microstructural Wear Mechanisms has not been Aptly Characterized for this Tribosystem 4
    1.4 Motivation #2 – The Current Metrics of Tool Wear are Inconsistent 10
    1.5 Concept / Approach 17
    1.6 Organization of this Dissertation 20

2. BACKGROUND 21

    2.1 The Machining Process 21
    2.2 Tool Material: Tungsten Carbide with Cobalt Binder (WC-Co) 30
    2.3 Workpiece Material: Titanium Alloy (Ti-6Al-4V) 37
    2.4 The Machining Tribosystem 42
    2.5 Tool Deterioration 47

Table of Contents (Continued)

Page

3. RESEARCH METHODOLOGY 64

3.1 Research Questions 64
3.2 Tasks 64
3.3 Summary 67

4. WEIGHTED MODELING OF MICROSTRUCTURAL WEAR MECHANISMS (RQ1) 69

4.1 Constraining the Tribosystem 69
4.2 Identification of Primary Factors Affecting Wear Mechanics 72
4.3 DOE of Tool & Process Factors for Modeling & Validation 83
4.4 Weighting Factors for Microstructural Wear Mechanisms 85
4.5 Maps of Dominant Wear Mechanisms 114
4.6 Weighted Multi-Mechanistic Comprehensive Wear Rate Model 123
4.7 Model-Based Estimation of Maximum Damage Depth 145
4.8 Discussion of Results 146
4.9 Summary & Takeaways 151

5. QUANTIFICATION & VALIDATION OF VOLUMETRIC TOOL WEAR EVOLUTION (RQ2) 152

5.1 Quantification of Volumetric Tool Wear 152
5.2 Validation of Predicted tool wear & Profile Evolution 175
5.3 Concept of the M-Ratio 208
5.4 Dominant Profile Evolution Trends 210
5.5 Discussion of Results 212
5.6 Summary & Takeaways 214

6. CONCLUSIONS & FUTURE WORK 216

A. SOFTWARE & HARDWARE CAPABILITIES PERTAINING TO THIS RESEARCH WORK 222

A.1 ThirdWave Systems AdvantEdge-FEM 222
A.2 HPC Cluster 223

Table of Contents (Continued)

Page

B. DOE STUDY FOR CHARACTERIZING FEED/SPEED DEPENDENCE (SIMULATIONS) 225

C. DOE STUDY FOR CHARACTERIZING CUTTING DEPTH DEPENDENCE (CUTTING TESTS) 228

C.1 Cumulative Work vs. Depth of Cut in Turning 229
C.2 Cumulative Work vs. Depth of Cut in Milling 233

D. TOOL GEOMETRY CHARACTERIZATION 238

D.1 Tool Geometry Characterization – Angle between Rake & Relief Faces 238
D.2 Tool Geometry Characterization – Tool Edge Radius 240

REFERENCES 243

LIST OF PUBLICATIONS 255

Refereed Journals 255
Refereed Conferences 256
Technical Reports 257
Seminars & Presentations 257

LIST OF ABBREVIATIONS

1D/2D/3D	One/Two/Three Dimensional
ANSI	American National Standards Institute
BC	Boundary Condition
BCC	Body Centered Cubic
BSE	Back Scattered Electron
CBN	Cubic Boron Nitride
Co	Cobalt
CU	Clemson University
CU-CCIT	Clemson Computing & Information Technology
DOE	Design Of Experiments
EDS	Energy Dispersive X-Ray Spectroscopy
FEA/FEM	Finite Element Analysis/Method
FF	Full Factorial
HCP	Hexagonal Close Packed
HPC	High Performance Computing
ISO	International Standards Organization
O/LH	Optimal/Latin Hypercube
PCD	Polycrystalline Diamond
PVD	Physical Vapor Deposition

RQ	Research Question
SEM	Scanning Electron Microscope
STEM	Scanning Transmission Electron Microscope
Ti-6Al-4V	Titanium – 6 Aluminum – 4 Vanadium
TiC/TaC/NbC	Titanium/Tantalum/Niobium Carbide
TRS	Transverse Rupture Strength
VTW	Volumetric Tool Wear
WC	Tungsten Carbide
WLI	White Light Interferometry

LIST OF SYMBOLS

A'	Cross-sectional area of abrasive groove
A_R	Real area of contact
B	Adhesive volume worn away
B'	Abrasive volume worn away
C	Chemical solubility in workpiece material
C_l	Cost of labor (Material handling)
C_m	Cost of machining
C_p	Total cost per part
C_s	Cost of setup
C_t	Cost of tooling
d_g	Grain size
E	Modulus of Elasticity
F	Frictional force
F_c	Cutting force
FL	Energy dissipated in sliding a distance L
f_n	Normal force on elemental tool segment
F_t	Thrust force
F_x	Force in x-direction
F_y	Force in y-direction

H	Hardness
H_a	Hardness of inclusions
H_t	Hardness of tool
HV	Vickers Hardness
K	Probability that a wear particle is expelled
KT	*Krater Tiefe* (Crater wear)
L	Sliding length
N	Normal force
P	Applied load
T	Temperature
t	Time
t_c	Chip thickness
t_o	Uncut chip thickness
u	Specific energy
V	Surface (cutting) speed
VB	*Verschleissmarken Breite* (Flank wear)
w_{Abr}	Weighting factor – Abrasive wear
w_{Adh}	Weighting factor – Adhesive wear
w_{Chem}	Weighting factor – Chemical wear
w_{Diff}	Weighting factor –Diffusive wear

W_{Net}	Net (total) wear
α	Rake angle
ΔE	Activation energy
θ	Roughness angle of abrasive grain
μ	Coefficient of friction
ρ	Density
σ	Stress (general)
$\sigma_{critical}$	Critical stress
σ_{max}	Maximum stress
σ_n	Normal stress
σ_y	Yield stress
ϕ	Shear angle

LIST OF TABLES

Table Page

Table 2-1: Relative machinability of Ti-6Al-4V against 4340 steel and 6061 aluminum [63]. 44

Table 4-1: Properties of Sandvik H10A & H13A grades 76

Table 4-2: Final DOE of machining setups tabulated for H10A WC-Co cutting insert showing 27 runs (1 – 9, 19 – 27, 37 – 45) with 3 discrete stock volume removal steps of 10 cm^3 each. 84

Table 4-3: Final DOE of machining setups tabulated for H13A WC-Co cutting insert showing 27 runs (10 – 18, 28 – 36, 45 – 54), with 3 discrete stock volume removal steps of 10 cm^3 each. 85

Table 4-4: Weighted Wear Mechanisms for H10A Grade Carbide Inserts 104

Table 4-5: Weighted Wear Mechanisms for H13A Grade Carbide Inserts 113

Table 4-6: Simulation Results of Maximum Steady-State Cutting and Feed Forces, Temperatures, Contact Pressures and Sliding Velocities for the Final DOE of Machining Runs 137

Table 4-7: Maximum wear depth as predicted by Usui's adhesive wear model which is a function of sliding velocity, normal stress, and temperature. Note that the wear rate was multiplied by the cutting time to obtain the wear depth. 138

Table 4-8: Wear rates from machining tests using TiC coated tools turning AISI 4340 steel [127]. 139

Table 4-9: Rankings of predicted abrasive wear and chemical dissolution wear rates at 700^0 C relative to TiC [127]. 140

Table 4-10: Maximum wear depth considering the dissolution wear mechanism. Since constant for the tribosystem of interest was not readily available, wear rates were estimated from calculating a relative wear rate with respect o TiC coatings and then multiplied by the cutting time to obtain the wear depth. 141

List of Tables (Continued)

Table Page

Table 4-11: Diffusion coefficient of the three tool elements from the cutting tool side into the Ti-6Al-4V chip [138]. (R is 8.314/mol-K)..... 141

Table 4-12: Maximum wear depth considering the diffusive wear mechanism. Diffusion coefficient equations were written for each of the three tool elements, W, C and Co based on the temperatures obtained earlier. The average diffusion rate was multiplied with the cutting time to obtain the wear depth..... 142

Table 4-13: Maximum model-based wear depths predicted by the comprehensive model of three wear mechanisms for H10A grade inserts (finer grain)..... 145

Table 4-14: Maximum model-based wear depths predicted by the comprehensive model of three wear mechanisms for H13A grade inserts (coarser grain). 146

Table 5-1: Flank wear and wear volumes of the 3 inserts..... 170

Table 5-2: 2^2 Full factorial experimental designs..... 177

Table 5-3: Resultant reference volumes (unworn) 183

Table 5-4: Volumetric tool wear of each of the 4 individual inserts (mm^3) (36 data points) 184

Table 5-5: Averaged Volumetric Tool Wear Results (mm^3)..... 185

Table 5-6: Specific Volumetric Tool Wear Rate 188

Table 5-7: Volumetric tool wear data of H10A grade turning inserts..... 198

Table 5-8: Volumetric tool wear data of H13A grade turning inserts..... 198

Table 5-9: Sum-of-squares for H10A grade inserts for each speed-regime. 207

Table 5-10: M-ratio Against the Cumulative Stock Removed..... 209

LIST OF FIGURES

Figure Page

Figure 1-1: Catastrophic failure of a NIAGARA high-performance solid-carbide end mill. This center-cutting tool failed a few minutes into milling Ti-6Al-4V when roughing the bottom of a drill hole. Note the discoloration due to overheating half-way up the cutting flutes. The other main cause was the retained high-temperature strength of Ti-6Al-4V, leading to welding and smearing of the tool (5-flute, TiAlN coated, ϕ0.5" end-mill), (Cost: $63.70 from Travers, Inc.). 2

Figure 1-2: Another catastrophically failed solid-carbide end mill that was used for milling Ti-6Al-4V. The gross tool failure was predominantly due to the high-temperature welding and adhesion of the tool to the workpiece material, leading to brittle fracture away from the cutting edge and far into the tool body – this is evident from absence of visual high-temperature damage on the failed tool (5-flute, ϕ0.5" center-cutting end-mill)..... 2

Figure 1-3: Catastrophic failure of a PVD-TiAlN coated carbide milling insert (flank face). Gross tool failure was again due to high-temperature welding and adhesion of the tool edge to the workpiece material, leading to brittle fracture within the tool body (IC928: Tough grade coated carbide, for machining titanium alloys), (Cost: ~ $27/insert, from ISCAR). 3

Figure 1-4: Catastrophically failed uncoated carbide milling insert (flank face). Brittle tool fracture within the tool body due to the tool edge region breaking off is evident. 3

Figure 1-5: Dry climb-milling of Ti-6Al-4V with carbide insert tools. (Undesirable) smoke is visible near the tool-workpiece interface, highlighting the fact that the majority of heat is not dissipated along with the chip. The portion of heat on the chip is however still substantial. 3

Figure 1-6: An overview of the causes, mechanisms, types and consequences of tool wear [2, 3]..... 6

Figure 1-7: Standard flank wear nomenclature [16] 12

Figure 1-8: Standard crater wear nomenclature [16] 13

List of Figures (Continued)

Figure Page

Figure 1-9: A face mill wear pattern: Flaking (*FL*) on face-mill [17] 14

Figure 1-10: An end mill wear pattern: Stair-formed face wear (*KT2*) on end-mill [17] .. 14

Figure 1-11: One among many inconsistent tool wear quantification scenarios, where rubbing wear is indistinguishable from material worn away 15

Figure 1-12: VTW modeling concept: (A) Contour map of predicted wear on a tibial insert [20], (B) Wear volume characterization of the 3D model of a worn milling insert, (C) Concept plot relating wear coefficients/volumes to tool & process factors, (D) Concept plot relating part and process monitoring variables to wear variables/volumes, and (E) Path to profitability 19

Figure 2-1: Qualitative plot of process optimization for the cost per piece of a typical machining scenario. Note that there is an optimum cutting speed (V*) for minimum cost [28]. 22

Figure 2-2: (A) Typical turning operation on a lathe, where the feed is in mm/rev or in./rev, and depth of cut is in mm or in. Note that feed in turning is equivalent to the depth of cut in orthogonal cutting (Figure 2-4), and the depth of cut in turning is equivalent to the width of cut in orthogonal cutting [28], (B) Image of an actual bar turning operation [37]. 24

Figure 2-3: Illustration showing the difference between conventional milling and climb milling [28]. Climb milling is recommended for machining titanium alloys. 24

Figure 2-4: Schematic illustration of orthogonal turning where the chip formation process can be considered to be two-dimensional [28]. Note the well-defined shear plane – such a treatment is also known as the Merchant model. 25

Figure 2-5: (A) Forces acting on a cutting tool in two-dimensional turning – these can be resolved into normal and shear force on the tool-chip interface or cutting and feed forces on the tool [28]. Note that the resultant forces, R, must be collinear (Source: After M.E. Merchant). Forces can also be resolved at the primary shear zone as F_n and F_s. Also, β is the friction angle, (B) 3D illustration of cutting forces [28]. F_c is the cutting force, F_t is the thrust or feed force (in the direction of feed), and F_r is the radial force that tends to push the tool away from the workpiece. 26

List of Figures (Continued)

Figure Page

Figure 2-6: Schematic illustration of the distribution of normal and shear stresses at the tool-chip interface (rake face). Note that, whereas the normal stress increases continuously toward the tool tip, the shear stress reaches a maximum value and remains fairly constant (sticking). 26

Figure 2-7: The balance of heat generation and heat dissipation in metal cutting [38] 28

Figure 2-8: Typical temperature distribution in the cutting zone [28]. Note the severe temperature gradients within the tool and the chip, and that the workpiece is relatively cool (Source: After G. Vieregge). 28

Figure 2-9: Proportion of the heat generated in cutting transferred to the tool, workpiece, and chip as a function of the cutting speed [28]. Note that most of the cutting energy is carried away by the chip (in the form of heat), particularly as speed increases. 29

Figure 2-10: Microstructure of WC-Co tool substrate (10000X BSE Image) and EDS of area with elemental composition 31

Figure 2-11: TEM micrographs of WC-10%Co (sintered at 1425C) showing (A) straight faceted WC grain, (B) WC/WC interface [8] 32

Figure 2-12: Microstructure of cemented carbide (85.5 WC-12 Co-3.5 Cr) showing a well dispersed eta phase, (WC grain size 3μm) (X 1500) [8] 35

Figure 2-13: The effect of Cobalt content of on the general mechanical properties of WC-Co cutting tools [28]. Note that hardness is directly related to compressive strength and hence, inversely to wear 36

Figure 2-14: Hardness of various cutting-tool materials as a function of temperature (hot hardness) [28]. The wide range in each group of tool materials results from the variety of compositions and treatments available for that group. The hot hardness of carbides decrease drastically after about a 1000^0C; during titanium machining, such temperatures can be frequently exceeded and hence temperature-controlled wear is a significant mechanism affecting carbide tools, especially with increasing relative surface speeds. 37

Figure 2-15: Lamellar structure of Ti-6Al-4V [6] 38

List of Figures (Continued)

Figure Page

Figure 2-16: Schematic of processing route for β annealed structure [52]..... 40

Figure 2-17: General input-output description of tribosystems adopted as a systems-level concept [62]..... 43

Figure 2-18: Types of wear observed in cutting tools at the three wear zones [38] 49

Figure 2-19: Tool life variation with cutting feeds and speeds [76] 55

Figure 2-20: Taylor's tool life model [39, 40]..... 58

Figure 2-21: Three wear zones of a typical wear curve [38]. Flank wear as a function of cutting time. Tool life T is defined as the cutting time required for flank wear to reach a value of VB_k. 59

Figure 2-22: Wear map for uncoated WC cutting tools when dry turning steel [110]. Note that boundaries have been re-plotted with all data points removed and various regions shaded. The data points were the log of flank wear per distance ($\log_{10}$(VB/L)). 62

Figure 2-23: Wear map for TiC coated WC cutting tools when dry turning steel [83]. Note that boundaries have been re-plotted with all data points removed and various regions shaded. The data points were the log of flank wear per distance (log10(VB/L)). Also note how the safety zone has expanded with the use of a thin coating of TiC, beneficial for machining steel. 63

Figure 4-1: Systems-level concept in metal cutting applied to the WC-Co / Ti-6Al-4V machining tribosystem showing the worn tool, cut stock, & chips as system outputs. 70

Figure 4-2: Subset of the systems-level metal cutting concept, where the cutting tool has been isolated & all its interactions are captured/treated as 'tool-system' inputs & outputs. 71

Figure 4-3: WC-Co property map showing the (A) Coercivity vs. inverse grain size relations, and (B) Coercivity vs. Cobalt content relations for different compositions [117]. 78

List of Figures (Continued)

Figure Page

Figure 4-4: A) Relevant technical specifications of the Sandvik CNGP 12 04 08 H10A insert [122], (B) Insert dimensions, (C) Solid model, and (D) Image of insert..... 80

Figure 4-5: (A) Relevant technical specifications of the Sandvik CNGP 12 04 08 H13A insert [122], (B) Insert dimensions, (C) Solid model, and (D) Image of insert..... 81

Figure 4-6: SEM micrograph of the H13A WC-Co insert surface at 11000 X. White sharp edged polygons are WC grains, and blank areas are the Co binder. The almost horizontal lines are the abrasive grooves due to polishing with SiC abrasive paper. Note that grains sizes vary from about 0.25 μm to about 2 μm in this area of examination. 82

Figure 4-7: EDS analysis of the above area, and estimated elemental composition. The lower % Co composition is assumed to be a local distribution. 83

Figure 4-8: Representative instances of wear mechanisms on coated WC cutting tools used for dry end-milling Ti-6al-4V (40X). (Each image size is 10mm x 10mm). (A) Adhesive wear indicated by micro-chipping or a "chunk" of material pulled away, (B) Abrasive wear indicated by wear scars or grooves on the tool caused by harder particles (or inclusions), (C) Chemical wear indicated by discoloration on the tool surface, (D) Diffusive wear indicated by smooth areas on the tool. 87

Figure 4-9: Chart identifying each of the nine machining setup conditions (feed-speed combinations) tested, and the dominant wear mechanism(s) identified at that condition by simultaneously analyzing SEM micrographs and EDS elemental results of the worn areas. Note that the locations of the cutting tests are marked with an "x" and that this chart is for H10A inserts with an average grain size of 0.54 μm (finer grain). Note the concentration of the dominant adhesive wear mechanism at the lower left corner of the chart (low speed and feed), while the generalized dissolution wear mechanism is more concentrated at the upper left corner of the chart (high speed and feed conditions). The recommended cutting condition for a 2mm cut depth is at the center "x", *i.e.*, a cutting speed of 60 m/min and feed of 0.15 mm/rev. 116

List of Figures (Continued)

Figure Page

Figure 4-10: Map of dominant wear mechanism distribution for H10A inserts. Two regions have been identified when adhesion and dissolution wear mechanisms are dominant. A main field boundary was drawn separating these two regions. The left and bottom regions of the feed-speed design space showed a dominance of adhesion wear mechanism, while the top right region showed dominance of dissolution wear. These were demarked on the basis of the percentage area that was affected on the wear surface. There was also a "grey" area at the high speed condition (120 m/min) where there was some transitioning happening between the dominance between adhesion and dissolution wear, *i.e.*, dissolution wear was becoming more dominant with increasing feed rate. 117

Figure 4-11: Failure and chatter conditions demarked on the map of dominant wear mechanism distribution for H10A inserts. The low speed, high-feed combination resulted in a chatter condition during the cutting process and caused smearing on the tool rake face – all of this smeared material was identified as titanium from EDS analysis. Further, the workpiece had chatter marks and unacceptable surface roughness – this resulted in identifying the region as a failure location. Note that this essentially represents the limit of mechanical load that the tool material can carry (feed has a direct relation with forces). Also, the high-speed, high-feed condition resulted in catastrophic failure of the tool, causing the region around it to be identified as a failure zone as well. Note that that this essentially represents the limit of thermal load that the tool material can carry (speed has a direct relation with temperature). 118

Figure 4-12: Final predictive map of dominant wear mechanisms for H10A carbide inserts dry turning Ti-6Al-4V. The additions in this chart include: (*i*) Region of notch discoloration on the tool (below a line in between the medium and high feed regions), (*ii*) Region of built-up-edge (BUE) formation (high speed and high feed conditions), and (*iii*) a safe region definition at medium to high feeds but low cutting speeds. 119

List of Figures (Continued)

Figure Page

Figure 4-13: Chart identifying each of the nine machining setup conditions (feed-speed combinations) tested, and the dominant wear mechanism(s) identified at that condition by simultaneously analyzing SEM micrographs and EDS elemental results of the worn areas. Locations of the cutting tests are marked with an "x" and this chart is for H13A inserts with an average grain size of 0.61 μm (coarser grain, about 12% larger). The only two differences of this chart with that of H10A inserts are the mechanism dominance at the two circled locations. With a coarser grain, some dissolution wear effects were observed at the lower feed and, dissolution became the more dominant wear mechanism at high speed. 120

Figure 4-14: Map of dominant wear mechanism distribution for H13A inserts. Two regions have been identified when adhesion and dissolution wear mechanisms are dominant. A main field boundary was drawn separating these two regions. 121

Figure 4-15: Final predictive map of dominant wear mechanisms for H13A carbide inserts dry turning Ti-6Al-4V. Besides the shape change of the field boundary, the additions in this chart include: (*i*) Region of notch discoloration on the tool (below a line in between the medium and high feed regions), (*ii*) Region of built-up-edge (BUE) formation (high speed and high feed conditions), and (*iii*) a safe region definition at medium to high feeds but low cutting speeds. 122

Figure 4-16: Relative relationships of tool-wear mechanisms with respect to cutting speeds or temperatures [134]..... 134

Figure 4-17: Estimated peak temperatures vs. Wear rate of TiC coatings when turning AISI 4340 steel. This plot was used for estimating the wear rates of TiC at different temperatures. 139

Figure 5-1: A typical titanium milling insert 158

Figure 5-2: Point cloud processing for VTW: (A) Intensity map, (B) Point cloud 3D model, (C) Point cloud in rectangular coordinates, (D) Surface model. 159

Figure 5-3: Reference entities for this insert type..... 160

Figure 5-4: Four bounding planes created off the earlier defined reference entities 160

List of Figures (Continued)

Figure Page

Figure 5-5: Solid model manipulation to obtain volume: (A) Solid model after split by 28^0 plane, (B) Split by remaining 3 planes (surface model superimposed) (C) Surface and solid models superimposed..... 161

Figure 5-6: VTW for a failed insert: (A) Insert image, (B) Point cloud 3D model, (C) Point cloud in rectangular coordinates, (D) Final surface/solid models overlaid, (E) Boundary extruded surface model, (F) Final volume, (G) Surface/solid models overlaid..... 162

Figure 5-7: VTW methodology for Sandvik CNGP style turning insert. Stitching in the XY-plane was needed for capturing the wear along the length of the tool edge..... 163

Figure 5-8: (A) Surface model of the worn volume and, (B) Solid model of VTW 163

Figure 5-9: General VTW Methodology Flowchart 166

Figure 5-10: Multiple scan procedure: (A) Rake face, (B) Raw scan #2, (C) Raw scan #3, (D) All 5 raw scans, (E) Top view, (F) All but one matched, (G) Point cloud, (H) Surface model 167

Figure 5-11: Next level of wear volume modeling for relating to wear mechanisms..... 168

Figure 5-12: Worn milling insert #1: (A) Magnified image at 40X, (B) Surface model ... 169

Figure 5-13: Worn milling insert #2: (A) Magnified image at 40X, (B) Surface model ... 169

Figure 5-14: Worn milling insert #3: (A) Magnified image at 40X, (B) Surface model ... 170

Figure 5-15: ANOVA Gauge R&R evaluation of system 171

Figure 5-16: ISCAR IC-28: (A, B) Flank, (C, D) Rake faces..... 172

Figure 5-17: Sandvik (milling): (A, B) Flank, (C, D) Rake faces 172

Figure 5-18: Sandvik (turning): (A, B) Flank, (C, D) Rake faces..... 173

Figure 5-19: Iscar milling insert with relevant dimensions [155]..... 177

List of Figures (Continued)

Figure Page

Figure 5-20: (A) Insert with BUE, (B) With BUE removed 178

Figure 5-21: Unworn (new) insert: (A) Microscope captured image, (B) Solid model along with reference surface 179

Figure 5-22: Insert matching alternative: (A) New and worn surface matching, (B) Solid model with reference surface 180

Figure 5-23: Insert after a cutting length of 154.8 mm: (A) Microscope image, (B) Solid model used for comparison 181

Figure 5-24: Insert after a cutting length of 309.6 mm: (A) Microscope image, (B) Solid model used for comparison 181

Figure 5-25: Insert after a cutting length of 464.4 mm: (A) Microscope image, (B) Solid model used for comparison 182

Figure 5-26: Average volumetric wear plotted against varying feeds and speeds for setups 1-3 185

Figure 5-27: Direct correlation of MRR with VTW. 187

Figure 5-28: The Correlation of Specific VTW Rate with MRR 190

Figure 5-29: Dependence of Accumulated Wear on VTW Rate 191

Figure 5-30: Average measured flank wear (4 inserts each) 194

Figure 5-31: Normalized average VTW (4 inserts each) 194

Figure 5-32: Flank land of L1 insert at end of step-1 (154.8 mm) 195

Figure 5-33: Flank land of L1 insert at end of step-2 (316.8 mm) 195

Figure 5-34: Flank land of L1 insert at end of step-3 (464.4 mm) 195

Figure 5-35: Final machined workpieces used for the turning DOE 197

List of Figures (Continued)

Figure Page

Figure 5-36: Volumetric tool wear of the H10A grade insert at a feed rate of 0.05 mm/rev for different cutting speeds..... 199

Figure 5-37: Volumetric tool wear of the H10A grade insert at a feed rate of 0.15 mm/rev for different cutting speeds..... 199

Figure 5-38: Volumetric tool wear of the H10A grade insert at a feed rate of 0.30 mm/rev for different cutting speeds. Note that the data point for a cutting speed of 120 m/min, though shown as 0.025 mm^3, is actually catastrophically failed. 200

Figure 5-39: Volumetric tool wear of the H13A grade insert at a feed rate of 0.05 mm/rev for different cutting speeds..... 201

Figure 5-40: Volumetric tool wear of the H13A grade insert at a feed rate of 0.15 mm/rev for different cutting speeds..... 201

Figure 5-41: Volumetric tool wear of the H13A grade insert at a feed rate of 0.30 mm/rev for different cutting speeds. Note that the data point for a cutting speed of 120 m/min, though shown as 0.025 mm^3, was actually catastrophically failed. 202

Figure 5-42: Comparison of the (A) actual VTW against the model-predicted tool wear at 30 m/min cutting speed for H10A grade inserts, (B) For different weighting factors. 203

Figure 5-43: Comparison of the (A) actual VTW against the model-predicted tool wear at 60 m/min cutting speed for H10A grade inserts, (B) For different weighting factors. 204

Figure 5-44: Comparison of the (A) actual VTW against the model-predicted tool wear at 120 m/min cutting speed for H10A grade inserts, (B) For different weighting factors. 204

Figure 5-45: Comparison of the (A) actual VTW against the model-predicted tool wear at 30 m/min cutting speed for H13A grade inserts, (B) For different weighting factors. 205

List of Figures (Continued)

Figure Page

Figure 5-46: Comparison of the (A) actual VTW against the model-predicted tool wear at 60 m/min cutting speed for H13A grade inserts, (B) For different weighting factors. 205

Figure 5-47: Comparison of the (A) actual VTW against the model-predicted tool wear at 120 m/min cutting speed for H13A grade inserts, (B) For different weighting factors. 206

Figure 5-48: The Correlation of the M-ratio with MRR 208

Figure 5-49: Geometric Coefficients Defined on 'Flank Face Plane' for Wear Tracking: (A) Intensity map, (B) 3D model 210

Figure 5-50: Wear profile evolution can be tracked using the axes of a half/quarter ellipsoid. 211

Figure 5-51: Geometric Coefficient Defined into the Tool Body for Wear Tracking: (A) 3D model, (B) Surface profile 211

Figure 5-52: Evolution of the Average of the Set of Geometric Coefficients for Each Pass 212

CHAPTER ONE

1. INTRODUCTION

1.1 OBJECTIVE

The objective of this research work is to create a comprehensive microstructural wear mechanism-based predictive model of tool wear in the tungsten carbide / Ti-6Al-4V machining tribosystem, and to develop a new topology characterization method for worn cutting tools in order to validate the model predictions. This is accomplished by blending first principle wear mechanism models using a weighting scheme derived from scanning electron microscopy (SEM) imaging and energy dispersive x-ray spectroscopy (EDS) analysis of tools worn under different operational conditions. In addition, the topology of worn tools is characterized through scanning by white light interferometry (WLI), and then application of an algorithm to stitch and solidify data sets to calculate the volume of the tool worn away.

1.2 THE PROBLEM

The fundamental (or superset) problem that this research work addresses is the difficult-to-predict cutting tool wear and failure when machining titanium alloys. To get a first-hand feel of this problem, a small subset of tool failures that resulted from previous work in titanium machining is depicted below.

Figure 1-1: Catastrophic failure of a NIAGARA high-performance solid-carbide end mill. This center-cutting tool failed a few minutes into milling Ti-6Al-4V when roughing the bottom of a drill hole. Note the discoloration due to overheating half-way up the cutting flutes. The other main cause was the retained high-temperature strength of Ti-6Al-4V, leading to welding and smearing of the tool (5-flute, TiAlN coated, ϕ0.5" end-mill), (Cost: $63.70 from Travers, Inc.).

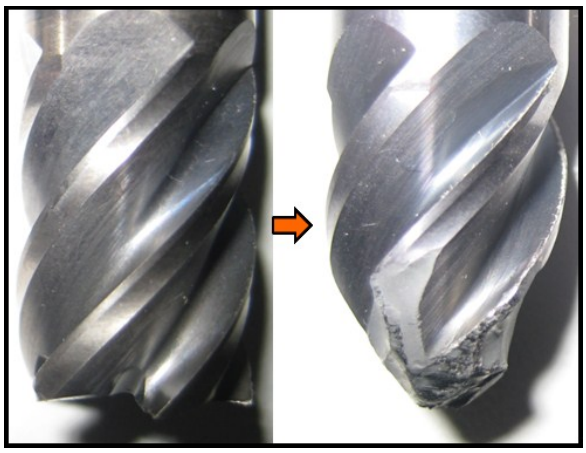

Figure 1-2: Another catastrophically failed solid-carbide end mill that was used for milling Ti-6Al-4V. The gross tool failure was predominantly due to the high-temperature welding and adhesion of the tool to the workpiece material, leading to brittle fracture away from the cutting edge and far into the tool body – this is evident from absence of visual high-temperature damage on the failed tool (5-flute, ϕ0.5" center-cutting end-mill).

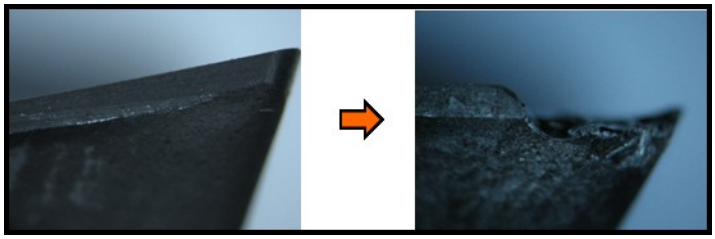

Figure 1-3: Catastrophic failure of a PVD-TiAlN coated carbide milling insert (flank face). Gross tool failure was again due to high-temperature welding and adhesion of the tool edge to the workpiece material, leading to brittle fracture within the tool body (IC928: Tough grade coated carbide, for machining titanium alloys), (Cost: ~ $27/insert, from ISCAR).

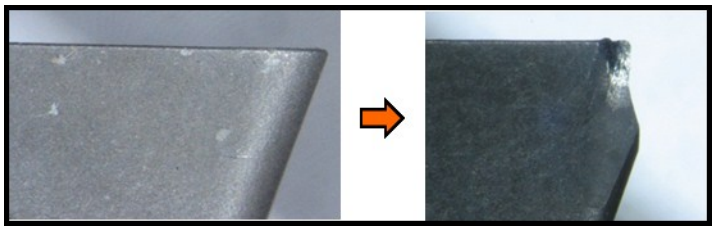

Figure 1-4: Catastrophically failed uncoated carbide milling insert (flank face). Brittle tool fracture within the tool body due to the tool edge region breaking off is evident.

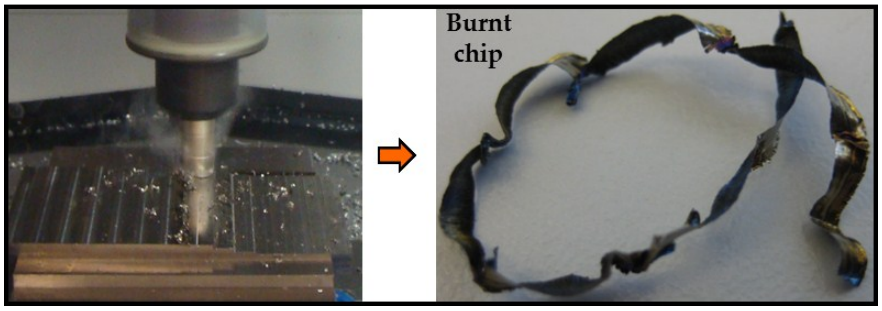

Figure 1-5: Dry climb-milling of Ti-6Al-4V with carbide insert tools. (Undesirable) smoke is visible near the tool-workpiece interface, highlighting the fact that the majority of heat is not dissipated along with the chip. The portion of heat on the chip is however still substantial.

In each of the above cases, the tools were operating under recommended (and conservative) cutting conditions. Further, the tool condition and extent of tool wear were

frequently visually checked, for each of the above tools to possibly detect the onset of failure – however, in all cases the tools failed catastrophically, and without warning.

Such unpredictable and catastrophic tool failures are not uncommon in industrial scenarios when machining titanium alloys; in fact, it was the aerospace industry that was one of the first to describe titanium alloys as "difficult-to-machine" materials.

It is also worth noting that, for the above-depicted set of failed tools, some, failed during tool wear tests (Figure 1-3, Figure 1-4 and Figure 1-5), while the others (Figure 1-1 and Figure 1-2), failed catastrophically during the machining of actual automotive component prototypes. This resulted in damage to the component surfaces which had to be 'fixed' by additional operations. Such a situation in an actual industrial scenario can be economically catastrophic, especially in the aerospace sector, where one would have to scrap the part, many of which cost upwards of $50,000 [1].

1.3 Motivation #1 – Evolving Dominance of Different Microstructural Wear Mechanisms has not been Aptly Characterized for this Tribosystem

Tool wear happens through a combination of microstructural wear mechanisms such as adhesion, abrasion, diffusion, fatigue and dissolution. Among these, the dominant microstructural wear mechanism (or a combination of wear mechanisms) affecting the machining tribosystem evolves with time as well as with significant tool factors and process conditions. This dominance-evolution, if not accounted for, can wrongly predict wear. Traditional modeling of tool wear treats these microstructural wear mechanisms

individually. Such limited characterization of dominant wear mechanism evolution does not capture the evolving wear mechanics effectively.

The issue is compounded by the relatively high temperatures and temperature gradients, and hence the higher tool wear rates commonly associated with titanium machining. Due to this drastic range of temperatures involved, wear mechanism dominance can switch frequently. Hence, quantifying the mechanism-dominance at different operational conditions through a comprehensive approach of combining and weighting wear mechanisms is essential for understanding wear, especially when machining titanium and its alloys – this is the first motivation for this work.

1.3.1 Microstructural Wear Mechanisms of Carbide Tools

Cutting tools essentially experience mechanical and thermal loads during machining, as well as combinations of the two. As a result, the tool deteriorates in the form of wear (or failure) at concentrated zones. These tool-chip and tool-workpiece interfaces, are typically about a millimeter long and about a quarter millimeter wide. The common microstructural wear mechanisms observed during machining are abrasion, adhesion, diffusion, oxidation, fatigue and plastic deformation as illustrated in Figure 1-6. These lead to tool wear profiles that are quantified by some geometry metric, typically flank or crater wear. The consequences of tool wear due to such microstructural wear mechanisms are high cutting forces, high temperatures, loss in dimensional accuracy and even workpiece surface and sub-surface damage.

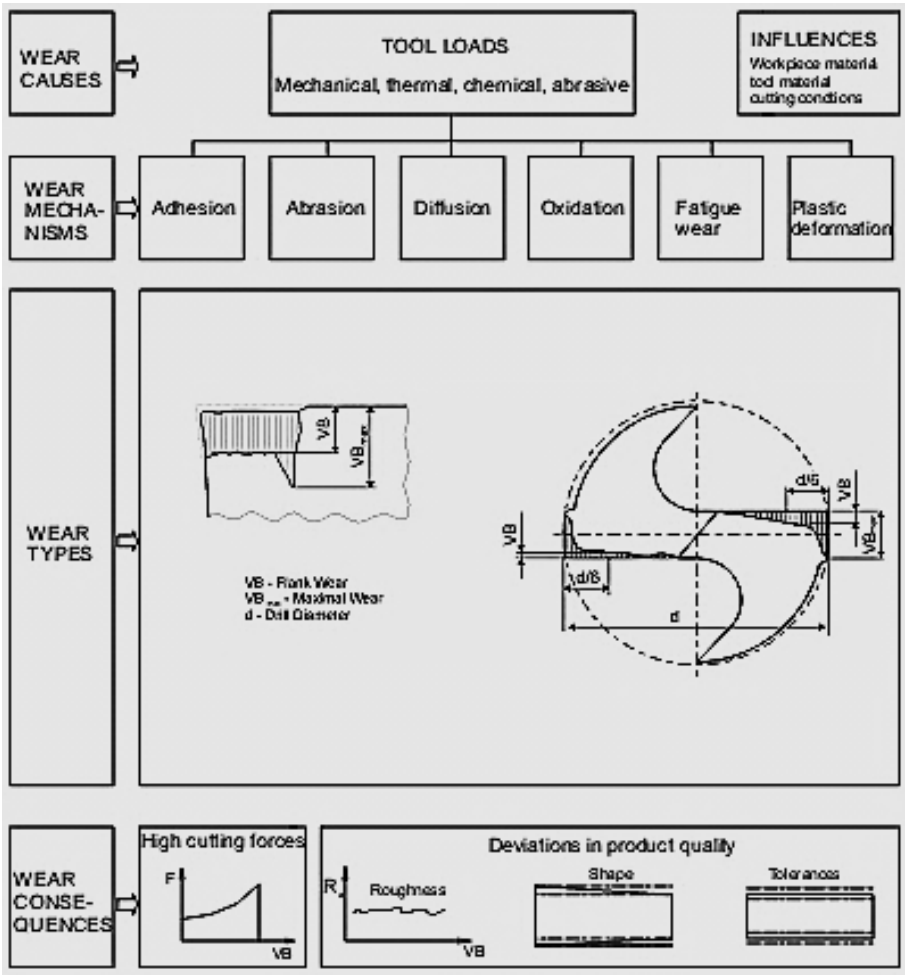

Figure 1-6: An overview of the causes, mechanisms, types and consequences of tool wear [2, 3]

This interfacial region where tool wear happens is not readily accessible either physically or from a process monitoring standpoint during the cut. Further, due to the complexities involved and multiple microstructural wear mechanisms seen in machining, it has been suggested that no unique solution exists for describing metal cutting completely [4]; added to this is the stochastic nature of the machining process as well. Thus, a first step for understanding the effects of different wear mechanisms controlling wear is to comprehensively combine and weight the mechanisms itself.

1.3.2 Traditional Approaches to Mitigate Tool Wear

Tool wear, as an input to cost or time-optimization of process parameters, is an essential factor for maximizing eventual profit. Cost and time contribution of wear in titanium machining is especially appreciable due to the adiabatic nature of the shear banding process, where the majority of heat generated transfers not to the chip and/or to the workpiece, but instead remains in the tool itself. This heat buildup causes loss of hardness and accelerated wear rates of the tool, leading to unexpected catastrophic failures, and thus limiting cutting speeds and material removal rates.

To address the fundamental problem, *i.e.*, to mitigate the (difficult-to predict) tool wear and failure when machining titanium alloys, four traditional solution approaches exist. These are:

1. Tool considerations: The use of more recent ultra-hard tool substrates, more wear resistant coatings, and optimum/special geometries.
2. Workpiece (stock) considerations: The alteration of stock microstructures for better machinability, and development of alternate lower grades of titanium alloys suited to the application (having lower unit raw-material cost).
3. Process conditions: Optimization of cutting parameters, control approaches, and alternate coolant delivery methods such as minimum quantity lubrication (MQL), and high-pressure coolant (HPC).

4. Non-conventional approaches: The use of alternate tool setups such as driven or self-propelled rotary tools, and alternate machining techniques such as ultrasonic machining (USM), and electrically-assisted machining (EAM).

However, each of these approaches has practical implementation issues in addition to a substantial cost increase associated with them.

When considering tool-related solutions, the obvious first option would be to use more advanced/recent substrates; however, even with the development of ultra-hard tool materials such as Polycrystalline Diamond (PCD) and Cubic Boron Nitride (CBN), the most economical cutters for titanium machining are still straight uncoated "throwaway" carbide inserts [5-8]. To get a first-hand feel of the numbers, quotes were requested for these inserts from a tool supplier [9]. The typical prices ranges are: (*i*) Carbide inserts ~ $2-$5/insert, (*ii*) CBN-tipped carbide inserts ~ $45, and (*iii*) PCD-tipped carbide inserts ~ $55/insert. Instead, if going with carbide inserts that are coated or non-straight (having substrate additives), besides the additional costs, the high reactivity is a concern, *i.e.*, common substrate additives such as TaC and TiC, as well as common coatings such as TiN and TiCN are highly reactive to titanium alloys [10], especially at the higher than average operating temperatures. Further, specialized tool geometries have had limited success as well [11], besides the added costs.

When considering workpiece-related solutions, microstructure modifications focused on increasing machinability of titanium alloys have not been explored substantially in the literature. Also, development of lower (and cheaper) grades of

titanium alloys has been hindered by the aerospace-dominated market. Both of these approaches have significant additional costs associated with them as well.

When considering process-related solutions, optimizing process parameters is the most common approach; however operating with the recommended (and conservative) cutting conditions can still result in catastrophic and unpredictable tool wear and failure, in addition to not operating in a cost-optimal regime. Advanced coolant delivery methods such as minimum quantity lubrication (MQL), and high-pressure coolant (HPC) have had some success; however, these have significant additional costs associated with them.

When considering non-conventional approaches, techniques such as ultrasonic machining (USM) have limited applicability, while electrically-assisted machining (EAM) is still in developmental stages. In addition, these special setups and equipment have additional associated costs as well.

1.3.3 Bounding the Problem

Straight uncoated carbide tools are therefore a traditionally accepted tooling solution for machining titanium alloys. This is especially true in the case of the aerospace sector, which frequently avoids coatings and substrate additives to prevent any possible contamination of aircraft parts. Thus, straight uncoated carbide is chosen for study.

Regarding alloy selection, Ti-6Al-4V is the workhorse titanium alloy, accounting for about 50% of the total titanium alloy production [6, 12, 13]. Further, alloy grade

development and characterization is a time and cost-intensive process that not many OEMs and suppliers typically take on. When considering automotive OEMs and suppliers, they will almost usually go with an existing alloy. Thus, Ti-6Al-4V is chosen for study.

Thus the original superset problem, *i.e.*, the difficult-to-predict tool wear and failure when machining titanium alloys, can now be bounded to the smaller WC-Co / Ti-6Al-4V machining tribosystem. Both cost drivers as well as industry needs substantiate studying this popular tool-workpiece combination. Besides, achieving the eventual objective of all tool wear studies, *i.e.*, profitable material removal rates (MRR), substantiate the focus on cheaper carbides versus more advanced tool substrates.

1.4 Motivation #2 – The Current Metrics of Tool Wear are Inconsistent

Wear is a three dimensional (3D) phenomenon. However, from the time of its inception, tool wear has historically always been measured in a single dimension (1D), most commonly as flank wear (*VB*) to eventually denote tool life in minutes of cutting time. Little has changed in the manner of its measurement over the last 100 years; the model by F.W. Taylor is still widespread in industry [14]. This is not because flank wear was completely versatile in accurately representing the wear process, but due to the fact that an adequate and accurate system of tool wear characterization has not been formulated yet.

Though the objective of most, if not all tool wear related studies are in general, to mitigate tool wear, the eventual goal for all such experiments/modeling is to obtain a satisfactory final part. For qualifying as an 'industrially' acceptable part, this usually translates to, (*i*) being dimensionally accurate, (*ii*) surface roughness being within limits, and (*iii*) having desirable surface/sub-surface properties such as minimal damage, minimal residual stresses, etc. Traditional tool wear parameters such as flank and crater wear numbers cannot be physically/directly related to the above mentioned final part requirements, except marginally in the case of extremely simplistic tool geometries such as in some single-point continuous turning scenarios. Instead, tool wear parameters are typically related to the final part requirements indirectly through purely empirical deductions.

1.4.1 Traditional (& Current) Assessment of Tool Wear

In the most general sense, tool failure is defined as the point at which the tool no longer makes economically satisfactory parts. This can be a limiting measure of a tool wear quantifier or indirectly imposed by limiting values of surface roughness, cutting forces, dimensional accuracy, vibration amplitudes, etc. When considering the flank face, the standard measure for the end of tool life for carbide inserts is a uniform average flank depth (VB_B) of about 0.3 mm or a localized wear depth (VB_{Bmax}) of about 0.6 mm [15] as shown in Figure 1-7. These limiting values can vary depending on the industry/application as well. Here, 'VB_C' and 'VB_N' are the nose wear and notch wear

respectively, in accordance with the three-zone cutting edge nomenclature (Zone C, Zone N, and Zone B) that is defined for measuring flank wear.

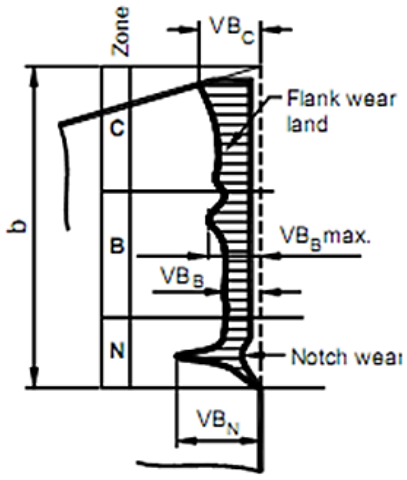

Figure 1-7: Standard flank wear nomenclature [16]

Similarly, wear on the rake face (Zone A) is characterized by parameters such as the crater depth (*KT*), crater width (*KB*), radius of curvature (R_C), the crater start distance (*KL*), and crater middle distance (*KM*) from the tool tip as depicted in Figure 1-8. The common ISO defined limiting value of crater wear (depth) for tool failure is:

$$KT = 0.06 + 0.3f \tag{1.1}$$

Where, *f* is the feed/rev. Note that these parameters and criteria were initially coined for single point turning tools with simple geometric profiles; however, these continue to be used today for all tools, regardless of machining type or drastically different geometries. Again, these limiting values can vary depending on the industry and application. For *e.g.*, aerospace component tolerances are much tighter than for automotive components;

hence, limiting values of crater wear are typically smaller for aerospace machining scenarios versus for automotive scenarios.

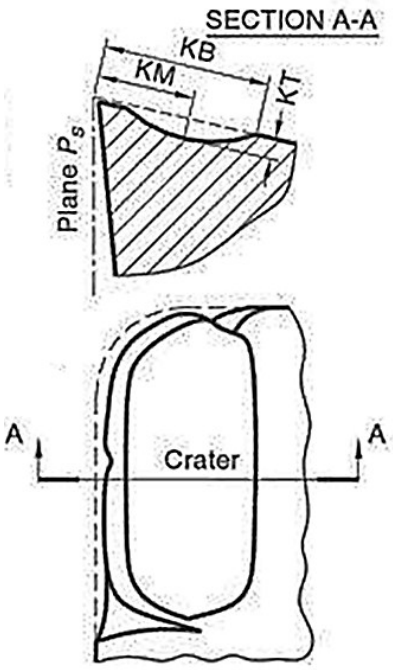

Figure 1-8: Standard crater wear nomenclature [16]

1.4.2 Tool Wear Characterization - A Qualitative Assessment

The ISO standards for tool life testing in milling [17] define 16 distinct tool deterioration phenomena as the coding system for tool life calculation in face milling, and 13 phenomena for end milling. For face milling, the 16 distinct tool deterioration parameters consist of flank wear measures (*VB1*, *VB2*, *VB3*), face wear measures (*KT1*, *KT2*), chipping measures (*CH1*, *CH2*, *CH3*, *CH4*), brittle edge failure measures (*BF*), cracking (*CR1*, *CR2*, *CR3*), flaking (*FL*), plastic deformation (*PD*) and catastrophic failure (*CF*). A typical flaking (*FL*) pattern on a face-milling insert, where tool fragments have

been lost in the form of flakes from the tool surface is depicted in Figure 1-9. For end milling, the 13 tool deterioration parameters consist of flank wear measures (*VB1*, *VB2*, *VB3*), face wear measures (*KT1*, *KT2*), chipping (*CH1*, *CH2*, *CH3*), flaking (*FL*), cracking (*CR1*, *CR2*, *CR3*) and catastrophic failure (*CF*). A stair-formed face wear (*KT2*) pattern on an end-mill flute, where the maximum scar depth is on the tool flank is depicted in Figure 1-10.

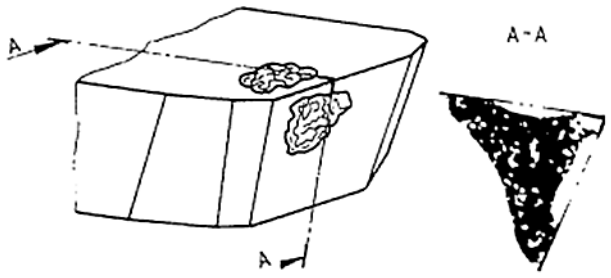

Figure 1-9: A face mill wear pattern: Flaking (*FL*) on face-mill [17]

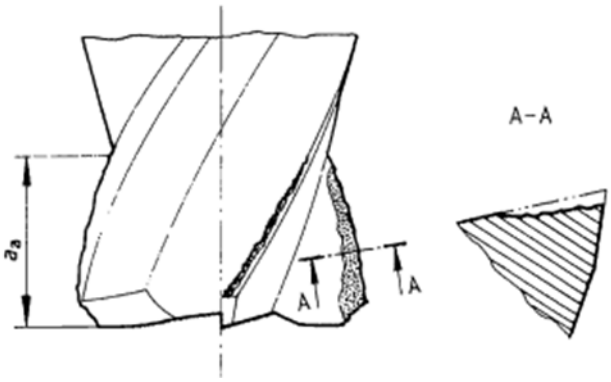

Figure 1-10: An end mill wear pattern: Stair-formed face wear (*KT2*) on end-mill [17]

Note that any tool wear status is almost always a combination of these parameters, some of which are quantitative, and the others qualitative. Thus, when describing the wear condition of a cutting tool as a diverse combination of these parameters, it is easy

to lose track of the evolution and interactions of each of these changing deterioration phenomena. Also, between two instances of tool condition measurement, the parameters needed to represent the tool status need not have to be the same. Additionally, two observers may not always choose the same set of parameters to represent an advanced tool wear status, nor does a particular wear parameter value represent the same wear condition for any two instances.

Such an instance of an inconsistent tool wear quantification scenario is schematically illustrated in Figure 1-11. The unequal rubbing patterns on the milling insert flank faces in (A) and (B), as well as the material worn away in (C), are all quantified as a single value of the traditional flank wear metric (*VB*), (as assessed by Figure 1-7); however, the wear status is not similar. Hence, strictly speaking, traditional tool wear assessments conducted by two independent investigators cannot be consistently or absolutely compared.

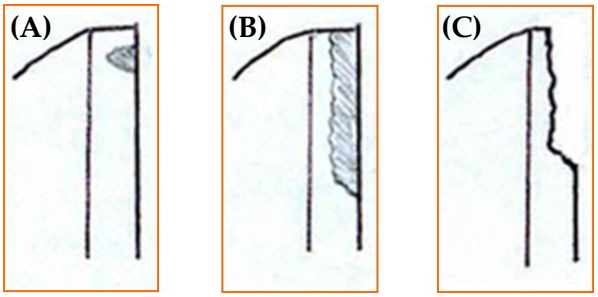

Figure 1-11: One among many inconsistent tool wear quantification scenarios, where rubbing wear is indistinguishable from material worn away

Such qualitative assessments of current tool wear quantifiers [18] show that traditional wear-parameters are not sufficient to satisfactorily represent the wear of most

tools; especially ones catered to 'difficult-to-machine' titanium alloys due to their complex geometric profiles. Thus, even with extensive ISO standardization [17], machining tool wear is still very ambiguous; hence, results are not directly comparable.

Thus, a more versatile quantification of tool deterioration needs to be formulated that is independent of the instance of measurement, the measurement system, and the combination of deterioration parameters selected to quantify it. Rightly so, machining tool wear has been historically described as "difficult to define without ambiguity" [19].

It is to be noted that such deficiencies in describing the tool condition might not be very significant for materials having high machinability such as aluminum and its alloys, which usually exhibit a 'fairly linear' tool deterioration response with cutting time. However, for materials generally classified as "difficult-to-machine," such as titanium and its alloys, standard tool life models eventually break down [16, 20-22], and these inadequacies are very pronounced.

1.4.3 Additional Difficulties due to Unique Tool Geometries

In the machining of traditionally difficult-to-machine materials such as titanium and its alloys, the wear behavior has been observed to be drastically different (more aggressive) than those of common steels and aluminum alloys. Consequently, tools with specific edge-profile requirements are recommended for machining titanium alloys [6, 23]; some of these include the use of very sharp tools (to reduce heat generation [24]), and high positive rake angles (for a shorter contact length between the chip and tool face

[24], as well as to reduce cutting forces and hence consume less power [25]). The complexity of these cutting edge profiles and the varying dominance of multiple wear mechanisms, make the development of relationships between the geometry of new and worn tools as well as studying their wear evolution, challenging. As a result, the characterization of the wear of tools used for difficult-to-machine materials, especially titanium alloys, has lagged behind those of tools used for steels and aluminum alloys.

1.5 CONCEPT / APPROACH

The concept of volumetrically quantifying wear has been successfully used in biomechanics to predict wear in artificial knee joints by combining joint kinematics, loads and material properties [26, 27]. The 3D wear profiles of these tibial inserts were predicted from wear models that were based on contact pressures and slip velocities of individual differential elements obtained by multi-body dynamic simulations. Polygonal surface models of new and worn tibial inserts were compared to obtain damage volumes. Refinement of this model and methodology is expected to help predict in-vivo joint wear even better. Though there is significant difference between biomechanics and machining regarding the dominant mechanisms (galling vs. a combination of wear mechanisms), extent of wear (mild vs. severe), and scales involved (micro vs. micro/macro), this concept can be adopted for understanding and modeling tool wear more accurately than at present.

Figure 1-12 illustrates this concept extended to machining tool wear characterization, modeling and application. Figure 1-1(A) shows contour maps of the wear damage on a tibial insert predicted by wear model simulations. The color bar indicates the damage depth in mm and the stars indicate locations of maximum wear. This approach can be expanded to machining tool wear by defining a number of geometric coefficients (*fa*, *fb* and *fc*) to characterize the damage volume as shown in Figure 1-12(B). Note that these geometric coefficients have been chosen arbitrarily for visualization purposes. Figure 1-12(C) shows the concept plot of a VTW and rate model that can relate the (geometric) wear coefficients (*fa*, *fb* and *fc*), as well as the actual tool volume worn away (V_{Worn}) and volumetric tool wear rate ($\dot{V}_{worn}$) to both macro and micro tool/process parameters. These variables can include common macro process factors such as surface speed (*V*), feed rate (*f*), cutting length (*l*), cutting depth (a_p), and radial immersion (a_e). Further, macro tool factors such as tool edge radius, rake angle, and relief angle, as well as micro tool factors such as grain size (d_g), distribution or spread of grain size (Δd_g), percentage Cobalt (*%Co*), and Contiguity (*C*), can be included as well. These geometric wear coefficients as well as the volume/rate tool wear can then be related to part requirements and process monitoring variables such as surface roughness (R_a), forces (*F*), vibration amplitudes and frequencies (*Hz*), as shown in the concept plot, Figure 1-12(D). Such relationships can help generate predictive wear maps which in turn can be deployed within real-time process control of titanium machining for profitability (Figure 1-12 (E)).

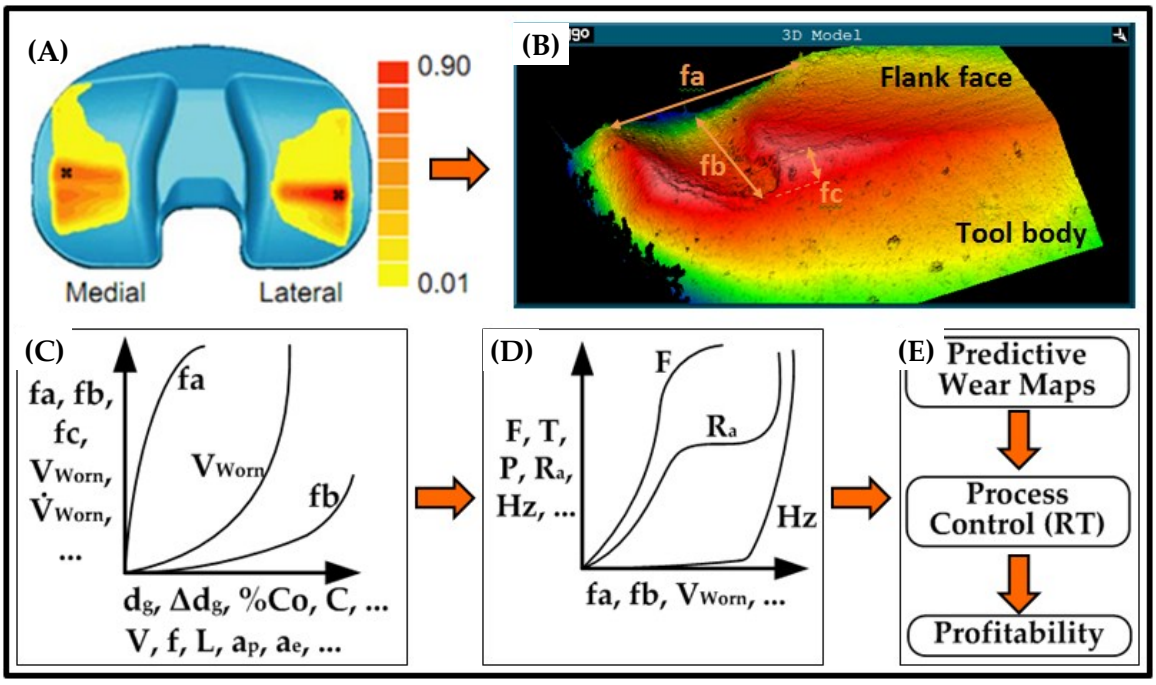

Figure 1-12: VTW modeling concept: (A) Contour map of predicted wear on a tibial insert [20], (B) Wear volume characterization of the 3D model of a worn milling insert, (C) Concept plot relating wear coefficients/volumes to tool & process factors, (D) Concept plot relating part and process monitoring variables to wear variables/volumes, and (E) Path to profitability

By enhancing tool wear from a 1D to 3D concept in this manner, the added spatial evolution information will help better relate tool and process factors to volumetric tool deterioration. This more accurate predictive capability can in turn be applied to the tribosystem for maximizing profit. Thus, this novel approach of quantifying tool wear from a more comprehensive perspective than how it has been done over the last 100 years, provides good potential for better understanding machining wear mechanics.

1.6 ORGANIZATION OF THIS DISSERTATION

This introductory chapter defined the objective of this work, as well explained the motivations and research approach for this work. Following this introduction is Chapter 2, which covers the relevant background for this work in varying detail. Chapter 3 lays out the research methodology by outlining the research questions, associated tasks, and outputs. Chapters 4 and 5, cover research questions 1 and 2 respectively. Finally, Chapter 6 assembles the main conclusions drawn from this work, as well as lays out recommendations for future work. A number of appendices are included to provide supplementary information. References and a list of publications generated from this work are appended to the dissertation.

CHAPTER TWO

2. BACKGROUND

This chapter covers the relevant background for this work. The background topics are grouped into five main sections for organization:

1. The Machining Process
2. Tool Material: Tungsten Carbide with Cobalt Binder (WC-Co)
3. Workpiece Material: Titanium Alloy (Ti-6Al-4V)
4. The Machining Tribosystem
5. Tool Deterioration

2.1 THE MACHINING PROCESS

Machining is one of the most prevalent among manufacturing processes, as it is used for primary processing and finishing of simple and complex profiles for low or high production volumes with good finishes, tolerances and generally low tooling costs and short setup times.

2.1.1 Machining Economics

The drive in almost any machining operation is to maximize productivity, which is usually a trade-off between shorter cycle times and too many tool changes, for which various optimization procedures exist. A plot of the machining cost per part that is calculated for a typical machining scenario is depicted in Figure 2-1. Note that, the

process of reducing the total cost per part by varying the cutting parameters (speed, feed, depth of cut, etc.) consists mainly of two conflicting factors: reduced cycle time and too many tool changes. An optimal cutting speed (V^*) can be solved for analytically, however it is usually unlikely that all factors contributing to the cutting process can be included satisfactorily. This conflict between reduced cycle time and too many tool changes is especially pronounced in the case of machining titanium alloys. A high tool wear rate, common when machining titanium result in more number of tool changes pointing to a reduction in machining parameters (speed, feed, depth of cut, etc.), however, such an action will increase the cycle time and hence the cost per part.

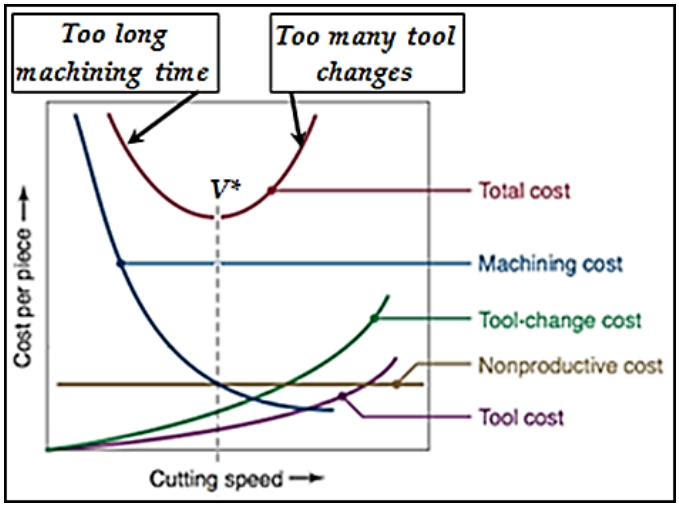

Figure 2-1: Qualitative plot of process optimization for the cost per piece of a typical machining scenario. Note that there is an optimum cutting speed (V*) for minimum cost [28].

The fundamental idea of machining economics is simply to obtain the lowest possible cost per part that is manufactured while maintaining the quality standards of the product. The material and processing cost of a component can be determined by

combining the raw material cost, the manufacturing cost elements and a number of other parameters. The fundamental application of a manufacturing cost model is to estimate the total cost of a complex process by considering the individual tasks and cost elements that define time-based consumption of resources. These models vary drastically across the type of manufacturing processes selected for fabricating the component as well. Elaborate cost models in varying detail have been developed for many of the common manufacturing processes like casting, forging, machining, welding, powder metallurgy, etc., and can be very elaborate as needed [28-34].

2.1.2 Mechanics

Machining is a complex process involving high strain/rate shear with two operations occurring simultaneously in close proximity with strong interaction: (*i*) large strain plastic deformation in a concentrated shear zone and, (*ii*) material transport along a heavily loaded region of relative chip-tool motion [35]. Among the various types of machining, the two relevant types for this work are turning and milling.

2.1.2.1 Turning

Turning is one among the most common types of machining. The workpiece (stock) material is held in the chuck of a lathe and rotated. The tool is held rigidly in a tool post and moved at a constant rate along the axis of the bar, cutting away a layer of metal to form a cylinder or a surface of more complex profile [36]. A schematic of a typical tuning operation as well as an image of actual bar turning is shown in Figure 2-2(A) and (B).

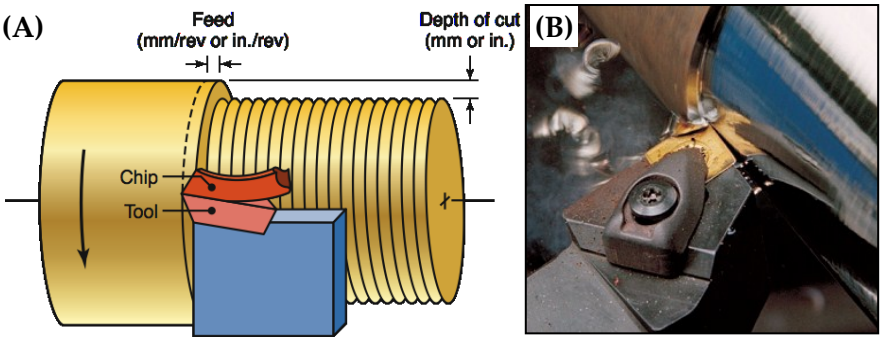

Figure 2-2: (A) Typical turning operation on a lathe, where the feed is in mm/rev or in./rev, and depth of cut is in mm or in. Note that feed in turning is equivalent to the depth of cut in orthogonal cutting (Figure 2-4), and the depth of cut in turning is equivalent to the width of cut in orthogonal cutting [28], (B) Image of an actual bar turning operation [37].

2.12.2 Milling

Milling is a process of producing flat and complex shapes with a multi-tooth milling cutter. The axis of rotation of the cutting tool is perpendicular to the direction of feed, either parallel or perpendicular to the machined surface. Milling is an interrupted cutting operation where the teeth of the milling cutter enter and exit the work during each revolution. This interrupted cutting action subjects the teeth to a cycle of impact force and thermal shock on every rotation [38].

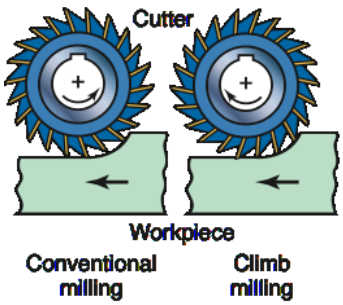

Figure 2-3: Illustration showing the difference between conventional milling and climb milling [28]. Climb milling is recommended for machining titanium alloys.

2.1.3 Cutting Forces & Temperatures

This research work primarily deals with orthogonal turning operations since they are more 'steady-state' compared to milling, and hence more suitable for study (However, some work is presented from milling experiments on titanium alloys as well).

2.1.3.1 Forces

The schematic for single-point turning is given in Figure 2-4, where the chip-formation process is essentially 2D.

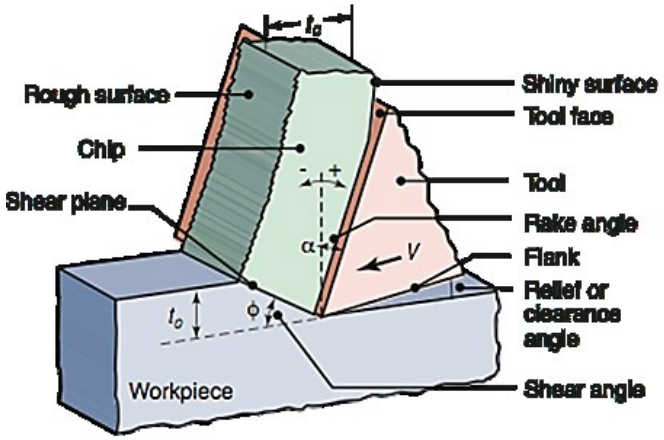

Figure 2-4: Schematic illustration of orthogonal turning where the chip formation process can be considered to be two-dimensional [28]. Note the well-defined shear plane – such a treatment is also known as the Merchant model.

Due to the large strain plastic deformation in concentrated shear zone as well as material transport along a heavily loaded chip-tool interface, the tool experiences very high forces which can be resolved into cutting (F_c) and thrust (F_t) forces on the tool, or normal (N) and friction (F) forces on the tool-chip interface as shown in Figure 2-5(A).

Figure 2-5(B) shows the 3D schematic of the turning operation showing the various forces involved and their relation to Figure 2-4.

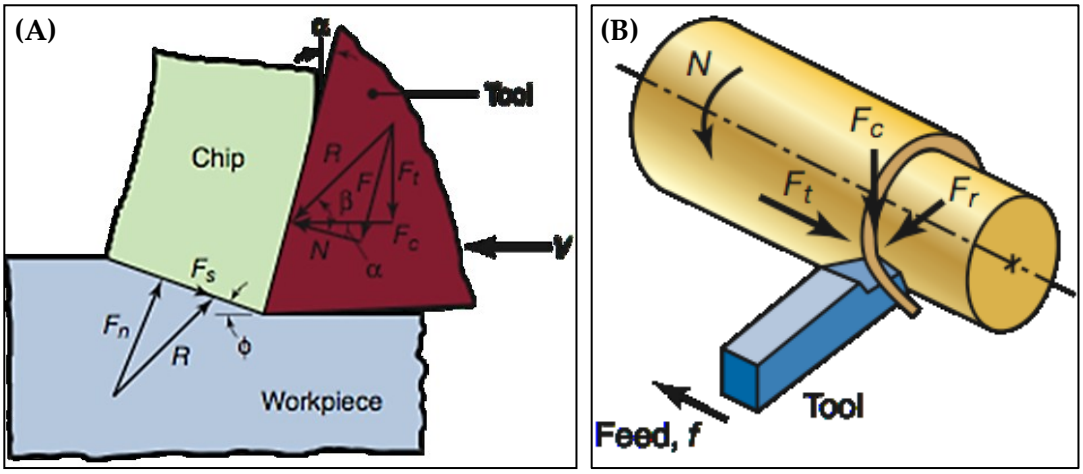

Figure 2-5: (A) Forces acting on a cutting tool in two-dimensional turning – these can be resolved into normal and shear force on the tool-chip interface or cutting and feed forces on the tool [28]. Note that the resultant forces, R, must be collinear (Source: After M.E. Merchant). Forces can also be resolved at the primary shear zone as F_n and F_s. Also, β is the friction angle, (B) 3D illustration of cutting forces [28]. F_c is the cutting force, F_t is the thrust or feed force (in the direction of feed), and F_r is the radial force that tends to push the tool away from the workpiece being machined at a rotational speed N.

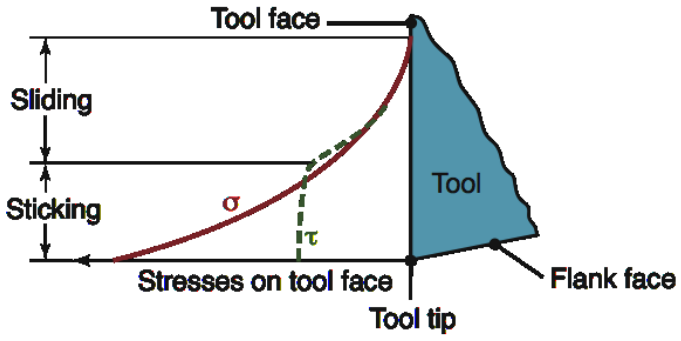

Figure 2-6: Schematic illustration of the distribution of normal and shear stresses at the tool-chip interface (rake face). Note that, whereas the normal stress increases continuously toward the tool tip, the shear stress reaches a maximum value and remains fairly constant (sticking).

Further, when considering the force variation along the rake face, it has been observed that normal stress (normal to the tool face) increases consistently toward the tip of the tool, while shear stress reaches a maximum value and remains fairly constant toward the tool tip – this is illustrated in Figure 2-6.

2.1.3.2 Temperatures

In metal cutting, nearly all of energy dissipated in plastic deformation is converted into heat which in turn raises the temperature in the cutting zone. The three main sources of heat in machining are [38]:

1. Plastic deformation by shearing in the primary shear zone (heat source Q_1)
2. Plastic deformation by shearing and friction on the face (heat source Q_2)
3. Friction between chip and tool on the tool flank (heat source Q_3)

This generated heat is mostly dissipated by the following heat sinks (Figure 2-7):

1. The discarded chip carries away about 60~80% of the total heat (q_1)
2. The workpiece acts as a heat sink drawing away 10~20% heat (q_2)
3. The cutting tool will also draw away ~10% heat (q_3)

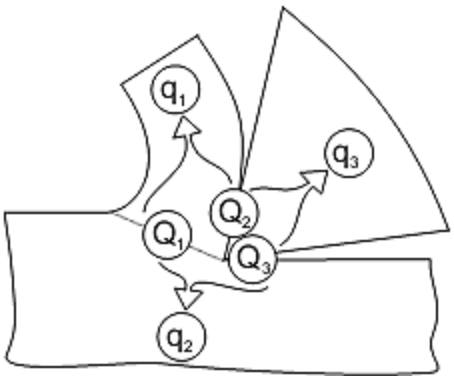

Figure 2-7: The balance of heat generation and heat dissipation in metal cutting [38]

A typical distribution of temperature in the cutting zone is depicted in Figure 2-8. Note the severe temperature gradients within the tool and the chip, and that the workpiece is comparatively cool. Typically, the majority of the heat is carried away from the cutting zone by the chip as shown in Figure 2-9.

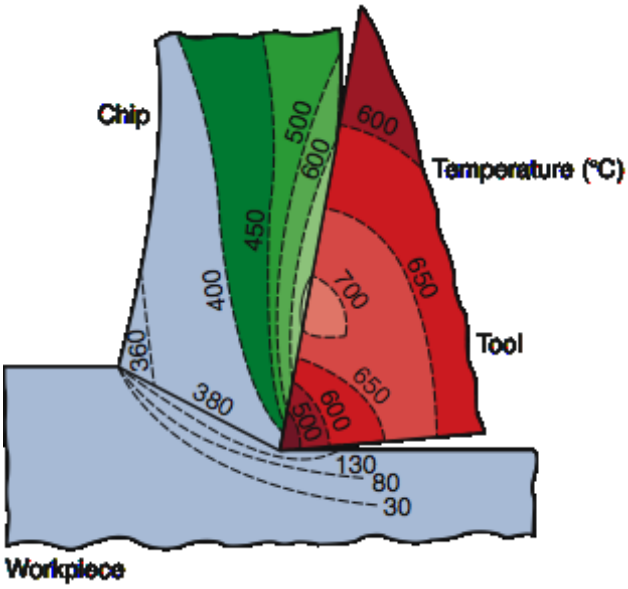

Figure 2-8: Typical temperature distribution in the cutting zone [28]. Note the severe temperature gradients within the tool and the chip, and that the workpiece is relatively cool (Source: After G. Vieregge).

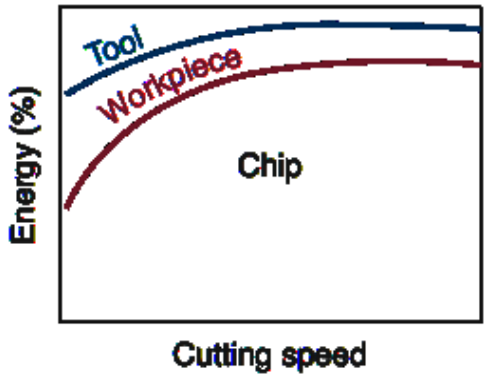

Figure 2-9: Proportion of the heat generated in cutting transferred to the tool, workpiece, and chip as a function of the cutting speed [28]. Note that most of the cutting energy is carried away by the chip (in the form of heat), particularly as speed increases.

It is known that cutting speed is one of the most important operating variables influencing tool temperature and hence tool life [35, 39, 40]. Average temperature conditions can be approximated by [28]:

$$T = \frac{1.2Y_f}{\rho c}\sqrt[3]{\frac{Vt_o}{K}} \tag{2.1}$$

where, T is the mean temperature of tool-chip interface (^{0}F), Y_f is the flow stress of the material (psi), V is the cutting speed (in./sec), t_o is the depth of cut (in.), ρ and c are the density and specific heat respectively of the workpiece stock respectively, and K is the thermal diffusivity (ratio of thermal conductivity (k) to volumetric specific heat) of the workpiece.

When considering titanium alloys, it is a high-strength material having a high specific cutting energy with poor conductivity and low density. This combination of material properties, result in higher tool temperatures, requiring much higher tool hot

hardness. Thus, temperatures increase with the cube root of cutting speed, often exceeding 1000 ^{0}F when machining titanium alloys. Along with this added heat coming in from the cutting zone, the material properties of even the best of tools eventually deteriorate with increasing temperatures [41]. This combination of intense added heat as well as deteriorating tool material properties causes the common catastrophic failures experienced when machining titanium alloys.

2.2 TOOL MATERIAL: TUNGSTEN CARBIDE WITH COBALT BINDER (WC-CO)

Tungsten Carbide (WC) is a cermet (a composite material composed of ceramic and metallic compositions), and is one of the most commonly used cemented carbides or hard metals. With Cobalt (Co) as a binder, they comprise the majority of turning and milling cutting tools. The microstructure of a WC-Co cutting insert tool (Sandvik CNMG 12 04 08-QM (H13A grade)) that was used for turning titanium alloy is shown in Figure 2-10(A) as a Back Scattered Electron (BSE) image. The corresponding Energy Dispersive X-Ray Spectroscopy (EDS) on the area (Figure 2-10(B)), helped quantify the volume fraction of Co in this case to be about 5%. Being near the cutting surface, note that a small amount of titanium (~2%) was detected on the WC-Co substrate – this is possibly diffused titanium from the Ti-6Al-4V workpiece.

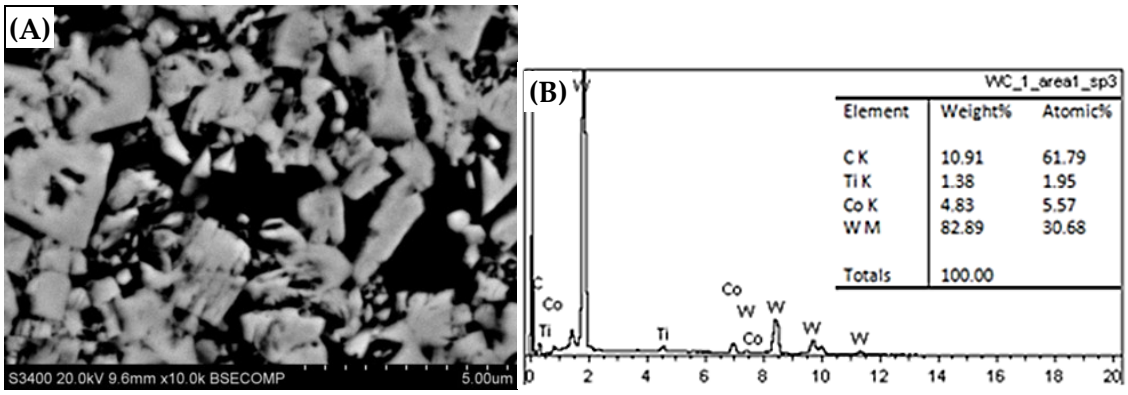

Figure 2-10: Microstructure of WC-Co tool substrate (10000X BSE Image) and EDS of area with elemental composition

2.2.1 Types of WC Tools

Tungsten Carbide – Cobalt (WC-Co) tools have evolved into two general categories: (1) The ISO K-type for non-ferrous metals (containing only WC and Co, or straight carbides), and (2) The ISO P-type for ferrous metals (some WC replaced with compounds such as TiC, TaC, and NbC). Under the ANSI classification, these are also categorized as C-type grades [8, 42, 43]. Further, there is also an ISO M-type grade recommended for ferrous and non-ferrous metals. As mentioned earlier, the K-type tool substrates are called 'straight' carbides and these contain hard WC-grains and about 4-12% of the softer or ductile Co-binder. Carbide tools containing less than 10% Co are capable of resisting plastic deforamation upto at least 700^0C. One of these straight carbides from Sandvik with about 10% Co concentration was selected for this work.

2.2.2 Microstructure

Modern grades of cemented carbides very often consist of a carbide grain sizes less than l μm. The two carbide grains sizes that are analyzed in this work are of grain sized less than l μm as well. There are two main phases in a WC-Co alloy: (*i*) the carbide phase, and (*ii*) the binder phase. These are detailed below:

2.2.2.1 Carbide Phase

Tungsten Carbide has a highly anisotropic structure. The anisotropic crystal shapes develop during crystal growth into flat triangular prisms or polygonal shapes with well-defined boundaries and truncated edges. Crystal defect densities in WC are fairly low, partly due to the residual stresses during sintering, which are accommodated by plastic deformation. Figure 2-11(A) shows the TEM micrographs [8] of WC-10%Co displaying the straight faceted WC grain, and . Figure 2-11(B) shows the WC/WC interface.

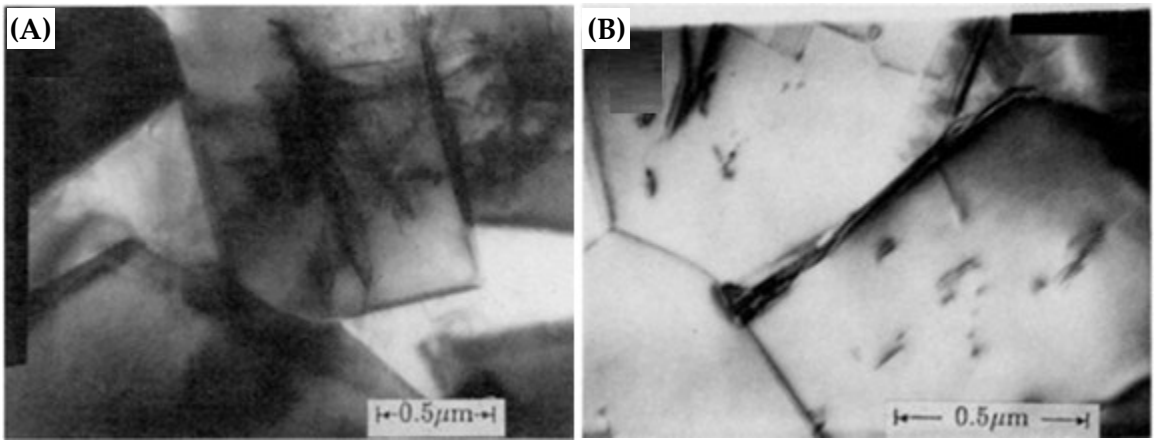

Figure 2-11: TEM micrographs of WC-10%Co (sintered at 1425C) showing (A) straight faceted WC grain, (B) WC/WC interface [8]

2.2.2.2 Binder Phase [8]

Cobalt is the most extensively used bonding metal or binder, and it is present in the microstructure as a continuous thin film separating the carbide particles. The Cobalt phase is normally associated with high dislocation density and stacking faults unlike the carbide phase aiding in deformation. The toughness of WC-Co tools is because of the ductility imparted by this cobalt phase in addition to the strength provided by the harder WC phase. At high percentages of Co, a cobalt skeleton forms in the microstructure in addition to the carbide skeleton. Cobalt is the most commonly preferred binder over iron and nickel, due to the higher solubility of WC in cobalt.

2.2.2.3 Third Phase in WC-Co Tools

The morphology and properties of the WC-Co tool and its phases have been quantified in numerous studies [8, 43-45]. There have been some conflicting studies regarding the presence of Cobalt at WC/WC interfaces for varying concentrations of the Cobalt binder. Among them, some authors observed a third phase, or an intermediate layer outside the WC grains. Regarding the intermediate layer however, there are conflicting theories supporting the “Skeletonized-Carbide” or “Dispersed-Carbide” structures common in explaining WC-Co behavior based on percentage cobalt). The Skeletonized-Carbide model describes the WC grains being distributed as one contiguous phase or large conglomerations of such WC grain clusters. The Dispersed-Carbide approach describes WC grains to be dispersed on their own in the matrix with Cobalt binder around them.

However, with the aid of STEM/EDS in later studies [46] a small amount of dispersed Cobalt was found around all WC grains, regardless of the percentage Co concentration. The presence of dispersed Cobalt around all WC grains can thus explain the high transverse rupture strength (TRS) of WC-Co tools even at very low %Co concentrations, leading to a compromise between the two theories. This intermediate layer is estimated to be about a monolayer thick with a density of about 9g/cm^3 [44].

The estimated atomic radius of Cobalt is 1.52 pm (1.52e-7 mm) [47]. So, the atomic diameter is 3.04 pm. Thus one monolayer (ML) is about 3.04 pm thick – such small dimensions cannot be easily seen using a standard SEM.

2.2.2.4 Eta Phase & Precipitates

Further, carbon content of cemented carbides must be controlled to within vary narrow limits, typically ±0.04 weight percent, to prevent formation of brittle lower carbides (η phase on the low carbon side) and carbon precipitates on the high carbon side (as free and finely divided graphite). In small amounts, these do not adversely affect machining. The eta-phase is recognizable as black portions in the microstructure (Figure 2-12).

Deficiency of Carbon forms a series of double carbides (η phase) (Co3W3C, Co6W6C), which causes severe embrittlement, *i.e.*, the dissolution of the original WC into Co binder. This gives rise to irregularly shaped regions in the microstructure.

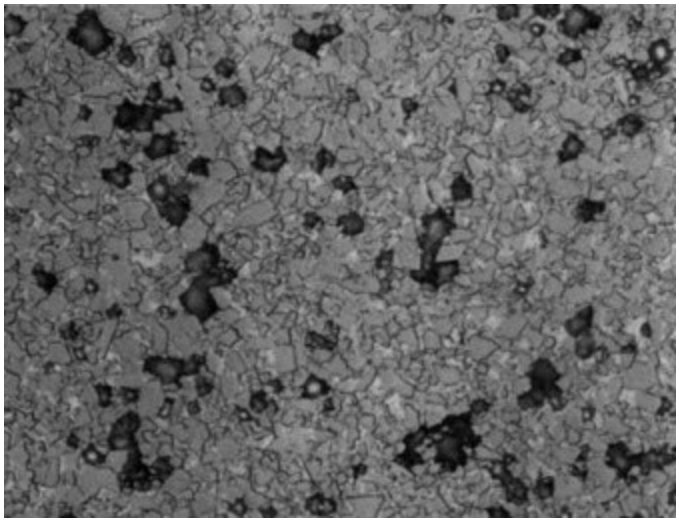

Figure 2-12: Microstructure of cemented carbide (85.5 WC-12 Co-3.5 Cr) showing a well dispersed eta phase, (WC grain size 3μm) (X 1500) [8]

Further, if graphite particles are present, they will form a greatly strained sub-surface layer of lower shear strength material. This weak surface layer of large oriented plates of graphite can prevent the formation of strong bonds with the tool (reducing adhesive wear), and also act as a diffusive barrier for carbon from tool to workpiece [48].

2.2.3 Thermo-Mechanical Properties & Response of WC-Co Tool Materials

The major constituent of cemented carbides consists of fine WC particles which are relatively hard and brittle, and the minor constituent is a cobalt-rich binder phase which is relatively soft and ductile [8]. The typical mechanical properties of interest for WC-Co tool as a function of the %Co content is shown in Figure 2-13. Tensile strength in bending is increased by Co content (at least about 6% Co is needed for a tool be sufficiently tensile and hence be practical). The predominant parameters of interest of

WC-Co tools are their Cobalt concentration (%Co), Carbide grain size (d_g), distribution of mean Carbide grain size (Δd_g), bonding layer thickness and carbon balance which determine their hardness (strength) and Transverse Rupture Strength (TRS), which is a measure of its toughness, or the amount of energy it can absorb until fracture.

With temperature, just as with any other tool material, the hardness of carbides decreases. WC tools are generally usable until about 800 ^{0}C, beyond which the hot-hardness is unsatisfactory. A plot of the variation in hardness of carbides relative to other common tool materials is shown in Figure 2-14. These temperatures are very easily exceeded when machining titanium alloys, especially at higher cutting speeds.

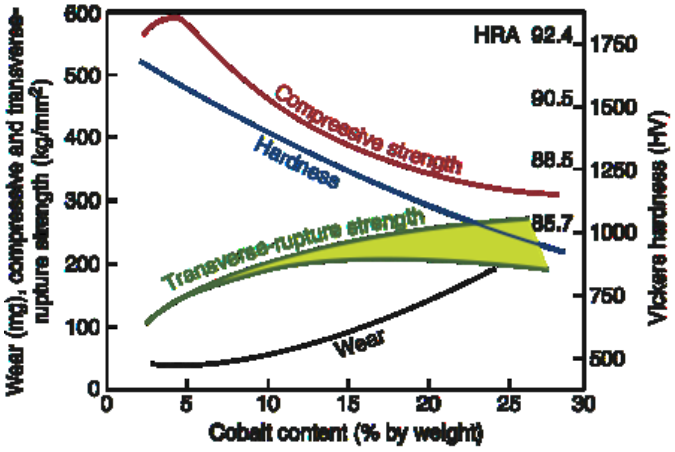

Figure 2-13: The effect of Cobalt content of on the general mechanical properties of WC-Co cutting tools [28]. Note that hardness is directly related to compressive strength and hence, inversely to wear

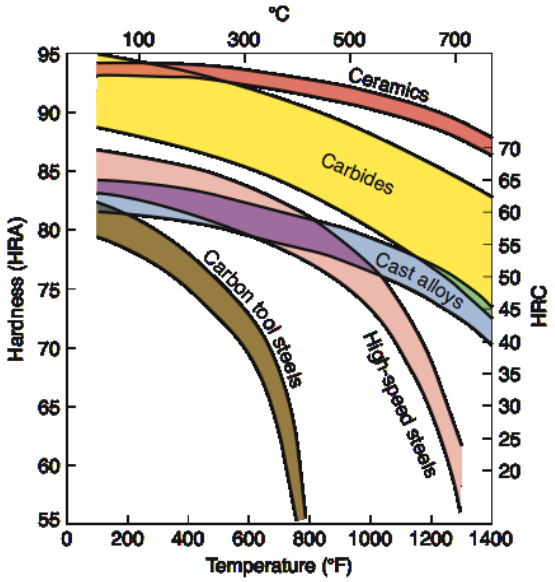

Figure 2-14: Hardness of various cutting-tool materials as a function of temperature (hot hardness) [28]. The wide range in each group of tool materials results from the variety of compositions and treatments available for that group. The hot hardness of carbides decrease drastically after about a 1000^{0}C; during titanium machining, such temperatures can be frequently exceeded and hence temperature-controlled wear is a significant mechanism affecting carbide tools, especially with increasing relative surface speeds.

2.3 WORKPIECE MATERIAL: TITANIUM ALLOY (TI-6AL-4V)

Titanium is the 7th most abundant metal and the 4th most abundant structural metal in earth's crust behind aluminum, iron and magnesium. Titanium and its alloys are considered as alternatives in many engineering applications due to their superior properties such as retained strength at elevated temperatures, high chemical inertness and resistance to oxidation. Titanium has traditionally been utilized as a lightweight, very strong and exceedingly corrosion resistant material in the aerospace industry, electric power plants, seawater desalination plants, and heat exchanges. Also, it has been

used in industrial applications such as petroleum refining, nuclear waste storage, food processing, pulp and paper plants, and marine applications [49]. Further, titanium alloys are a commonly preferred material for biomedical applications and in medicine due to their excellent bio-compatibility. Titanium alloys also find wide use as an important pigment for industrial, domestic and artistic applications, as it is extremely opaque and sunfast, and hence find use in sunscreen applications [50].

2.3.1 Alloys of Titanium

All of the 100+ titanium alloys are classified as α (HCP), β (BCC), or α-β alloys. A majority of Ti-6Al-4V (α+β) is slow-cooled into the two-phase region from β-transus for α-phase nucleation/grain-growth resulting in a lamellar micro-structure (Figure 2-15) often called plate-like alpha.

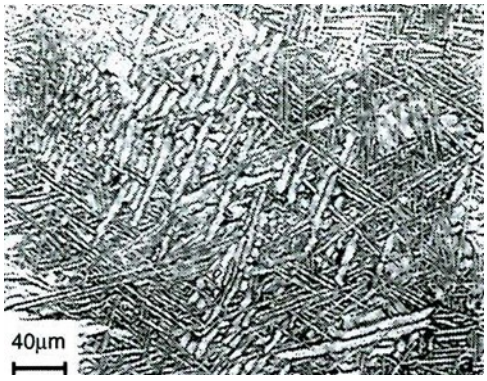

Figure 2-15: Lamellar structure of Ti-6Al-4V [6]

The main factors that contribute to the poor machinability of Ti-6Al-4V are its combination of low thermal conductivity and elastic modulus, and high chemical reactivity and temperature strength. The low thermal conductivity aids in forming

adiabatic shear bands at high strain rates (as in machining), and results in the majority of the generated heat flowing into the tool edge (about 80%) [51], rather than the chip or the stock. Additionally, the combination of a low modulus of elasticity, high yield stress, susceptibility to work-harden, and tendency to react with tool materials, causes rapid/catastrophic wear.

2.3.2 Microstructure

When titanium alloys are cooled at sufficiently low rates from the β phase field into the α+β phase field, the α phase, first nucleates at preferential sites and continue to grow into the β grain as parallel plates. The resulting grain structure is the common lamellar microstructure of Ti-6Al-4V (Figure 2-15). Such lamellar microstructures can be obtained in the final steps of the processing route by an annealing treatment in the β phase field; hence they are also called "β annealed" structures. In the schematic drawing of the whole processing route (Figure 2-16), this corresponds to step III. This recrystallization temperature in step III is usually kept within 30-50 °C above the β-transus to maintain control of the β grain size to obtain a grain size of about 600 μm for fully lamellar microstructures. The cooling rate from the β phase field in step III determines the characteristic features of the lamellar microstructure, such as the lamellae size, colony size, and the thickness of layers [52].

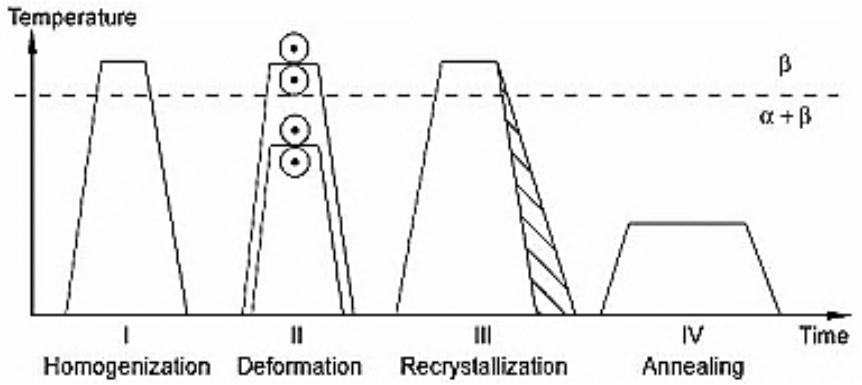

Figure 2-16: Schematic of processing route for β annealed structure [52]

2.3.3 High Strain & Strain-Rate Response - Adiabatic Shear Bands in Ti-6Al-4V

Many high-strength metallic alloys such as dual-phase α+β titanium alloys, when deformed at high strain rates, are susceptible to undergo a shear strain localization process, referred to as adiabatic shear banding. This is often accompanied by an abrupt loss of load-carrying capacity (*i.e.*, load instability). These have been observed in high strain rate phenomena such as in ballistic impact, machining, high strain rate compression, explosive fragmentation of thin-walled containers, etc.

In Ti-6Al-4V, adiabatic shear bands appear as narrow discrete surfaces of highly sheared material, a few μm wide, recognizable by distorted grains or texture lines appearing as bands. These shear zones often act as precursor sites for eventual failure of the material. Adiabatic shear results from plastic instability arising when the combined effects of strain and strain rate hardening are outweighed by the thermal softening caused by effectively adiabatic plastic deformation and heating.

Shear localization can be trigged by external geometric factors, resulting from stress and strain concentration, or material internal microstructural factors, arising from structural softening mechanisms. The occurrence of shear instability is usually followed by failure with low ductility and toughness. A number of investigators have developed constitutive models for predicting shear banding based on critical conditions for plastic flow instability (critical strains/strain rates). Material scientists are focused on understanding how the microstructural parameters influence the occurrence of shear instability so as to design a material for better performance [53].

Over the years a number of investigators have explored and characterized shear instability pertaining to titanium alloys which are especially susceptible to shear localization and adiabatic heating [54-61]. General sub-areas of interest/conflict span the differences in the grain size, micro-hardness and cavity shape/distribution within the shear band, along its edges and in the parent metal (three distinct zones in α+β alloys). Also, conflicting views on the occurrence of recrystallization/phase transformation within the shear bands exist. These are not very easy to examine microscopically due to the very thin region of shear deformation localization. The characteristic spacing and periodic distribution of the bands have been found to be a function of material parameters. Other observations have been made regarding the varying thickness of the bands, and shape/size of the coalescing voids as well as fracture mechanisms within shear bands on titanium alloys. In addition significant work has been done in the characterization of shear band spacing and organization as well as modeling the shear

band as a propagating well-defined front. More recent approaches of characterizing shear localization involve the stored energy of cold work as the driving force for microstructural rearrangement by dynamic recrystallization or as a critical total strain energy density, instead of being the result of thermal softening as universally assumed.

2.4 THE MACHINING TRIBOSYSTEM

2.4.1 Definition of Terms

2.4.1.1 Tribosystem

Tribology is defined as "the science and technology of interacting surfaces in relative motion and of the practices related thereto" [62]. Tribology embraces the scientific investigation of all types of friction, lubrication, and wear. Applying a systems-level of thinking or analysis to the tribological process, leads to an input-output description of the process, *i.e.*, a tribosystem can be considered as a closed systems with a number of inputs and outputs, along with which are affected by some disturbances as well as experience some losses as shown in Figure 2-17.

For analyzing the machining tribosystem, a relevant portion of the system can be cut out by an envelope that is located as closely as possible to the elements in the tribological area of interest, *i.e.*, the tool chip interface region and/or the tool-workpiece region where tool wear occurs.

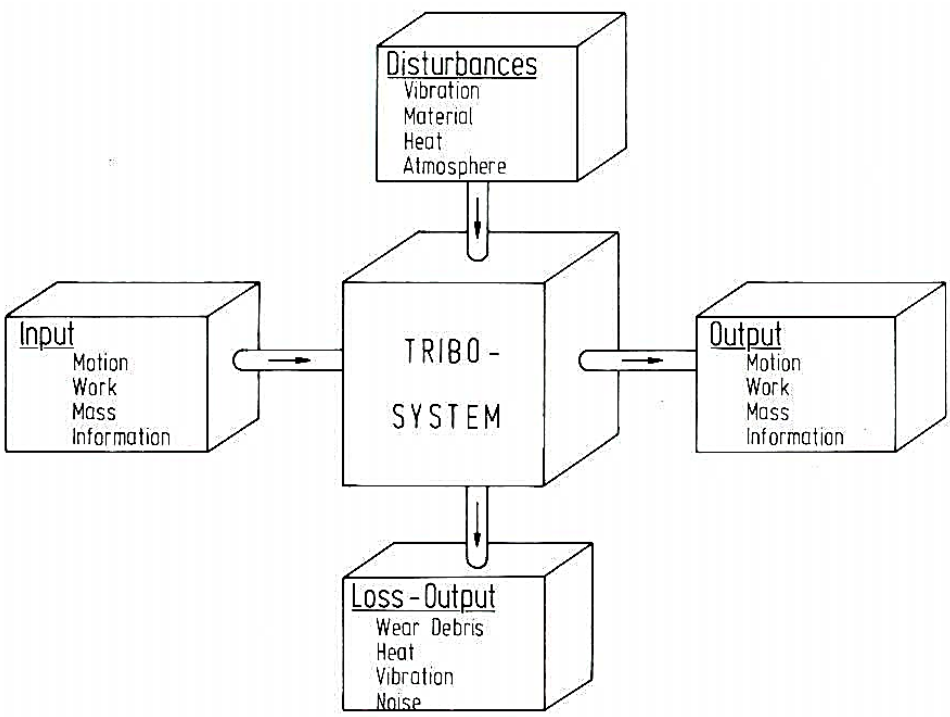

Figure 2-17: General input-output description of tribosystems adopted as a systems- level concept [62]

2.4.1.1 Machinability

Machinability is considered as the ease with which a material can be machined and it is customary to speak of it as a material property. Although there is no physical quantity to rate the machinability, it can sometimes be quantified as a combination of factors such as the machinability index, chip formation characteristics, tool wear, cutting forces acting on the tool, material removal rates, and achievable surface finish. Usually good machinability translates to a combination of cutting with minimum energy, minimum tool wear, good surface finish, etc.

For a closer definition of machinability, a quantitative judgment in the form of machinability index is often quoted. The machinability index K_M is defined as:

$$K_M = \frac{V_{60}}{V_{60R}} \tag{2.2}$$

Where, V60 is the cutting speed for the target material that ensures tool life of 60 min, and V60R is the same for the reference material. If KM is greater than 1, the machinability of the target material is better that this of the reference material, and vice versa. Note that this system can be misleading because the index is different for different machining processes [38].

Titanium alloys are considered to have very poor machinability especially when compared to aluminum alloys and most steels. For instance, Table 2-1 shows the relative machinability of Ti-6Al-4V against 4340 steel and 7075 aluminum.

Table 2-1: Relative machinability of Ti-6Al-4V against 4340 steel and 6061 aluminum [63].

	Machinability	Thermal Conductivity	Modulus of Elasticity
7075-T6 Alum	80%	900	10400
4340 Steel	57%	309	29700
6-4 Titanium	40%	49	16500

Using a rating system based on AISI B1112 steel, the machinability of Ti-6Al-4V is rated at 22% of B1112 steel [64]. Thus, regardless of the rating system used, titanium alloys, and especially Ti-6Al-4V has poor machinability.

2.4.2 Issues in Machining Titanium Alloys

The main adverse properties of titanium and its alloys that classify it as a "difficult-to-machine" material are summarized below:

2.4.2.1 Low Thermal Conductivity

Due to the relatively low thermal conductivity of titanium, the majority of the heat generated during the cutting process is transferred to the cutting tool edge and tool face rather than to the chips or the workpiece. It has been reported that 80% of the heat of cutting is transferred to the tool when cutting titanium as compared to 50% when cutting steel [51]. As a result, the tool temperature becomes very high creating high thermal gradients which significantly affect the tool properties leading to rapid tool wear and even catastrophic failure.

High Speed Steel (HSS) tools experience a loss of hardness at temperatures greater than 600^{o} C. During titanium machining, this leads to severe plastic deformation of the tool. Cemented carbide and ceramic tools also experience plastic deformation leading to cracks by thermal shock. With tungsten carbide (WC-Co) tools, the high temperatures and high thermal gradients cause mechanical and cyclic stresses as well as adhesion of pieces of the titanium workpiece to the tool furthering flank wear [49].

2.4.2.2 Low Elastic Modulus:

The low elastic modulus of the titanium causes large deflection of the workpiece during machining. The deflections are twice that experienced with steel [49]. These large

deflections cause chatter, vibration, rubbing with the tool and increase in temperature during machining [49] which in turn leads to poor surface finish.

2.4.2.3 High Chemical Reactivity:

The high chemical reactivity of titanium causes the workpiece to adhere to the tool which leads to chipping of the tool and eventually tool failure [49]. This alloying tendency is more pronounced at elevated temperatures often causing galling, welding, or smearing of the workpiece.

2.4.2.4 High Strength at Elevated Temperatures:

Though appearing to be a favorable property, titanium's tendency to maintain its strength at higher temperatures hinders chip formation. This leads to the formation of small chips which result in small contact areas between the tool tip and workpiece and hence higher stresses in the cutting zone [49]. It has been observed that these high stresses are a result of the small contact area (about a third that of steel) and not due to an increase in forces. Though the forces and hence power requirement for machining titanium is lower than that of steel, titanium's lower thermal conductivity results in more rapid tool wear than steel. Their specific cutting energies are given below:

- Specific cutting energy of Steel: 2.7 Ws/mm^3 to 9.3 Ws/mm^3
- Specific cutting energy of Titanium: 3.0 Ws/mm^3 to 4.1 Ws/mm^3

Additionally, when machining titanium, a high shear angle is typically formed ahead of the cutting edge which leads to small segmented (saw-tooth) chips [65]. These

segmented chips result in high cutting forces, high temperatures and very high stresses in the cutting zone.

2.5 TOOL DETERIORATION

2.5.1 Definition of Terms

2.5.1.1 Tool Wear

Wear is the progressive loss of material from the surface of a solid body due to contact and relative motion (DIN 50320). Wear is primarily caused by the disintegration of interacting overstressed material in the immediate vicinity of the surface. Wear (and friction) are not intrinsic material properties, but depend on the elements of the particular engineering system (tribosystem). Seldom do two nominally equal tribosystems show identical wear behavior in practice. Earlier classifications of wear types included: (*i*) Grooving wear, representing a wear mechanism dominated by abrasion, and (*ii*) Sliding wear, representing an absence of abrasion as a wear mode.

For wear considerations, a compromise between high strength (hardness) and sufficient ductility has to be looked for in practice, since these can be dramatically inversely proportional. Fracture toughness (K_{Ic}) is another useful measure of sufficient ductility in wear, and it is the resistance of a material against the propagation of a crack.

2.5.1.2 Tool Failure

Unlike wear, which is relatively gradual process, tool failure typically refers to a sudden event which renders the tool unfit for future use. This can be brought about by a number of process combinations such as cracking, plastic deformation and gross failure.

2.5.2 Types of Tool Deterioration Profiles [38]

The life of a cutting tool can be terminated by a number of means, although they fall broadly into two main categories:

- Gradual wearing of certain regions of the face and flank of the cutting tool,
- Abrupt tool failure.

Considering the more desirable case, the life of a cutting tool is therefore determined by the amount of wear that has occurred on the tool profile and which reduces the efficiency of cutting to an unacceptable level, or eventually causes tool failure. This gradual wear occurs at three principal locations on a cutting tool. Accordingly, three main types of tool wear can be distinguished: Crater wear, Flank wear, and Corner wear. These three types of tool wear are illustrated in Figure 2-18.

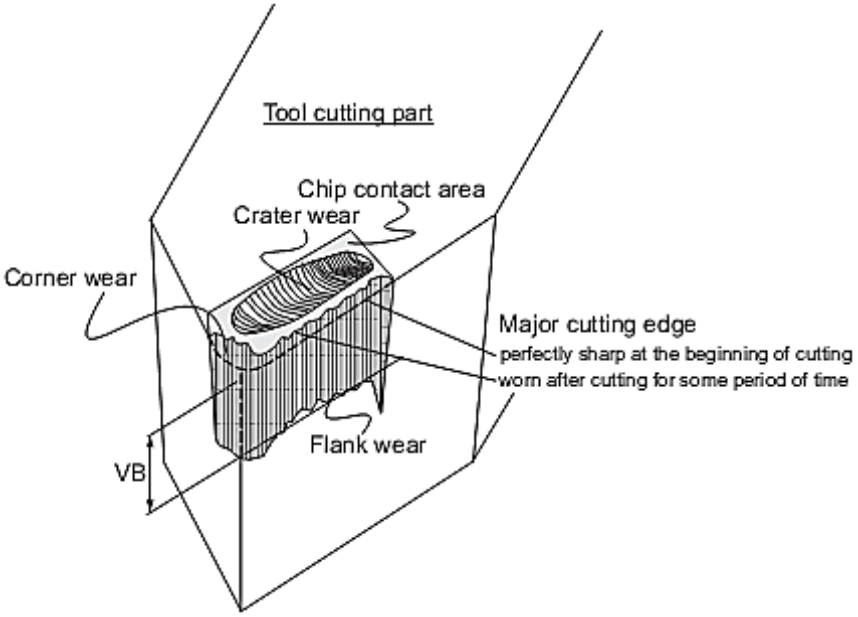

Figure 2-18: Types of wear observed in cutting tools at the three wear zones [38]

Crater wear consists of a concave section on the tool face formed by the action of the chip sliding on the surface. Crater wear affects the mechanics of the process increasing the actual rake angle of the cutting tool and consequently, making cutting easier. At the same time, the crater wear weakens the tool wedge and increases the possibility for tool breakage. In general, crater wear is of a relatively small concern.

Flank wear occurs on the tool flank as a result of friction between the machined surface of the workpiece and the tool flank. Flank wear appears in the form of so-called wear land and is measured by the width of this wear land, *VB*. Flank wear affects to the great extend the mechanics of cutting. Cutting forces increase significantly with flank wear. If the amount of flank wear exceeds some critical value, then the excessive resulting cutting force might cause tool failure.

Corner wear occurs on the tool corner. Can be considered as a part of the wear land and respectively flank wear since there is no distinguished boundary between the corner wear and flank wear land. We consider corner wear as a separate wear type because of its importance for the precision of machining. Corner wear actually shortens the cutting tool thus increasing gradually the dimension of machined surface and introducing a significant dimensional error in machining.

2.5.3 Types of Tool Deterioration Mechanisms

Tool deterioration falls under three major classes: wear, brittle failure and plastic deformation. The common wear mechanisms are [66]: adhesion, abrasion, chemical wear and solid-state diffusion. These lead to wear profiles characterized as crater wear, flank wear, notching, etc., as described earlier. General tool wear mechanism maps exist that represent safe operating zones [67, 68]. These are explained in detail in Section 4.6.1.

2.5.4 Tool Wear & Failure Mechanisms when Machining Ti-6Al-4V

For turning titanium alloys, throwaway type carbide tools are recommended for higher production rates, as well as minimum overhang and copious cutting fluids to prevent seizing and smearing on the tool flank [6]. Also, lower cutting speeds are recommended for cost savings since it is one of the most important operating variables influencing tool temperatures and hence tool life [35, 39-41].

In milling, titanium chips tend to weld to the cutting edge, and wears the cutting edge when knocked off on re-entering the stock, especially in the case of carbide inserts.

Climb milling produces thinner chips as the cutter leaves the work and reduces this tendency to weld. In titanium milling, the cutting insert has been observed to usually fail by chipping. Thus, cutting tools for machining titanium require high abrasion resistance, hot hardness and thermal shock resistance, as well as low reactivity.

While the cutting forces in titanium are only slightly higher than steel, the combination of a small chip-tool contact area (about 1/3rd of steel) and low thermal conductivity (about 1/6th of steel) results in very high cutting temperatures, leading to catastrophic tool failure [10]. Also, as the tool dulls by this welding action, cutting forces can increase 3-4 times due to a built-up-edge (BUE). This combination of a higher thrust force and low elastic modulus is catastrophic.

This combination of material properties, result in much higher temperatures. Titanium's low thermal conductivity [69] aids the formation of adiabatic shear bands at high strain rates (as in machining), and results in the majority of the generated heat flowing into the tool edge (about 80%) [70], rather than the chip or the stock. Additionally, the combination of a low modulus of elasticity, high yield stress, susceptibility to work-harden, and tendency to react with tool materials, causes rapid and catastrophic wear.

2.5.5 Titanium Machining: Need for Better Wear Assessment

The cutting inserts recommended for machining titanium alloys usually have much more complex geometric profiles compared to conventionally used tools. These 'sharp'

features characterized by unique combinations of high positive rake and relief angles as well as the very small edge radii of its profile features render the measurement of traditional flank/crater wear difficult. Additionally, the changing dominance of different wear mechanisms over time (as well as across different process conditions) combined with the higher order 'non-linearity' of the wear curve [16, 19-21] when machining Ti-6Al-4V, makes it challenging to develop accurate tool wear relationships. Thus, the fact that almost all existing tool wear related empirical work is based off flank/crater wear numbers, as well as the fact that wear characterization, at least in more recent FE simulation efforts, have shifted focus to volumetric wear rates, necessitate an improved tool wear assessment methodology, especially when machining Ti-6Al-4V and similar titanium alloys.

2.5.6 Mitigation

2.5.6.1 Cutting Tool Technologies to Improve Machinability

Recent research on improving the machinability of the titanium cutting process has mainly focused on the following four areas [49, 71]:

Tool Materials:

Tooling materials that are less resistant to wear or failure has been the primary focus. The most important parameters when considering a tool material for titanium is that it must have a high hardness at elevated temperatures (hot hardness), high thermal conductivity to mitigate thermal gradients and shocks, a high chemical inertness with

titanium, and a high compressive and shear strength. High Speed Steel (HSS) tools experience a loss of hardness at temperatures greater than 600° C, leading to severe plastic deformation of the tool and hence being ineffective for titanium machining [49]. Yet, in recent years, the development of new tool materials has increased dramatically with the addition of coated carbides, ceramics, cubic boron nitride (CBN), and polycrystalline diamond (PCD). However, ceramics have not found much success as they are poor thermal conductors, have relatively low fracture toughness and react aggressively with titanium [72]. Additionally, CBN and PCD materials show increased tool life, however, these tooling materials have not had great success as a result of their additionally high costs [73]. Also, it has been suggested that binderless CBN (BCBN) tools are the most functional material for machining titanium alloys. A BCBN tool is created without the traditional metal or ceramic binders which limit the bonding strength. Note however that this tooling material is expensive.

Tool Geometry

Different tooling geometries that could increase the machinability of titanium by reducing cutting forces and hence extending tool life have been investigated. In a study [49] using self-propelled rotary tools, it has been demonstrated that the rotary tool is more successful in removing heat from the cutting zone and lowering cutting forces. Rotary tools utilize circular discs which rotate and move in the main cutting and feed directions [74]. Rotary tools do provide viable means for increasing tool life; however,

they have not gained much popularity as a result of their inability to machine complex geometries and their requirement for shallow cutting depths.

Another common practice for increasing tool life is to chamfer the cutting edge, thus reducing the propensity of tool tip chipping (edge preparation). This is derived from an old machinist practice of applying a diamond edge stone to the edge of the cutting tip. This chamfer helps to reduce chipping, thereby extending tool life, however it decreases tool performance as well. It usually creates a plowing effect on the workpiece and changes chip direction leading to crater wear mostly. A recent development called Engineered Micro-Geometry utilizes a defined shaped round edge instead of the chamfer to protect the edge of the tool. With this, the negative aspects of chamfering are not encountered, yet it has been proven to protect against normal edge failure [75].

Process Parameters

For the identification of optimal process parameters for the cutting conditions at hand, numerous studies have examined different combinations of cutting feeds, speeds and depth of cuts. It has been reported that cutting speeds have the most substantial effect on tool life [76]. This is depicted in Figure 2-19, where it can be observed that tool life is greatly reduced at higher tool speeds when machining Ti-6Al-4V using a carbide tool. Additionally, it has been ascertained that the feed rate also has a significant effect on the life of a tool when machining titanium or its alloys. The decrease in tool life is reported to vary exponentially as the cutting feed increases [49]. This effect can also be

observed from Figure 2-19, for a given cutting speed. Also, as would be expected, with an increasing cutting depth, the tool life decreases rapidly when machining titanium.

A general recommendation of startup values for the approximate range of cutting parameters for milling operations on titanium alloys is as follows [28]: For carbide or diamond cutting tools, recommended cutting speeds are 40-150 m/min for a depth of cut of 1-8 mm and feed/tooth of 0 .08-0.46 mm/rev.

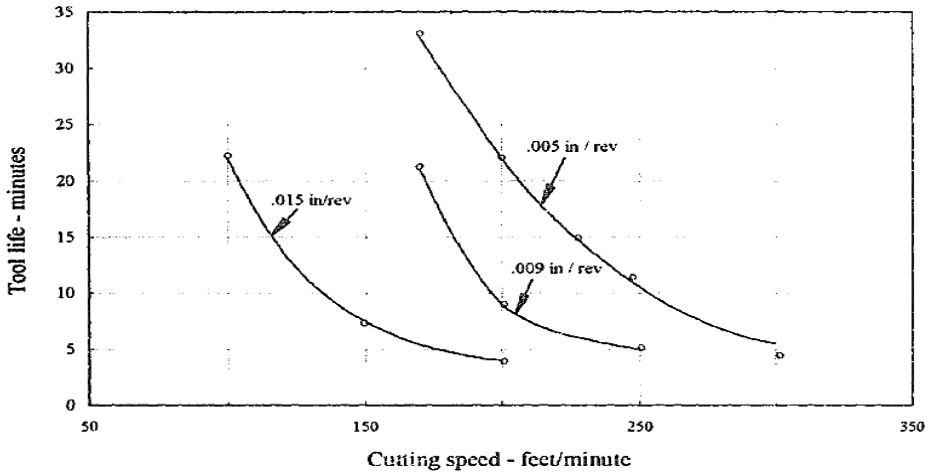

Figure 2-19: Tool life variation with cutting feeds and speeds [76]

Additional work involving the development of elaborate machining models for titanium have been conducted, generating both extended analytic material property based models as well as finite element models. A better understanding of the titanium cutting process and chip formation has been explored through these studies. One of the studies includes a model that is capable of predicting chip morphology as well as cutting forces for titanium machining [65, 77].

Cutting fluids

As a result of the high temperatures encountered during the cutting process as well as the tendency for welding of chips to the tool, the use of coolant during the cutting process helps to alleviate these problems while increasing tool life. A plentiful amount of coolant will allow for good chip removal as well as a reduction in the thermal gradients present [49]. One particular study examined various cooling methods and discovered that a compressed cold nitrogen gas and oil mist provided the best extended tool life while milling Ti-6Al-4V with a coated cemented carbide tool [78]. Also, it was noted in one particular study that the addition of liquid nitrogen cooling through a micro-nozzle could produce increased tool life up to five times greater than current emulsion cooling [79]. Another technique used to enhance tool life when machining is to use high pressure coolant. The addition of the coolant aids in lowering the tool temperature and also aids in reducing the welding of chips to the tool since the high pressure flow aids in creating discontinuous chips [80].

2.5.6.2 Machining Strategy

A good resource for specific recommendations on achieving good machinability can be obtained from tooling manufacturers. Some of their recommendations specifically pertaining to titanium include, but are not limited to [24]:

- Medium/high pressure coolant (1000 psi) applied through the spindle.
- Range of recommended cutting speeds, feeds, spindle specifications, etc.
- Improvement of tool life for low approach angle (round) inserts.

- Specific limits on surface cutting speeds for roughing and finishing.
- The optimum cutter diameter to width of cut ratio (very important).
- Selection of cutter and insert types, machine, power and geometric requirements as well as recommended start cutting data.

In certain instances, it would be beneficial to adopt a combination of newer machining (milling) techniques/concepts for increased machinability compared to traditionally followed tool paths for plunging, slotting, pocket milling, roughing, profiling, etc. Some examples of such suggestions include [81]: Slice milling techniques, Roll-in methods, Angle cutting, Straight and Helical ramping, Circular and Helical interpolation, Trochoidal Milling, etc. A combination of these techniques has been employed to demonstrate the improved machinability characteristics (cycle time, surface finish, lesser number of tool changes) of common materials [82].

2.5.7 Modeling Tool Wear

2.5.7.1 Traditional Models

The most prevalent tool wear model used today happens to be also the very first machining tool wear model that was formulated over a 100 years ago. The Taylor's tool life model (as it is called) was introduced in December 1906 by F.W. Taylor, at the opening address of the ASME annual meeting in New York, NY, and was titled "On the Art of Cutting Metals" [14].

Based on flank and crater wear nomenclature, Taylor's fundamental tool wear model predicts tool life based on the cutting time T it takes to reach a specific flank wear depth at a cutting speed V, as given by the following equation, where n and C are process-specific empirical constants [14].

$$VT^n = C \tag{2.3}$$

The Taylor's tool life model and its derivatives (Figure 2-20) are still being used in the industry today as originally conceived or in modified forms [39, 40].

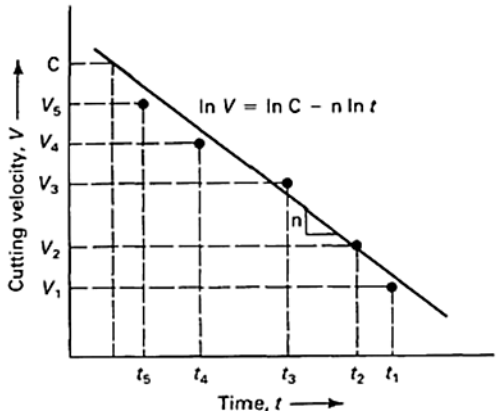

Figure 2-20: Taylor's tool life model [39, 40]

Besides the Taylor's tool life model, a number of other empirical tool life models have been proposed and adapted over the years for predicting flank and crater wear, especially when machining titanium alloys [39, 40, 65, 83-93]. Consequently, a general set of recommendations have been proposed such as the use of sharp cutting tool geometries, lower surface speeds, adequate cutting fluids, uniform feed, climb milling, rigid setups, maximum number of teeth, round inserts [24], and reduced arc of engagement for cooling of cutter teeth between subsequent engagements.

The general progression of tool wear with time is observed to generally pass through three zones or having three rates of wear, *i.e.*, a break-in period, a steady-state wear region, and failure region as shown in Figure 2-21. Generally wear progresses faster towards failure with increasing cutting speeds.

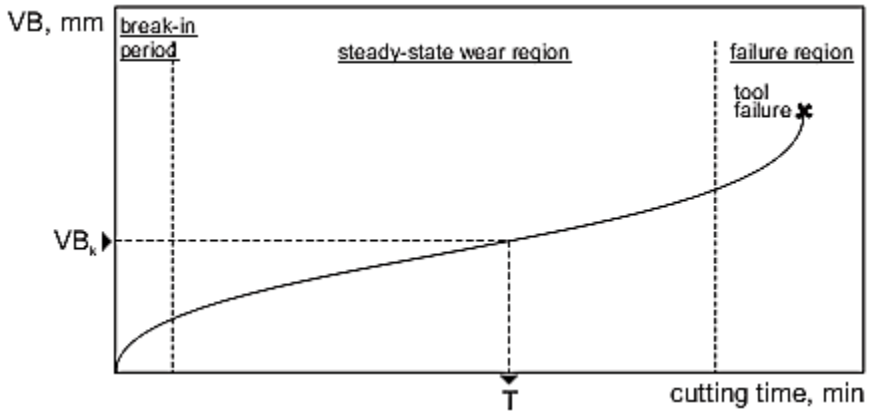

Figure 2-21: Three wear zones of a typical wear curve [38]. Flank wear as a function of cutting time. Tool life T is defined as the cutting time required for flank wear to reach a value of VB_k.

2.5.7.2 Rate Models

Another class of tool wear models that are more relevant to this work, predict a wear rate, which is defined as the local volume loss rate on a tool face per unit area per unit time. These wear rates were originally derived to characterize the fundamental wear mechanics of adhesion, abrasion and diffusion mechanisms and hence were originally functions hardness, load, sliding length, real contact areas, probabilities of generating wear particles, etc. The most commonly used adhesive wear rate model is the Usui's model [94] that predicts adhesive wear rate as a function of contact pressure, sliding velocity and temperature (Usui derived this wear model starting from Shaw's [35]

adhesive wear equations). Other commonly used wear rate models include Takeyama and Murata's model [95] for predicting abrasive wear rate as a function of sliding velocity and feed as well as the Arrhenius form diffusive wear rate model as a function of activation energy and temperature. Note that these models include tool-workpiece combination dependent constants that are 'assumed' to hold across the typical design space. These models can therefore be used to predict a volumetric wear rate based on continually updated contact stresses and temperatures and hence find good use especially in finite element simulations of the cutting process. Thus, the development of the volumetric assessment of tool wear is an essential first step in this direction.

2.5.7.3 Finite Element Models

Due to the complexities involved and multiplicity of mechanisms in machining tool wear, it has been suggested that no unique solution exists for describing metal cutting completely [4]; added to this is the stochastic nature of the machining process as well. Hence, the finite element method (FEM) is a natural tool for handling such involved non-linearities [36, 96]. FE modeling of the machining process has been investigated by a number of researchers [97, 98]; among them, the tool has been modeled in FE by a subset of researchers with vary levels of success, most notably [87, 99-104]. From among these, microstructure-level modeling of the tool has been conducted by two researchers: Fischmeister [105, 106] in 1988, and more recently by Park [107-109] in 2007. Note that this was for predicting gross tool fracture only through crack propagation/chipping.

2.5.7.4 Wear Mapping

The purpose of wear mapping is to characterize the friction and wear properties of tribological systems. The most common approach [67, 110] is to obtain appropriate values of wear rates (such as weight loss over sliding distance, and volumetric loss over sliding distance) under specific tribological and environmental conditions. These values can be precise for a material pair for a particular state or condition, but information on changes to the tribological characteristics is typically not available. This could be compensated by the wear mapping approach.

A beneficial wear map is one that summarizes data and models for wear, showing how the mechanisms interface, and allowing the dominant mechanisms for any given set of conditions to be identified. Within each field, contours of predicted normalized wear rates are superimposed. Expanding on the original map, a companion wear-mechanism map and a wear-transition map can be developed. It was also considered that friction maps might be useful companions for the wear maps of similar sliding systems. Many wear maps are constructed based on pin-on-disk experiments and theoretical models.

When considering machining operations, wear mapping has been extended beyond laboratory tests to study coating wear for use in industrial applications. Graphical representations of tool wear first appeared in the late 1950s with Trent's machining charts [36]. The main objective or feature of a typical machining wear map is the safety zone, which is defined as a region of gradual wear associated with predictable and

reliable tool performance. The intention of all wear maps is to find machining conditions that would give rise to the least amount of tool wear. Most of the traditional mapping work was has been done for various uncoated and coated tools in turning steels. Figure 2-22and Figure 2-23 show the wear maps for uncoated and TiC coated WC tools for the dry turning of steels, respectively. Note how the safety zone (range of machining usable parameters) has expended by the use of TiC WC tools that are better for turning steel.

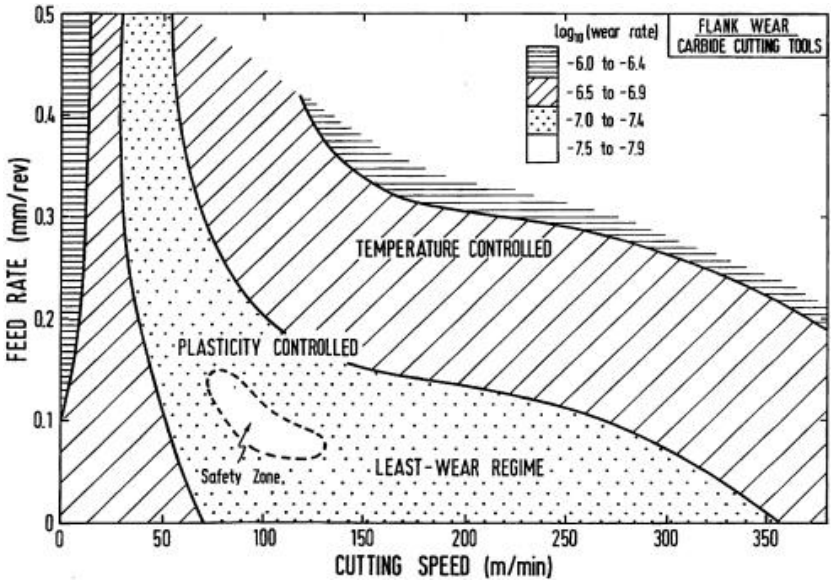

Figure 2-22: Wear map for uncoated WC cutting tools when dry turning steel [110]. Note that boundaries have been re-plotted with all data points removed and various regions shaded. The data points were the log of flank wear per distance ($\log_{10}$(VB/L)).

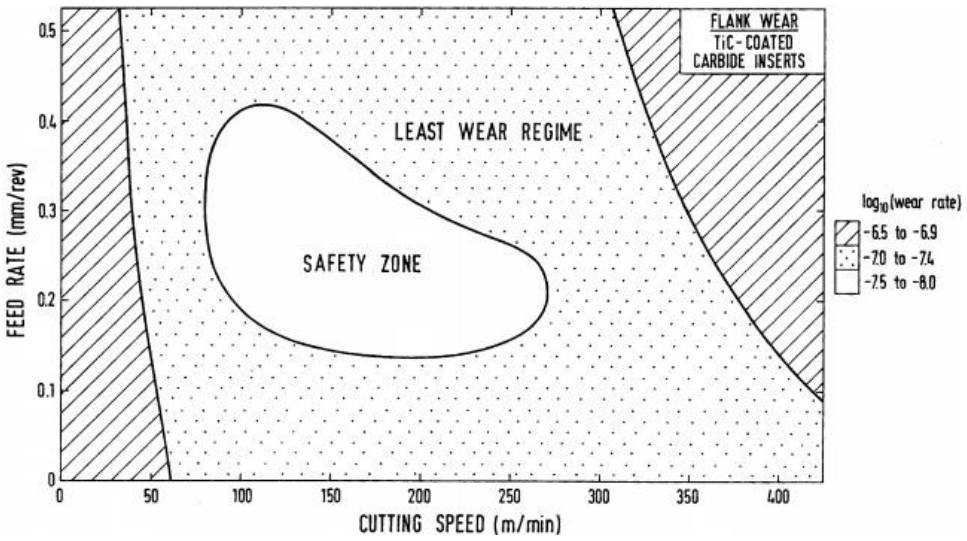

Figure 2-23: Wear map for TiC coated WC cutting tools when dry turning steel [83]. Note that boundaries have been re-plotted with all data points removed and various regions shaded. The data points were the log of flank wear per distance (log10(VB/L)). Also note how the safety zone has expanded with the use of a thin coating of TiC, beneficial for machining steel.

CHAPTER THREE

3. RESEARCH METHODOLOGY

This chapter outlines the research methodology that was followed for achieving the objective of this work. Besides coining the research questions (RQ) in this chapter, their associated tasks, methodology, assessment metrics, and outputs are outlined as well.

3.1 RESEARCH QUESTIONS

Two research questions were asked for achieving the objective of this work:

6. How can microstructural wear mechanism models be effectively combined to predict the volume of the tool worn away? (RQ1)
7. How can worn surfaces on complex tool geometries be accurately quantified in three dimensions to measure wear volumes? (RQ2)

3.2 TASKS

For addressing each research question, the following tasks were defined:

3.2.1 Tasks – RQ1 (Modeling)

RQ1 was asked for effectively combining microstructural wear mechanism models to predict the volume of the tool worn away. Task 1-A constructed predictive maps of the dominant wear mechanisms in the design space of tool and process factors, and Task 1-B modeled the tribosystem wear mechanics by combining and weighting wear mechanism models for predicting volumetric wear rates. The methodology involved the following:

(i) Formulating a final DOE of machining runs,

(ii) Determining weighting factors for each wear mechanism by quantifying the percentage area occupied by that particular wear mechanism, through the examination of scanning electron microscopy (SEM) images and energy dispersive x-ray spectroscopy (EDS) analysis,

(iii) Constructing predictive maps of dominant wear mechanisms in the design space of tool and process variables,

(iv) Selecting suitable wear rate models for each wear mechanism that can be employed for predicting the tool volume worn away,

(v) Estimating the tool-workpiece-specific model constants,

(vi) Formulating speed-regime based wear characteristic equations, and

(vii) Calculating the maximum values of model-predicted wear.

Assessment primarily involved checking for any major inconstancies in the model-predicted wear and dominant wear mechanisms against peer-reviewed literature, logic, and previous work/experience in titanium machining. The major outputs were:

(i) Predictive maps of dominant wear mechanisms in the design space of tool and process variables,

(ii) Weighted multi-mechanistic comprehensive wear characteristic equations for each speed regime, and

(iii) Model-based predicted tool wear values at the end of cut for each machining design of experiments (DOE) run.

3.2.2 Tasks – RQ2 (Validation)

RQ2 was asked for accurately quantifying the bulk-3D wear volume and evolution of worn surfaces on complex tool geometries, and validating the model through physical cutting experiments. Task 2-A developed a methodology for quantifying the bulk-3D wear and wear profile evolution, Task 2-B validated the model-predicted wear against the worn tool volumes obtained from corresponding cutting experiments, and Task 2-C constructed predictive maps of bulk-3D wear profile evolution patterns in the design space of tool and process variables. The methodology involved the following:

(i) Developing a new metrology method for accurately quantifying the bulk-3D wear and wear profile evolution,

(ii) Assessing the resolution and repeatability of this metrology method,

(iii) Acquiring suitable cutting inserts, and conducting the machining DOE to obtain volumetric wear, rates, and profile evolution information,

(iv) Validating the model-predicted wear volumes against the actual tool volumes worn away, as obtained from the cutting experiments,

(v) Quantifying the goodness of fit of the model with actual wear volumes, and

(vi) Mapping the bulk-3D wear profile evolution patterns using a set of geometric coefficients in the design space of tool and process variables.

Assessment involved checking the predicted vs. actual tool volumes worn to be within acceptable limits, as well as checking against literature, logic, and previous work in titanium machining for any major inconsistencies. The major outputs were:

(i) A validated methodology for characterizing the wear topology,

(ii) Validation of predicted wear for each speed-regime, and

(iii) Predictive maps of bulk-3D wear profile evolution patterns in the design space of tool and process variables.

3.3 SUMMARY

For an organized view of the research methodology, a summary of the two research questions, and their associated tasks, methodology and outputs is outlined below:

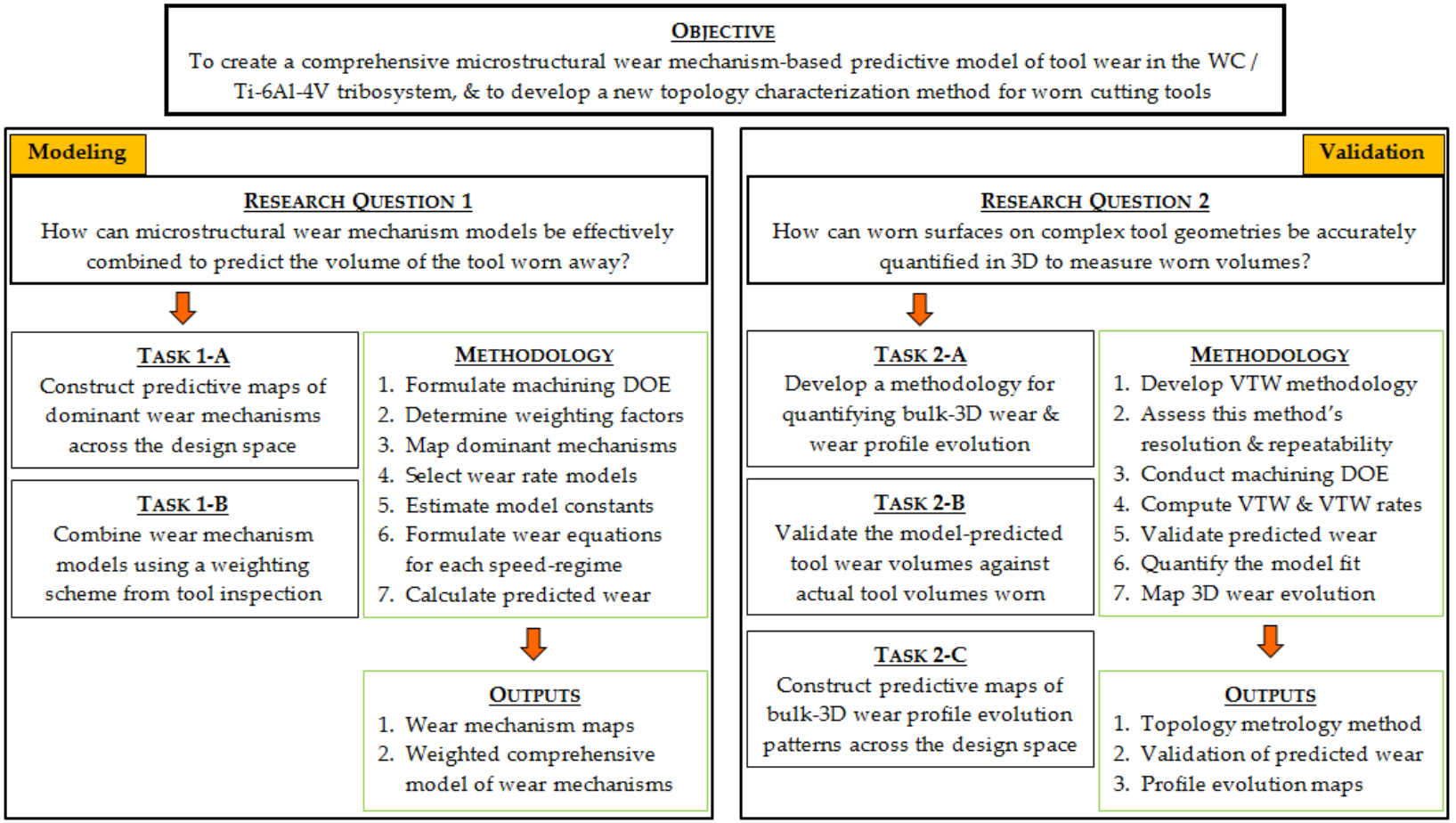
OBJECTIVE
To create a comprehensive microstructural wear mechanism-based predictive model of tool wear in the WC / Ti-6Al-4V tribosystem, & to develop a new topology characterization method for worn cutting tools
Modeling
RESEARCH QUESTION 1
How can microstructural wear mechanism models be effectively combined to predict the volume of the tool worn away?
TASK 1-A
Construct predictive maps of dominant wear mechanisms across the design space
TASK 1-B
Combine wear mechanism models using a weighting scheme from tool inspection
METHODOLOGY
1. Formulate machining DOE
2. Determine weighting factors
3. Map dominant mechanisms
4. Select wear rate models
5. Estimate model constants
6. Formulate wear equations for each speed-regime
7. Calculate predicted wear
OUTPUTS
1. Wear mechanism maps
2. Weighted comprehensive model of wear mechanisms
Validation
RESEARCH QUESTION 2
How can worn surfaces on complex tool geometries be accurately quantified in 3D to measure worn volumes?
TASK 2-A
Develop a methodology for quantifying bulk-3D wear & wear profile evolution
TASK 2-B
Validate the model-predicted tool wear volumes against actual tool volumes worn
TASK 2-C
Construct predictive maps of bulk-3D wear profile evolution patterns across the design space
METHODOLOGY
1. Develop VTW methodology
2. Assess this method's resolution & repeatability
3. Conduct machining DOE
4. Compute VTW & VTW rates
5. Validate predicted wear
6. Quantify the model fit
7. Map 3D wear evolution
OUTPUTS
1. Topology metrology method
2. Validation of predicted wear
3. Profile evolution maps

CHAPTER FOUR

4. WEIGHTED MODELING OF MICROSTRUCTURAL WEAR MECHANISMS (RQ1)

This chapter serves to answer research question 1 (RQ1), *i.e.*, "How can microstructural wear mechanism models be effectively combined to predict the volume of the tool worn away?" The objective of RQ1 is therefore to combine and weight the different microstructural wear mechanism models to predict volumetric wear.

Two tasks were charted out for answering RQ1, *i.e.*, Task 1-A, to construct predictive maps of the dominant wear mechanisms in the design space of tool and process factors, and Task 1-B, to model the tribosystem wear mechanics by combining and weighting wear mechanism models for predicting volumetric wear rates. The major outputs from these two tasks were: (*i*) predictive maps of dominant wear mechanisms in the design space of tool and process variables, (*ii*) weighted multi-mechanistic comprehensive wear characteristic equations for each speed regime, and (*iii*) model-based predicted tool wear values at the end of cut for each machining DOE run.

4.1 CONSTRAINING THE TRIBOSYSTEM

The inherent complexity and multi-scale nature of the WC-Co / Ti-6Al-4V machining tribosystem requires that certain constraints need to be imposed first, to simplify the problem at hand. For this, it is beneficial to apply a systems-level of thinking to the tribosystem, and focus on the desired outputs. The system concept in metal cutting [111]

primarily includes the tool, workpiece, and chip (with time variable), where some input energy removes workpiece stock material [22]. This systems-level concept applied to the WC-Co / Ti-6Al-4V machining tribosystem can be visualized as given in Figure 4-1.

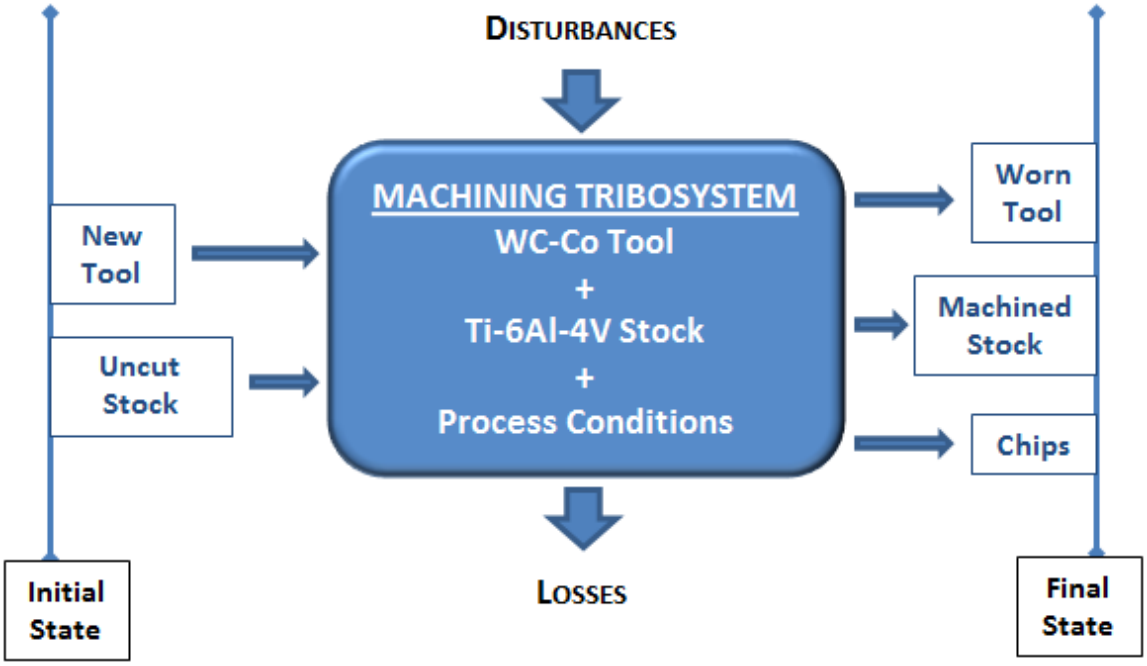

Figure 4-1: Systems-level concept in metal cutting applied to the WC-Co / Ti-6Al-4V machining tribosystem showing the worn tool, cut stock, & chips as system outputs.

In Figure 4-1, the components at the initial-state are the new tool and uncut workpiece stock (with known characteristics and material properties). These, when subjected to selected process conditions (feed rate, surface speed, etc.), and unavoidable disturbances (vibrations, atmosphere, etc.), with losses (wear debris, heat, etc.), result in the components at the final-state, *i.e.*, the worn tool, machined stock, and chips (their properties being quantifiable). On adding additional real variables to this system such as coolant type, machine dynamics, etc., the problem quickly becomes unmanageable.

For managing the complexity of the WC-Co / Ti-6Al-4V machining tribosystem while still capturing the underlying wear mechanics, a derivative or subset of the above metal cutting system is apt, *i.e.*, isolate the cutting tool, and consider all tool related interactions as inputs to the tool - this approach can be visualized from Figure 4-2.

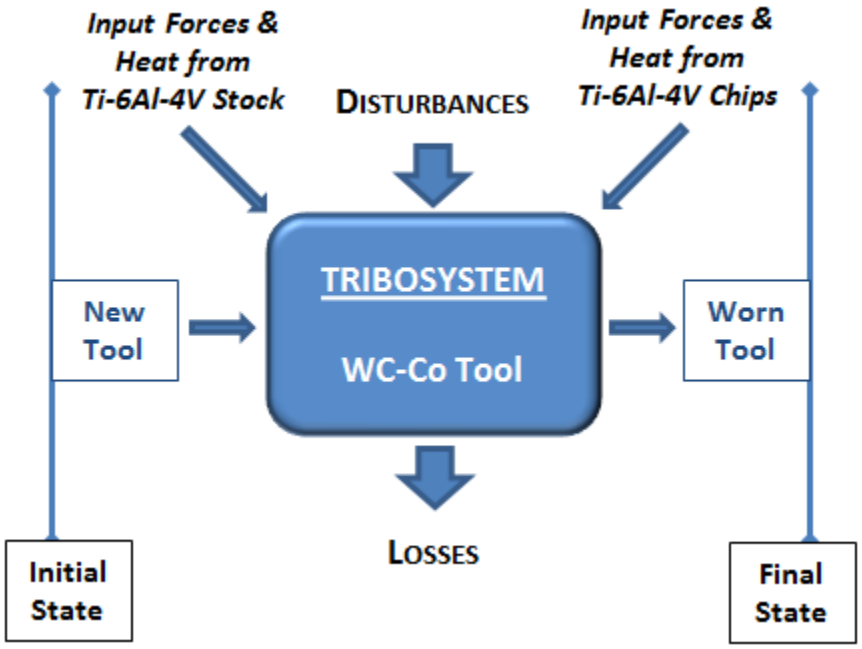

Figure 4-2: Subset of the systems-level metal cutting concept, where the cutting tool has been isolated & all its interactions are captured/treated as 'tool-system' inputs & outputs.

On isolating the cutting tool, the forces and heat generated at the stock-tool and chip-tool interfaces, as well as process conditions and quantifiable disturbances, can be considered as inputs to the tool. During machining, the tool substrate material properties deteriorate with increasing temperature. Further, the tool body loses mass in the form of wear debris, as well as energy in the form of heat, vibration, noise, etc.

Thus, to render this complex tribosystem manageable for the purpose of modeling and predicting its wear mechanics, the following two constraints were imposed:

8. The titanium stock was not modeled; however, it's evolving material properties and effects on the tool were captured and applied as tool inputs.
9. The chip formation process was not modeled as well; its evolving properties and effects on the tool were however captured and applied as tool inputs.

4.2 Identification of Primary Factors Affecting Wear Mechanics

Identifying the primary factors that significantly affect the tribosystem wear mechanics is the essential first step for formulating a DOE for modeling and validation. For the sake of organization, these are classified as macroscopic and microscopic factors.

4.2.1 Macroscopic Factors Affecting Wear

For identifying the macroscopic factors affecting the wear mechanics of this tribosystem, a large number of machining simulations were conducted using Third Wave Systems' AdvantEdge FEM machining simulation software [112] (Appendix A) on Clemson University's High Performance Computing cluster (Appendix A). Results were subjected to multiple linear regression and best subsets regression analyses in Minitab to identify key factors and outliers. The analyses showed that increasing speed significantly increased temperature, while increasing feed increased forces. Following a mini-DOE experiment set to ascertain cutting depth dependence (Appendix B), the final DOE consisted of varying feeds and speeds, while keeping cutting depths at 2mm.

4.2.2 Microscopic Factors Affecting Wear

When looking at the WC-Co / Ti-6Al-4V machining tribosystem from a micro-scale standpoint, three main areas of interest exist:

1. (Ti-6Al-4V) Workpiece microstructural factors such as:
    a. grain size,
    b. fraction of α and β beta phases,
    c. morphology of these phases,
    d. distribution of the alloying elements (Al and V),
    e. width of the lamellae,
    f. lamellar spacing,
    g. width of the adiabatic shear bands formed during machining,
    h. differences in stock (virgin) material microstructure vs. the machined surface microstructure,
    i. phase changes happening on the machined surface when exceeding the β-transus temperature,
    j. material property differences when this happens,
    k. degree of segmentation of the machined chips affecting cutting forces.
2. (Machining) Process microstructural factors such as:
    a. material transfer at the tool chip interface,
    b. material transfer between the tool and machined workpiece,
    c. residual stresses imparted on the machined workpiece surface,

d. sub-surface damage on the workpiece,

e. material properties of the coolant,

f. cooling and lubricating capabilities of the cutting fluid,

g. degree of atomization of the coolant mist,

h. droplet size of the coolant in the case of minimum quantity lubrication,

i. flash points and melting of the tool and workpiece at the interface,

j. extent of penetration of the coolant at the cutting interface.

3. (WC-Co) Tool microstructural factors such as:

a. grain size (average),

b. mean grain size distribution,

c. number of vertices per grain,

d. carbide volume fraction (% Cobalt for straight carbide),

e. weight percentage,

f. Co binder mean free path,

g. distribution of free paths,

h. contiguity of carbide phase,

i. angularity of carbide phase,

j. texture (orientation, misorientation, grain boundary plane normal),

k. aspect ratio of the grains,

l. crystal structure transition of Co binder during processing,

m. presence and amount of the η phase (carbon deficiency),

n. presence and amount of precipitates (excess of carbon),

o. degree of porosity.

p. WC/WC and WC/Co grain boundary aspects.

The above list is by no means exhaustive, and is a good indication of the complexity of the machining process just from the micro-scale standpoint. To handle this inherent complexity of the WC-Co / Ti-6Al-4V machining tribosystem, a systems-level approach was introduced in Section 4.1. By adopting this approach, the workpiece (Ti-6Al-4V), though microscopic in structure, its effects on (inputs to) the tool can be considered as macroscopic in the form of input forces and temperatures on the tool edge. In the same manner, the process (Machining) variables have been constrained suitably to greatly reduce the complexity of the tribosystem (for *e.g.*, not using coolant, and not considering the effects on the workpiece). When considering the tool (WC-Co), to limit the myriad of factors to consider, and consequently the large number of simulation runs and machining experiments to be conducted, the starting point was to look at grain sizes. Other microstructural parameters will need to be addressed in future studies.

4.4.2.1 WC Grain Size

Grain size of the WC grain is most important microstructural parameter affecting the properties and performance of WC-Co cutting tools [8, 43]. It has a direct impact on the two vital properties of WC-Co cutting tools [6, 8, 39, 43, 113, 114]: (*i*) hardness (measure of strength and wear resistance), and (*ii*) transverse rupture strength (measure of

toughness). Further, grain sizes also significantly influence the fracture toughness of the WC-Co composite as well as its creep and fatigue properties. It is commonly known that with decreasing grain size, the yield strength increases [115, 116] (within limits) as per the Hall-Petch relationship. This is at a "model-test" level [62], *i.e.*, at a level of tribosystem testing equivalent to pin-on-disc experiments. However, when considering the "field-test" level [62], *i.e.*, at a level of tribosystem testing similar to actual machining experiments, the effects of grain size need to be characterized separately. For this purpose, two cutting inserts with two different grain sizes were chosen for this research work, they are:

1. Sandvik CNGP 12 04 08 H10A
2. Sandvik CNGP 12 04 08 H13A

For these two straight uncoated carbide turning inserts, the tooling manufacturer (Sandvik) provided the following grade information:

Table 4-1: Properties of Sandvik H10A & H13A grades

Grade	Composition - %		Density	Hardness	Coercivity
	Co	WC	g/cm^3	(HV3)	(kA/m)
H10A	10.2	89.8	14.96	1675	19.7
H13A	10.2	89.8	14.96	1580	17.3

It can be seen that both grades are straight carbides with only WC (89.8 %) and Co (10.2 %) as constituents, *i.e.*, no additives such as TiC, TaC, and TiAlN. Further, they have the same density, *i.e.*, 14.96 g/cm^3. Further, these inserts are ground to the final

dimensions; this holds the size of the insert within a 0.0015" tolerance from insert to insert, compared to the standard molded inserts (which holds on average 0.0035" - 0.004" difference in size). These two inserts have the exact same geometry as well, *i.e.*, same rake angle, relief angle, cutting edge radius, and nose radius.

Though an official grain size distribution was not provided, the WC grain size can be estimated [8, 43, 117] from the coercivity, which is a measurement used by the tool manufacturer (Sandvik) for quality control. Typically, the magnetic saturation (moment) is another measurement (used along with coercivity) for the quality control of hard metals such as WC-Co; this allows one to estimate the Co-W-C binder phase composition. These magnetic measurements are non-destructive testing (NDT) standards (ISO 3326 [118], ASTM B887 [119]) for controlling the consistency of hard metal products in industry. They rely on the fact that Cobalt is ferromagnetic, and measurement of its magnetic properties can be reliably used for assessing quality.

Initial work [120] with 6 wt% Co hard metals gave a relationship between magnetic coercivity and arithmetic mean linear intercept of grain size, as given by [117]:

$$K = a + \frac{b}{d_{WC}} \tag{4.1}$$

Where, K is the coercivity in kA/m, a, b are constants, and d_{WC} is the WC arithmetic mean linear intercept in of grain size in μm. However, due to the substantial scatter in the measurements made, especially at grain sizes greater the 2 μm, a bilinear fit was

performed and grain size coefficients were compiled for a % Co range from 6 through 25% [120, 121]. The resulting expression for K for 6 < Co < 25 wt% is:

$$K = c_1 + d_1 W_{Co} + \left(\frac{c_2 + d_2 W_{Co}}{d_{WC}} \right) \tag{4.2}$$

Where, W_{Co} is the wt% Co in the hard metal and c_1 = 1.44, c_2 = 12.47, d_1 = 0.04, and d_2 = -0.37. By plotting this expression as property maps (Figure 4-3(A) and (B)), the grain size can be estimated by drawing/extending suitable lines for a 10.2% Co composition.

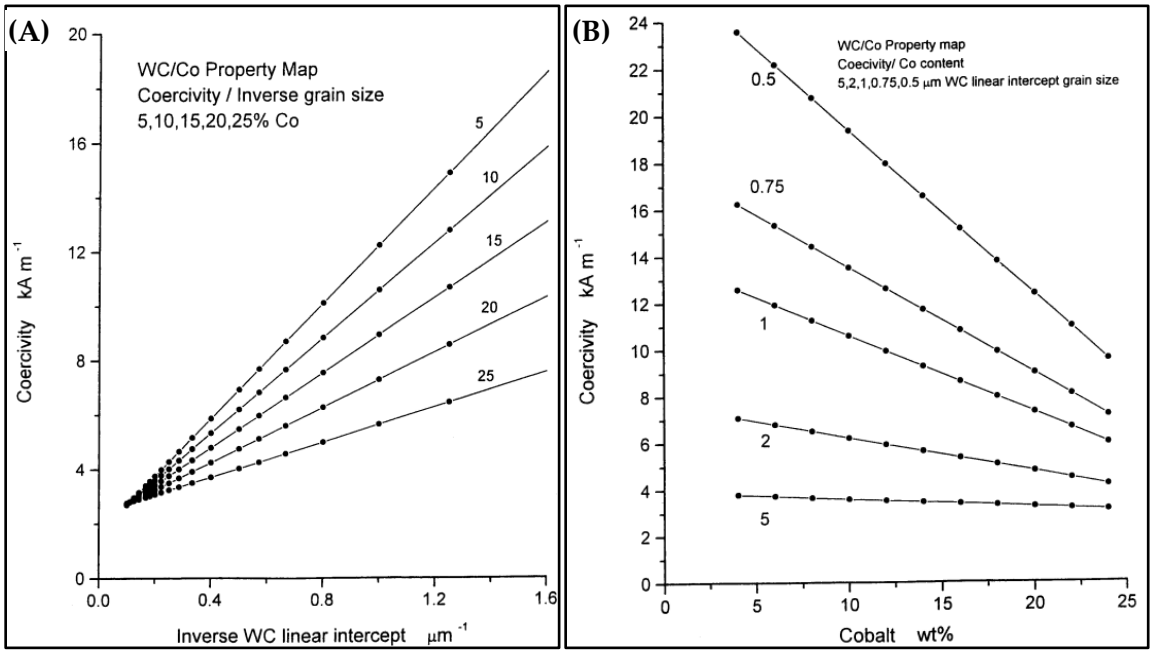

Figure 4-3: WC-Co property map showing the (A) Coercivity vs. inverse grain size relations, and (B) Coercivity vs. Cobalt content relations for different compositions [117].

From the above plots, the grain sizes of the two turning inserts can be estimated in the following manner for H10A and H13 A respectively:

$$K_{(H10A)} = c_1 + d_1 W_{Co} + \left(\frac{c_2 + d_2 W_{Co}}{d_{WC(H10A)}} \right) \quad (4.3)$$

$$K_{(H13A)} = c_1 + d_1 W_{Co} + \left(\frac{c_2 + d_2 W_{Co}}{d_{WC(H13A)}} \right) \quad (4.4)$$

The estimate of the average grain sizes of the two inserts from above equations are:

- d_g (H10A) ~ 0.54 μm
- d_g (H13A) ~ 0.61 μm

This estimation is in line with the hardness measurements from Sandvik where the grade with the lower grain size, *i.e.*, H10A, has the higher hardness as expected. Besides, H13 is known to be a coarser grade compared to the H10A grade [37]. It is to be noted that, besides estimating grain size from coercivity, it should also be measured from micrographs of polished and etched microstructures. A finite number of measurements using any standard method such as intercept measurement will provide a good representation of the relative mean grain sizes of both inserts.

4.4.2.2 H10A Grade WC-Co Insert

H10A is an uncoated straight carbide grade (denoted as *HW*) which combines good abrasive wear resistance and toughness for the medium to rough turning of heat resistant steels and titanium alloys [37]. Further, H10A is classified as a *S10* grade insert, which is suitable for machining heat resistant super alloys (HRSA) and titanium alloys (The H10A grade was originally designed to compete with an old Seco Carboloy grade at Pratt & Whitney, and is still used today purchased as a special from Sandvik).

Relevant technical specifications of the Sandvik CNGP 12 04 08 H10A insert [122], as well as the insert dimensions, solid model, and image follow:

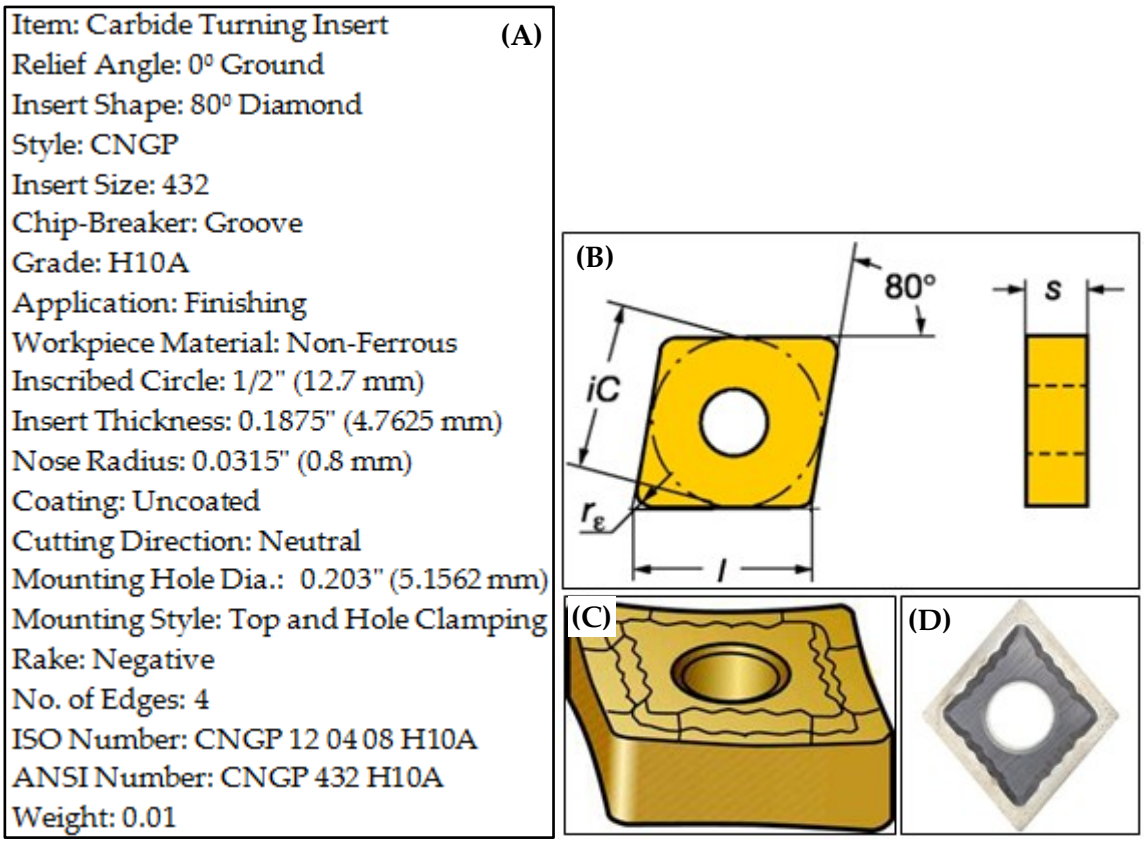

Figure 4-4: A) Relevant technical specifications of the Sandvik CNGP 12 04 08 H10A insert [122], (B) Insert dimensions, (C) Solid model, and (D) Image of insert

4.4.2.3 H13A Grade WC-Co Insert

H13A is an uncoated straight carbide grade (denoted as *HW*) which combines good abrasive wear resistance and toughness for the rough to finish turning of heat resistant alloys, titanium alloys, cast irons, and aluminum alloys [37]. Further, H13A is classified as a *S15* grade insert, which is suitable for machining heat resistant super alloys (HRSA)

and titanium alloys. The technical specifications of the Sandvik CNGP 12 04 08 H13A insert follow [122]:

(A)

Item: Carbide Turning Insert
Relief Angle: 0º Ground
Insert Shape: 80º Diamond
Style: CNGP
Insert Size: 432
Chip-Breaker: Groove
Grade: H13A
Application: Finishing
Workpiece Material: Non-Ferrous
Inscribed Circle: 1/2" (12.7 mm)
Insert Thickness: 0.1875" (4.7625 mm)
Nose Radius: 0.0315" (0.8 mm)
Coating: Uncoated
Cutting Direction: Neutral
Mounting Hole Dia.: 0.203" (5.1562 mm)
Mounting Style: Top and Hole Clamping
Rake: Negative
No. of Edges: 4
ISO Number: CNGP 12 04 08 H13A
ANSI Number: CNGP 432 H13A
Weight: 0.01

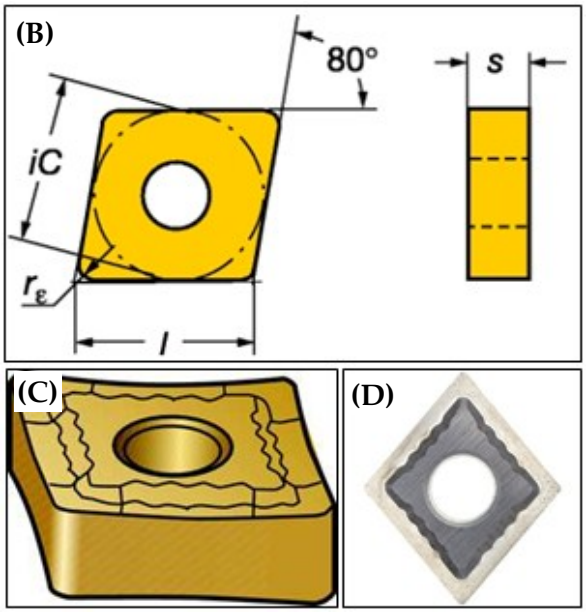

Figure 4-5: (A) Relevant technical specifications of the Sandvik CNGP 12 04 08 H13A insert [122], (B) Insert dimensions, (C) Solid model, and (D) Image of insert

Additionally, the microstructure of this H13A grade straight uncoated carbide insert was examined using a Hitachi S-3400N Fully Automatic Varaible Pressure (VP) Scanning Electron Microscope (SEM) to confirm the average grain size and other microstructural parameters, and subjected to Energy Dispersive X-Ray Spectroscopy (EDS) to confirm the composition (% Co). For this, one of the corners of a brand new H13A grade insert was polished manually using three consecutively finer grades of

Silicon Carbide (SiC) abrasive paper using diamond paste. On attaining a mirror-like finish, the inserts were examined under the SEM/EDS without etching. Results follow:

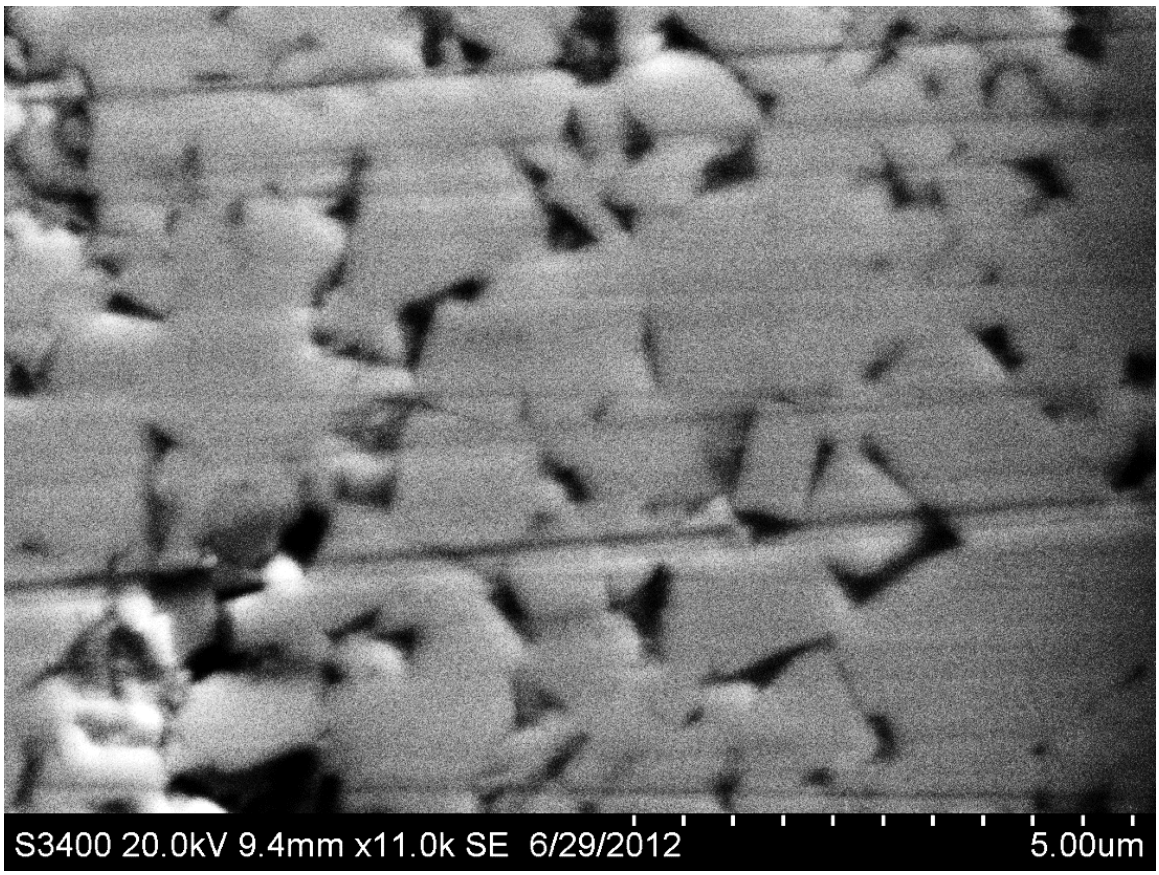

Figure 4-6: SEM micrograph of the H13A WC-Co insert surface at 11000 X. White sharp edged polygons are WC grains, and blank areas are the Co binder. The almost horizontal lines are the abrasive grooves due to polishing with SiC abrasive paper. Note that grains sizes vary from about 0.25 μm to about 2 μm in this area of examination.

Subjecting the above selected area for elemental analysis using EDS, the composition of Co was estimated to be about 5% as shown in Figure 4-7. This lower composition of Co is assumed to be a local distribution, and the 10.2 % of Co specified by the insert manufacturer for the whole cutting insert is retained.

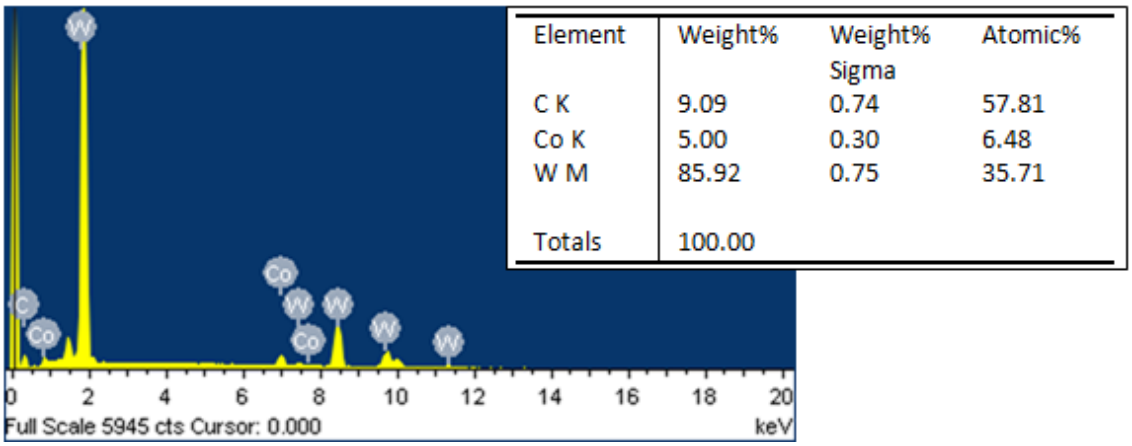

Element	Weight%	Weight% Sigma	Atomic%
C K	9.09	0.74	57.81
Co K	5.00	0.30	6.48
W M	85.92	0.75	35.71
Totals	100.00		

Figure 4-7: EDS analysis of the above area, and estimated elemental composition. The lower % Co composition is assumed to be a local distribution.

4.3 DOE OF TOOL & PROCESS FACTORS FOR MODELING & VALIDATION

Based on the above identification and characterization of macroscopic and microscopic tool and process factors affecting the tribosystem wear mechanics, a final DOE was put together for modeling and validation experiments. Additional constraints were imposed for greatly reducing its complexity and any variability as follows:

1. Prior problem bounds were retained: Straight, uncoated WC-Co / Ti-6Al-4V,
2. Dry, orthogonal turning operations at a constant 2 mm depth of cut (DoC),
3. Workpiece stock volume removal: 3 cutting steps of 10 cm^3 each,
4. No pre-stressing or preheating of the workpiece stock,
5. One batch of workpiece stock to minimize batch-to-batch variability,
6. Using 3 identical stock bars of 2" diameter and machining at the same locations with the same stock overhang for all 3 stock volume steps,
7. One batch of tools to minimize batch-to-batch variability.

For formulating the final DOE, the recommended parameter range for turning Ti-6Al-4V [6] in the annealed state with a Brinell hardness (HB) of about 310 - 350, when using indexable uncoated carbide tools is:

- For a DoC = 1 mm, V = 69 m/min, and f = 0.13 mm/rev (C3 grade),
- For a DoC = 4 mm, V = 59 m/min, and f = 0.2 mm/rev (C2 grade).

From these recommended parameter ranges, the settings for a DoC of 2 mm can be interpolated to a cutting speed (V) of 65 m/min, and a feed rate (f) of 0.15 mm/rev. Centered on this recommend set of conditions, a DOE spanning the corners of the feed-speed design space for two cutting inserts with different grains sized was tabulated:

Table 4-2: Final DOE of machining setups tabulated for H10A WC-Co cutting insert showing 27 runs (1 – 9, 19 – 27, 37 – 45) with 3 discrete stock volume removal steps of 10 cm³ each.

For H10A WC-Co Insert (d_g ~ 0.54 μm)				
Run Info	Process Parameters			Total Cut Stock Volume
Run (#)	DoC (mm)	f (mm/rev)	V (m/min)	
Runs 1 - 9	2	0.05	30	10 cm³
	2	0.05	60	
	2	0.05	120	
	2	0.15	30	
	2	0.15	60	
	2	0.15	120	
	2	0.30	30	
	2	0.30	60	
	2	0.30	120	
Runs 19 - 27	Same as above			20 cm³
Runs 37 - 45	Same as above			30 cm³

Table 4-3: Final DOE of machining setups tabulated for H13A WC-Co cutting insert showing 27 runs (10 – 18, 28 – 36, 45 – 54), with 3 discrete stock volume removal steps of 10 cm^3 each.

For H13A WC-Co Insert (d_g ~ 0.61 μm)				
Run Info	Process Parameters			Total Cut Stock Volume
Run (#)	DoC (mm)	f (mm/rev)	V (m/min)	
Runs 10 - 18	2	0.05	30	10 cm^3
	2	0.05	60	
	2	0.05	120	
	2	0.15	30	
	2	0.15	60	
	2	0.15	120	
	2	0.30	30	
	2	0.30	60	
	2	0.30	120	
Runs 28 - 36	Same as above			20 cm^3
Runs 45 - 54	Same as above			30 cm^3

4.4 Weighting Factors for Microstructural Wear Mechanisms

In this section, the wear mechanics of the WC-Co / Ti-6Al-4V machining tribosystem is modeling more realistically by using weighting factors for dominant wear mechanisms in the comprehensive wear rate model. For this, the 54-run final DOE of turning experiments that was tabulated earlier (Section 4.3) was completed on the OKUMA Space Turn LB4000-EX lathe. Each of these cutting inserts was cleaned of any wear debris, and then examined under the SEM, as well as subjected to EDS elemental analysis. Besides observing the amount of wear and its evolution, the dominant wear

mechanisms were observed and quantified in this section. This led to the formulation of weighting factors for each microstructural wear mechanism, which were then fed into a comprehensive wear-mechanisms model for predicting volumetric wear.

Weighting factors for each wear mechanism was determined by quantifying the percentage area of the worn surface that was worn by the wear mechanism in question. For this, both the SEM micrographs of worn tool surfaces as well as EDS elemental analysis of the worn areas were analyzed simultaneously. Some general guidelines were used to identify the wear mechanisms [123-125]:

- Micro-chipping or indications of "chunks" of material pulled away as indicators for adhesive wear,
- Wear scars or grooves on the tool caused by harder particles (or inclusions) as indicators for abrasive wear,
- Discolorations for oxidation or chemical wear, and
- Smooth surfaces on the tool for diffusive wear.

Representative instances of these four wear mechanisms on coated WC tools used for dry end-milling Ti-6Al-4V are shown in Figure 4-8.

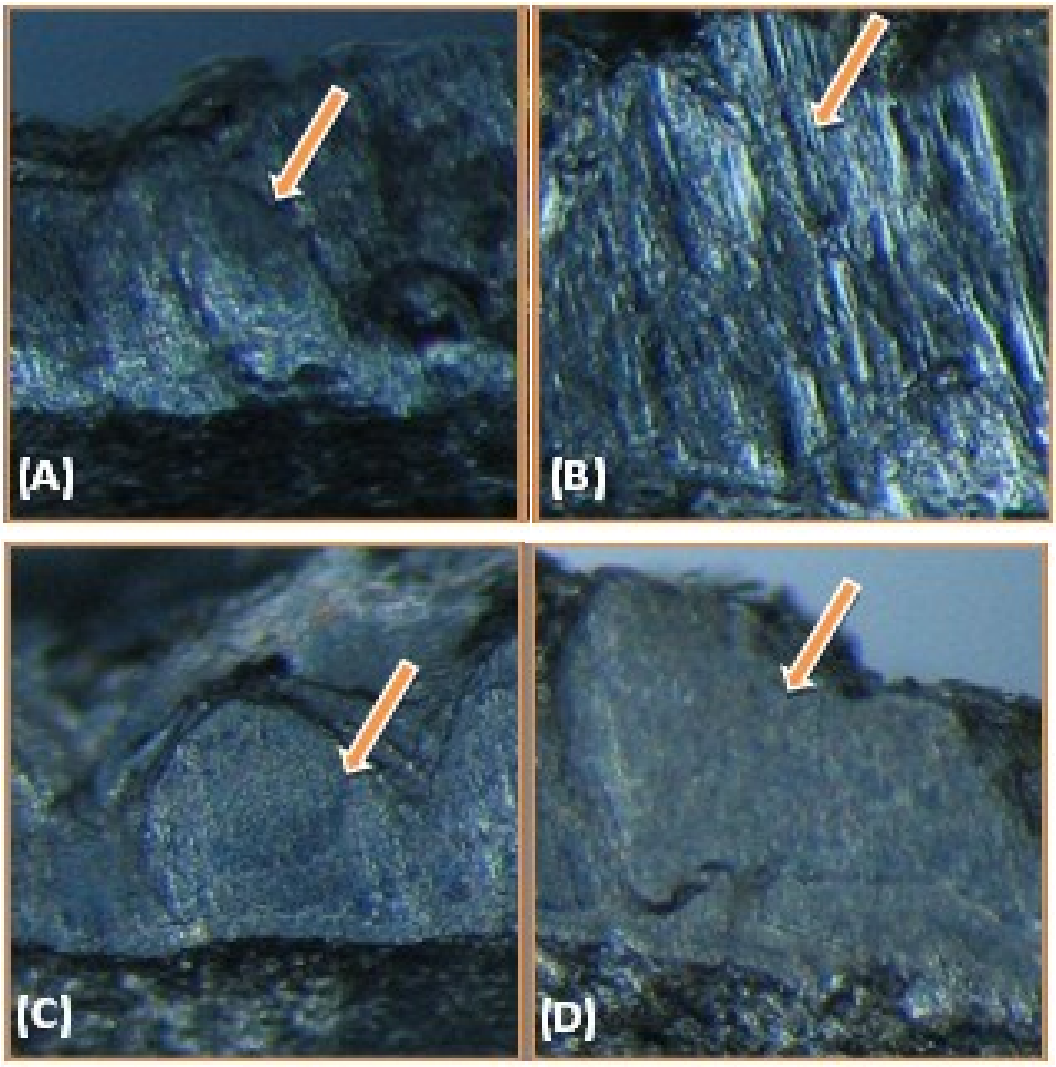

Figure 4-8: Representative instances of wear mechanisms on coated WC cutting tools used for dry end-milling Ti-6al-4V (40X). (Each image size is 10mm x 10mm). (A) Adhesive wear indicated by micro-chipping or a "chunk" of material pulled away, (B) Abrasive wear indicated by wear scars or grooves on the tool caused by harder particles (or inclusions), (C) Chemical wear indicated by discoloration on the tool surface, (D) Diffusive wear indicated by smooth areas on the tool.

In the turning tests that were conducted as part of the 54-run final DOE, a similar approach was undertaken. Since this was a qualitative classification at this point, EDS elemental analysis of the worn area was also simultaneously examined to determine the elemental composition of the worn surface. The results from this section were used for mapping the dominant wear mechanisms in Section 4.5.

The following sections detail some of the relevant SEM micrographs and portions of the EDS analysis that were used for identifying the dominant wear mechanisms under each cutting condition, as well as the procedure for quantifying them as weighting factors. The feed-speed related terminology used in the following sections is:

- 0.05 mm/rev – Low feed
- 0.15 mm/rev – Medium feed
- 0.30 mm/rev – High feed
- 30 m/min – Low speed
- 60 m/min – Medium speed
- 120 m/min – High speed

This terminology relates consistently with the recommended parameter range for turning Ti-6Al-4V at a depth of cut of 2mm, since the center point of the design space is a (feed, speed) combination of (0.15 mm/rev, 60 m/min) [6], and all other combinations are distributed at the corners of the testing space or on its edges.

4.4.1 H10A Inserts - Weighting (Stock Volume Cut = 10 cm^3)

4.4.1.1 Feed Rate of 0.05 mm/rev (Runs 1 – 3)

Run 1: Surface Speed of 30 m/min

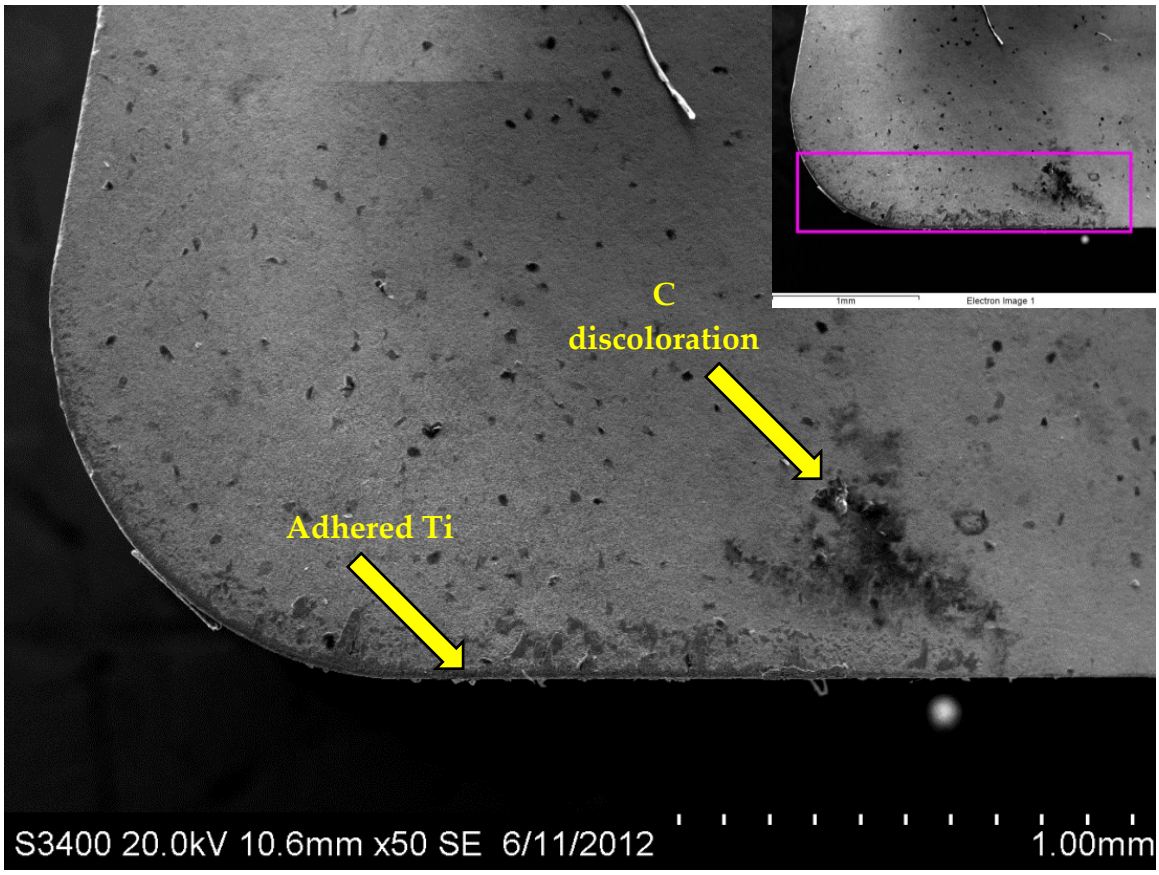

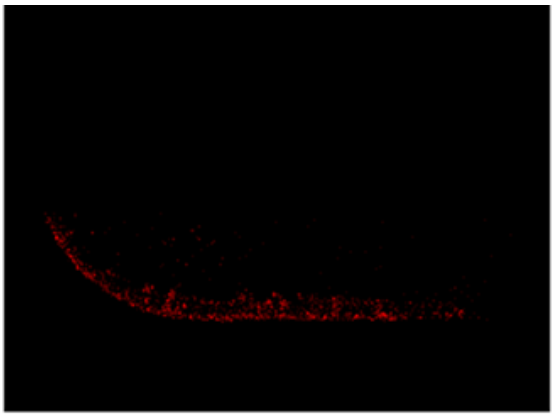
Ti Ka1

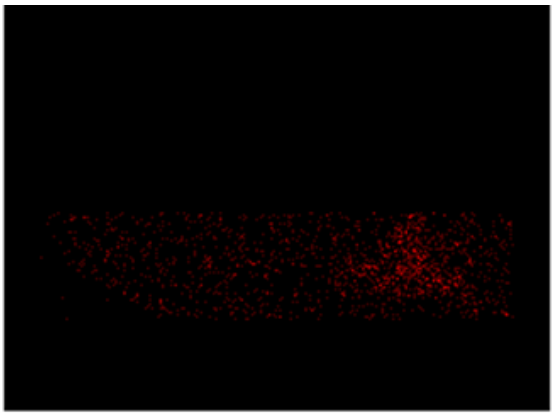
C Ka1_2

Run 2: Surface Speed of 60 m/min

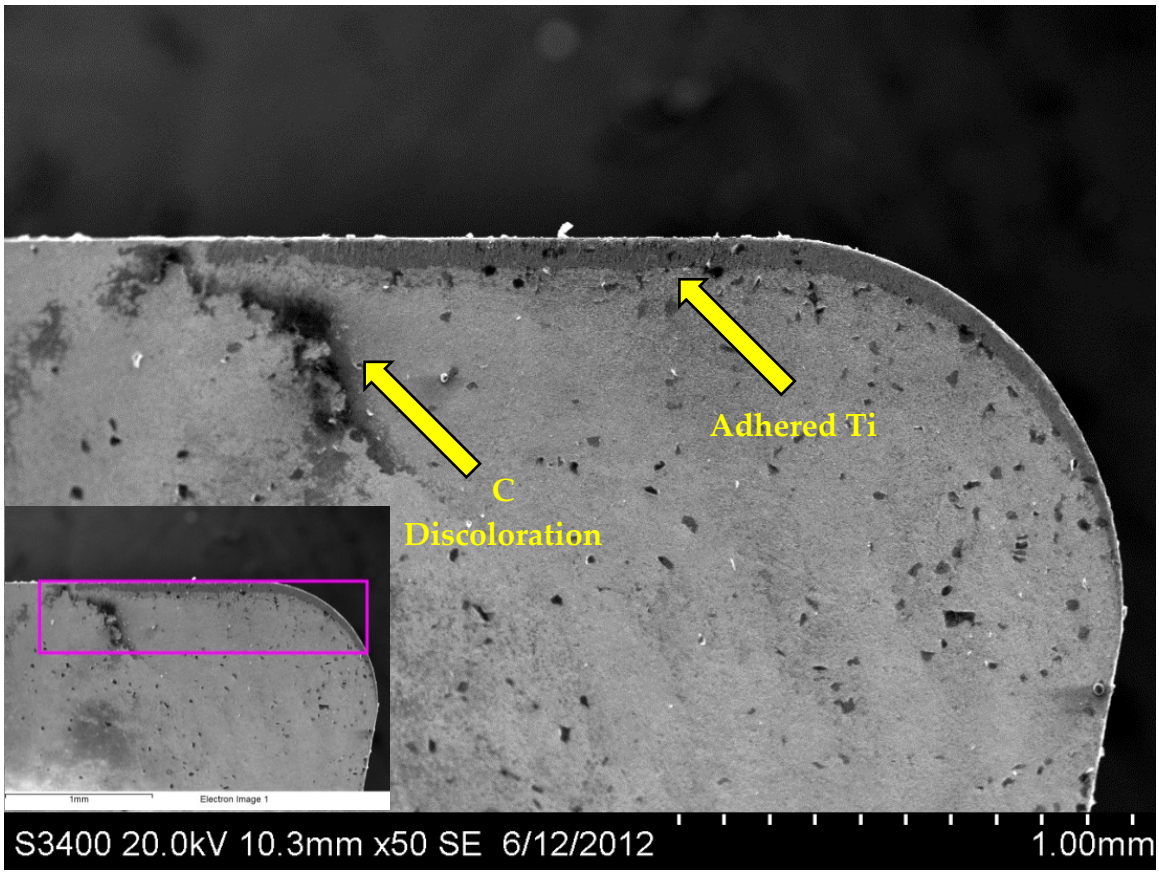

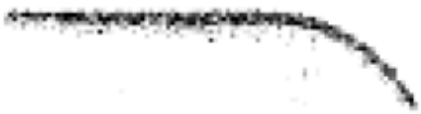

Ti Ka1

C Ka1_2

Run 3: Surface Speed of 120 m/min

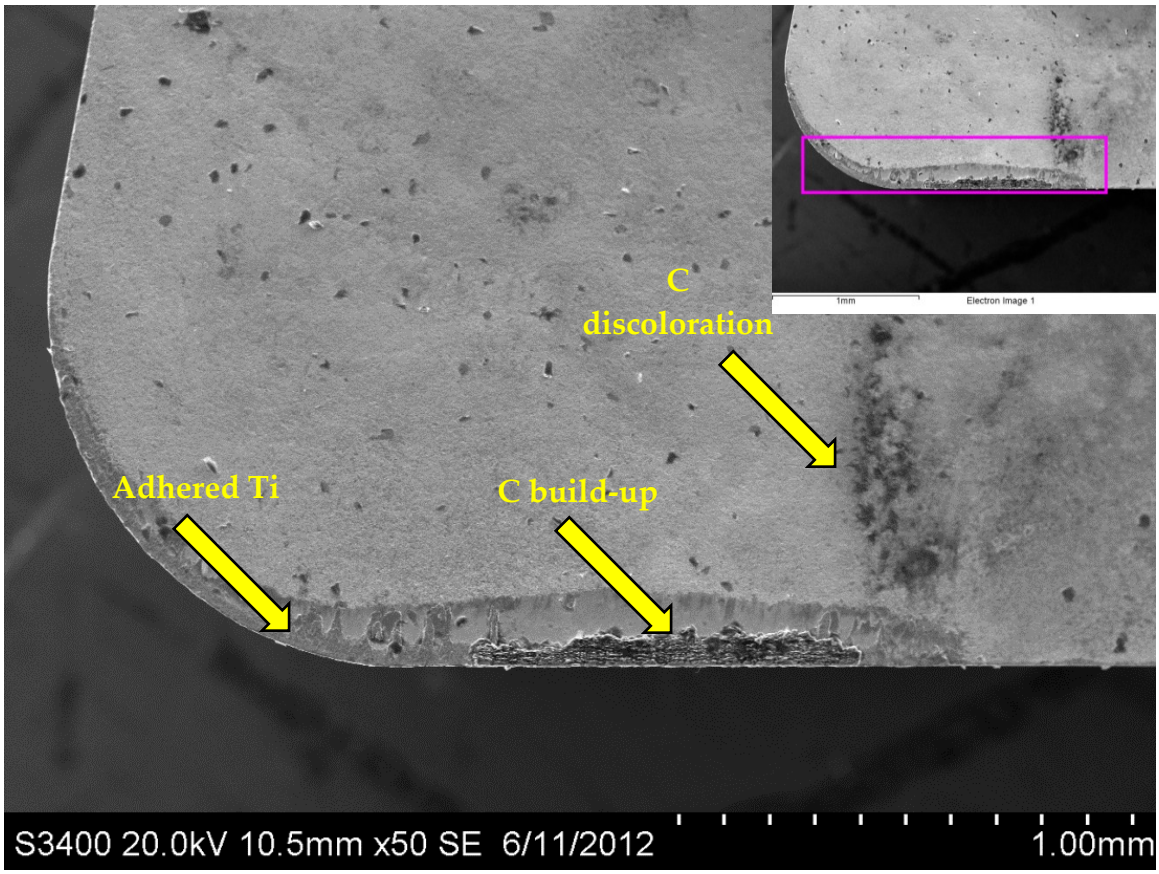

C Ka1_2

Ti Ka1

W La1

Co Ka1

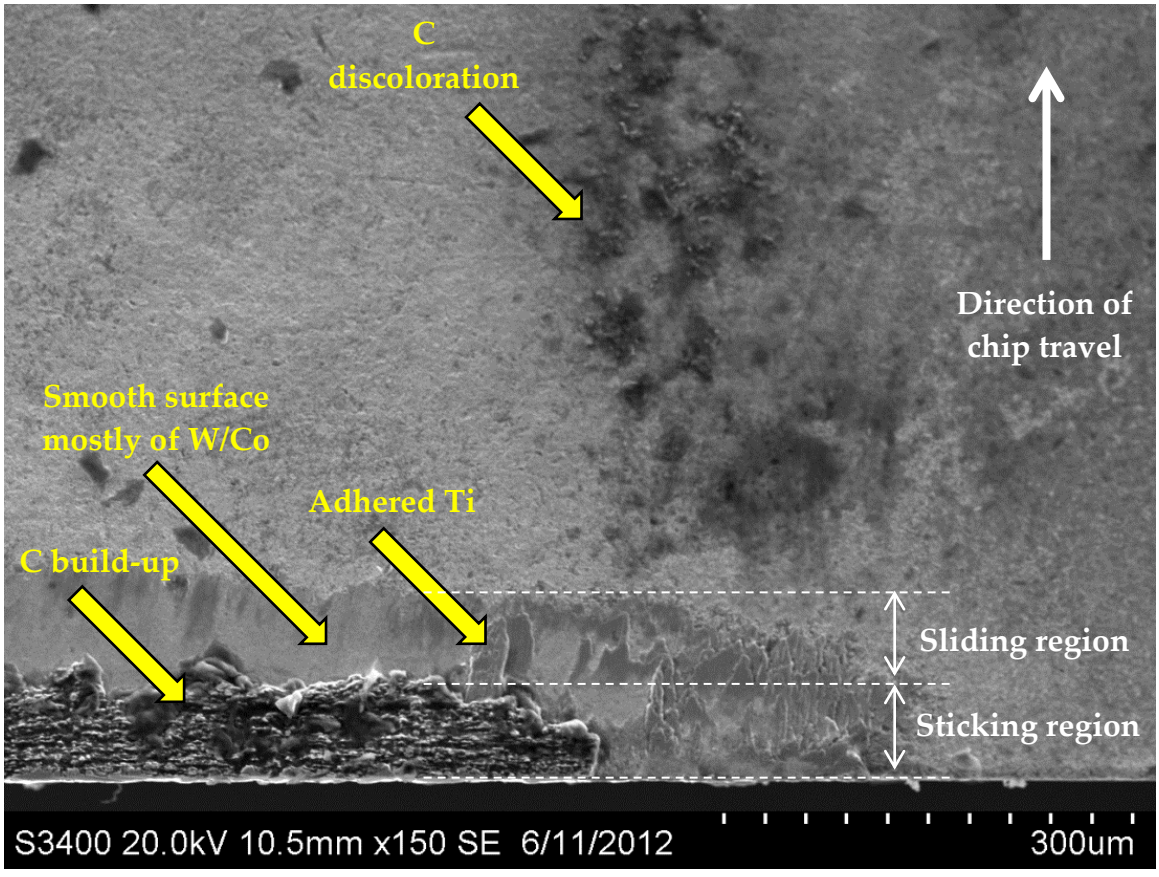
C
discoloration
Direction of
chip travel
Smooth surface
mostly of W/Co
Adhered Ti
C build-up
Sliding region
Sticking region
S3400 20.0kV 10.5mm x150 SE 6/11/2012
300um

Summary of Observations

At a feed rate of 0.05 mm/rev, minor amounts of titanium were found adhered to the outer edge of the tool at all speed levels. There was slightly higher adhered titanium when going from low to medium speed. At the high speed, in addition of the adhered titanium, a crater was formed due to the WC grains, W, C, and Co binder leaving with the chips. The smooth surface in the crater is a result of the high temperature generalized dissolution wear. This is evident from EDS where the smooth region of the crater trough is predominantly composed of tungsten and cobalt only.

Additionally, carbon discoloration was observed at the notch region on the rake face at all speeds. Another interesting observation was the presence of significant carbon build-up on the tool edge from EDS. Further, the smooth regions of the wear trough had very sparse composition of carbon. That this means regarding carbon is that:

- Carbon leaves the crater trough easily with the chip by generalized dissolution, as evident by its sparse eventual distribution in the trough,
- The chips carry away carbon, as evident from the carbon discoloration on the notch region, and
- The carbon build-up on the tool edge suggests that carbon is being "chemically-pulled" out of the tool, *i.e.*, due to a chemical-potential. Further, this build-up cannot be deposited from the chip (as in the case of the notch region), since it is in the opposite direction of chip flow. The distribution of

the carbon build-up is however in conformance with the chip-sticking and chip-sliding regions of chip flow that is common to turning operations.

Though the discoloration at the notch region was deduced to be carbon from EDS analysis, further examination may be necessary. One option would be to section the tool such that both the concentration gradients as well as Vickers hardness values starting from the surface and going down into the tool body could be measured. This is expected to provide necessary proof of the discoloration being carbon.

Finally, no indication of abrasive wear was observed (scratches in the chip flow direction). One of the reasons is because this is an uncoated tool, and there is no chance of the harder coating particles disintegrating and scribing the tool surface. Other reasons could be that the workpiece material contains very few "hard" impurities, besides the carbide tool being of sub-micron grade.

4.4.1.2 Feed Rate of 0.15 mm/rev (Runs 4 – 6)

Run 4: Surface Speed of 30 m/min

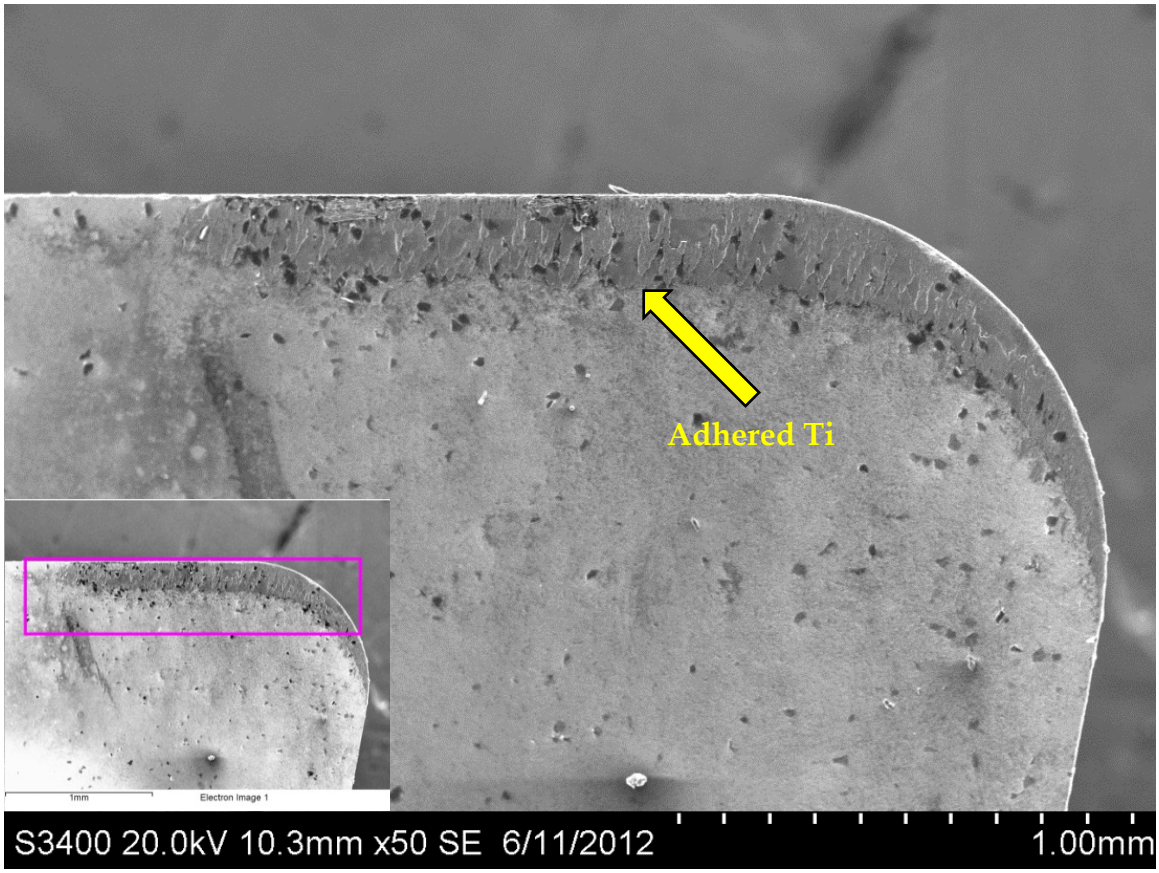

C Ka1_2

Ti Ka1

Run 5: Surface Speed of 60 m/min

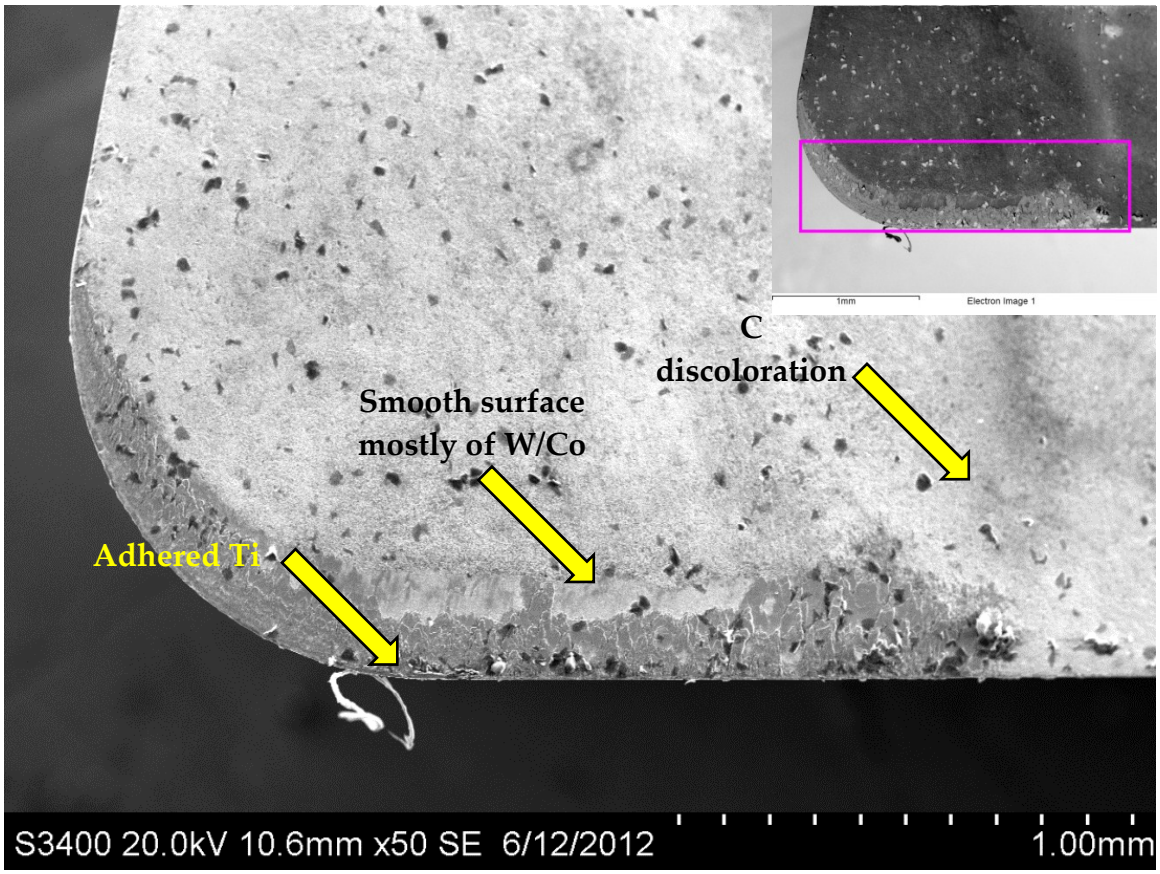

C Ka1_2

Ti Ka1

Run 6: Surface Speed of 120 m/min

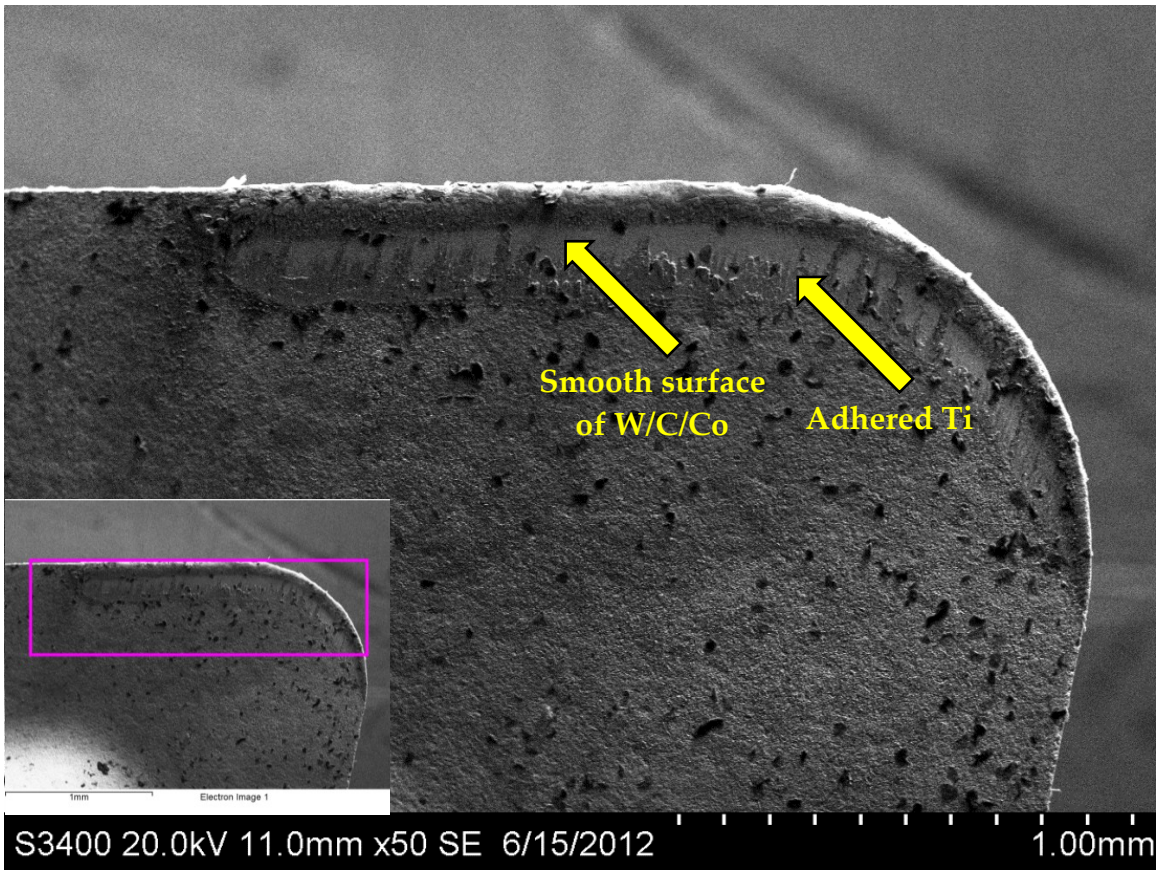

C Ka1_2 Ti Ka1

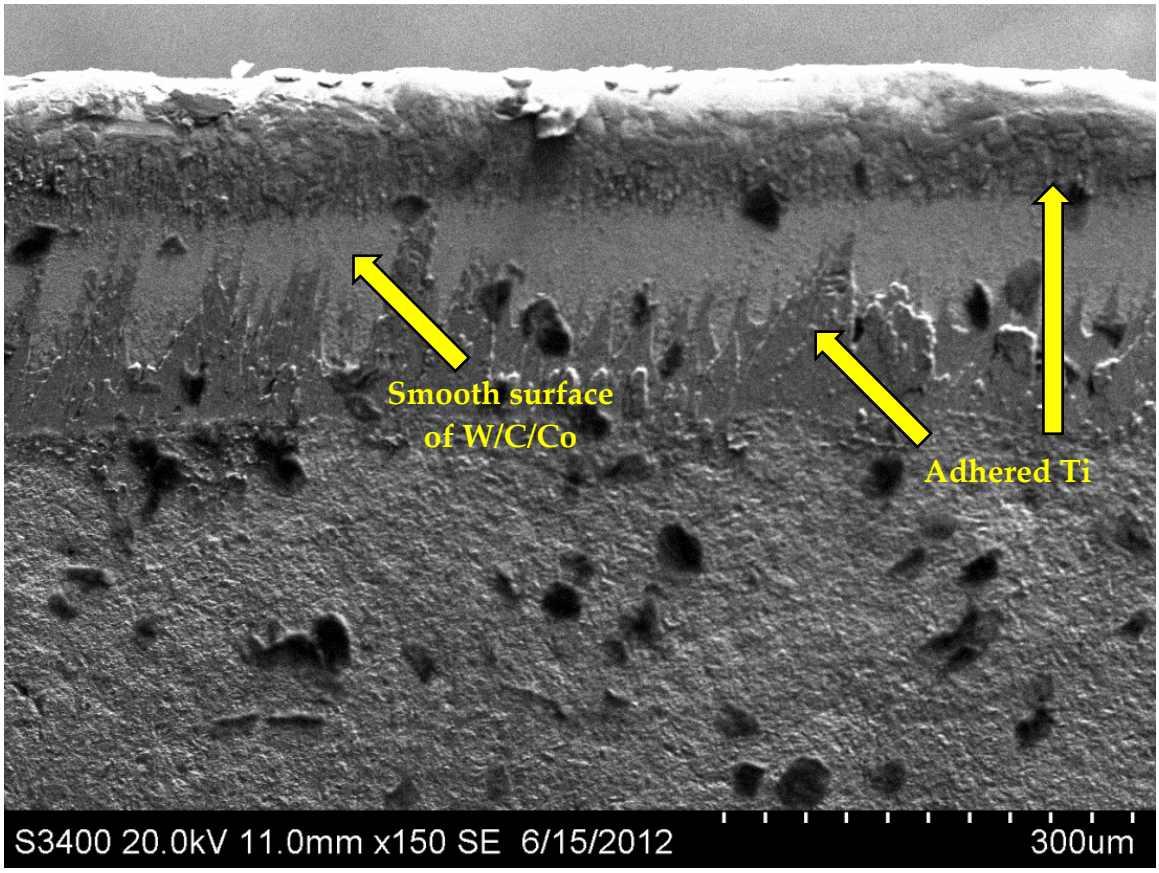

Summary of Observations

At a feed rate of 0.15 mm/rev, medium to major amounts of titanium were found adhered to the worn areas of the tool at all speeds. The amount of adhered titanium was major and covered the whole worn surface at the low speed, while this amount reduced when going higher up in speeds; at the outer edge only at the medium speed, while at both inner and outer edges at the high speed. At medium and high speeds, in addition of the adhered titanium, wear troughs were gouged out due to the WC grains, W, C, and Co binder leaving with the chips. The smooth surface in the trough is a result of the high

temperature generalized dissolution wear. This is evident from EDS where the smooth region of the crater trough is composed of tungsten, carbon and cobalt.

Additionally, minor carbon discoloration was observed at the notch region on the rake face at all speeds. Another observation at the high speed was the appearance of the adhered titanium being smeared (or being smoothened out). This means that the adhered titanium was now being worn away by the action of generalized dissolution. This conclusion is supported by the fact that the dissolution has happened first at the maximum crater depth (smooth region in figure) which is also the region of maximum temperature as known from chip flow in turning, and then starting to wear away the two edges of the crater trough. Again, no indication of abrasive wear was observed.

4.4.1.3 Feed Rate of 0.30 mm/rev (Runs 7 – 9)

Run 7: Surface Speed of 30 m/min

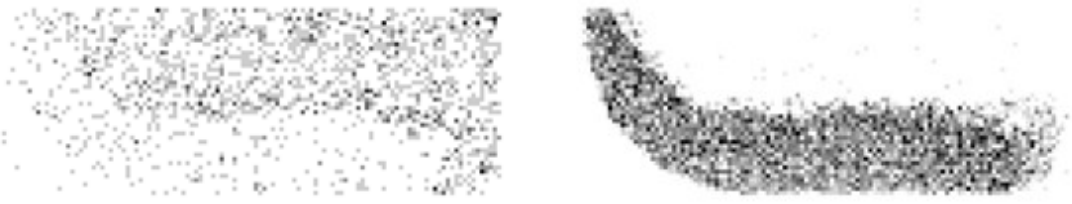

C Ka1_2 Ti Ka1

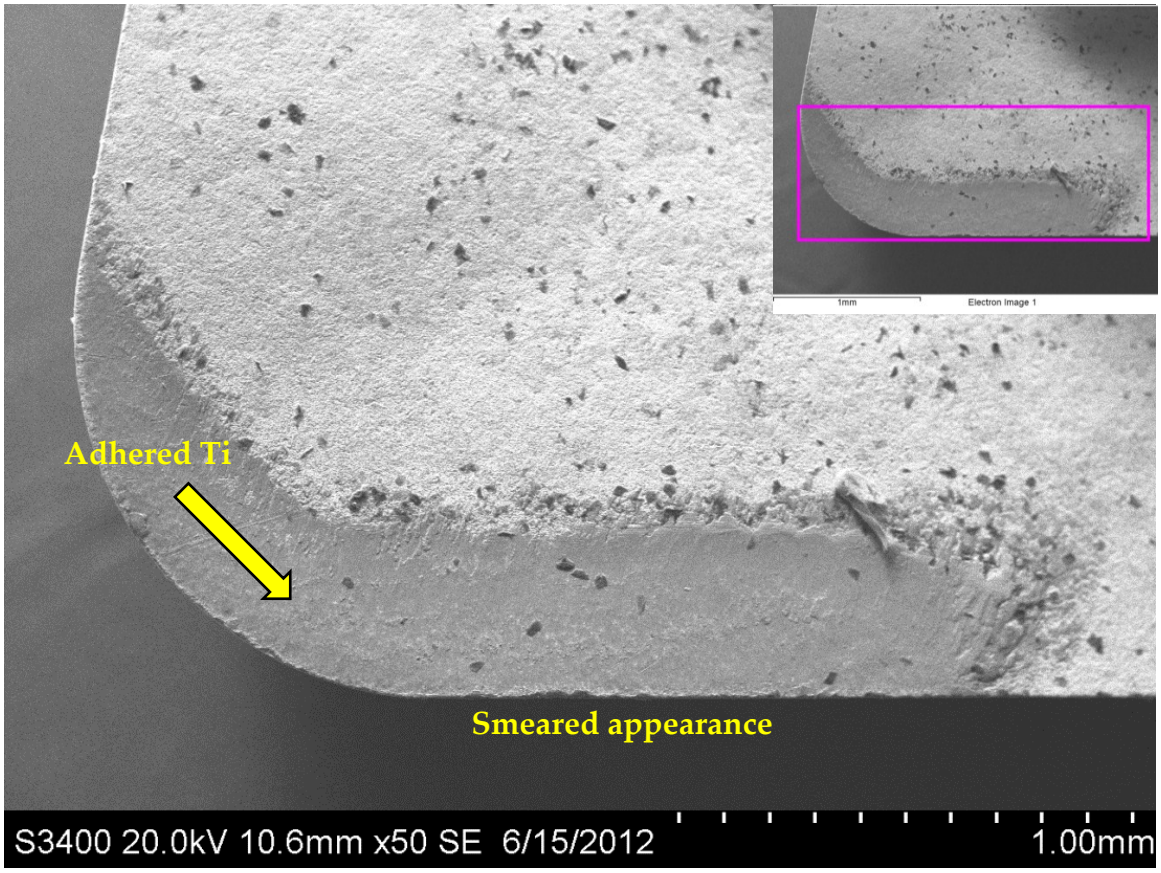

Run 8: Surface Speed of 60 m/min

C Ka1_2

Ti Ka1

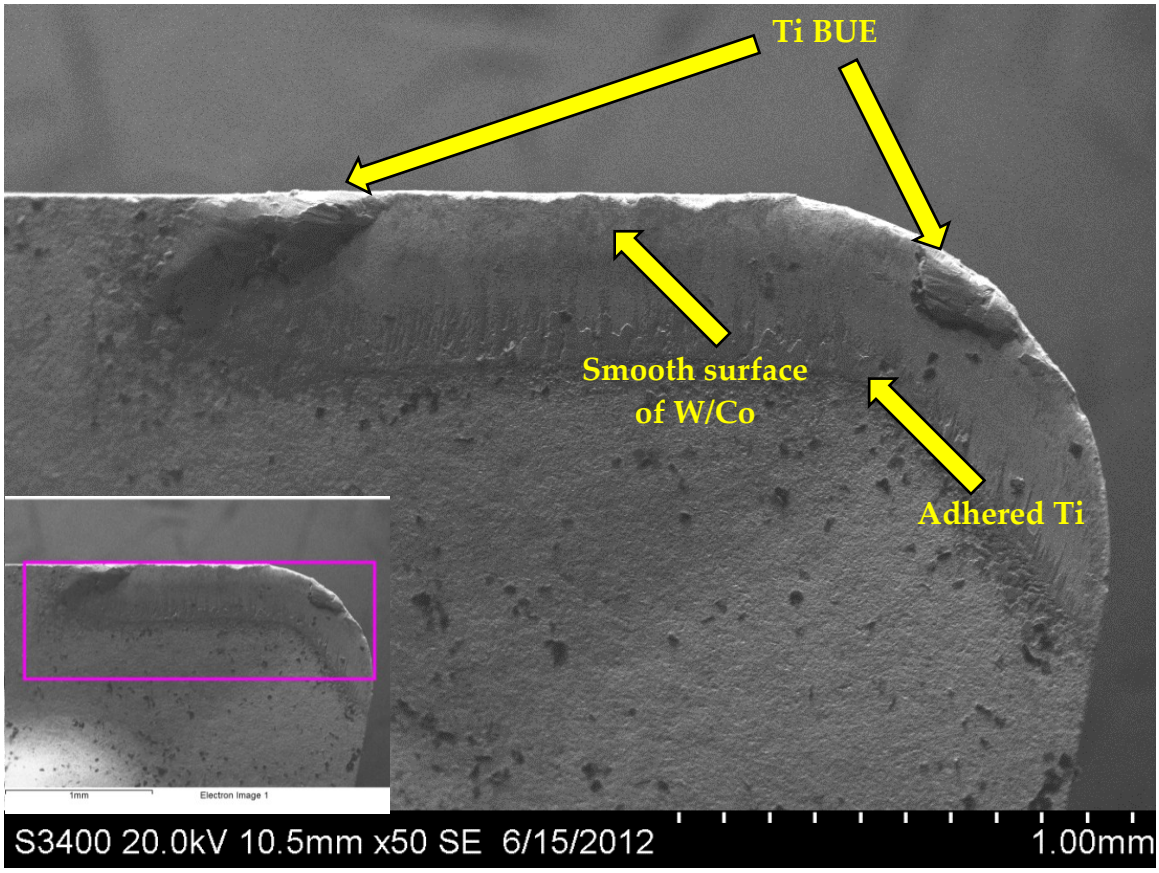

Run 9: Surface Speed of 120 m/min

C Ka1_2 Ti Ka1

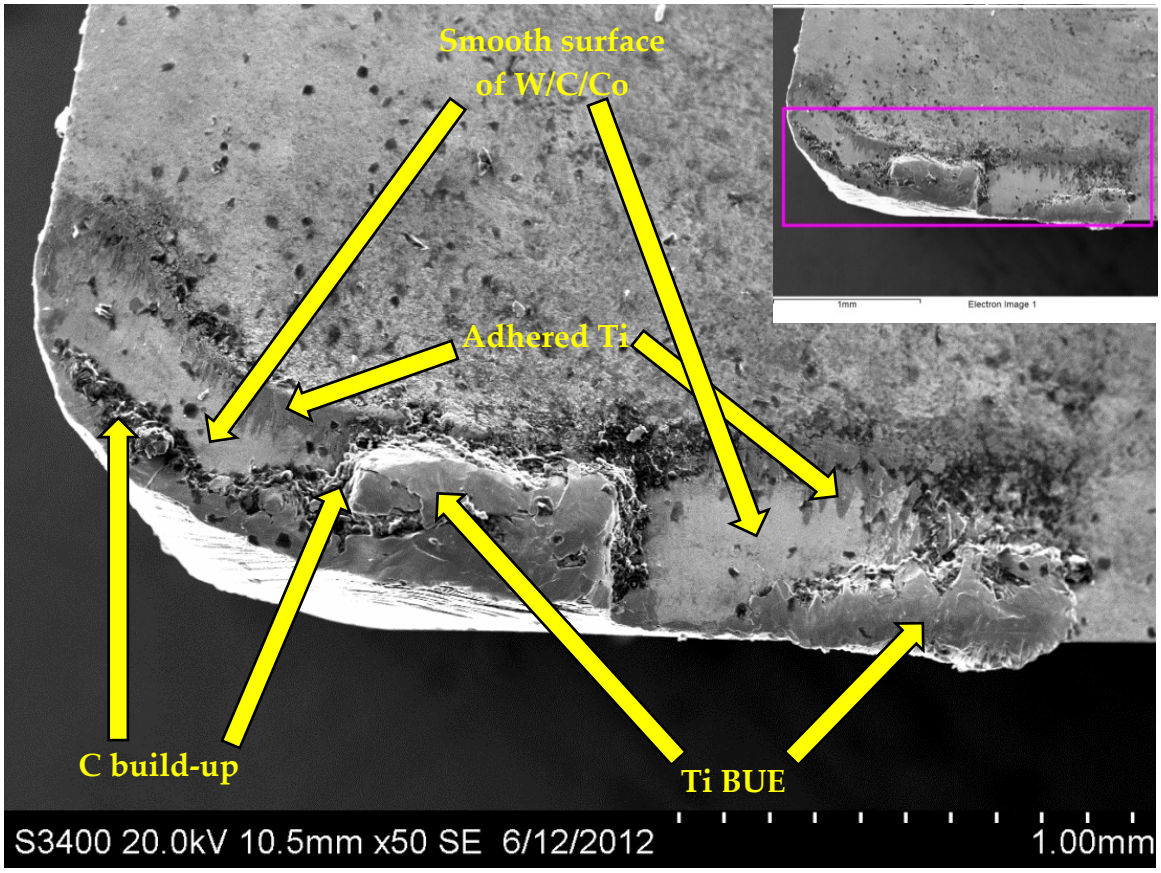

Summary of Observations

At a feed rate of 0.30 mm/rev, minor to major amounts of titanium were found adhered to the worn areas of the tool at all speeds. The amount of adhered titanium was major and covered the whole worn surface at the low speed, then reduced to a medium amount and covered about half of the worn area at medium speed, and finally was minor and present on the inside and outside edges at the high speed. In general, adhesion reduced when going higher up in speeds. This is in conformance with known behavior that adhesion reduces as surface speeds increase.

At medium and high speeds, in addition of the adhered titanium, wear troughs were gouged out due to the WC grains, W, C, and Co binder leaving with the chips. The smooth surface in the trough is a result of the high temperature generalized dissolution wear. This is evident from EDS where the smooth region of the crater trough is composed of tungsten, carbon and cobalt. Additionally, at the low speed, the adhered titanium seemed to be smeared onto the worn surface resulting in a much smoother adhesion surface than seen before. One of the reasons for this could be the severe chatter that was experienced during this cut which vibrated the tool in the additional thrust direction thereby smearing the adhered titanium.

No carbon discoloration was observed at any speed for this feed rate. Another observation at the medium and high speeds was the formation of titanium built-up-edges (BUE) on the tool edges. Further, at the high speed, the tool experienced failure through a combination of wear mechanisms; adhered titanium, W/C/Co troughs, carbon build-up, and BUE were observed. Again, no indication of abrasive wear was observed.

The table of these observations for the above 9 runs are summarized below. Note that the "extent" column denotes (absolute wear, % of area covered by mechanism). Thus a "Minor/100% adhesion" means that the amount of total adhesive wear was minor (qualitative), and the portion of the wear area covered by adhesion was 100% (quantitative). In contrast, a "Major/100% adhesion" means that the amount of total adhesive wear was major (qualitative), and the portion of the wear area covered by adhesion was 100% (quantitative).

Table 4-4: Weighted Wear Mechanisms for H10A Grade Carbide Inserts

	0.05 mm/rev - 30 m/min (Run 1)			60 m/min (Run 2)			120 m/min (Run 3)		
	Extent	**Mechanism**	**Location**	**Extent**	**Mechanism**	**Location**	**Extent**	**Mechanism**	**Location**
Wear: 1^0	Minor/ 100%	Adhesion	Outer edge	Medium/ 100%	Adhesion	Outer edge	Major/ 50%	Gen-Diss	Full trough
Wear: 2^0							Minor/ 50%	Adhesion	Outer edge
Others	Notch discoloration			Notch discoloration			Notch discoloration		
EDS	Ti-adh, C-disc			Ti-adh, C-disc			Ti-adh, C-disc, C-build, W/Co-trough		

	0.15 mm/rev - 30 m/min (Run 4)			60 m/min (Run 5)			120 m/min (Run 6)		
	Extent	**Mechanism**	**Location**	**Extent**	**Mechanism**	**Location**	**Extent**	**Mechanism**	**Location**
Wear: 1^0	Major/ 100%	Adhesion	Full area	Medium/ 50%	Gen-Diss	Full trough	Major/ 50%	Gen-Diss	Full trough
Wear: 2^0				Medium/ 50%	Adhesion	Outer edge	Medium/ 50%	Adhesion	Inner & outer edges
Others	Notch discoloration			Notch discoloration			Notch discoloration		
EDS	Ti-adh, C-disc			Ti-adh, C-disc, W/Co-trough			Ti-adh, C-disc, W/Co-trough		

	0.30 mm/rev - 30 m/min (Run 7)			60 m/min (Run 8)			120 m/min (Run 9)		
	Extent	**Mechanism**	**Location**	**Extent**	**Mechanism**	**Location**	**Extent**	**Mechanism**	**Location**
Wear: 1^0	Major/ 100%	Adhesion	Full area	Medium/ 50%	Gen-Diss	Full trough	Major/ 50%	Gen-Diss	Full trough
Wear: 2^0				Medium/ 50%	Adhesion	Outer edge	Major/ 50%	Adhesion	Inner & outer edges
Others	Smearing			BUE			BUE		
EDS	Ti-adh			Ti-adh,W/Co-trough			Ti-adh, C-build, W/Co-trough		

Nomenclature	
Ti-adh	Adhered titanium
C-disc	Carbon discoloration
C-build	Carbon build-up
W/Co-trough	Smooth surface of W/Co
Gen-Diss	General dissolution wear

4.4.2 H13A Inserts - Weighting (Stock Volume Cut = 10 cm^3)

4.4.2.1 Feed Rate of 0.05 mm/rev (Runs 10 – 12)

Run 10/11/12: Surface Speed of 30/60/120 m/min

Runs 10, 11 and 12 for the H13A grade displayed very similar patterns as for the H10A grade runs of 1, 2 and 3.

Summary of Observations

At a feed rate of 0.05 mm/rev, minor amounts of titanium were found adhered to the outer edge of the tool at all speed levels. There was slightly higher adhered titanium when going from low to medium speed. At the high speed, adhered titanium was found on both inner and outer edges. Further, at the high speed, a wear trough was gouged out due to the WC grains, W, C, and Co binder leaving with the chips. The smooth surface in the trough is a result of the high temperature generalized dissolution wear. This is evident from EDS where the smooth region of the crater trough is predominantly composed of tungsten and cobalt only.

Additionally, carbon discoloration was observed at the notch region on the rake face at all speeds. Finally, no indication of abrasive wear was observed. The only main difference with the previous H10A inserts was the adhered titanium being found on both inner and outer edges at the high speed.

4.4.2.2 Feed Rate of 0.15 mm/rev (Runs 13 – 15)

Run 13: Surface Speed of 30 m/min

Run 13 for H13A grade displayed very similar patterns as for the H10A grade run 4.

Run 14: Surface Speed of 60 m/min

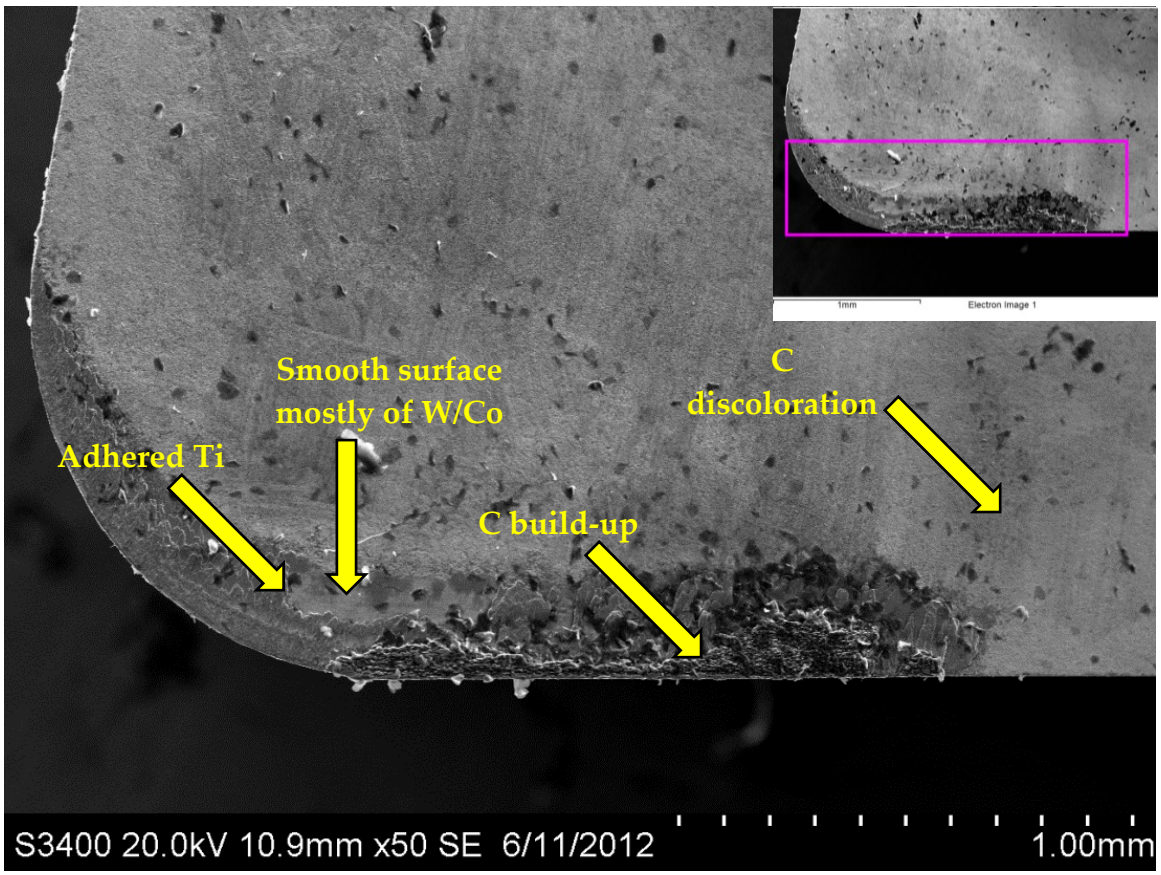

C Ka1_2 Ti Ka1

Run 15: Surface Speed of 120 m/min

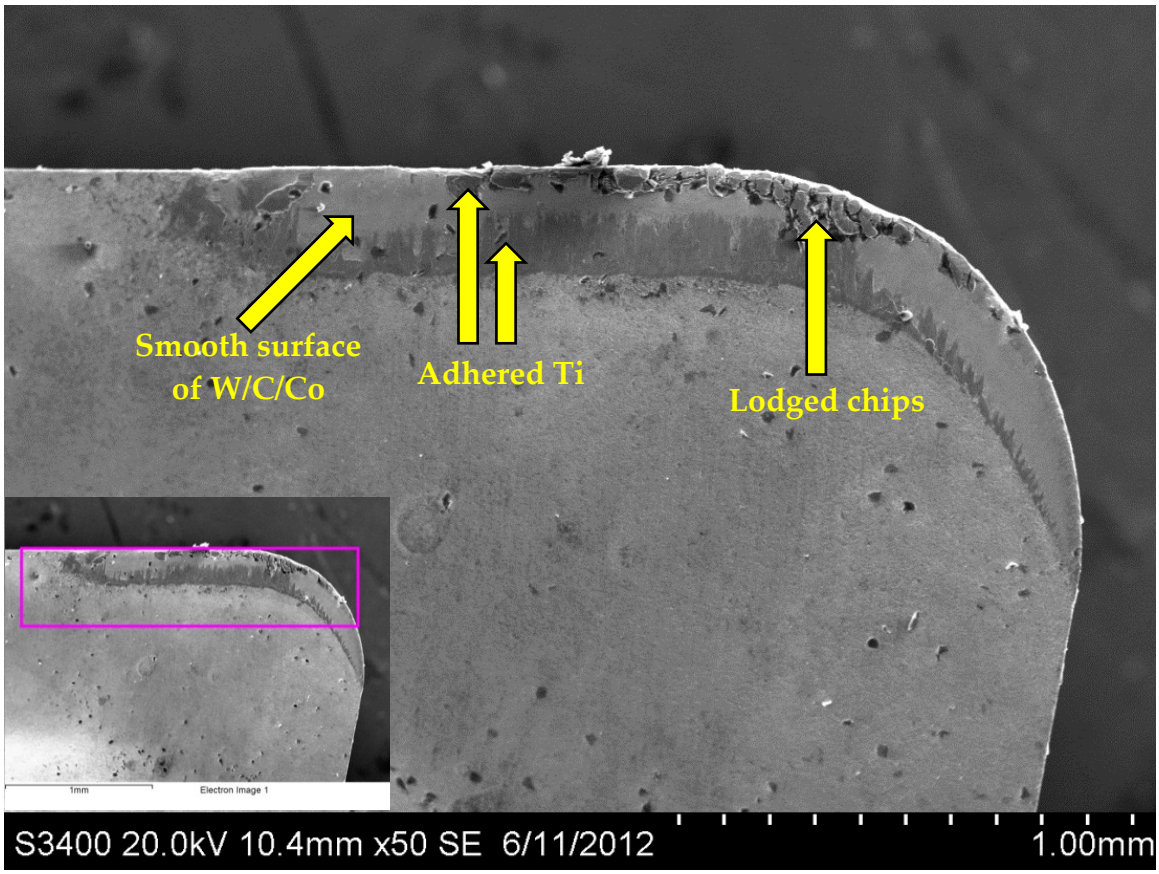

C Ka1_2

Ti Ka1

W La1

Co Ka1

Summary of Observations

At a feed rate of 0.15 mm/rev, medium to major amounts of titanium were found adhered to the worn areas of the tool at all speeds. The amount of adhered titanium covered about 75% of the worn surface at the low speed, while this amount reduced to about 50% when going higher up in speed Again the adhesive pattern was seen at the outer edge only for the low and medium speeds, while at both inner and outer edges at the high speed.

In this case, the gouged out wear troughs were observed at all speeds, with its dominance (% area) increasing with cutting speed. The smooth surface in the trough is a result of the high temperature generalized dissolution wear. This is evident from EDS where the smooth region of the crater trough is composed of tungsten, carbon and cobalt.

Additionally, minor carbon discoloration was observed at the notch region on the rake face at all speeds. An additional observation at the medium speed was the presence of carbon build-up at the tool edge. Also, at the high speed, the adhered titanium appeared to be smeared; this means that the adhered titanium was now being worn away by the action of generalized dissolution. Further, some chips were observed to be lodged on the tool edge as well. Again, no indication of abrasive wear was observed. The only main difference with the previous H10A inserts was the generalized dissolution mechanism showing up at the low speed.

4.4.2.3 Feed Rate of 0.30 mm/rev (Runs 16 – 18)

Run 16: Surface Speed of 30 m/min

Run 16 for H13A grade displayed very similar patterns as for the H10A grade run 7.

Run 17: Surface Speed of 60 m/min

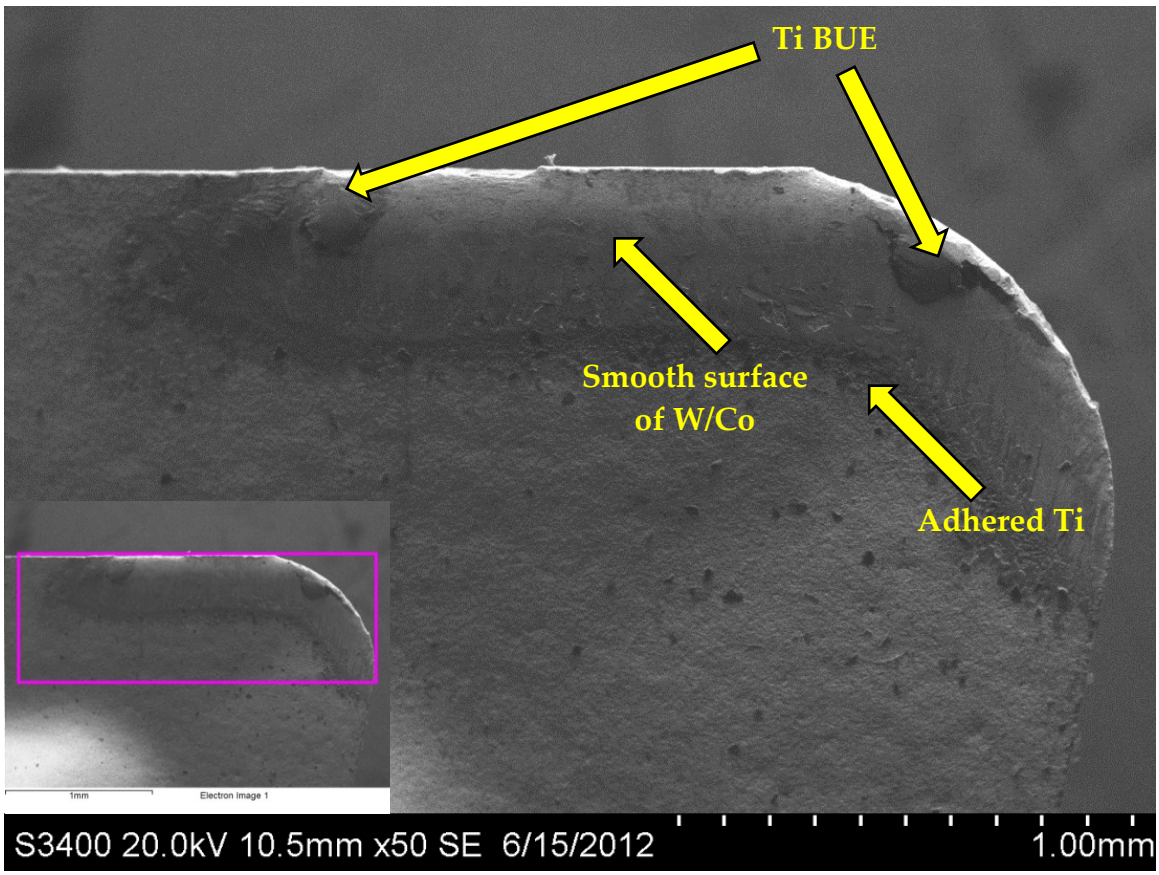

Run 18: Surface Speed of 120 m/min

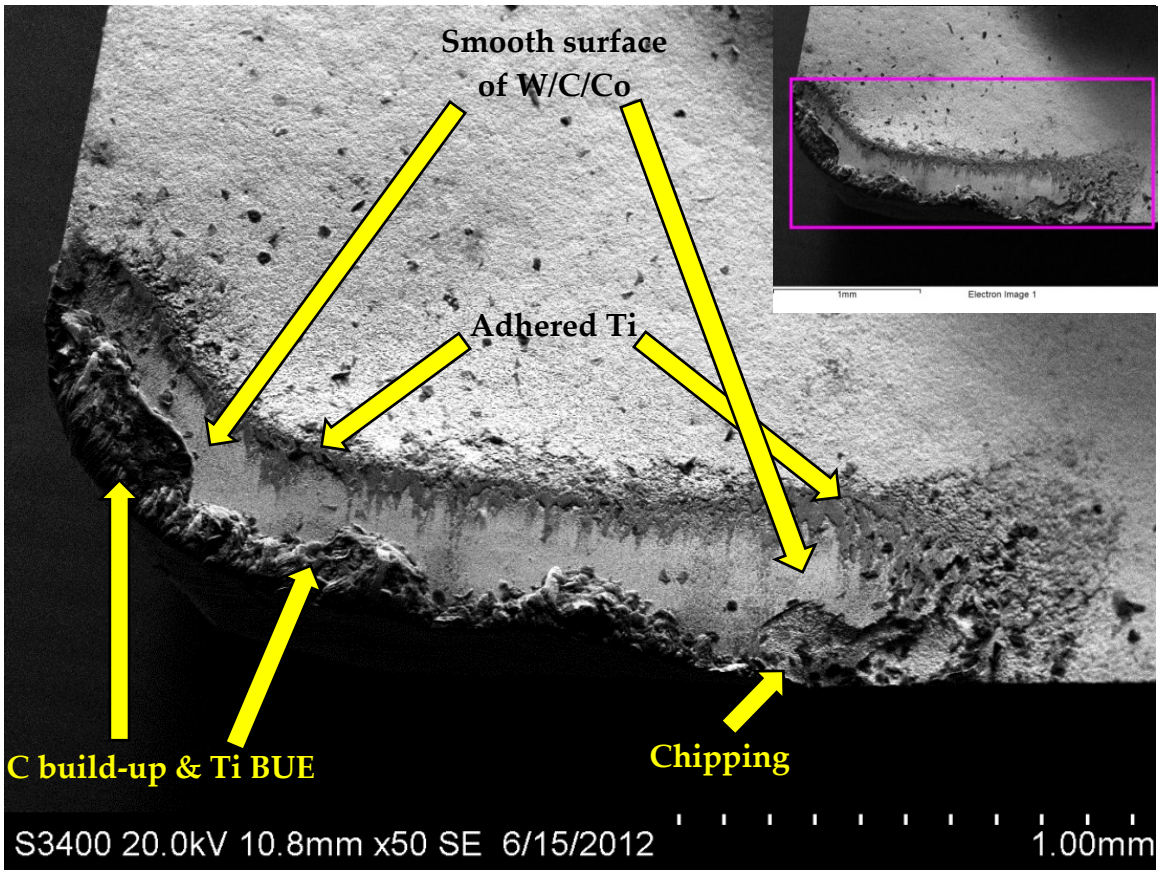

C Ka1_2

Ti Ka1

W La1 Co Ka1

Summary of Observations

At a feed rate of 0.30 mm/rev, minor to major amounts of titanium were found adhered to the worn areas of the tool at all speeds. The amount of adhered titanium was major and covered the whole worn surface at the low speed, then reduced to a medium amount and covered about half of the worn area at medium speed, and finally was minor and present on the inside and outside edges at the high speed as in the case of H10A inserts. In general, adhesion reduced when going higher up in speeds. This is in conformance with known behavior that adhesion reduces as surface speeds increase.

At medium and high speeds, in addition of the adhered titanium, wear troughs were gouged out due to the WC grains, W, C, and Co binder leaving with the chips. The smooth surface in the trough is a result of the high temperature generalized dissolution wear. This is evident from EDS where the smooth region of the crater trough is composed of tungsten, carbon and cobalt. Additionally, at the low speed, the adhered

titanium seemed to be smeared onto the worn surface resulting in a much smoother adhesion surface than seen before. One of the reasons for this could be again, the severe chatter that was experienced during this cut which vibrated the tool in the additional thrust direction thereby smearing the adhered titanium.

No carbon discoloration was observed at any speed for this feed rate. Another observation at the medium and high speeds was the formation of titanium built-up-edges (BUE) on the tool edges, and almost at the exact same locations as with H10 inserts. Further, at the high speed, the tool experienced failure (severely worn) through a combination of wear mechanisms; adhered titanium, W/C/Co troughs, and a combined carbon build-up and BUE were observed. Again, no indication of abrasive wear was observed. The only main difference with the previous H10A inserts was that the adhered titanium moved to the inner edge (vs. outer for Ha10A) at the medium speed, and at the high speed, chipping was observed on the rake face closer to the notch area.

The table of these observations for the above 9 runs are summarized below. Note that the "extent" column denotes (absolute wear, % of area covered by mechanism).

Table 4-5: Weighted Wear Mechanisms for H13A Grade Carbide Inserts

	0.05 mm/rev - 30 m/min (Run 10)			60 m/min (Run 11)			120 m/min (Run 12)		
	Extent	**Mechanism**	**Location**	**Extent**	**Mechanism**	**Location**	**Extent**	**Mechanism**	**Location**
Wear: 1^0	Minor/ 100%	Adhesion	Outer edge	Medium/ 100%	Adhesion	Outer edge	Major/ 50%	Gen-Diss	Full trough
Wear: 2^0							Minor/ 50%	Adhesion	Inner & outer edges
Others	Notch discoloration			Notch discoloration			Notch discoloration		
EDS	Ti-adh, C-disc			Ti-adh, C-disc			Ti-adh, C-disc, W/Co-trough		

	0.15 mm/rev - 30 m/min (Run 13)			60 m/min (Run 14)			120 m/min (Run 15)		
	Extent	**Mechanism**	**Location**	**Extent**	**Mechanism**	**Location**	**Extent**	**Mechanism**	**Location**
Wear: 1^0	Medium/ 75%	Adhesion	Inner & outer edges	Medium/ 50%	Gen-Diss	Full trough	Major/ 75%	Gen-Diss	Full trough
Wear: 2^0	Minor/ 25%	Gen-Diss	Full trough	Major/ 50%	Adhesion	Outer edge	Medium/ 25%	Adhesion	Inner & outer edges
Others	Notch discoloration			Notch discoloration			Smearing, Chips recut		
EDS	Ti-adh, C-disc, W/Co trough			Ti-adh, C-disc, W/Co-trough, C-build			Ti-adh, C-disc, W/Co-trough		

	0.30 mm/rev - 30 m/min (Run 16)			60 m/min (Run 17)			120 m/min (Run 18)		
	Extent	**Mechanism**	**Location**	**Extent**	**Mechanism**	**Location**	**Extent**	**Mechanism**	**Location**
Wear: 1^0	Major/ 100%	Adhesion	Full area	Medium/ 50%	Gen-Diss	Full trough	Major/ 75%	Gen-Diss	Full trough
Wear: 2^0				Medium/ 50%	Adhesion	Inner edge	Major/ 25%	Adhesion	Inner & outer edges
Others	Smearing			BUE			BUE		
EDS	Ti-adh			Ti-adh,W/Co-trough			Ti-adh, C-build, W/Co-trough		

For employing the weighting factors, the design space was divided into three zones:

- A low-speed regime (around 30 m/min),
- A medium-speed regime (around 60 m/min) which is recommended, and
- A high-speed regime (around 120 m/min).

These are essentially three cutting-temperature-dependent regimes (since cutting temperature is directly proportional to speed [35, 39, 40]). Since dominance of wear mechanism were found to differ with surface speeds, three sets of weighting factors were used for better characterizing the wear mechanics of this tribosystem. They are:

4.4.3 Factors for H10A grade inserts

- In the low-speed regime, adhesion = 100%,
- In the medium-speed regime, adhesion = 50% and dissolution = 50%,
- In the high-speed regime, adhesion = 50% and dissolution = 50%.

4.4.4 Factors for H13A grade inserts

- In the low-speed regime, adhesion = 100%,
- In the medium-speed regime, adhesion = 50% and dissolution = 50%,
- In the high-speed regime, adhesion = 25% and dissolution = 75%.

4.5 Maps of Dominant Wear Mechanisms

The inputs for this task are the wear mechanisms that were identified for each of the two inserts types for each machining setup. This dominant wear mechanism information

from Section 4.4 was used to chart predictive maps of dominant wear mechanisms for this machining tribosystem with cutting speed and feed rate as the axes.

Each of the turning inserts that was used in the final DOE of machining experiments was cleaned and inspected under a SEM. By simultaneously analyzing the SEM micrographs of worn tool surfaces and the EDS elemental results of the worn areas, dominant wear mechanism were identified. The percentage areas damaged by each wear mechanism was quantified and tabulated for both cutting insert types, *i.e.*, H10A (finer grain) and H13A (coarser grain), as given in Table 4-4and Table 4-5 respectively.

These were then charted onto a graph with cutting speed and feed rate as the two axes. Note that in turning especially, the feed rate has a direct correlation with the cutting force experienced by the tool and hence it represents the mechanical load experienced by the tool material. Similarly, cutting speed has a direct correlation with the surface speed, especially in turning Ti-6Al-4V, and hence it represents the thermal "load" experienced by the tool material. The mapping for H10A starts from Figure 4-9.

The general procedure for constructing a wear map is outlined below:

1. Decide on the mode of contact for the material pair (machining - turning).
2. Begin by identifying dominant wear mechanisms or their contribution,
3. Select suitable map axes and their ranges (feed-speed combination),
4. Mark each machining test conducted and the wear mechanisms experienced,
5. Demarcate the dominance of each wear mechanism using field boundaries,
6. Identify a recommended range of operation.

4.5.1 Dominant Wear Mechanism Map for H10A Inserts (Finer grain)

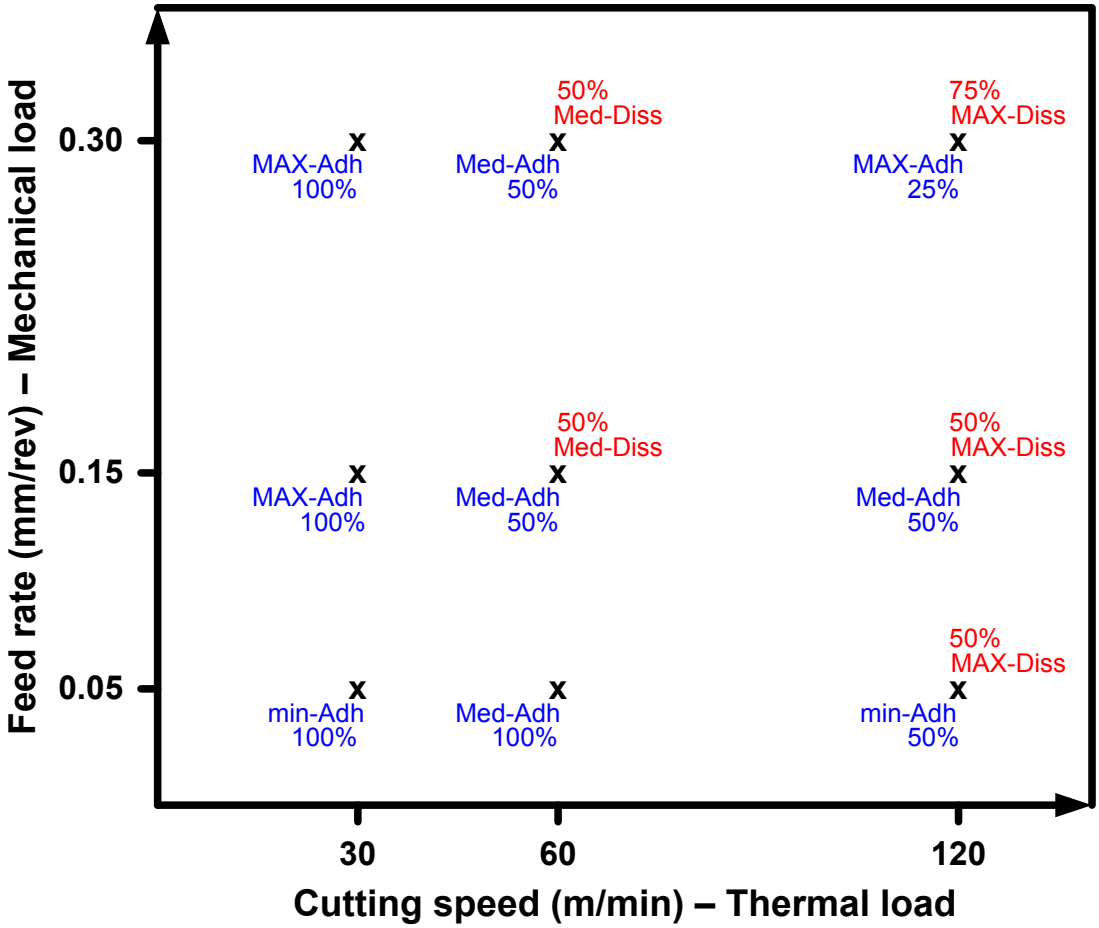

Figure 4-9: Chart identifying each of the nine machining setup conditions (feed-speed combinations) tested, and the dominant wear mechanism(s) identified at that condition by simultaneously analyzing SEM micrographs and EDS elemental results of the worn areas. Note that the locations of the cutting tests are marked with an "x" and that this chart is for H10A inserts with an average grain size of 0.54 μm (finer grain). Note the concentration of the dominant adhesive wear mechanism at the lower left corner of the chart (low speed and feed), while the generalized dissolution wear mechanism is more concentrated at the upper left corner of the chart (high speed and feed conditions). The recommended cutting condition for a 2mm cut depth is at the center "x", *i.e.*, a cutting speed of 60 m/min and feed of 0.15 mm/rev.

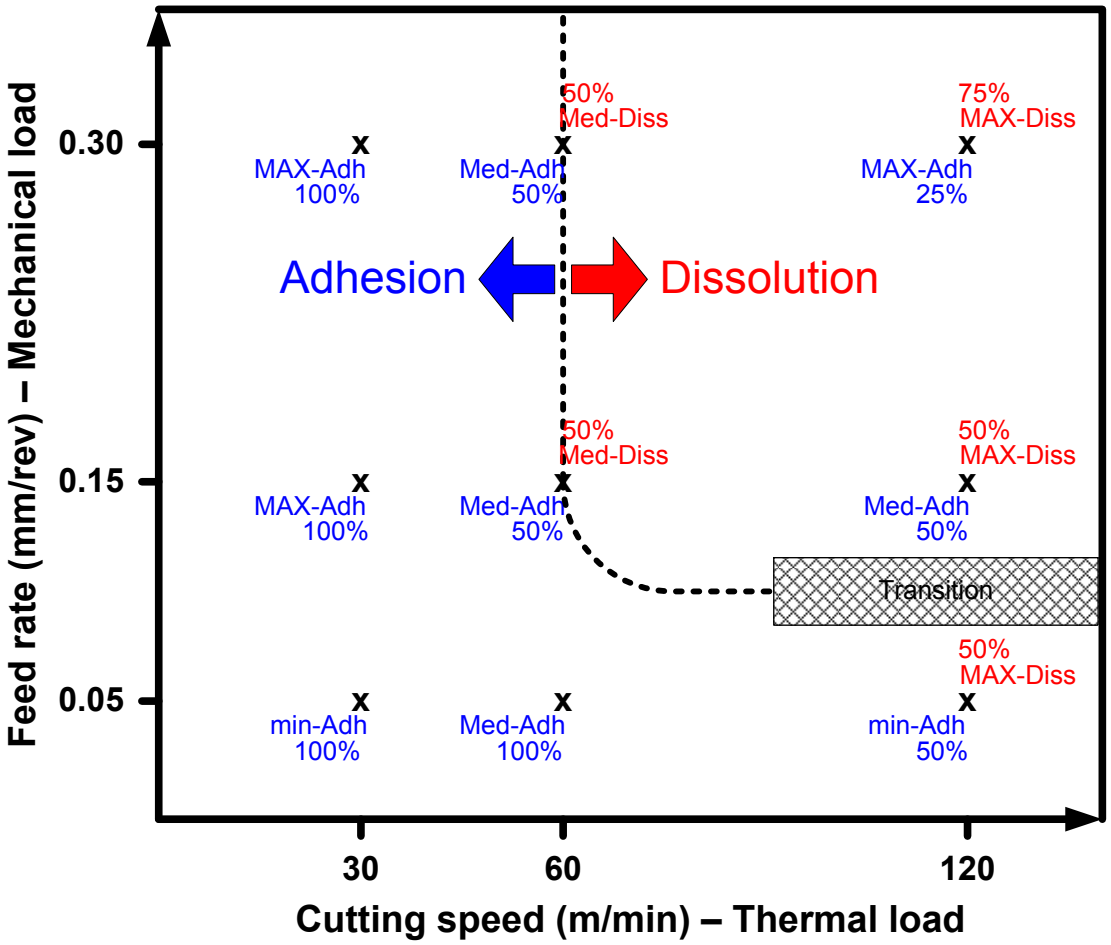

Figure 4-10: Map of dominant wear mechanism distribution for H10A inserts. Two regions have been identified when adhesion and dissolution wear mechanisms are dominant. A main field boundary was drawn separating these two regions. The left and bottom regions of the feed-speed design space showed a dominance of adhesion wear mechanism, while the top right region showed dominance of dissolution wear. These were demarked on the basis of the percentage area that was affected on the wear surface. There was also a "grey" area at the high speed condition (120 m/min) where there was some transitioning happening between the dominance between adhesion and dissolution wear, *i.e.*, dissolution wear was becoming more dominant with increasing feed rate.

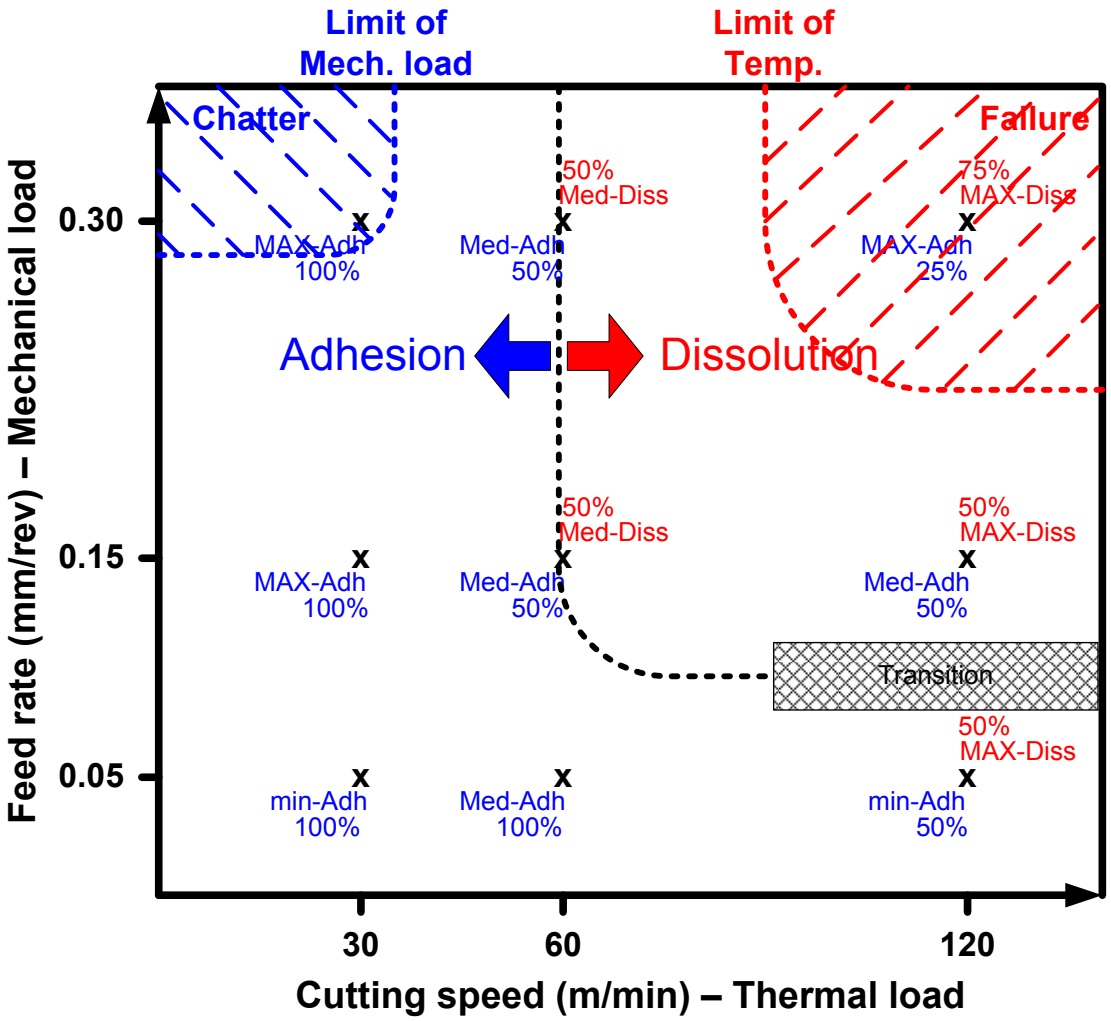

Figure 4-11: Failure and chatter conditions demarked on the map of dominant wear mechanism distribution for H10A inserts. The low speed, high-feed combination resulted in a chatter condition during the cutting process and caused smearing on the tool rake face – all of this smeared material was identified as titanium from EDS analysis. Further, the workpiece had chatter marks and unacceptable surface roughness – this resulted in identifying the region as a failure location. Note that this essentially represents the limit of mechanical load that the tool material can carry (feed has a direct relation with forces). Also, the high-speed, high-feed condition resulted in catastrophic failure of the tool, causing the region around it to be identified as a failure zone as well. Note that that this essentially represents the limit of thermal load that the tool material can carry (speed has a direct relation with temperature).

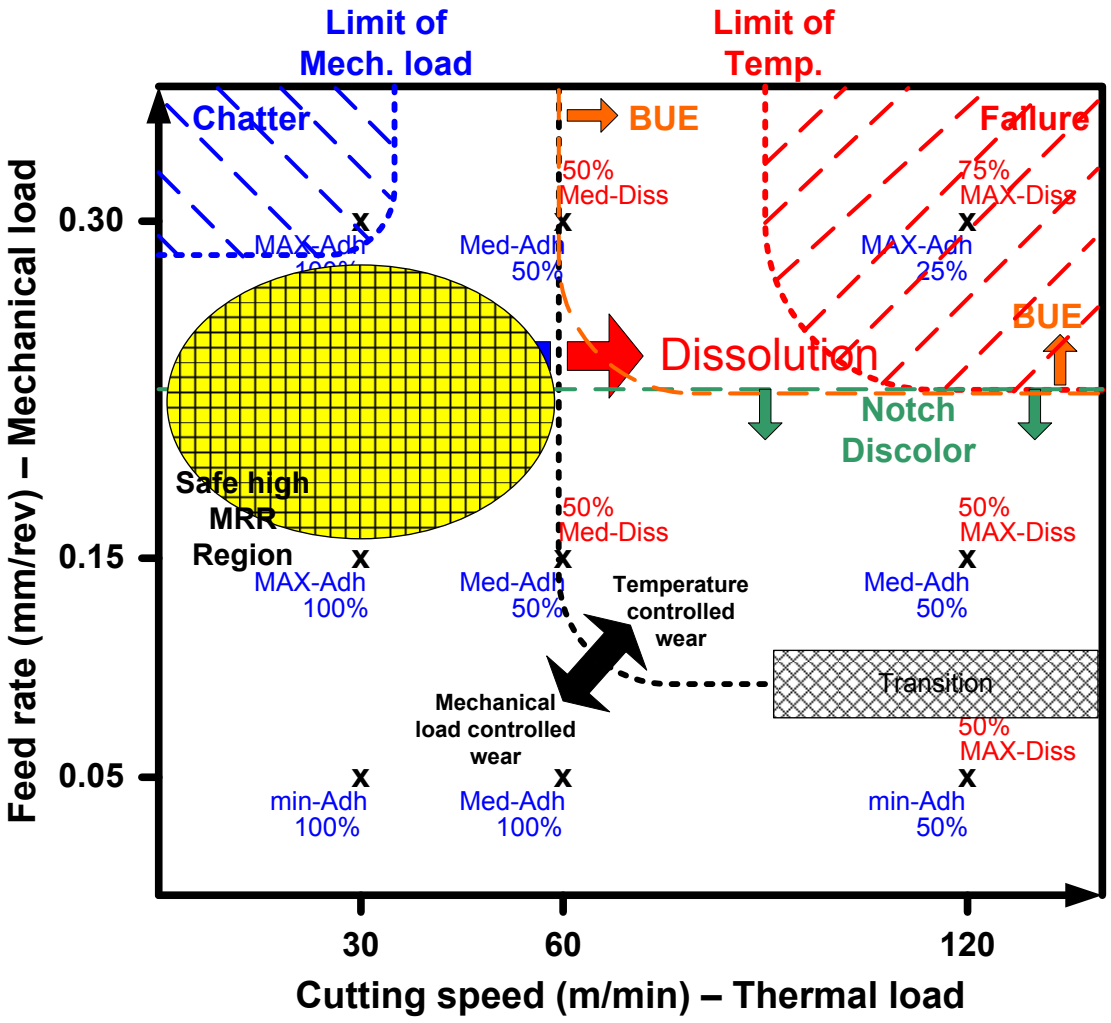

Figure 4-12: Final predictive map of dominant wear mechanisms for H10A carbide inserts dry turning Ti-6Al-4V. The additions in this chart include: (*i*) Region of notch discoloration on the tool (below a line in between the medium and high feed regions), (*ii*) Region of built-up-edge (BUE) formation (high speed and high feed conditions), and (*iii*) a safe region definition at medium to high feeds but low cutting speeds.

Thus, from the above maps, it is seen that the main line demarking the two dominant wear mechanisms essentially represent the line separating high temperature controlled wear from the region of high mechanical load controlled wear.

4.5.2 Dominant Wear Mechanism Map for H13A Inserts (Coarser grain)

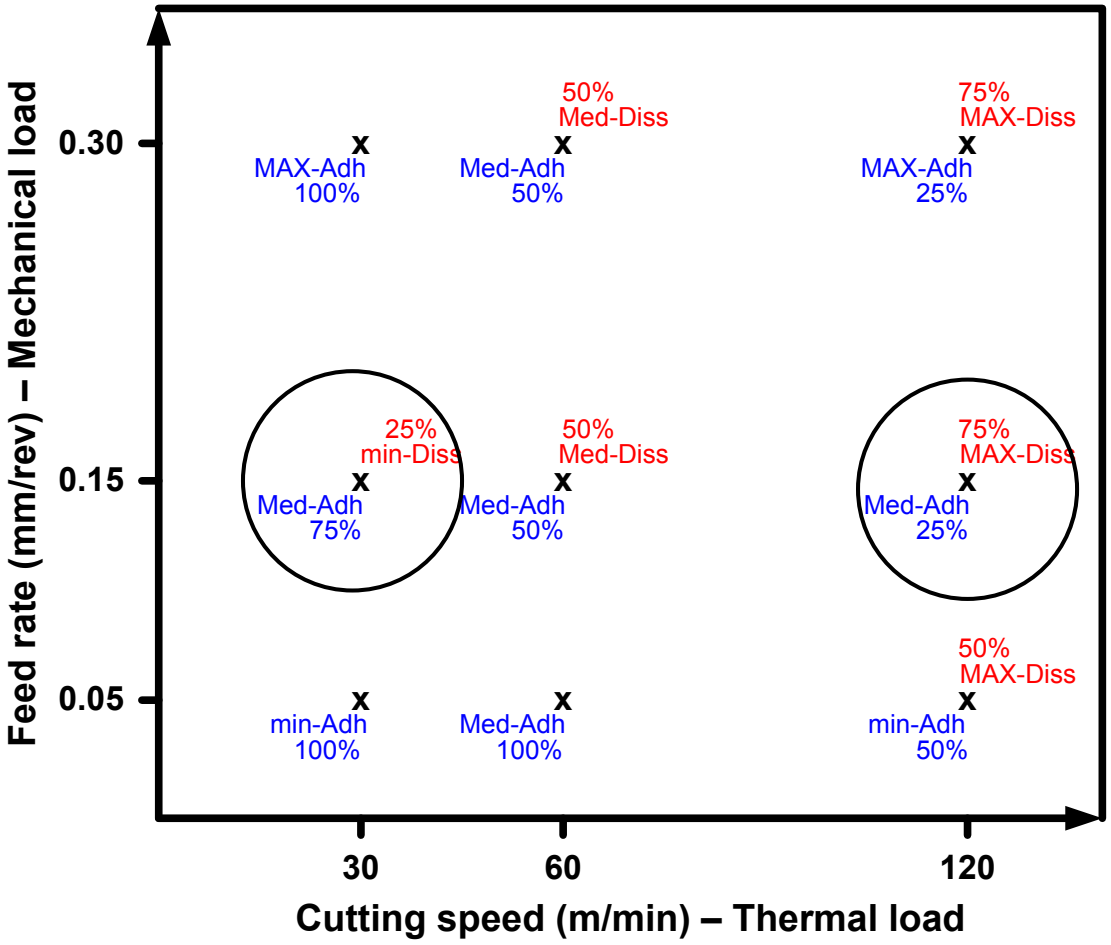

Figure 4-13: Chart identifying each of the nine machining setup conditions (feed-speed combinations) tested, and the dominant wear mechanism(s) identified at that condition by simultaneously analyzing SEM micrographs and EDS elemental results of the worn areas. Locations of the cutting tests are marked with an "x" and this chart is for H13A inserts with an average grain size of 0.61 μm (coarser grain, about 12% larger). The only two differences of this chart with that of H10A inserts are the mechanism dominance at the two circled locations. With a coarser grain, some dissolution wear effects were observed at the lower feed and, dissolution became the more dominant wear mechanism at high speed.

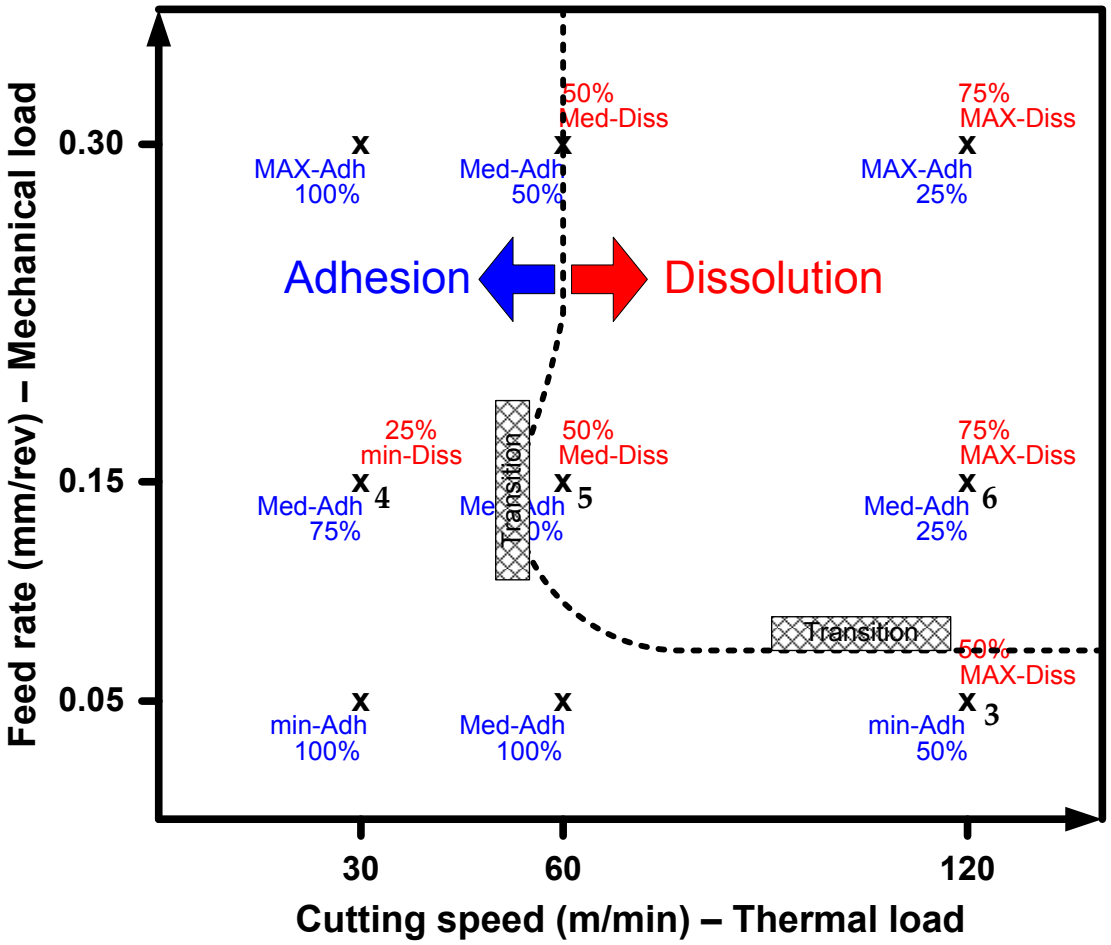

Figure 4-14: Map of dominant wear mechanism distribution for H13A inserts. Two regions have been identified when adhesion and dissolution wear mechanisms are dominant. A main field boundary was drawn separating these two regions.

Compared with the previous H10A inserts, two differences exist: (*i*) at high speed (120 m/min), dissolution wear dominance was observed much earlier when going up in feed rate. Consequently the field boundary between points #3 and #6 was lowered, and (*ii*) Effects of dissolution wear also showed up at point #6. Consequently, the field boundary was shifter to the left between points #4 and #5.

These failure zones were similar to those seen in the finer H10A inserts. This could be an early indication of these regions being classified as failure zones regardless of the grain size or other tool material properties; they could instead only feed/speed based.

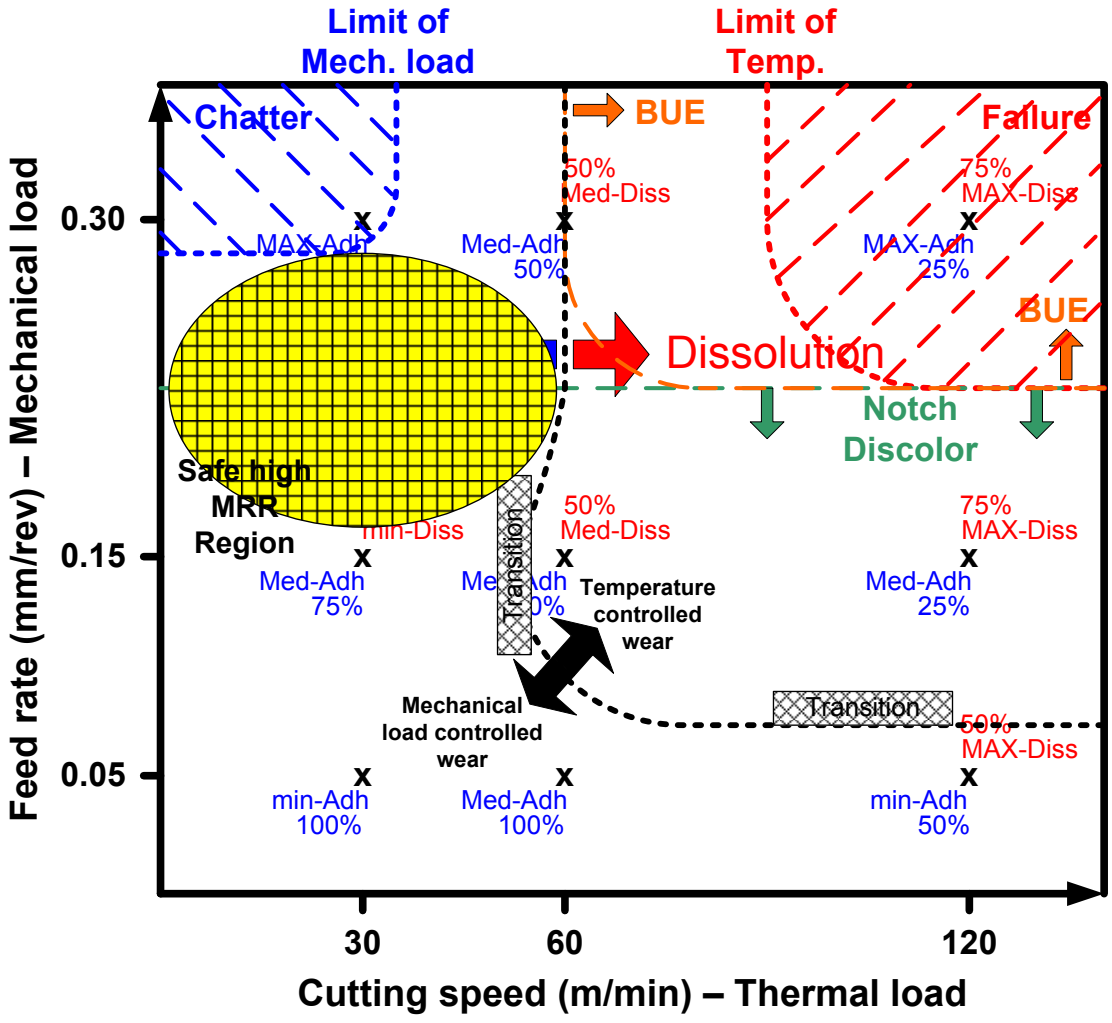

Figure 4-15: Final predictive map of dominant wear mechanisms for H13A carbide inserts dry turning Ti-6Al-4V. Besides the shape change of the field boundary, the additions in this chart include: (*i*) Region of notch discoloration on the tool (below a line in between the medium and high feed regions), (*ii*) Region of built-up-edge (BUE) formation (high speed and high feed conditions), and (*iii*) a safe region definition at medium to high feeds but low cutting speeds.

In general, for both inserts, the main line demarking the two dominant wear mechanisms essentially represented the line separating high temperature controlled wear from the region of high mechanical load controlled wear. For both inserts (H10A and H13A), the region where adhesive wear was a dominant mechanism was at lower cutting speeds. In contrast, dissolution wear became the more dominant mechanism with increasing cutting speeds, and especially along with higher feeds. There were some regions of transition where the dominant wear mechanism was transitioning from one type to another. Further, with the H13A (coarser grain) inserts, dissolution wear dominance was observed much earlier when going up in feed rate, at a common high speed. Also, effects of dissolution wear showed up at a lower feed rate as well.

Thus, when going up in grain sizes from a finer 0.51 μm grain to a coarser 0.61 μm grain, the dominance of dissolution wear increased relative to adhesive wear on uncoated carbide inserts dry-turning Ti-6Al-4V.

4.6 Weighted Multi-Mechanistic Comprehensive Wear Rate Model

4.6.1 Wear/Rate Models Suitable for Predicting VTW

A number of conflicting conclusions [6, 7, 10, 68, 91, 126] have been drawn over the years regarding the dominant wear mechanisms when machining titanium alloys. Abrasive and/or adhesive wear mechanisms have been stated as the dominant mechanism by some authors, while others point to diffusive and chemical wear mechanisms as the dominant mechanism of tool wear when machining titanium alloys.

What is known for sure is that the tool wear process in machining Ti-6Al-4V is primarily a high-temperature driven process [6, 10, 35]. Notably, Usui [86, 94] acknowledged the fact that mutual chip and tool diffusion was important in the development of crater wear of carbide tools at higher cutting speeds, but it was not clear whether diffusion rate was the controlling factor for the wear rate or sliding distance was still important.

From previous experience in machining titanium alloys (both milling and turning), dominant wear mechanisms were observed to change with process parameters, especially cutting speed. Further, there were preliminary indications of a combination of wear mechanisms becoming dominant over time. This was the one of the main motivations for coining a weighted multi-mechanistic wear model.

As mentioned earlier (Section 2.5.7), there are two types of tool wear models: (*i*) traditional models that relate flank or crater wear with cutting speed or time, and (*ii*) rate models that predict a wear rate, which is defined as the local volume loss rate on a tool face per unit area per unit time. These second type of models are capable of predicting a specific volume worn away from the tool. Relevant ones are selected:

4.6.1.1 Adhesive Wear Model for Predicting VTW

Adhesion is a local phenomenon which happens when mating surfaces under high temperature and pressure form strong bonds. When these bonds (or welds) are or become stronger than local material, particles from the weaker material tend to fragment and break away – this is adhesive wear. This can either be due welds forming bonds that are simply stronger than the parent material, or the strength and integrity of the parent

material being compromised due to the high forces and temperatures involved in the rubbing and mating process. If the fragments or particles that are formed as a result of adhesive wear are very small or sub-microscopic, then the deterioration mechanism is termed as attritious wear; if visible under microscope, then it is called galling [35].

Usui's Extension of Shaw's Adhesive Model for Predicting the Volume Worn [94]

Usui analyzed whether sliding distance was the dominant controlling factor for wear rate by starting with Shaw's [35] work on adhesive wear rearranged as:

$$\frac{dW}{dL} = A_r \left(\frac{c}{b} \right) Z \tag{4.5}$$

Where, dW is the wear volume for a sliding distance of dL, A_r is the real area of contact, c is the height of the postulated plate-like wear particle, b is the mean spacing of the asperity, and Z is the probability for producing a wear particle per asperity encounter (Holm's probability). The real area of contact can now be written in terms of the normal stress as:

$$A_r = \frac{\sigma_t}{H} \tag{4.6}$$

Where, H is the asperity hardness, and σ_t is the normal stress on the contact surface.

In the previous equation, c/b can be regarded as a constant due to the relatively small size effect, and the variation of the strain and the strain rate in the practical cutting range for carbide tools is neglected. Further, the hardness (temperature dependent), H is dependent on bulk properties of the softer pair of mating surfaces and is written as:

$$H = A_1 e^{\left(\frac{A_2}{T}\right)} \tag{4.7}$$

Where, A_1, A_2 are constants, and T is the temperature of the chip surface.

Holm's probability may be considered as the probability needed to yield a weld that is strong enough to produce a wear particle when an asperity encounter takes place, Weld formation being a thermally activated process, the Holm's probability is:

$$Z = B_1 e^{\left(\frac{-\Delta E}{kT}\right)} \tag{4.8}$$

Where, B_1 is a constant, K is the Boltzmann's constant, and ΔE is the activation energy.

When substituting this expression of the Holm's probability into Shaw's adhesive wear equation:

$$\frac{dW}{dL} = K\sigma_t e^{-\left(\frac{(\Delta E + kA_2)}{kT}\right)} \tag{4.9}$$

Where, K is a constant, and ($\Delta E+kA_2$) can be regarded as a constant α.

This is re-written as the Usui's model in the final form as:

$$\frac{dW}{dL} = K\sigma_t e^{-\left(\frac{\alpha}{T}\right)} \tag{4.10}$$

Though, many approximations were made in deriving this model for adhesive wear, it is simple and intuitive for practical use, since it predicts adhesive wear rate as a function of contact pressure, sliding velocity and temperature. Further, it contains not only the Boltzmann's canonical distribution (diffusion coefficient), but also includes mechanical effects represented by σ_t and dL. This is most commonly used form of the

adhesive wear rate model [94], and it was used as the adhesive wear constituent of the more comprehensive wear model that was developed later in this section.

4.6.1.2 Abrasive Wear Model for Predicting VTW

Abrasion is the process of a harder particle creating grooves on a softer body. In the case of machining, this can be hard particles (inclusions) from the workpiece or the chip rubbing against the tool and causing scores/scratches. In the case of a coated tool, the hard coating particles can break away and then in turn rub against the tool while being carried away with the chips. Such an instance is show in Figure 4-8(B). Depending on the cutting condition, both 2-body and 3-body abrasion can take place.

Kramer's Abrasive Wear Model for Predicting the Volume Worn [127]

Most metallic alloys contain hard, second-phase particles that strengthen the alloys by pinning dislocations. Additionally, impurity particles may be inadvertently included during production. These hard particles are forced against the tool surface during machining causing abrasive wear. It has been shown that hard inclusions can substantially reduce cutting tool life [128]. However normal quality controlled alloys do not contain substantial quantities of inclusions, as in the case of this batch of Ti-6Al-4V.

The material removal rate (of the tool) in abrasive wear dramatically decreases when the hardness of the metal approaches that of the abrasive. Larsen –Basse [129] has shown that there is a transition in the wear mechanism when the hardness of the abrasive decreases below 1.2 times the hardness of the surface being abraded. For abrasive

hardness above the critical value, material is removed (worn) by a machining mechanism and chips are cut from the surface. For soft abrasives, a fatigue-type mechanism produces sub-surface cracks and wear is due to delamination.

To predict abrasive wear rate, Rabinowicz's quantitative results are the starting point. The abrasive wear behavior may be separated into 3 regions, depending on the ratio of the hardness of the abrasive to that of the abraded surface (in this case, any workpiece inclusions onto the tool material). In each hardness regime, the wear volume (V_m) that is removed from the surface in sliding a distance x is:

$$V_m = \frac{xLTan\theta}{3P_t}, \text{for } P_t / P_a < 0.8 \tag{4.11}$$

$$V_m = \frac{xLTan\theta}{5.3P_t}\left(\frac{P_t}{P_a}\right)^{-2.5}, \text{for } 1.25 > P_t / P_a > 0.8 \tag{4.12}$$

$$V_m = \frac{xLTan\theta}{2.43P_t}\left(\frac{P_t}{P_a}\right)^{-6.0}, \text{for } P_t / P_a > 1.25 \tag{4.13}$$

Where, L is the applied normal force between the surfaces, $Tan\theta$ is the average tangent of the roughness angle of the abrasive grains (a measure of the particle shape or sharpness), Pt is the tool hardness, and Pa is the hardness of the inclusions. For this, a database containing the hardness as a function of temperature for tool materials and abrasive particles is needed, for *e.g.*, in machining AISI 4340 steel, cementite particles will account for most of the abrasive wear.

From the above formulation, the absolute abrasive wear rate can be calculated. The abrasive wear volume is dependent on the distance slid. It is reasonable to assume that the abrasive wear rate will be proportional to V. The abrasive wear rate is also proportional to $K\frac{P_a^{n-1}}{P_t^n}$, where Pa and Pt are at the cutting temperature of interest. The constant, n, depends on the relative tool to abrasive hardness.

- For $P_t/P_a < 0.8$, n = 1.0 and K = 0.333
- For $1.25 > P_t/P_a > 0.8$, n = 3.5 and K = 0.189
- For $P_t/P_a > 1.25$, n = 7.0 and K = 0.416

The absolute abrasive wear rate has been calculated as: $AVK\frac{P_a^{n-1}}{P_t^n}$, where, A is a calibration constant to be determined by best fit, and V is the cutting speed in ft/min.

Takeyama and Murata's Extension for Predicting the Volume Worn [95]

Building on the above formulated abrasive wear models, Takeyama and Murata coined a simple model [95] for predicting abrasive wear rate as a function of sliding velocity, normal stress and sliding distance as given by the following equation.

$$\dot{V}_{Abr} = k_1 \sigma_n^n VL \tag{4.14}$$

This is the form of the abrasive wear model that has been adopted for using in the comprehensive wear model in a later section.

4.6.1.3 Generalized Dissolution Wear Model for Predicting VTW

The three chemically driven mechanisms of diffusion, dissolution and chemical reaction have been grouped together into a "generalized dissolution" wear mechanism. This generalized wear mechanism consists of [130]:

1. Dissociation of tool material into W, C, and Co,
2. Chemical reaction of dissociated species with work material if possible,
3. Atomic transport across the tool-chip interface, and
4. Diffusion of the dissociated species that have not been consumed.

The reason for such a grouping is the interaction and dependency of all these processes with each other. In general, the two main factors which affect chemically driven wear, is the temperature and the chemical affinity of the tool and workpiece material constituents for each other.

Diffusion [130]:

Solid-state diffusion takes place from regions of high atomic concentration to regions of low atomic concentration. The diffusion rate increases exponentially with temperature and can occur in metal cutting due to the intimate contact at high temperatures in a very narrow reaction zone between the tool and the chip [131, 132]. An estimate for the diffusion happening in the tribosystem can be made by:

$$\dot{V}_{Diff} \quad - - \quad ^{\left(\frac{\Delta E}{kT}\right)} \tag{4.15}$$

Where, c is a constant, k is the Boltzman's constant, ΔE is the activation energy and T is the temperature. Diffusion wear becomes a possibility when interface temperatures of sliding are relatively high and velocities are low. Such a condition can be reached in machining titanium alloys even though lower speeds result in lower temperatures, since titanium has a really low thermal conductivity thus exponentially increasing temperatures with cutting speed.

Dissolution [127]:

The chemical solubility of the tool material in the workpiece increases exponentially with temperature, and hence at high cutting speeds it is a significant wear mechanism. For a given tool material of composition AxBy, its chemical solubility in a particular workpiece material may be determined as:

$$C_{A_xB_y} = e^{\left[-\frac{1}{x}\left(\frac{\Delta G_{A_xB_y} - x\Delta\bar{G}_A^{xs} - y\Delta\bar{G}_B^{xs} - yRT\ln\frac{y}{x}}{(x+y)RT}\right)\right]} \quad (4.16)$$

Where, C_{AxBy} is the chemical solubility of the coating material in the w/p (mole fraction), ΔG_{AxBy} is the free energy of formation of the coating material, AxBy, $\Delta\bar{G}_A^{xs}$ is the relative partial molar excess free energy of solution of component A of the tool material in the w/p, $\Delta\bar{G}_B^{xs}$ is the excess free energy of solution of component B, R is the universal gas constant, and T is the absolute temperature.

A database of thermochemical properties as a function of temperature has been assembled for select workpiece-tool combinations. Since this model attempts to calculate the absolute wear rate as a function of cutting speed, an estimate of the velocity dependence is necessary. From mass transport fundamentals of boundary layers, the dissolution wear rate can be calculated as:

$$V_{Diss} = BMCV^{0.5} \tag{4.17}$$

Where, B is the dissolution wear constant, to be determined by best fit to cutting data, M is the molar volume of the coating material in cm3/mole, C is the chemical solubility of the coating material in the workpiece at the cutting temperature, and V is the cutting speed in ft/min.

Chemical Reaction [130]:

The dissolution theory breaks down when machining highly reactive materials such as titanium, where a chemical reaction followed by diffusion is more plausible [133]. If a chemical reaction occurs, it can affect tool wear when the tool material reacts with the work material or other chemicals to form compounds that are carried away in the chip stream or in the new generated surface of the workpiece [96]. Chemical wear become s predominant as cutting speed increases when machining highly reactive materials such as titanium alloys.

In case of machining titanium alloy with uncoated carbide tools, a TiC layer from the carbon atoms (dissociated from tungsten carbide) and titanium in the work material

was found at the interface [133]. The diffusion rate of carbon through this reaction layer was much lower as compared to the case where a reaction layer is not present, thus reducing the wear rate. Consequently, many coated tools do not outperform uncoated carbide tool when machining titanium alloys.

Note that the above models include tool-workpiece combination dependent constants that are 'assumed' to hold across the typical design space. These models can therefore be used to predict a volumetric wear rate based on continually updated contact stresses and temperatures and hence find good use especially in finite element simulations of the cutting process. Thus, the development of the volumetric assessment of tool wear is an essential first step in this direction.

4.6.2 Comprehensive Tool Wear Equation of Microstructural Wear Mechanisms

In the WC-Co / Ti-6Al-4V turning tribosystem, the wear mechanisms that have been commonly observed [6, 7, 10, 68, 91, 126] are adhesive wear, abrasive wear, chemical dissolution wear and diffusive wear (in the order of increasing surface speeds). A fundamental one dimensional wear map [134] plotted against surface speed (Figure 4-16) forms the basis of relatively characterizing the onset of various wear mechanisms. Here, adhesive wear is prevalent at low speeds when weld between the tool and workpiece material at the interface is capable of being formed. When going up in cutting speed, the onset of abrasion occurs; this is the scoring of a harder material (or its

inclusions) on the softer material. With further increasing speeds, oxidation, thermal softening and diffusive mechanisms become more dominant.

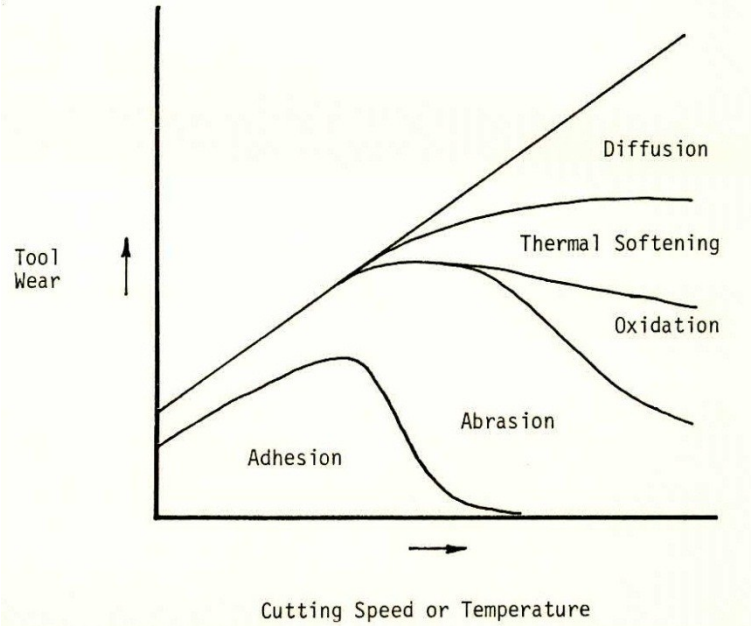

Figure 4-16: Relative relationships of tool-wear mechanisms with respect to cutting speeds or temperatures [134].

Note that micro-chipping/attrition wear is a form of the more basic adhesive wear mechanism, and that fatigue wear is not dominant due to the 'steady-state' nature (forces) of turning operations; hence, these mechanisms will not be included in this analysis. For constructing a comprehensive model, suitable volumetric wear equations for each mechanism was adopted from the previous section (Section 4.6.1). To account for the simultaneous occurrences of multiple wear mechanisms in the WC-Co tool during the machining of Ti-6Al-4V, a weighted multi-mechanistic wear model was assembled by combining these models and assigning weighting factors, as follows:

$$w = w_{adh} + w_{abr} + w_{diss} \tag{4.18}$$

Where, w is the weighted net wear rate, w_{adh}, w_{abr}, w_{diss} are the weighted adhesive, abrasive and generalized dissolution wear rates respectively. Note that the sum of these weighted wear rates is equal to unity.

Assembling the previously explained models into the general equation, we get:

$$\dot{V}_{Net} \quad \frac{dW_{Net}}{dt} = \left(K\sigma_n V e^{\left(-\frac{\alpha}{T}\right)} \right) w_{Adh} + \left(c_1 \sigma_n V L \right) w_{Abr} + \left(BMC_{WCxCoy} V^{0.5} + c_2 e^{\left(-\frac{\Delta E}{kT}\right)} \right) w_{Diss} \tag{4.19}$$

Where, $\dot{V}_{Net}$ is the composite wear rate, and W_{Net} is the total wear. Note that each of these models predicts a wear value which is in terms of the volume of material worn away. So, the wear values and rates that are an output of this equation is the volumetric tool wear (VTW) and VTW rate predictions, normalized in 1D, *i.e.*, over a unit area over unit time. It is also to be noted that some interaction between the wear mechanisms was observed as is expected. Thus, it would be important to examine these interaction effects as future work.

4.6.3 Model-Based Prediction of Volumetric Tool Wear

There are two inputs for this task: (*i*) The final DOE of primary factors from RQ1, and (*ii*) the comprehensive multi-mechanistic wear model and speed-based weighting factors from the previous sections.

The procedure for estimating model-based tool wear is detailed:

1. Each machining setup from the final DOE of runs was simulated in a commercial machining simulation software (AdvantEdge FEM), and peak steady-state values of cutting and feed forces, temperatures, sliding velocities and normal pressures were tabulated for each of the 9 combinations.
2. These were fed into the multi-mechanistic comprehensive tool wear model.
3. Tool-workpiece specific constants for each mechanism was identified.
4. Weighting factors for each of the 3 speed-regimes were substituted into this model and a resulting final wear rate was calculated.
5. This wear rate was multiplied with the cutting time specific to each feed-speed combination scenario to obtain the wear distance (depth) – these values will later be compared with actual tool wear for validation.

4.6.3.1 Simulation of the Final DOE of Machining Runs

The final DOE of feed-speed combinations was simulated in a commercial machining simulation software (ThirdWave Systems AdvantEdge FEM) to obtain the peak steady-state values of cutting forces, feed forces, temperatures, sliding velocities, and contact pressures. The sliding velocity is the relative velocity between the tool and the workpiece or the chip sliding across the tool face. The normal pressure is the stress (perpendicular to the face) experienced by the tool as a result of this sliding action. The DOE of machining setups and corresponding tabulated parameters follow:

Table 4-6: Simulation Results of Maximum Steady-State Cutting and Feed Forces, Temperatures, Contact Pressures and Sliding Velocities for the Final DOE of Machining Runs

Run (#)	f (mm/rev)	V (m/min)	Fx / $F_{cutting}$ (N)	Fy / F_{feed} (N)	Temperature (^{0}C)	Pressure (MPa)	Velocity (m/min)
1	0.05	30	400	350	710.9	125	19.7
2	0.05	60	350	300	961.5	112.5	32.8
3	0.05	120	400	350	1122	90.8	77.5
4	0.15	30	800	750	827.3	169.1	15.7
5	0.15	60	800	600	1008	162.7	34.8
6	0.15	120	800	600	976.5	170.9	43.22
7	0.3	30	1350	1150	801	254.3	17.6
8	0.3	60	1350	1000	1146	256	28.9
9	0.3	120	1300	950	1217	229.5	64.5

4.6.3.2 Estimation/Identification of Tool-Workpiece Specific Constants for the Model

The weighted multi-mechanistic comprehensive tool wear model assembled in the previous chapter is reproduced here for convenience:

$$\dot{V}_{Net} = \frac{dW_{let}}{dt} = \left(K\sigma_n V e^{\left(-\frac{\alpha}{T}\right)} \right) w_{Adh} + \left(c_1 \sigma_n V L \right) w_{Abr} + \left(BMC_{WCxCoy} V^{0.5} + c_2 e^{\left(-\frac{\Delta E}{kT}\right)} \right) w_{Diss} \quad (5.20)$$

Since the weighting factors for abrasive wear were zero, the abrasive wear model constants need not be determined. For adhesive wear, the constants used in the Usui model [94] are K and α. Values of these Usui model constants (K and α), for the case of carbides cutting Ti-6Al-4V have been estimated by researchers [135-137]. These are:

- K = 7.8e-09 Pa^{-1}
- α = 2500 Kelvin

Values of the normal stress (σ_n), sliding velocity (V), and temperature (T) for each of the 9 DOE setups of machining runs are obtained from Table 4-6. Using these values, the damage depth predicted by Usui's adhesive wear mechanism is given in Table 4-7.

Table 4-7: Maximum wear depth as predicted by Usui's adhesive wear model which is a function of sliding velocity, normal stress, and temperature. Note that the wear rate was multiplied by the cutting time to obtain the wear depth.

Usui wear rate	Usui wear rate in Microns	Cutting time for each cut	Maximum wear depth
mm/min	um/min	min	um
0.000432	0.432	3.3	1.44
0.001174	1.174	1.7	1.96
0.003888	3.888	0.8	3.24
0.001286	1.286	1.1	1.43
0.004055	4.055	0.6	2.25
0.006034	6.034	0.3	1.68
0.002831	2.831	0.6	1.57
0.007433	7.433	0.3	2.06
0.019459	19.459	0.1	2.70

For Kramer's chemical dissolution wear model, extensive data was only available for titanium carbide coated (TiC) turning AISI 4340 steel as shown in Table 4-8.

Table 4-8: Wear rates from machining tests using TiC coated tools turning AISI 4340 steel [127].

Cutting speed (ft/min)	Average temp. (K)	Estimated peak temp. (K)	Wear rate (μm/min)
200	804	1082	0.080
300	886	1208	0.116
400	916	1255	0.145
500	970	1338	0.442
600	1021	1418	0.869
700	1030	1432	1.271

From the above table, the estimated maximum temperatures were then plotted against the wear rate of these TiC coatings given in μm/min. Though cutting speed regime based classification is intended to be done, maximum temperatures were plotted in this case; the reasoning was that the same cutting speed would result in much higher average and peak temperatures in Ti-6al-4V due to its lower thermal conductivity. Therefore, starting with temperatures is the more correct approach; this was plotted against the material wear rate as shown in Figure 4-17.

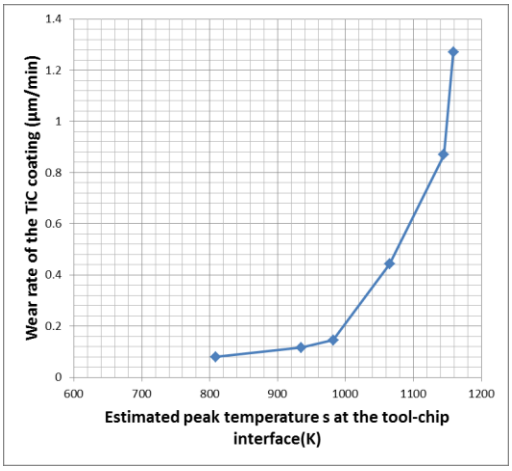

Figure 4-17: Estimated peak temperatures vs. Wear rate of TiC coatings when turning AISI 4340 steel. This plot was used for estimating the wear rates of TiC at different temperatures.

From this plot, the wear rates of TiC that correspond to the same temperatures generated in the 9 DOE runs tabulated in Table 4-6 for turning Ti-6Al-4V was picked out. The rates of WC tool wear at these 9 temperatures that are relative to the TiC coating wear rates were tabulated using the factor from Table 4-9.

Table 4-9: Rankings of predicted abrasive wear and chemical dissolution wear rates at 700^0 C relative to TiC [127].

Relative abrasive wear rate		Relative chemical wear rate	
SiC	0.004	Al_2O_3	0.0000
WC	0.008	TiO_2	0.0000
Si_3N_4	0.030	TiO	0.0000
Al_2O_3	0.075	HfN	0.0009
HfN	0.28	TiN	0.018
HfC	0.34	HfC	0.035
ZrC	0.79	$TiC_{0.75}O_{0.25}$	0.098
TiB_2	0.89	HfB_2	0.32
TiC	1.0	ZrC	0.36
TaC	1.0	TiC	1.0
$TiC_{0.75}O_{0.25}$	1.3	TaC	1.1
HfB_2	1.6	NbC	1.9
NbC	2.2	TiB_2	5.3
TiO_2	2.2	Si_3N_4	250
TiO	2.8	WC	5 200
Mo_2C	110	Mo_2C	12 000
TiN	170	SiC	24 000

This provided the wear rate of WC tool materials at each of the temperatures obtained in the 9 runs DOE of turning Ti-6Al-4V. These wear rates were them multiplied with the total cutting time corresponding to each machining setup to obtain the wear depth due to dissolution wear. These are tabulated in Table 4-10.

Table 4-10: Maximum wear depth considering the dissolution wear mechanism. Since constant for the tribosystem of interest was not readily available, wear rates were estimated from calculating a relative wear rate with respect o TiC coatings and then multiplied by the cutting time to obtain the wear depth.

Run	Temp. in turning Ti-6Al-4V	Wear rate of TiC at this temp.	Rate of WC wear w/r/t TiC	Machining time for each cut	Maximum wear depth
(#)	(^{0}C)	(μm/min)	(μm/min)	(min)	(μm)
1	710.9	0.08	4.16	3.3	13.9
2	961.5	0.125	6.5	1.7	10.8
3	1122	0.72	37.44	0.8	31.2
4	827.3	0.08	4.16	1.1	4.6
5	1008	0.22	11.44	0.6	6.4
6	976.5	0.145	7.54	0.3	2.1
7	801	0.08	4.16	0.6	2.3
8	1146	0.84	43.68	0.3	12.1
9	1217	2	104	0.1	14.4

Now, for the constants in the Arrhenius form equation of diffusive wear, a number of researchers have estimated the diffusion rates for carbide tools when machining Ti-6Al-4V. This is tabulated in Table 4-11.

Table 4-11: Diffusion coefficient of the three tool elements from the cutting tool side into the Ti-6Al-4V chip [138]. (R is 8.314/mol-K)

Elements	Frequency factor D_0 [m^2/s]	Activation energy Q_d [J/mol]	Diffusion coefficient D [m^2/s]
W	2.475×10^{-1}	313,800	$D_w = 2.475 \times 10^{-1} \exp[-313{,}800/(RT)]$
Co	9.0×10^{-3}	334,720	$D_{Co} = 9.0 \times 10^{-3} \exp[-334{,}720/(RT)]$
C	1.5×10^{-5}	133,888	$D_C = 1.5 \times 10^{-5} \exp[-133{,}888/(RT)]$

Using the diffusion coefficient equations from the above table, equations for W, C and Co were written using the earlier tabulated temperatures and the average of these were taken (instead of the sum) to obtain the diffusive wear rate and wear depth.

Table 4-12: Maximum wear depth considering the diffusive wear mechanism. Diffusion coefficient equations were written for each of the three tool elements, W, C and Co based on the temperatures obtained earlier. The average diffusion rate was multiplied with the cutting time to obtain the wear depth.

Diffusions Coefficients (mm^2/min)				Wear depth (μm)
W	Co	C	Average	
3.2635E-10	9.2005E-13	7.0276E-05	2.3426E-05	0.078
7.8563E-07	3.7221E-09	1.9480E-03	6.4961E-04	1.083
2.6469E-05	1.5854E-07	8.7365E-03	2.9210E-03	2.434
1.8877E-08	6.9749E-11	3.9692E-04	1.3231E-04	0.147
2.3831E-06	1.2158E-08	3.1277E-03	1.0434E-03	0.580
1.1340E-06	5.5054E-09	2.2783E-03	7.5980E-04	0.211
8.1500E-09	2.8474E-11	2.7737E-04	9.2461E-05	0.051
4.1826E-05	2.5828E-07	1.0620E-02	3.5540E-03	0.987
1.4853E-04	9.9808E-07	1.8237E-02	6.1288E-03	0.851

4.6.4 Wear Characteristic Equations for each Speed-Regime

The next step was to substitute the weighting factors determined in the previous chapter into the comprehensive wear characteristic equations for both the inserts, based on a cutting-speed classified regime as follows:

4.6.4.1 Comprehensive Model Equations for H10A inserts:

In the low speed regime (~ 30 m/min):

$$\dot{V}_{Net-Low} \quad \frac{dW_{Net-Low}}{dt} = \left(7.8*10^{-9}\sigma_n Ve^{(-\frac{2500}{273+T})}\right)*(1)+\left(c_1\sigma_n VL\right)(0)$$
$$+\left(BMC_{WCxCoy}V^{0.5}+c_2e^{\left(-\frac{\Delta E}{kT}\right)}\right)(0)=7.8*10^{-9}\sigma_n Ve^{(-\frac{2500}{273+T})} \quad (1.21)$$

In the medium speed regime (~ 60 m/min):

$$\dot{V}_{Net-Med} \quad \frac{dW_{Net-Med}}{dt} = \left(7.8*10^{-9}\sigma_n Ve^{(-\frac{2500}{273+T})}\right)*(0.5)+$$
$$\left(c_1\sigma_n VL\right)(0)+\left(BMC_{WCxCoy}V^{0.5}+c_2e^{\left(-\frac{\Delta E}{kT}\right)}\right)(0.5)= \quad (1.22)$$
$$\left(7.8*10^{-9}\sigma_n Ve^{(-\frac{2500}{273+T})}\right)*0.5+\left(DOE\ Setup\ Specific\ Rate\right)*0.5$$

In the high speed regime (~ 120 m/min):

$$\dot{V}_{Net-High} \quad \frac{dW_{Net-High}}{dt} = \left(7.8*10^{-9}\sigma_n Ve^{(-\frac{2500}{273+T})}\right)*(0.5)+\left(c_1\sigma_n VL\right)(0)$$
$$+\left(BMC_{WCxCoy}V^{0.5}+c_2e^{\left(-\frac{\Delta E}{kT}\right)}\right)(0.5)=\left(7.8*10^{-9}\sigma_n Ve^{(-\frac{2500}{273+T})}\right)*0.5+ \quad (1.23)$$
$$\left(DOE\ Setup\ Specific\ Rate\right)*0.5$$

4.6.4.2 Comprehensive Model Equations for H13A inserts:

In the low speed regime (~ 30 m/min):

$$\dot{V}_{Net-Low} \quad \frac{dW_{Net-Low}}{dt} = \left(7.8*10^{-9}\sigma_n Ve^{\left(-\frac{2500}{273+T}\right)}\right)*(1)+\left(c_1\sigma_n VL\right)(0)+$$
$$\left(BMC_{WCxCoy}V^{0.5}+c_2e^{\left(-\frac{\Delta E}{kT}\right)}\right)(0)=7.8*10^{-9}\sigma_n Ve^{\left(-\frac{2500}{273+T}\right)} \tag{1.24}$$

In the medium speed regime (~ 60 m/min):

$$\dot{V}_{Net-Med} \quad \frac{dW_{Net-Med}}{dt} = \left(7.8*10^{-9}\sigma_n Ve^{\left(-\frac{2500}{273+T}\right)}\right)*(0.5)+\left(c_1\sigma_n VL\right)(0)$$
$$+\left(BMC_{WCxCoy}V^{0.5}+c_2e^{\left(-\frac{\Delta E}{kT}\right)}\right)(0.5)=\left(7.8*10^{-9}\sigma_n Ve^{\left(-\frac{2500}{273+T}\right)}\right)*0.5+ \tag{1.25}$$
$$\left(DOE\ Setup\ Specific\ Rate\right)*0.5$$

In the high speed regime (~ 120 m/min):

$$\dot{V}_{Net-High} \quad \frac{dW_{Net-High}}{dt} = \left(7.8*10^{-9}\sigma_n Ve^{\left(-\frac{2500}{273+T}\right)}\right)*(0.25)+\left(c_1\sigma_n VL\right)(0)$$
$$+\left(BMC_{WCxCoy}V^{0.5}+c_2e^{\left(-\frac{\Delta E}{kT}\right)}\right)(0.75)=\left(7.8*10^{-9}\sigma_n Ve^{\left(-\frac{2500}{273+T}\right)}\right)*0.25+ \tag{1.26}$$
$$\left(DOE\ Setup\ Specific\ Rate\right)*0.75$$

4.7 Model-Based Estimation of Maximum Damage Depth

Based on the above assembled wear characteristic equations, the maximum wear model-based wear depth can be estimated by adding using the weighting factors. Note that the table given below if for H10A inserts.

Table 4-13: Maximum model-based wear depths predicted by the comprehensive model of three wear mechanisms for H10A grade inserts (finer grain).

Maximum Model-Based Wear Depth Predictions for H10A Inserts						
Run	Feed Rate	Cutting Speed	Adhesive Wear Depth	Dissolution Wear Depth	Diffusion Wear Depth	Weighted Wear Depth
(#)	(mm/rev)	(m/min)	(μm)	(μm)	(μm)	(μm)
1	0.05	30	1.44	13.87	0.08	**1.44**
2	0.05	60	1.96	10.83	1.08	**6.94**
3	0.05	120	3.24	31.20	2.43	**18.44**
4	0.15	30	1.43	4.62	0.15	**1.43**
5	0.15	60	2.25	6.36	0.58	**4.59**
6	0.15	120	1.68	2.09	0.21	**1.99**
7	0.3	30	1.57	2.31	0.05	**1.57**
8	0.3	60	2.06	12.13	0.99	**7.59**
9	0.3	120	2.70	14.44	0.85	**9.00**

A similar table can be put together for the H13 inserts with slightly different weighting factors as given below:

Table 4-14: Maximum model-based wear depths predicted by the comprehensive model of three wear mechanisms for H13A grade inserts (coarser grain).

Maximum Model-Based Wear Depth Predictions for H13A Inserts						
Run	Feed Rate	Cutting Speed	Adhesive Wear Depth	Dissolution Wear Depth	Diffusion Wear Depth	Weighted Wear Depth
(#)	(mm/rev)	(m/min)	(μm)	(μm)	(μm)	(μm)
1	0.05	30	1.44	13.87	0.08	**1.44**
2	0.05	60	1.96	10.83	1.08	**6.94**
3	0.05	120	3.24	31.20	2.43	**10.84**
4	0.15	30	1.43	4.62	0.15	**1.43**
5	0.15	60	2.25	6.36	0.58	**4.59**
6	0.15	120	1.68	2.09	0.21	**1.83**
7	0.3	30	1.57	2.31	0.05	**1.57**
8	0.3	60	2.06	12.13	0.99	**7.59**
9	0.3	120	2.70	14.44	0.85	**5.85**

These wear rates and maximum wear depth values will be compared with the actual tool wear for validation purposes.

4.8 Discussion of Results

The main conclusions from this chapter and a discussion of the results follow:

- To handle the inherent complexity and multi-scale nature of the WC-Co / Ti-6Al-4V machining tribosystem, two things were done: (*i*) an envelope around the tool chip interface region was cut out, and (*ii*) a number of constraints were imposed by holding constant certain factors. This rendered the problem manageable, while still capturing the behaviors of interest at both scales.
- Considering macroscopic factors, feed and speed were identified as significant variables, while keeping the cutting depth constant at 2mm. On considering the

large number of micro-scale factors affecting this tribosystem, the starting point was set to the most dominant one – grain size.

- The final DOE of 54 machining experiments was set up for 3 feed rates, 3 surface speeds, and 2 sub-micron grain sizes.
- SEM micrographs and EDS elemental analysis of the worn areas were simultaneously examined to determine weighting factors for each of the dominant wear mechanisms on the selected two WC-Co tool grades.
- In general, varying amounts of titanium were found adhered to the edges of the crater region at all speed levels. These were more prominent at lower speeds, and decreased as the speeds went up. At the high speeds, in addition of the adhered titanium, wear troughs were gouged out due to the WC grains, W, C, and Co binder leaving with the chips. The smooth surface in the trough is a result of the high temperature generalized dissolution wear. This was evident from EDS where the smooth region of the crater trough is predominantly composed of tungsten and cobalt only.
- The chips carry away carbon, as evident from the carbon discoloration on the notch region.
- There was carbon build-up on the tool edge in some cases. This suggests that carbon is being "chemically-pulled" out of the tool, *i.e.*, due to a chemical-potential. Further, this build-up cannot be deposited from the chip (as in the case of the notch region), since it is in the opposite direction of chip flow. The

distribution of the carbon build-up is in conformance with the chip-sticking and chip-sliding regions of chip flow that is common to turning operations.

- Additionally, carbon discoloration was observed at the notch region on the rake face at low and medium speeds. Further, the smooth regions of the wear trough had a very sparse composition of carbon.
- Finally, no indication of abrasive wear was observed (scratches in the chip flow direction). One of the reasons is that this is an uncoated tool, and there is no chance of the harder coating particles disintegrating and scribing the tool surface. Other reasons could be that the workpiece material contains very few "hard" impurities, besides the carbide tool being of sub-micron grade.
- Another observation at high speeds was the appearance of the adhered titanium being smeared (or being smoothened out). This means that the adhered titanium was now being worn away by the action of generalized dissolution. This conclusion is supported by the fact that the dissolution has happened first at the maximum crater depth (as evident from adhered titanium being formed on these smoothened craters) which is also the region of maximum temperature. Only after that are the two edges of the crater trough starting to wear away.
- At the high feed rate, no carbon discoloration was observed, while built-up-edges (BUE) were formed on the tool edges.
- The H13A tool's wear progression was similar to the H10 A grade, the main difference being that dissolution wear was more dominant at higher speeds.

- Weighting factors for H10A grade inserts were: (*i*) In the low-speed regime, adhesion = 100%, (*ii*) In the medium-speed regime, adhesion = 50% and dissolution = 50%, and (*iii*) In the high-speed regime, adhesion = 50% and dissolution = 50%.
- Weighting factors for H13A grade inserts were: (*i*) In the low-speed regime, adhesion = 100%, (*ii*) In the medium-speed regime, adhesion = 50% and dissolution = 50%, and (*iii*) In the high-speed regime, adhesion = 25% and dissolution = 75%.
- Mapping the dominant wear mechanisms showed a general dominance of the adhesive wear mechanism at low speeds and feeds, while the dissolution wear mechanism was more dominant at high speed and feed conditions.
- At the low-speed high-feed corner of the design space, chatter was experienced consistently. This resulted in identifying the region as a failure zone. This essentially represents the limit of mechanical load that the tool material can carry (feed has a direct relation with forces).
- At the high-feed high-speed corner of the design space, catastrophic tool failures were experienced consistently. This classified it as a failure zone as well as it essentially represents the limit of thermal load that the tool material can carry (speed has a direct relation with temperature).
- Thus, from the wear maps, it was seen that the main line demarking the two dominant wear mechanisms essentially represented the line separating high

temperature controlled wear from the region of high mechanical load controlled wear.

- There were some regions of transition where the dominant wear mechanism was transitioning from one type to another. Further, with the H13A (coarser grain) inserts, dissolution wear dominance was observed much earlier when going up in feed rate, at a common high speed. Also, effects of dissolution wear showed up at a lower feed rate as well.
- When going up in grain sizes from a finer 0.51 μm grain to a coarser 0.61 μm grain, the dominance of dissolution wear increased relative to adhesive wear on uncoated carbide inserts dry-turning Ti-6Al-4V.
- Suitable volumetric wear rate models were selected for each of the constituent wear mechanisms of the comprehensive wear model.
- Using these weighting factors, a comprehensive multi-mechanistic wear model was assembled containing adhesive, abrasive, and dissolution wear rates that were normalized in volume, *i.e.*, over a unit area over unit time.
- For the tool-workpiece combination of study, certain constant for the comprehensive wear model had to be estimated since information was relevant not readily available. This was the case with the dissolution wear mechanism where, wear rates of the WC tool had to be estimated from the wear rates of TiC coatings turning AISI 4340 steel. The constant for the adhesive wear mechanism was available in literature, and the diffusion wear rates were calculated directly.

- Each of the three wear mechanisms included in the comprehensive wear model generated wear depths for the time the tool was in the cut. In general, diffusive wear rates and depths were the least, followed by adhesive wear rates and resulting wear depths. The dissolution wear rates and depths were the maximum among the three.
- Wear characteristic equations for both H10A (finer-grain) and H13A (coarser-grain) inserts were assembled for the low, medium, and high-speed regimes using the earlier computed weighting factors. Using these 6 wear equations, total maximum weighted wear depths were computed.

4.9 SUMMARY & TAKEAWAYS

This chapter served to answer RQ1. The objective of this chapter was to combine and weight the different microstructural wear mechanism models to predict volumetric wear. For realistically modeling this tribosystem, dominant wear mechanisms were quantified as weighting factors through SEM/EDS analyses for each of the three speed regimes. These were then employed in a comprehensive model of microstructural wear mechanisms (adhesive and dissolution) to obtain the maximum predicted wear depth.

Besides constructing predictive maps of dominant wear mechanisms, this chapter served to compute the model-based predicted wear values, which will be compared with the actual wear of cutting inserts obtained through machining experiments.

CHAPTER FIVE

5. QUANTIFICATION & VALIDATION OF VOLUMETRIC TOOL WEAR EVOLUTION (RQ2)

This chapter serves to answer Research Question 2 (RQ2), *i.e.*, "How can worn surfaces on complex tool geometries be accurately quantified in three dimensions to measure wear volumes?" The objective of RQ2 is to accurately quantify the bulk-3D wear volume by a new topological characterization method for surface measurement, and validate the model through physical cutting experiments.

Three tasks were charted out for answering RQ2, *i.e.*, Task 2-A, to develop a methodology for quantifying the bulk-3D wear and wear profile evolution, Task 2-B, to validate the model-predicted wear against the worn tool volumes obtained from corresponding cutting experiments, and Task 2-C, to construct predictive maps of bulk-3D wear profile evolution patterns in the design space of tool and process variables.

The major outputs from these three tasks were: (*i*) a validated methodology for characterizing the wear topology, (*ii*) validation of predicted wear for each speed-regime, and (*iii*) predictive maps of bulk-3D wear profile evolution patterns in the design space of tool and process variables.

5.1 QUANTIFICATION OF VOLUMETRIC TOOL WEAR

A qualitative assessment of the inadequacies of the current manner of tool wear measurement was conducted [18]; this highlighted the critical need to develop a more

comprehensive approach for machining tool wear characterization. It was evident that traditional parameters used for tool wear representation such as flank and crater wear were no longer self-sufficient to satisfactorily represent the advanced wear status of more recent cutting tools with complex geometric profiles. These complexities in tool geometries are all the more pronounced when catered to difficult-to-machine materials such as titanium and its alloys. Hence, alternatives to traditional tool wear assessment parameters were explored and a suitable one was selected, that will help understand the very nature of the evolving wear profile from a three dimensional standpoint. This assessment methodology, termed as Volumetric Tool Wear (VTW), was further developed and standardized, and suggestions for future use and deployment were provided. Further, the measurement system was evaluated using an Analysis of Variance (ANOVA) gauge repeatability and reproducibility (R&R) study.

5.1.1 Alternatives to Traditional Wear & Failure Assessment of Cutting Tool Inserts

Keeping in mind the ultimate goal of a dimensionally accurate final part, a number of alternate tool wear assessments have been suggested [22, 139] that may collectively be referred to as "dimension tool life criteria." They include the dimension wear rate (rate of cutting tip shortening perpendicular to machined surface), the relative surface wear (wear per unit area of machined surface), the specific dimension tool life (area of machined surface per μm wear), and volumetric wear. In contrast, on quantifying wear volumetrically, almost any level of tool profile complexity can be represented accurately

by using a suitable approach. In addition to providing the actual tool material volume worn away, the evolving 3D shape of the wear volume can be characterized by geometrical variables and can be related to process parameters and eventually to the wear mechanics itself. Thus, volumetrically quantifying wear has the advantage of not being tool-workpiece-process combination restricted, and can be used for almost any complex tool profile or wear behavior. Additionally, volumetric wear can be related to mass tool wear based on tool substrate density equivalents.

For modeling tool wear volumetrically, as a first step, one needs to closely track the actual 3D evolution of tool deterioration as a function of process parameters. Additionally, if one could 'watch' the evolution of the 3D wear profile mapped onto the ISO coding system [17], it will help identify the interactions of the different stages and classes of flank wear, crater wear, chipping, cracking, flaking, etc. This is critical to a holistic understanding of the wear process. Currently, tool wear is best tracked by a set of successive photomicrographs of either the flank or rake face, at periodic instances during the cutting process, which provide no information on how one wear profile led to another or on any key interactions between the deterioration phenomena that led to the progressed wear profile. An understanding of such progression/interactions will provide insights into the behavior and response of tool condition monitoring (TCM) parameters used for indirectly measuring tool wear, such as forces, vibrations (accelerations), frequency/acoustic parameters, etc. This was noted as a need in the recent ASME state-of-the-art paper on TCM [140].

5.1.2 Prior Efforts Related to Volumetric Wear

There are two general approaches for volumetrically quantifying tool wear. First, a partially analytical approach where the volume lost is predicted using equations of two/three body contact-wear mechanics and material failure mechanisms. Second, an empirical approach where the tool volume lost is optically assessed and related to process parameters.

In the first approach by a number of researchers, the wear rate of the flank and crater lands are predicted from tool geometry, cutting conditions, and tool/workpiece material properties by using abrasive, adhesive and diffusive wear models, whose elementary effects are added together to obtain a total wear volume [141-144]. A number of wear related constants are determined for each tool-workpiece combination and worn volumes are idealized and then approximated by geometrical equations.

In the second approach by other researchers, the worn profile is evaluated by optical techniques and then related to experimental parameters. Some of the relevant technical efforts follow:

(i) Crater depth measurements were made using white light interferometery (WLI), followed by evaluation with cutting forces in the dry turning of steel with uncoated inserts [145],

(ii) Tool wear land areas (flank/nose) were measured by electron beam induced deposition (EBID) and multiplied with the cutting width to compare the

estimated wear to cutting forces in the precision turning of aluminum and steel with diamond tools [146],

(iii) Crater depth was measured by a method of fringe projection with phase shifting that was captured by a CCD camera as a 256-graylevel image, which was then processed to obtain a 3D map of the crater after filtering and removing background noise (*i.e.*, by converting a phase value to a physical dimension) [147],

(iv) Crater roughness profile was estimated using a stylus-based profilometer in the dry turning of steel with uncoated and coated carbide inserts - Here, a standardized area within the scanned crater was projected onto a least squares fitted reference plane that was multiplied with the crater height to get the volume [148],

(v) Flank and crater topography was obtained by WLI - After aligning the data with six transformations variables, the volume difference between the new and worn surfaces is calculated by numerical integration of the residuals from the worn set or by multiplying the worn triangular area extruded through the contact length with the contact length in the turning of steel with uncoated and coated CBN inserts [21, 149, 150],

(vi) The volume or mass (m_w) of the tool material lost is approximated by comparing the idealized topographies of the worn cutting wedge with that of a new tool [22].

Additionally, a number of authors have approximated an idealized volume using linear measurements and known tool geometry [22, 35, 141-143, 150-153].

5.1.3 Surface Characterization for Quantifying 3D Wear

5.1.3.1 Methodology

The methodology for volumetrically quantifying tool deterioration needs to be able to accommodate complexities in tool geometry as well as progressed tool wear conditions. A number of approaches have been developed for obtaining a final wear volume. One such approach particularly suitable for milling inserts having sharp profile features is outlined below. This is an improvement to an earlier methodology of VTW involving surface matching of new and worn tool profiles [20].

The volumetric wear assessment methodology essentially involves capturing point cloud data of the cutting region of the tool insert by a 3D optical surface profiler. This 3D scan data is imported into a reverse engineering software which performs mesh buildup to generate parametric CAD solid models that accurately depict the surface characteristics of the new/worn tool inserts. Damage area and volume of the worn tool is obtained directly and accurately from the CAD software by measuring the volume of a 3D region of interest cordoned off by reference bounding planes created on the worn/unworn tool solid models. An appropriate tool insert holding fixture was designed for consistent and repeatable positioning of the inserts in the magnified field of

view. ISO recommended guidelines for wear measurement (of *VB*, for comparison) and BUE/BUL (built-up-layer) related procedures were followed as well.

The general procedure for a typical VTW measurement is outlined next. Figure 5-1(A) shows a coated tough grade milling insert (ISCAR APCR 100304PDFR-P IC928) recommended for machining titanium alloys. It has a relatively complex geometry that is characterized by positive, helical, sharp cutting edges and a high rake angle (Figure 5-1(B)). This complex geometry is difficult to accurately quantify volumetrically.

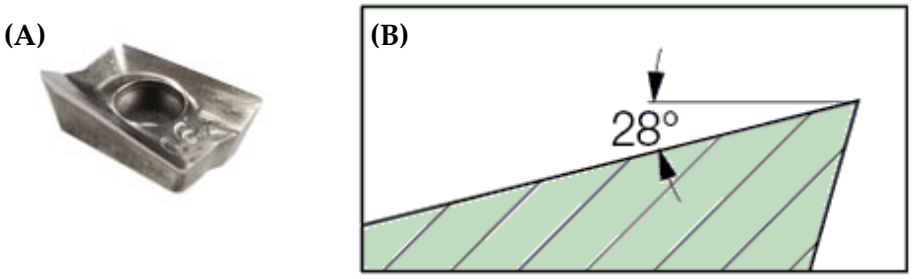

Figure 5-1: A typical titanium milling insert

Figure 5-2(A) and Figure 5-2(B) show the intensity map and point cloud 3D model of the above unworn tool insert obtained using the ZYGO NewView 7200 3D Optical Surface Profiler. The effective magnification was 2.5X, with a field of view of 2.83 mm x 2.12 mm, at a High 2G resolution of 4.42 μm. Figure 5-2(C) shows this point cloud data in ".xyz" format as imported into reverse engineering software (Rapidform XOR/Redesign) using ASCII conversion. Figure 5-2(D) shows the original point cloud data that has been converted into a surface model through auto surfacing using a number of adaptive surface elements.

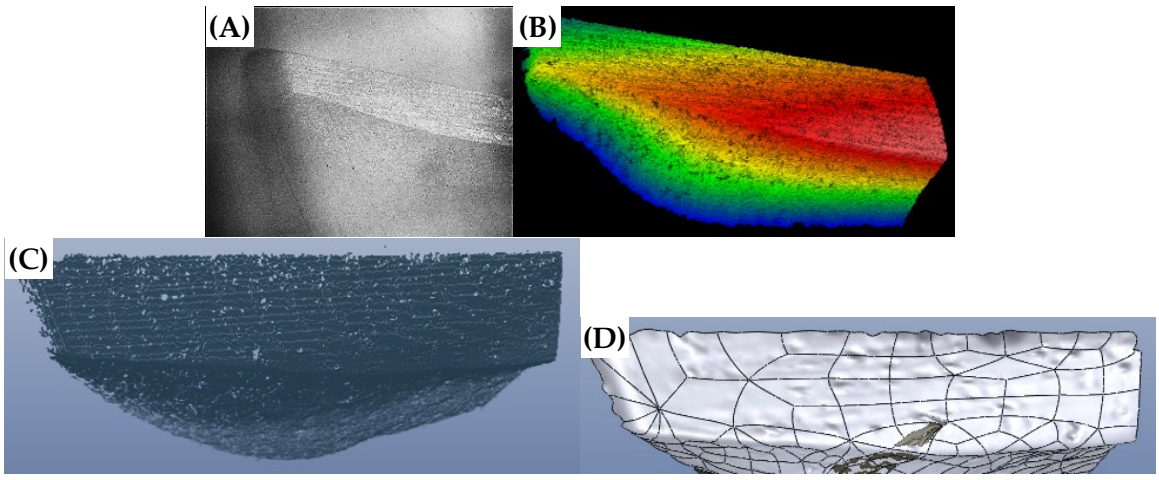

Figure 5-2: Point cloud processing for VTW: (A) Intensity map, (B) Point cloud 3D model, (C) Point cloud in rectangular coordinates, (D) Surface model.

Figure 5-3 shows the reference entities chosen for this particular insert type which are (1) the unworn portion of the "cutting edge line," and (2) a triple-point termed as a "nose point" where the flat flank portion meets the curved nose region and the tool body (distinct to this insert type). Both these reference entities will remain unaltered and maintain integrity through normal operational limits. Note that, reference entities can be any geometric feature, either existing or parametrically constructed off existing elemental features, that are outside the general wear area and which can be identified and reliably reproduced for the same insert type. This flexibility of being able to define specific sub-regions of interest, provides the investigator the freedom to easily vary the sub-regions of wear study as well as not having to map out the whole insert body (for *e.g.*, tool failure criterion for aerospace applications is typically about 0.25 mm VB_{max}; hence, only a suitable sub-region needs to be mapped). Additionally, this versatility

enables accurate and concentrated analysis of almost any insert type/profile; just that the reference entities just need to be kept consistent across a measurement set.

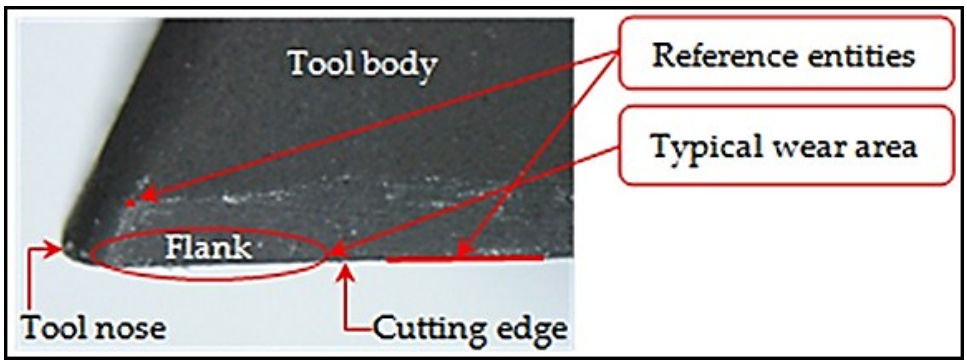

Figure 5-3: Reference entities for this insert type

Figure 5-4 shows the surface model imported into a standard CAD software (CATIA V5) onto which 4 bounding planes were defined, that were constructed off the 2 reference entities.

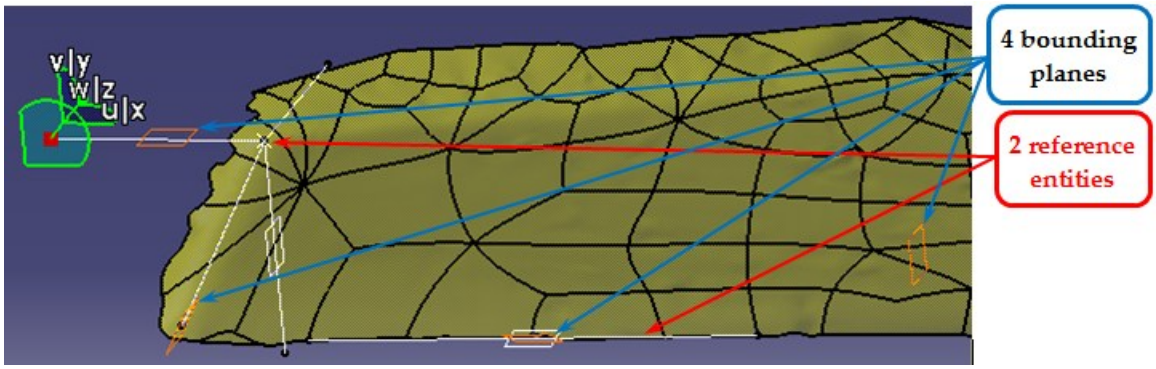

Figure 5-4: Four bounding planes created off the earlier defined reference entities

Following this, the surface boundary is extruded and split by one of the bounding planes (the 28° plane, as per tool manufacturer info), after which it is closed to convert it into a solid model as shown in Figure 5-5(A). The solid model is further split using the

remaining three bounding planes to obtain the final volume, computed directly by the software ('measure inertia' function in CATIA) as shown in Figure 5-5(B), onto which the initial surface is superimposed for perspective. In this case, the final volume was directly obtained as 0.19 mm^3 (unworn base volume). Note that, depending on the CAD software, a length (1D) calibration might need to be done initially as well.

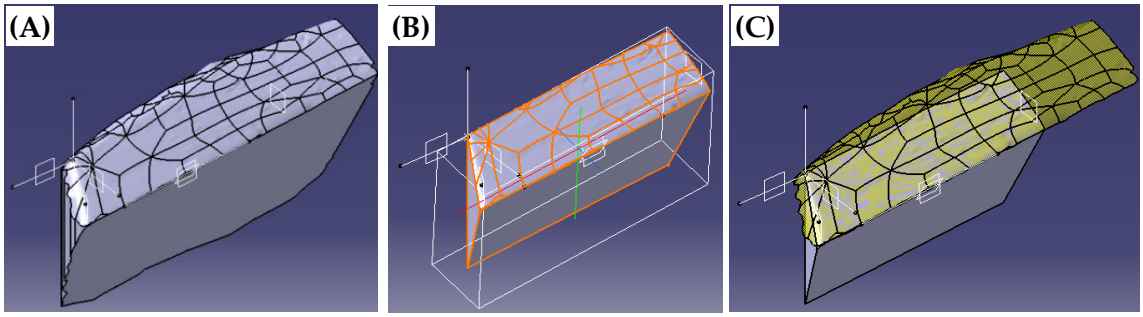

Figure 5-5: Solid model manipulation to obtain volume: (A) Solid model after split by 28^0 plane, (B) Split by remaining 3 planes (surface model superimposed) (C) Surface and solid models superimposed

A similar procedure can be employed for measuring the volume of a worn insert as well by subtracting it from unworn base volume. Also, even an extreme wear status case such as a catastrophically failed insert (by chipping) can be volumetrically quantified as shown in Figure 5-6. Thus, the VTW method has the capability to provide the absolute volumetric tool wear (in mm^3) of the flank, crater, nose, notch or other wear regions, both individually and collectively (within limits).

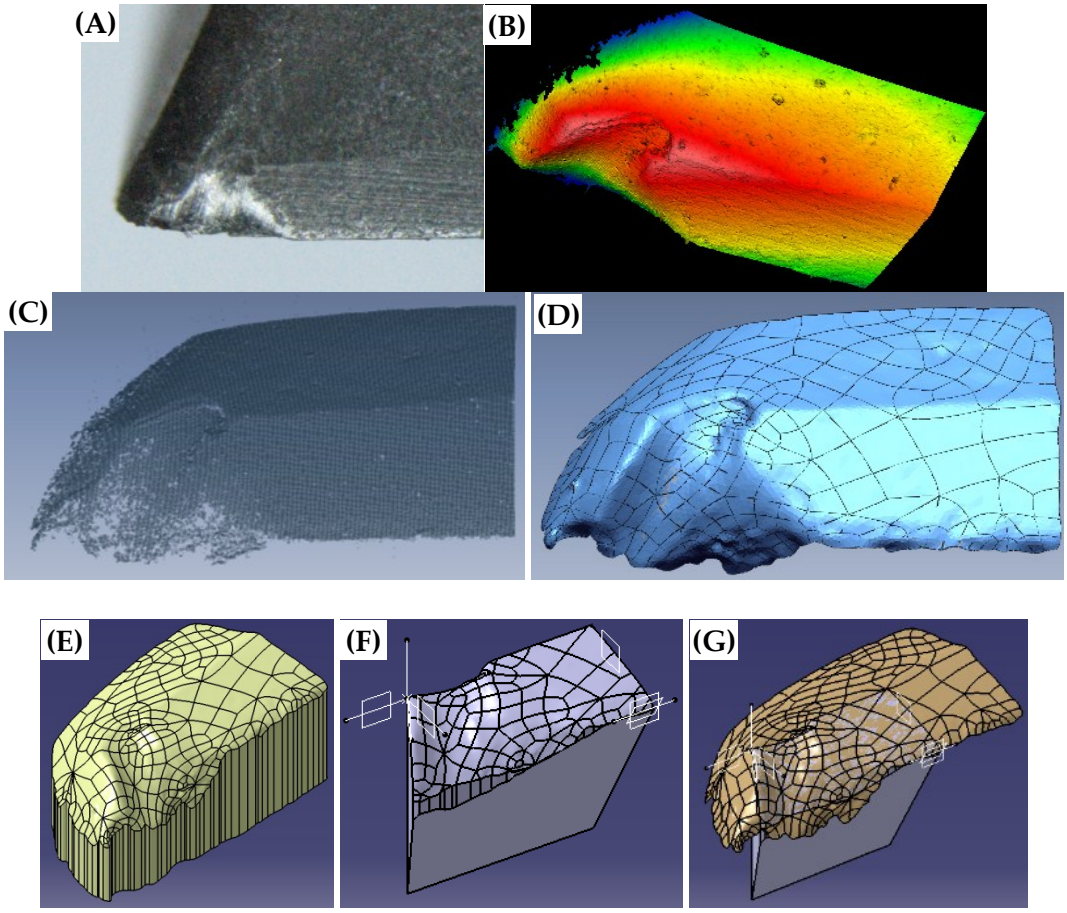

Figure 5-6: VTW for a failed insert: (A) Insert image, (B) Point cloud 3D model, (C) Point cloud in rectangular coordinates, (D) Final surface/solid models overlaid, (E) Boundary extruded surface model, (F) Final volume, (G) Surface/solid models overlaid.

A similar methodology can be employed for accurately capturing the volumetric tool wear of turning inserts. In this case, since rake faces were being characterized (in contrast to flank faces for milling inserts), stitching in the XY-plane was needed to capture the full length of the tool edge as shown in Figure 5-7. The resulting stitched surface model and sectioned solid model are show in Figure 5-8(a) and (B).

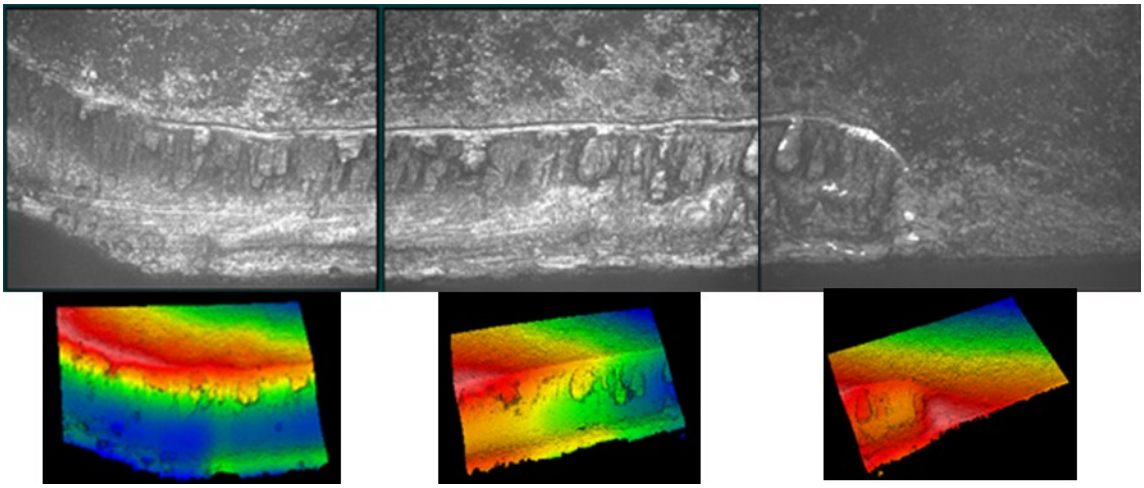

Figure 5-7: VTW methodology for Sandvik CNGP style turning insert. Stitching in the XY-plane was needed for capturing the wear along the length of the tool edge.

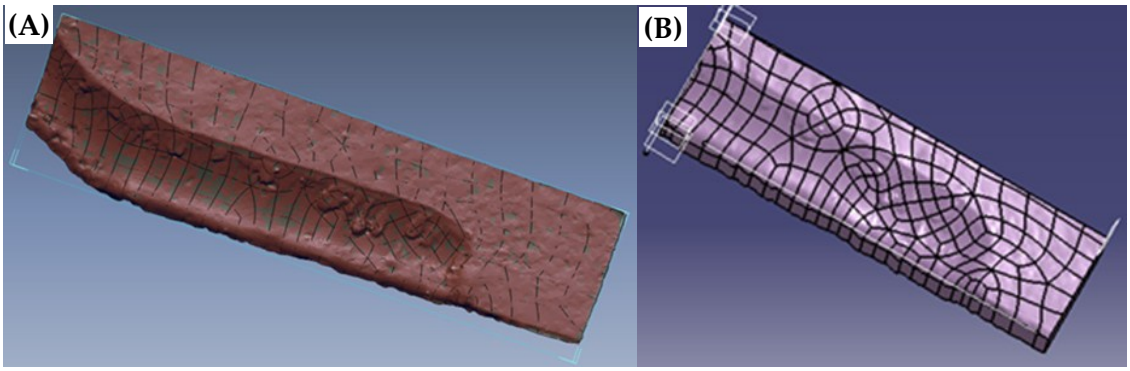

Figure 5-8: (A) Surface model of the worn volume and, (B) Solid model of VTW

5.1.3.2 The Necessity & Advantages over Prior VTW Quantification Efforts

This section lists the critical differences of the above formulated VTW methodology from the volumetric wear related efforts of other authors that were outlined earlier, thus showcasing its need and significant advantages:

1. All of the other authors' works are catered to single-point continuous turning of aluminum/steels under practical cutting conditions (defined as low feed rate,

small depth of cut, and gentle cutting speed). The situation is very different when machining titanium alloys having a unique material property combination and different wear mechanisms/outcomes. Also, unlike finish turning, the highly intermittent nature of rough/finish milling operations (especially when pushing productivity limits) essentially engages 'completely different tool edges' at each tooth engagement of a single/multi-tooth mill. Additionally, the authors' models are not valid for the modeling of interrupted cutting scenarios [21, 145-148].

2. Almost 'linear' wear growth conditions were assumed/ predicted by most authors. This is not true especially when machining titanium alloys which have been shown to exhibit 'non-linear' wear rates [21, 149, 150, 154].
3. As suggested by other authors as well as some of the listed authors, calibrating a new set of empirical wear constants for this tool-material combination cannot be always assumed to work, especially for titanium alloys due to their unique properties and differences in wear mechanics, let alone assuming the valid additive property of the elemental wear mechanisms, without considering any interactions and interaction effects.
4. More importantly, in all cases, tool geometries and wear profiles have either been approximated or idealized with equations for obtaining an approximate volume, and that too for inserts with very simple geometric profiles. With the current state of tool profile design and optimization, this is hardly the case, especially in the case of geometrically complex tools recommended for titanium machining

having very sharp edges and high rake/relief angles. An accurate measurement of the volume worn is the fundamental requirement for any kind of volumetric wear measurement and characterization. The above outlined VTW methodology is capable of providing accurate wear volumes of complex milling inserts.

5. Authors who approximated worn volumes numerically, used an aligning/matching procedure to compare new and worn profiles, by visual comparison or by least squares surface fit methods. These algorithms have inherent difficulties and repeatability and reproducibility (R&R) errors associated with them. The matching process has been eliminated in the above outlined methodology.
6. Another factor that the authors have not addressed is the issue of built-up edge (BUE) or built-up layer (BUL) residues remaining on tool wear lands. Not treating (cleaning) it according to ISO recommendations, will result in adhered work material being accounted in the wear volume calculations as well.

The above formulated VTW methodology is able to capture all optically needed info accurately, and therefore is a more accurate quantification of worn tool volumes.

5.1.3.3 Assessment Methodology Standardization

For the eventual objective of obtaining a wear volume as well as characterizing the evolving wear profile, numerous approaches can be employed depending on the cutting edge profile and wear status. A snapshot of the main procedure as well as some of the alternate paths and options involved is depicted by the flowchart shown in Figure 5-9.

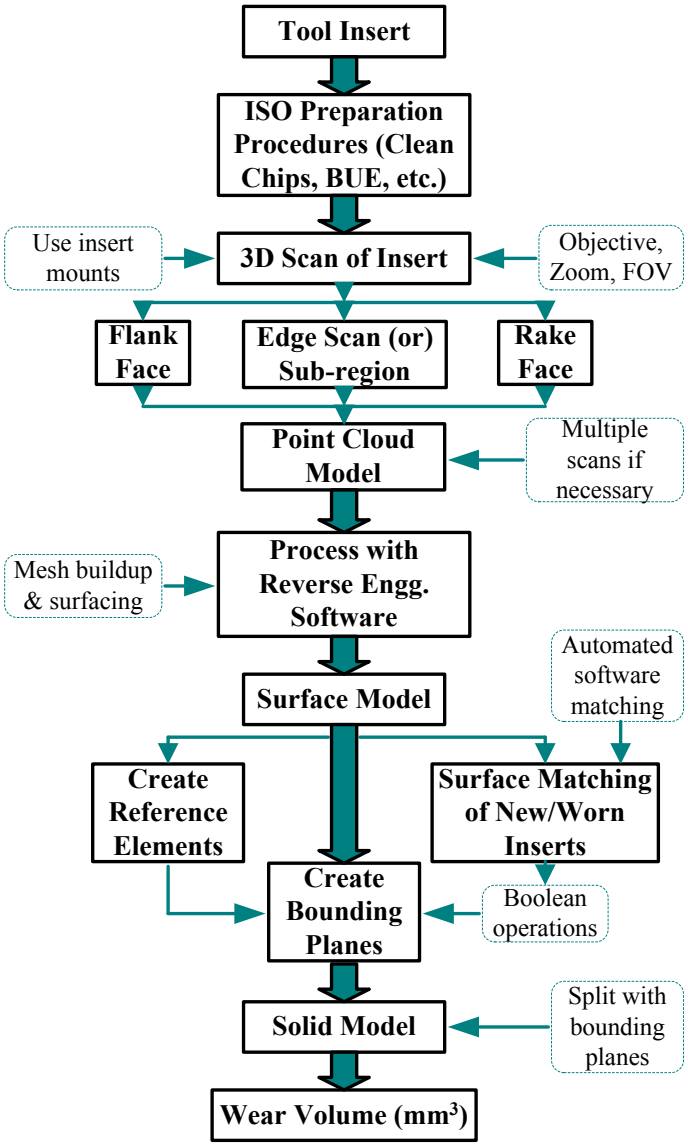

Figure 5-9: General VTW Methodology Flowchart

The first major step involves preparing the wear surface by following ISO preparation guidelines that involve cleaning, removing any BUE, etc., so that only the tool material is accounted for when assessing volumetric wear. Following this, a 3D scan of the flank, rake, another concentrated sub-region, or at an intermediate angle capturing relevant

portions of the flank and rake faces together can be captured depending on the wear status. Also, if needed, a number of partially overlapping vertical scans can be conveniently combined within the software to accommodate 'large' scan heights. For instance, the 3D optical surface profiler that was used had a maximum scan height (at a high 2G resolution) of 150 μm per downward vertical scan. Thus, multiple overlapping vertical scans of 150 μm each were required in order to characterize all of the surface area of the rake face of the ISCAR IC-28 new uncoated milling insert shown in Figure 5-10(A). The second and third successive scan instances of 150 μm each are shown in Figure 5-10(B) and (C). Figure 5-10(D) shows all five successive raw successive scans and Figure 5-10(E) shows the top view before matching. Note that a z-height offset is the only processing step needed. Figure 5-10(F) shows all but one scan matched, and Figure 5-10(G) and (H) show the point cloud and surface model of the rake face respectively.

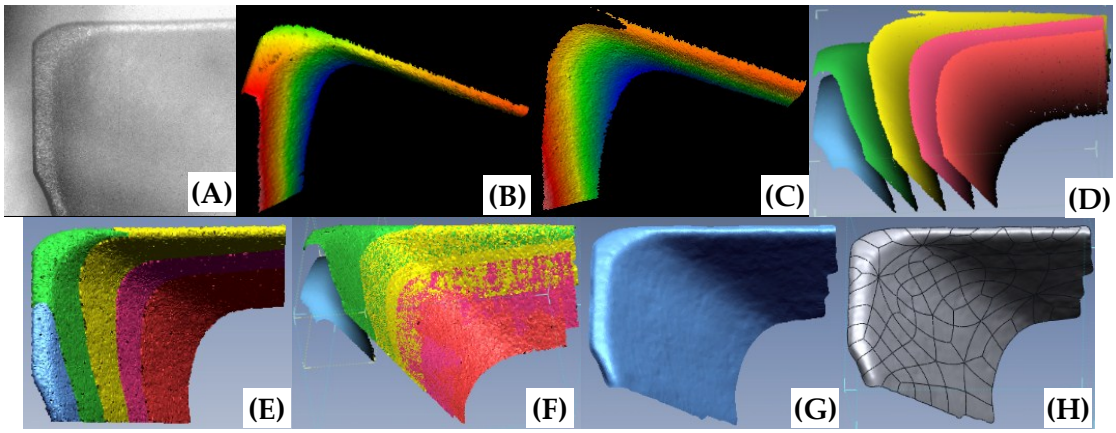

Figure 5-10: Multiple scan procedure: (A) Rake face, (B) Raw scan #2, (C) Raw scan #3, (D) All 5 raw scans, (E) Top view, (F) All but one matched, (G) Point cloud, (H) Surface model

Additionally, in an uncommon scenario of having difficulty in defining reference elements (for instance, if the tool profile is completely made of 'extreme' curves), one can initiate the surface matching feature, whereby the reverse engineering software automatically aligns the new and worn surfaces on top of each other. This takes out the difficulty and variability associated with manually (visually) accomplishing it or by using computationally intensive techniques such as manual least squares fitting, transforming matrices, etc.

At the next level, by using the wear volume (and damage area) and the geometric variables characterizing the evolution of the wear volume shape, they can be related to the process parameters, final part requirements, and eventually to the wear mechanisms itself, thereby constituting a VTW model (the concept is depicted in Figure 5-11).

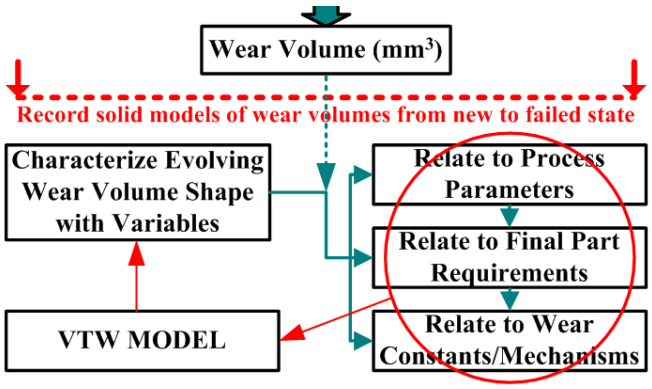

Figure 5-11: Next level of wear volume modeling for relating to wear mechanisms

5.1.3.4 Volumetric Measurement Resolution of the System

In order to examine this methodology's capability to assess varying levels of tool wear as well as to differentiate among seemingly 'similar' flank wear states, a number of

worn milling inserts are assessed for VTW. Figure 5-12(A) through Figure 5-14(A) show the wear status (Segment scale = 0.5mm) of three different milling inserts that were employed for machining Ti-6Al-4V at different cutting conditions and Figure 5-12(B) through Figure 5-14(B), their surface models. Also, their respective flank wear and corresponding wear volumes are tabulated in Table 5-1.

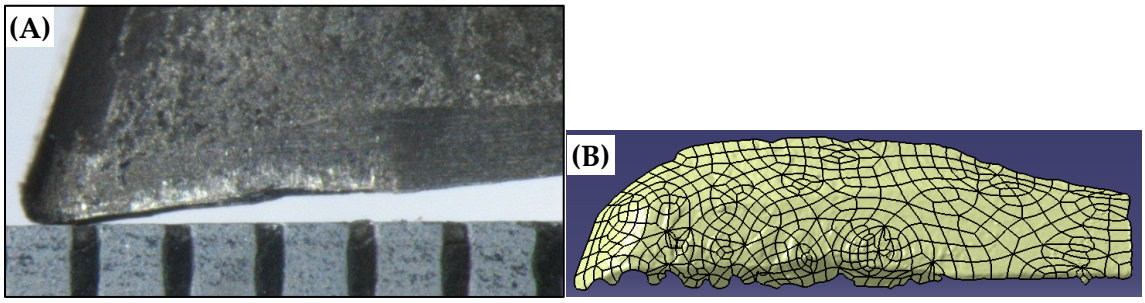

Figure 5-12: Worn milling insert #1: (A) Magnified image at 40X, (B) Surface model

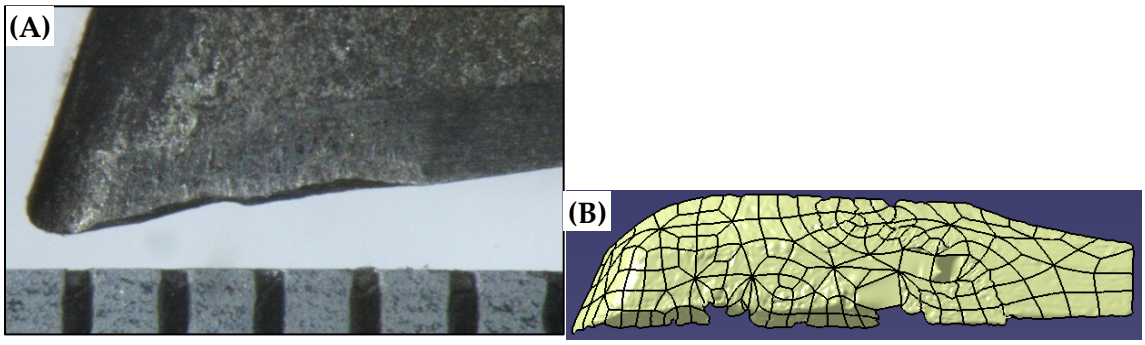

Figure 5-13: Worn milling insert #2: (A) Magnified image at 40X, (B) Surface model

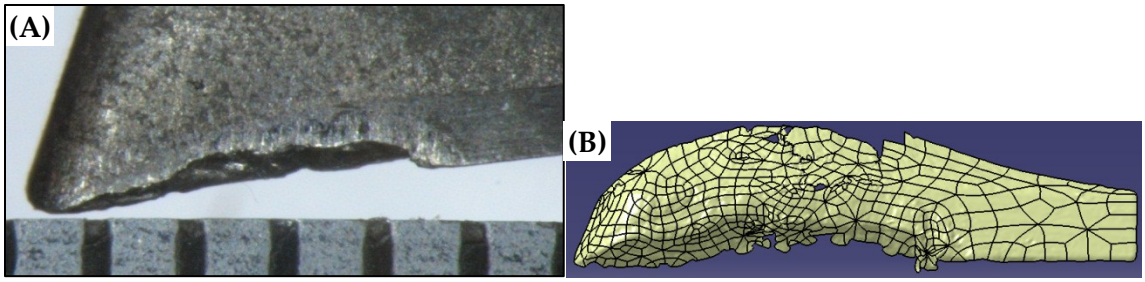

Figure 5-14: Worn milling insert #3: (A) Magnified image at 40X, (B) Surface model

Table 5-1: Flank wear and wear volumes of the 3 inserts

Insert #	VB_{Bmax} (mm)	VTW (mm^3)
1	0.26	0.089
2	0.31	0.068
3	0.36	0.116

Note that, the (maximum localized) flank wear values of all three inserts are fairly close to each other; however, insert 1 and 2 have the upper limit of their VB_{Bmax} set by a rubbing wear region (abrasion), while insert 3 has this determined by where the material has worn away – a conflicting scenario. The recorded wear volumes however, represent this wear condition more correctly with the almost double volumetric wear for insert 3, thus depicting the adequate resolution of this measurement system.

5.1.3.5 Gauge R&R Evaluation of the Measurement System

To assess the amount of variability in the measurement system (operator, equipment and methodology), a short-form ANOVA Gauge repeatability and reproducibility (R&R) study was undertaken with 2 operators conducting 2 repetitions each of 5 tool insert measurements. All five insert specimens were of the same type as the one used in the previous section outlining the methodology, *i.e.*, ISCAR APCR 100304PDFR-P IC928.

One of them was in new condition, three were at different stages of wear and the last one was a catastrophically failed one. The settings and methodology used were exactly the same as outlined before. The gauge R&R study showed less than 7% total variation due to measurement error as shown in Figure 5-15 which is indicative of the high fidelity of the measurement system (less than 10% is acceptable with need for improvement). Note that, the high part-to-part variation is due to five different inserts with different levels of wear being studied.

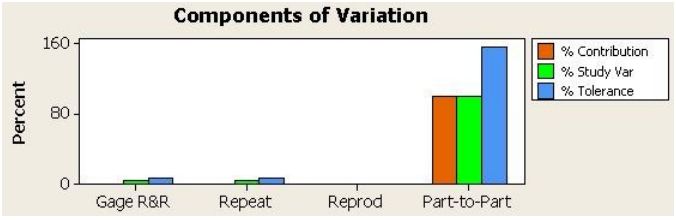

Figure 5-15: ANOVA Gauge R&R evaluation of system

5.1.3.6 Applicability to Other Insert Types

The methodology has been tried out for other insert types as well. In all cases, the tool profiles, no matter how complex they seemed, were represented satisfactorily. The flank and rake faces of three new inserts were tested and Figure 5-16 to Figure 5-18 show the original milling insert images and surface models side-by-side.

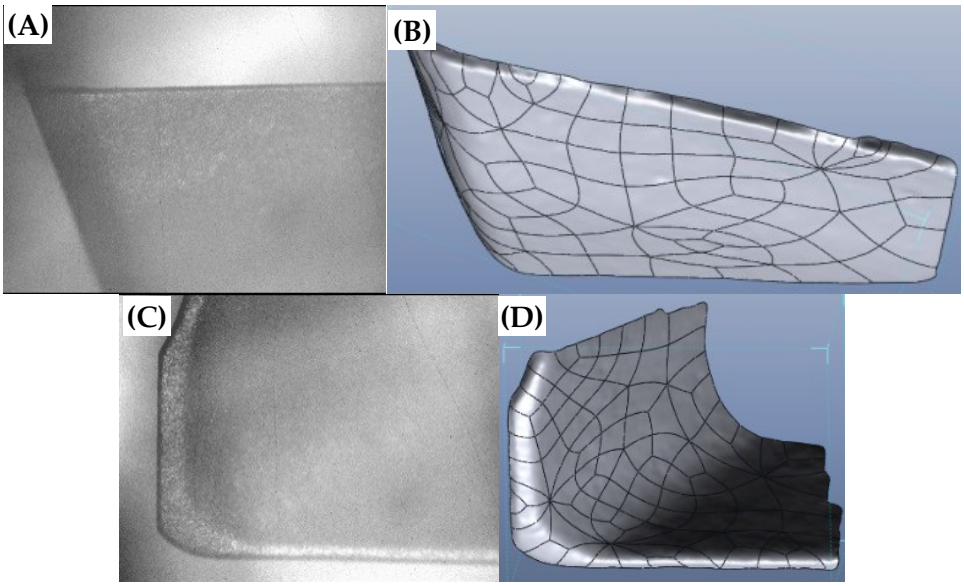

Figure 5-16: ISCAR IC-28: (A, B) Flank, (C, D) Rake faces

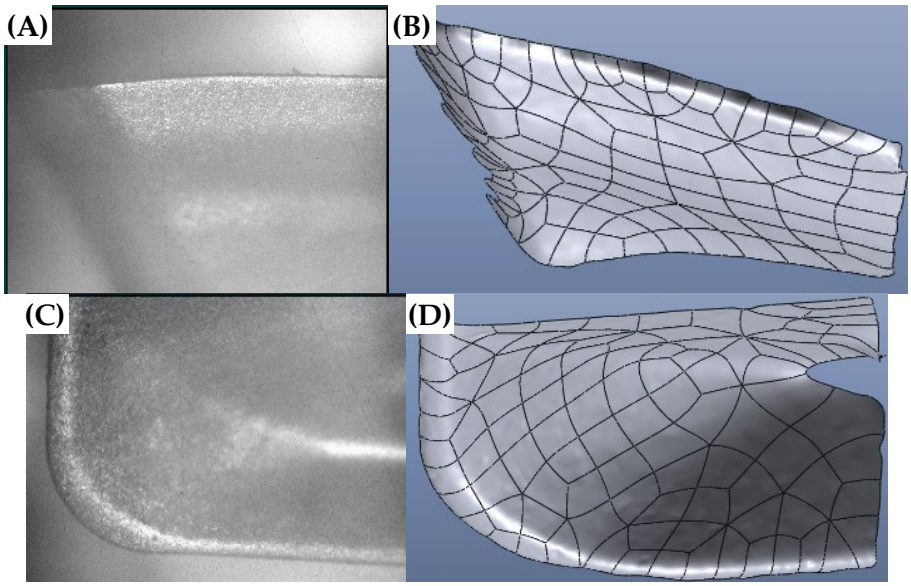

Figure 5-17: Sandvik (milling): (A, B) Flank, (C, D) Rake faces

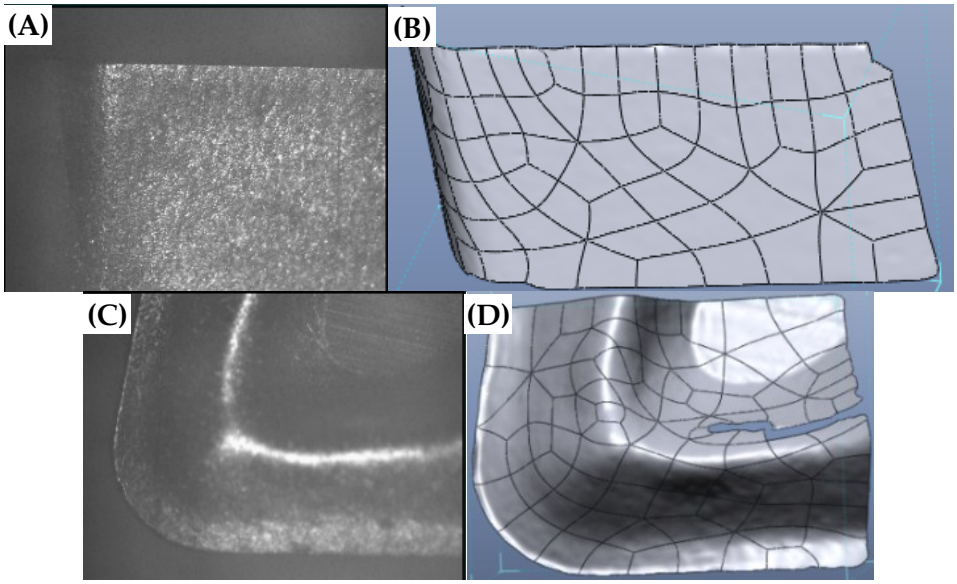

Figure 5-18: Sandvik (turning): (A, B) Flank, (C, D) Rake faces

Thus, by adapting a suitable VTW methodology that is catered to the insert type and sub-region, as well as adapting it on-the-fly to wear status and dominant wear mechanism (if needed), one can obtain the absolute volumetric tool wear (in mm^3) of the flank, crater, nose, notch or other sub-regions, either individually or collectively.

5.1.4 Limitations of the VTW Methodology

Some of the limitations of the VTW methodology that are inherent to the procedure as well as those which were identified during its development are detailed below:

1. The time-intensiveness of the procedure is the primary limitation of following this VTW methodology. On an average, the clocked time from dismounting the tool holder from the CNC machine to obtaining a wear volume value is about 15-20 minutes. Efforts are underway for reducing the

time intensiveness of the procedure as well as partially automating some of the steps involved.

2. Another limitation is the requirement of suitable special equipment and software for post-processing; the quality and usability of the final solid model is directly dependent on the quality of the captured original point cloud data.
3. Though the wear volume is a suitable wear parameter, it is not one which encompasses all characteristics of the wear status; shape characterization needs to be coupled with it as well – this can be quantified by a set of geometric coefficients.

5.1.5 Additional Suggestions

Some additional suggestions pertaining to the volumetric wear characterization of cutting tools are given below:

- Since the worn volume is obtained by subtracting the worn solid from the new, bounding planes can be changed between measurements if needed.
- When analyzing multi-cutter (milling) tools, it would be advantageous to use a suitable fixture for mounting and indexing the tool holder body, rather than removing each insert every time; otherwise an insert holder will suffice.
- Though the flank/rake faces and the nose region could be captured separately during the 3D scan, it would be advantageous to use one properly aligned

scan to capture the complete overlapping region depending on the wear condition. Otherwise the 3D scans could be stitched to get a full tool profile.

- Comparing 3D scans of subsequently worn tool profiles or with the unworn base volume model has definite potential to detect and record edge plastic deformation as well as any BUE fragments not removed in the first place.
- Another wear volume validation method would be to compare the changing tool insert mass against the volume.
- For sensitive/doubtful cases of BUE/BUL residues, X-ray diffraction could be conducted on the tools.

5.2 VALIDATION OF PREDICTED TOOL WEAR & PROFILE EVOLUTION

There are three inputs for this task: (*i*) the final DOE of primary factors that was assembled, (*ii*) the wear depths predicted by the comprehensive wear model, and (*iii*) the methodology that was developed for quantifying VTW. In this task, the methodology for quantifying VTW will be used to measure the worn volumes of tools used to conduct the machining DOE, and compared with the model-predicted wear.

The methodology was to acquire suitable cutting inserts for the machining experiments, and to conduct the machining DOE runs on CNC machining centers to obtain volumetric wear, wear rates, and profile evolution information for each setup.

At this point, it is to be noted that the final DOE of machining experiment runs was formulated for analyzing turning experiments. However, before these turning

experiments were conducted, a number of machining runs using coated carbide tools for dry end-milling Ti-6Al-4V was conducted. The purpose of this was to improve the VTW methodology for extending them to turning tools. Some relevant insights were obtained and these are presented first.

5.2.1 Validation: Milling Experiments

5.2.1.1 Experimental Design/Setup

A full factorial DOE of accelerated wear test setups were employed to experimentally investigate the progression of volumetric wear in Ti-6Al-4V milling. The geometries of new and worn inserts were measured by the volumetric approach developed previously. The workpiece used was grade 5 titanium alloy (Ti-6Al-4V) purchased from Grandis Titanium. The tool used for mounting the inserts was an Iscar Helimill HM90 E90A D1.00-4-W.75 indexable end mill with a 1″ cutting diameter and 0.75″ shank. The experiments were performed on an OKUMA MB-46VAE 3-axis vertical machining center with BT-40 type tool holders. The inserts selected were Iscar HM90 APCR 100304 PDFR-P IC928 tough grade coated carbide (PVD TiAlN) recommended for interrupted and heavy milling of stainless steels and high temperature alloys. Note that these inserts had helical cutting edges and a polished rake with a high positive rake angle of 28^0 as shown in Figure 5-19; some relevant insert dimensions are shown as well [155]. The tool holder holds up to four indexable inserts and all four inserts were used in each experimental pass for better accounting of the variability of tool wear.

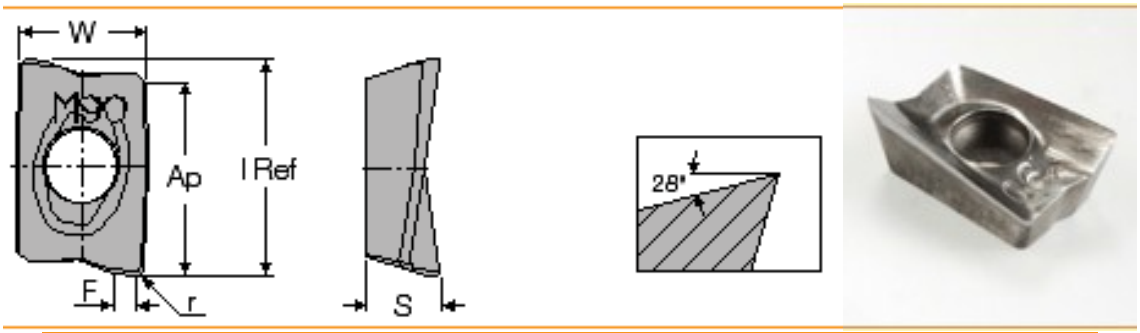

W	l	Ap	S	r	F
6.52	11.25	10.18	3.85	0.40	1.52

Figure 5-19: Iscar milling insert with relevant dimensions [155].

The 2^2 full factorial DOE of accelerated wear test setups are shown in Table 5-2. This DOE consisted of two levels of table feeds and cutting speeds which were the corners of the recommended feed-speed design space. The depth of cut was held constant at 2 mm. In order to eliminate effects due to coolant, these experimental runs were conducted dry.

Table 5-2: 2^2 Full factorial experimental designs

Experimental Setup	Design		Parameters	
	Speed	Feed	Speed (m/min)	Feed (mm/rev)
1 (L1)	+	+	200	0.5
2 (L2)	-	-	70	0.2
3 (L3)	+	-	200	0.2
4 (L4)	-	+	70	0.5

For each experimental setup shown in Table 5-2, three consecutive milling passes were conducted. Each milling pass was a half-immersion shoulder cut, 12.7 mm (0.5") wide and 154.8 mm long. Therefore, each insert was used for a total length of cut of 464.4 mm with a stock removal volume of 11795.76 mm^3. The wear volume of the relevant cutting region of each insert was recorded four times for each experimental

setup: once before machining (new condition) and after each of the three milling passes. This measurement procedure was followed for all four inserts on the tool holder for each experimental setup.

As detailed previously, the optical measurements were facilitated with the ZYGO NewView 7200 3D Optical Surface Profiler and the photomicrographs were recorded using an Olympus SZX-10 stereomicroscope. An insert mounting fixture was utilized to hold the inserts in place on the profiler's stage. Visible chips and loose material that could be removed easily were brushed away before measurement as described in the ISO milling standard [17]. In case of a visible built-up-edge (BUE), it was 'gently' removed as well; an example with and without a BUE is shown in Figure 5-20(A) and Figure 5-20(B), respectively.

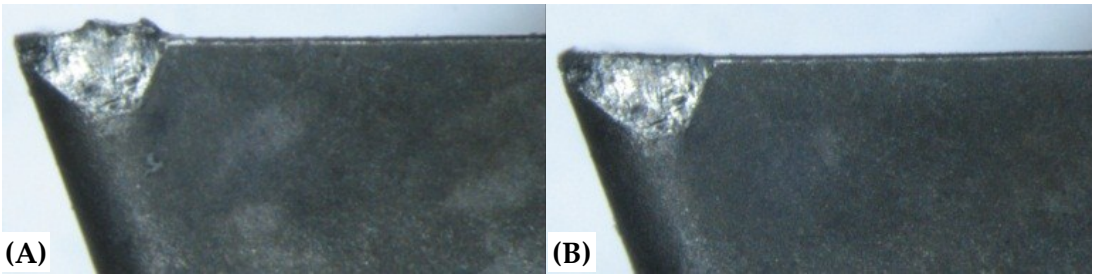

Figure 5-20: (A) Insert with BUE, (B) With BUE removed

This was done to ensure that the calculated volumetric wear did not account for any significant workpiece material adhered to the tool. No other formal (chemical) cleaning process was used. If required, for sensitive/doubtful cases of BUE/BUL residues, XRD (X-ray diffraction) could be conducted to detect any retained workpiece elements.

5.2.1.2 Results/Analyses: Volumetric Characterization of Wear Evolution

This section details the results of the tracking of volumetric wear progression by following the wear evolution of one of the four milling inserts used in experimental setup 1, *i.e.*, design (++) at a table feed of 0.5 mm/rev, and cutting speed of 200m/min. Note that, this insert was run to failure beyond the DOE specified total cut length of 464.4 mm.

Figure 5-21(A) shows a microscope image of the flank face of the unworn (new) insert at 40X magnification. Figure 5-21(B) shows the corresponding solid model of the flank region of this same insert onto which a reference surface model (see Figure 5-22) is superimposed. As can be seen from Figure 5-21 and the following figures in this sub-section, only the top portion of the flank region (region between the cutting edge line and the line separating the plane surface containing the flank face with the remaining body of the insert, that are almost parallel to each other) was investigated for volumetric wear measurement, as this is the only portion in contact with the workpiece within normal wear limits. The solid model has therefore been trimmed accordingly to only constitute the portions of interest.

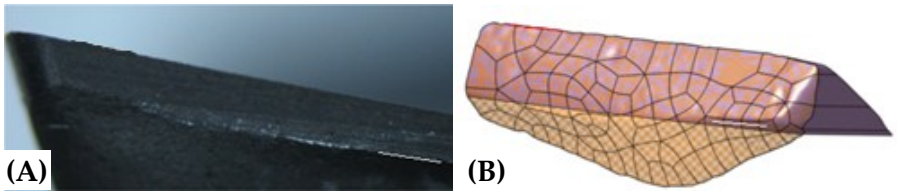

Figure 5-21: Unworn (new) insert: (A) Microscope captured image, (B) Solid model along with reference surface

Figure 5-22(A) and Figure 5-22(B) illustrate an alternate path for calculating VTW as given in the general VTW methodology flowchart (Figure 5-9), *i.e.*, of surface matching of the new and worn inserts' flank surfaces. This can be accomplished manually by Boolean manipulations or semi-automatically by software through least squares fitting. As can be seen in Figure 5-22(A) and Figure 5-22(B) that the unworn reference surface was retained during the comparisons with worn surface models for the correct determination of flank region wear volume for each cutting pass. Figure 5-22(A) depicts the matched set of worn and unworn surface models after a cut length of 154.8 mm (end pass 1, experiment 1). Figure 5-22(B) shows the corresponding solid model with the unworn reference surface model superimposed. Note how the worn and unworn surfaces have been matched closely (to be as coincident as possible, manually) in Figure 5-22(A) by aligning the circled left edges and the (almost horizontal) line separating the surface containing the flank face with the remaining insert body.

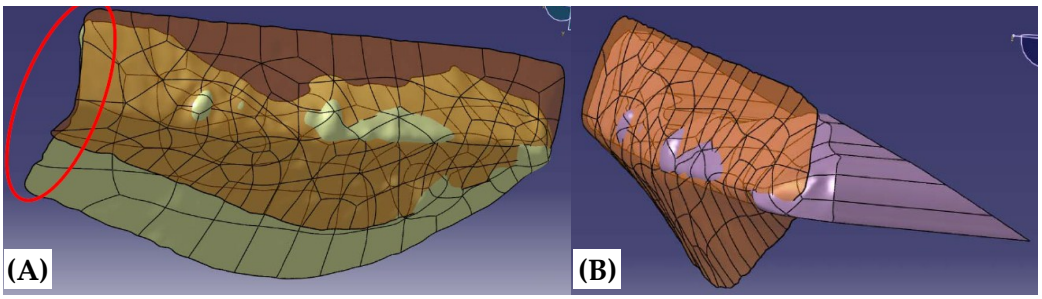

Figure 5-22: Insert matching alternative: (A) New and worn surface matching, (B) Solid model with reference surface

Figure 5-23(A) shows the microscope image of this insert and Figure 5-23(B) depicts its corresponding relevant portion of the solid model after a cutting length of 154.8 mm

(experiment 1, pass 1). Though not shown, the reference surface of the unused insert shown above in Figure 5-22 was used as a reference to ensure that the right region was selected for modeling.

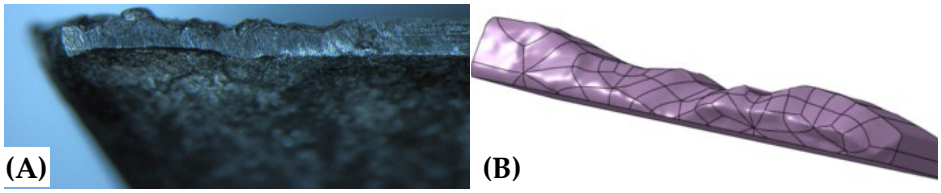

Figure 5-23: Insert after a cutting length of 154.8 mm: (A) Microscope image, (B) Solid model used for comparison

Following through in this manner, the microscope image and the related partial solid model are shown in Figure 5-24(A) and Figure 5-24(B) respectively, after a cutting length of 309.6 mm (end of pass 2). As can be observed, the wear stage has further progressed from the end of pass 1. The solid model for volumetric quantification was derived as before.

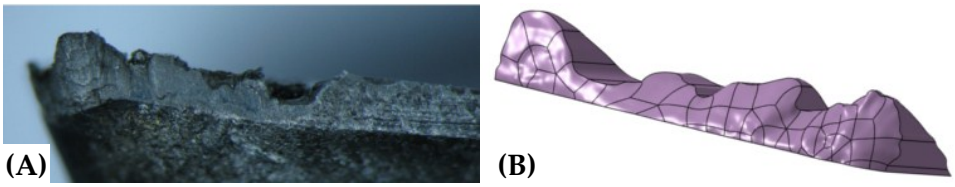

Figure 5-24: Insert after a cutting length of 309.6 mm: (A) Microscope image, (B) Solid model used for comparison

Figure 5-25(A) shows again a microscope image of the same insert together with the partial solid model in Figure 5-25(B) after a cutting length of 464.4 mm (end of pass 3), which has reached an advanced wear status. Besides the even further progression of

wear, note how the wear stage has progressed beyond the line separating the surface containing the flank face with the remaining body of the insert that was intact until before.

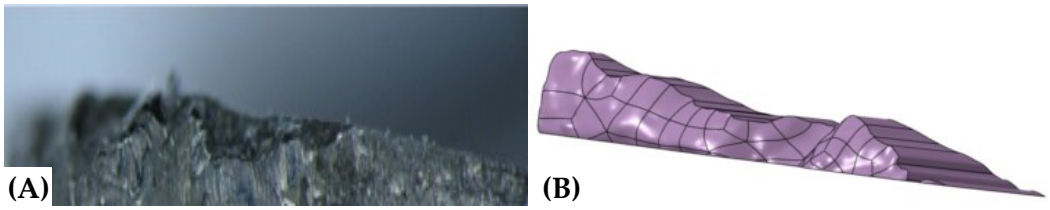

Figure 5-25: Insert after a cutting length of 464.4 mm: (A) Microscope image, (B) Solid model used for comparison

Thus, tracking the wear evolution of this insert as outlined above by volumetrically quantifying wear shows that even advanced wear status such as the ones after pass 2 and 3 can be effectively captured by following this methodology. The worn volumes and their analyses are tabulated next.

5.2.1.3 Results/Analyses: Volumetric Tool Wear Data Analysis

The volumetric wear characterization procedure outlined earlier was used to derive wear volumes of each of the four worn inserts used in each of the four machining experimental setups. At the end of each cutting pass, the machine was stopped and the point cloud data of the tool and other associated parameters were recorded. After processing it through reverse engineering and CAD software, the actual VTW values were computed by subtracting the retained volume of each of the inserts from the average volume of four identical unworn (new) reference inserts, as given by:

$$VTW_j = \left[\frac{\sum_{i=1}^{4} \left(Vol.Ref_i \right)}{4} \right] - \left(Vol.Ret \right)_j \tag{5.1}$$

Where, VTW_j is the volume worn away from insert j (j = 1-4), $Vol.Ref_i$ is the average unworn reference volume of four new inserts, and $(Vol.Ret)_j$ is the retained volume of the cordoned off solid model of insert j.

Note that the resultant reference volume (within square brackets), is the average of the unworn reference volumes of each new insert separately recorded by two investigators for the sake of a quick check of measurement repeatability as well as to obtain a better averaged value. These reference volumes are tabulated in Table 5-3.

Table 5-3: Resultant reference volumes (unworn)

Investigator	**Insert 1**	**Insert 2**	**Insert 3**	**Insert 4**
A	5.59	6.06	6.15	6.79
B	5.61	6.06	6.15	6.69
Resultant $Vol.Ref_j$	**5.60**	**6.06**	**6.15**	**6.74**
SD b/w investigators	0.01	0.00	0.00	0.07

The measurement repeatability between investigators computing the VTW of the same insert is within acceptable limits as portrayed by the maximum standard deviation (±3σ) of ±0.21 mm^3 which is less than 4.5% of the resultant reference insert volumes, and less than 15% of the average '0pass-to-3pass' or 'new-to-worn' volumetric wear

measurement ranges. Note that the two investigators measured the VTW on two separate days on independent setups. This suggests that the differences in reference volumes between inserts (1-4) is predominantly due to different size solids being cordoned off for computing VTW (through some variability from the manufacturer can be expected as well), which portrays another flexible aspect of the methodology, that one needs to be consistent across an insert only and not necessarily across the whole experimental setup.

The raw data of volumetric tool wear is tabulated in Table 5-4 which lists the volumetric tool wear of each of the four inserts at the end of each of the three passes, for all the four setups. Note that setup 4 suffered catastrophic failure and hence no wear data was obtained.

Table 5-4: Volumetric tool wear of each of the 4 individual inserts (mm^3) (36 data points)

Experiment Setup	Pass	Tool Insert Material Worn (mm^3)			
		Insert 1 (Purple)	Insert 2 (Red)	Insert 3 (White)	Insert 4 (Yellow)
Setup 1 (L1) (++)	1	1.28	1.01	2.22	0.63
	2	1.77	1.70	2.37	1.98
	3	3.76	2.76	3.16	4.22
Setup 2 (L2) (--)	1	0.05	0.04	0.05	0.04
	2	0.09	0.10	0.19	0.10
	3	0.25	0.28	0.22	0.35
Setup 3 (L3) (+-)	1	0.03	0.04	0.06	0.09
	2	0.26	0.34	0.31	0.31
	3	0.84	0.75	1.15	0.49
Setup 4 (L4) (-+)	1	Tool Failure			
	2				
	3				

Further, Table 5-5 tabulates the average of volumes worn away from all four independently mounted inserts at the end of each of the three milling pass, for each experimental setup.

Table 5-5: Averaged Volumetric Tool Wear Results (mm^3)

Pass	Cumulative Length of Cut (mm)	Cumulative Stock Volume Removed (mm^3)	Tool Material Worn (mm^3)			
			Setup 1	Setup 2	Setup 3	Setup 4
			++ (L1)	-- (L2)	+- (L3)	-+ (L4)
1	154.8	3931.92	1.29	0.05	0.06	Tool Failure
2	309.6	7863.84	1.96	0.12	0.31	
3	464.4	11795.76	3.47	0.27	0.81	
MRR (cm^3/min)			31.8	4.5	12.7	11.1

Figure 5-26 shows a selection of plots taken from the above tabulated volumetric wear data (Table 5-5). It compares the average volumetric wear in mm^3 at the end of each pass plotted against feed at a constant cutting speed of 200 m/min, as well as volumetric wear plotted against varying speeds at a constant feed rate of 0.2 mm/rev.

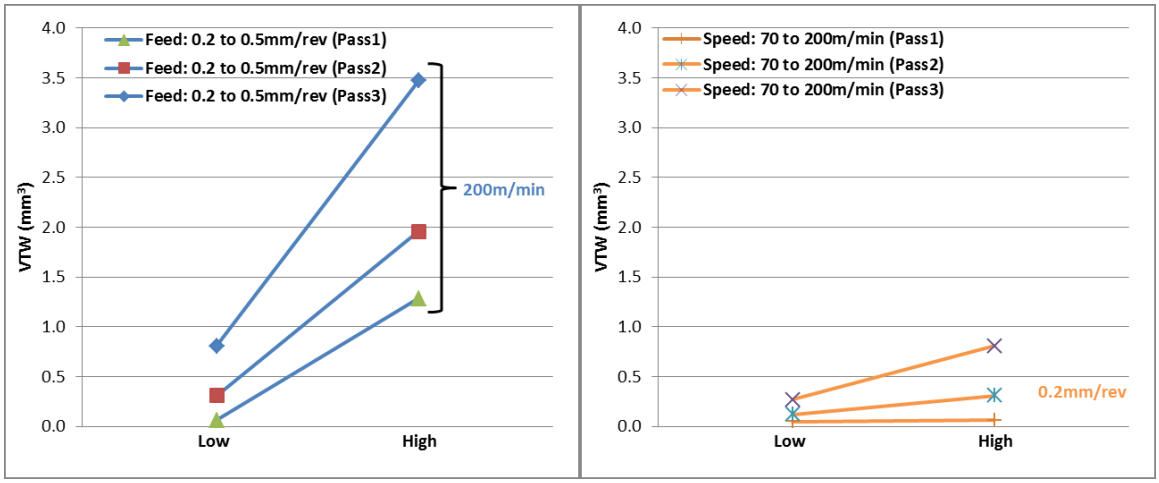

Figure 5-26: Average volumetric wear plotted against varying feeds and speeds for setups 1-3

As expected, the volumetric wear of all the inserts increased monotonically with cutting length, *i.e.*, stock material volume removed. On plotting the VTW against cutting speeds and feeds, it was observed that increasing the feed (2+ times) from 0.2 mm/rev to 0.5 mm/rev had a greater influence on volumetric wear (larger slope on similar axes scales) than increasing the cutting speed (2+ times) from 70 m/min to 200 m/min, as shown in Figure 5-26. Further, increasing feed at any constant surface speed resulted in an increase of VTW. Similarly, increasing the surface speed at a constant table feed of 0.2 mm/rev resulted in an increase of VTW; however, at a constant feed of 0.5 mm/rev, it resulted in a decrease of VTW.

5.2.1.4 Results/Analyses: VTW vs. MRR

This seemingly contradictory behavior can be better visualized when looking at the scenario from the standpoint of MRR, i.e., at a cutting speed of 200 m/min, an MRR increase from 12.7 to 31.8 cm^3/min (ΔMRR = 19.1 cm^3/min) results in more volumetric tool wear than an MRR increase from 4.5 to 12.7 cm^3/min (ΔMRR = 8.2 cm^3/min) at 0.2 mm/rev feed. Thus, regardless of the feed and speed combinations, there seems to be a direct correlation between VTW and MRR. This correlation is further evident from Figure 5-27 which plots MRR vs. the average VTW at the end of each pass (each data point is the average VTW of four inserts).

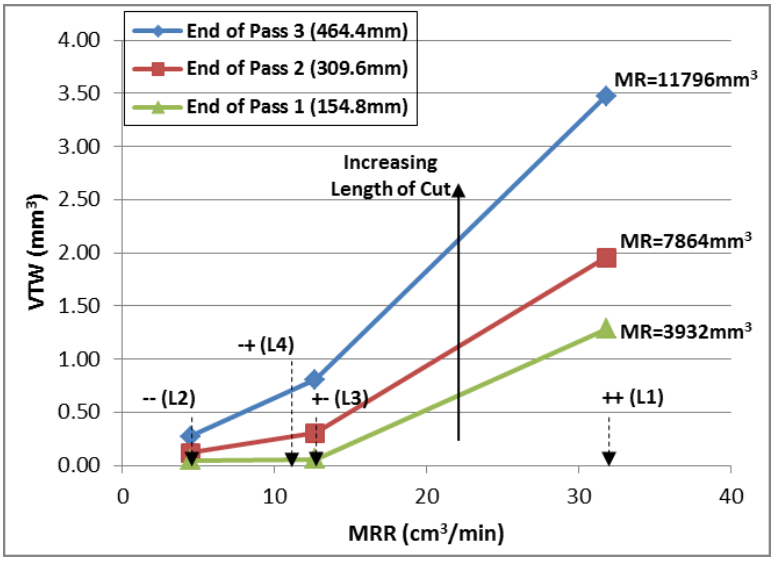

Figure 5-27: Direct correlation of MRR with VTW.

On examining Figure 5-27, a pattern of clear proportionality is evident. As expected, the VTW increases consistently with the length of cut, *i.e.*, stock material removed (MR), regardless of the feed-speed combinations. Note that, all three curves in Figure 5-27 are lines of constant stock volume removal – this means that for a given volume of workpiece material removed, the VTW increases with increasing MRR regardless of feed or speed. It is known that an increase in surface speed leads to a direct exponential increase in interfacial tool temperature, which is all the more exacerbated by the low thermal conductivity of titanium alloys, leading to higher tool wear rates and hence failures. This fact has traditionally suggested that cutting speed is the predominant factor affecting tool failure when machining titanium alloys. The above results however seem to suggest that MRR might be the more critical higher order factor to be controlled, for better predicting the actual (3-D) wear, specifically when machining titanium alloys.

5.2.1.5 Results/Analyses: VTW Rate vs. MRR

Another interesting observation from Figure 5-27 is the fact that the slopes of each of the three 'constant stock volume' line segments get larger with an increasing MRR. This suggests that both the VTW and the rate of VTW have dependencies on MRR, *i.e.,* as the MRR increases, volumetric wear accelerates – this can be seen by the almost quadratic (2^{nd} order) curve fit of the data points within any constant 'stock-material volume' curve. The resulting rate of VTW is tabulated in Table 5-6, both with respect to the specific stock volume removed and time.

Table 5-6: Specific Volumetric Tool Wear Rate

Pass	Total Cut Stock (mm^3)	Setup 1	Setup 2	Setup 3	Setup 4
		Volumetric Tool Wear Rate (mm^3/mm^3 of stock)			
1	3931.92	0.33	0.01	0.01	Tool Failure
2	7863.84	0.17	0.02	0.06	
3	11795.76	0.39	0.04	0.13	
		Volumetric Tool Wear Rate (mm^3/min)			
		10.39	0.05	0.18	Tool Failure
		0.67	0.08	0.80	
		12.27	0.18	1.62	

Conversely, as the VTW consistently increases with an increasing length of cut, the wear rate also increases. This means that the VTW rate is dependent on the wear itself, *i.e.,* the wear rate is proportional to the accumulated volumetric wear. This 'asymptotic/singularity-type' dependency of the wear rate on the cumulative wear itself might actually be the reason for the sudden catastrophic tool failures that are typical of

the titanium alloy machining process, as opposed to a gradual linear climb of wear in aluminum/steel machining.

Figure 5-28 plots the specific VTW rate with respect to time (from Table 5-6), against the MRR. Note that each of these wear rates were computed by dividing the tool material volume worn away at the end of each pass, by the total time taken for that particular milling pass. Looking at the constant stock-material-volume-removed curves at the end of pass 1 and 3, the wear rates are seen to increase with MRR in a quadratic fashion. This suggests that the volumetric wear rate increases, or the VTW accelerates with MRR, regardless of the combination of feeds and speeds. However, the wear rate curve at the end of pass 2 decreases with MRR – these decreasing and lower wear rates could be an indication of wear progression through the 'steady-state' portion of typical wear behavior, *i.e.*, the portion of the wear-curve where the tool most efficiently cuts material (in between the break-in and catastrophic failure portions of a typical wear process). Note that these wear rates were obtained as the average rates of four independently mounted inserts.

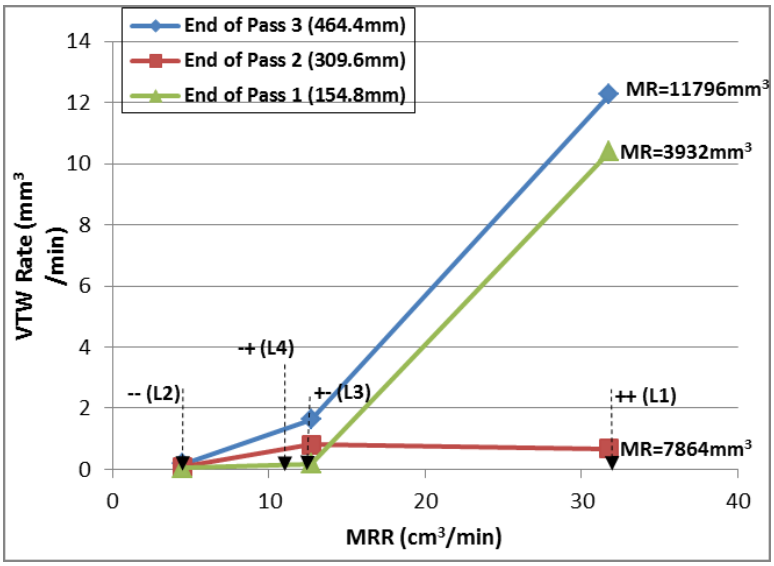

Figure 5-28: The Correlation of Specific VTW Rate with MRR

5.2.1.6 Results/Analyses: Correlation of VTW and Rate

From Figure 5-27 and Figure 5-28, the general conclusions that can be drawn are that both the VTW and the VTW rate are proportional to MRR, in a quadratic fashion as:

$$V_{Pi} = a_i MRR^2 + b_i MRR + c_i \tag{5.2}$$

$$\dot{V}_{Pi} = a_i MRR^2 + e_i MRR + f_i \tag{5.3}$$

Where, V_{Pi} and $\dot{V}_{Pi}$ are the VTW and rates at the end of each pass i (i = 1-3), and a_i - d_i are curve-fit coefficients.

On adding the above two equations and deriving the general solution of the differential equation, a complex empirical relationship resulted. In order to derive a more fundamental relationship, a more basic analysis follows.

Figure 5-29 shows a plot of the specific VTW rate (with respect to time), against VTW for the end of each pass. It is seen that for pass 1 and pass 3, as the wear increases, the

wear rate increases as well, *i.e.*, the wear rate is a function of the cumulative accumulated VTW. The constant stock-removal curve for the end of pass 2 shows that the wear rate does not increase with accumulated wear. This is in conformance with the earlier stated explanation of the wear progressing through the 'steady-state' stage of the wear curve.

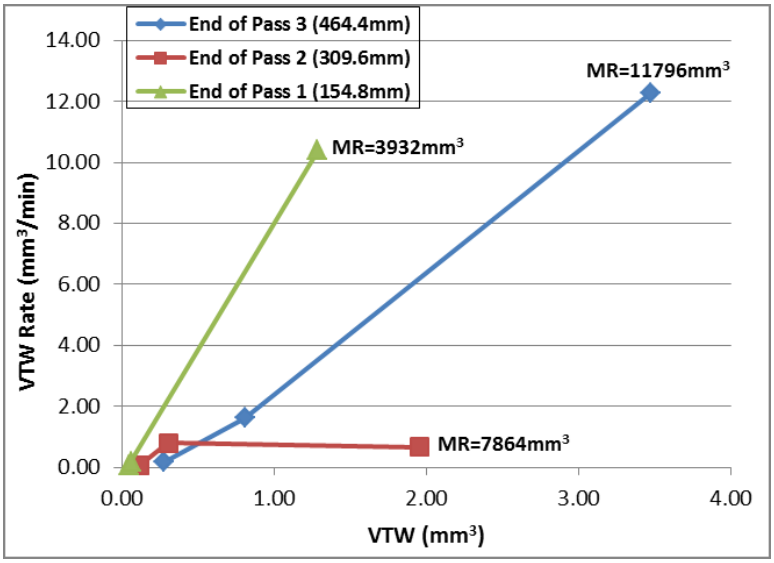

Figure 5-29: Dependence of Accumulated Wear on VTW Rate

To capture this inherent dependence of wear rate on the accumulated wear, linear curve fit coefficients were computed for each of the above three curves based on the equation:

$$\dot{V}_{\mu l} \quad \ldots_{l} \quad _{\mu l} + C_i \tag{5.4}$$

Where, m_i and C_i are linear curve-fitting coefficients for each of the three constant stock-removal volume curves. On converting this to a standard form, multiplying by an integrating factor, and further manipulation, the general solution takes the form:

$$V_{Pi} = -\frac{C_i}{m_i} + D_i e^{m_i t} \tag{5.5}$$

Where, D_i is the constant of integration and t is the time in minutes of cutting time, for each pass. On applying the initial condition of $V_{Pi} = 0$, at time $t = 0$, the constant D_i is found to be C_i/m_i. Thus, the final solution is:

$$V_{Pi} = \frac{C_i}{m_i}\left(e^{m_i t} - 1\right) = \frac{C_i}{m_i}\left(e^{\frac{Mm_i}{MRR}} - 1\right) \tag{5.6}$$

Where, stock-volume machined ($M = 3.932$ cm^3) is constant regardless of setup; thus Mm_i is a constant for each pass.

This solution suggests that the VTW has an exponential dependence with time and with MRR. However, the negative signs of some of the curve-fitting coefficients for each pass generate negative wear values. Examining the initial condition, $V_{Pi} = 0$, at time $t = 0$; this means that all y-intercepts have to be zero, *i.e.*, $C_i = 0$. Thus the curve-fits are:

$$\dot{V}_{Pi} \quad \ldots \quad V_{Pi} \tag{5.7}$$

The solution of this standard differential equation takes the following form, where 'E_i' is a constant:

$$V_{Pi} = E_i e^{m_i t} \tag{5.8}$$

Using the curve-fit coefficients of each of the three passes, the time-progression of VTW behavior can thus be modeled by a corresponding set of equations. Note that E_i will need to be function of time (or the stock volume removed, M), such that at time $t = 0$, $E_i = 0$, for zero wear. Such an equation set holds for all three setups, and the time t for

each pass is the same within each setup. What this means is that, if the wear progression is divided into three segments based on the stock machined, the volumetric wear rate will increase and be high in the first and last segments, while it will decrease and be low in the middle section – this deduction is in conformance with the earlier explanation of the steady-state portion of the wear curve.

Additionally, since the cutting length and stock-volume machined (M = 3.932 cm^3) are constant for each pass regardless of setup, the above equation can be rewritten as:

$$V_{Pi} = E_i e^{\frac{m_i M}{MRR}} \tag{5.9}$$

$$V_{Pi} = E_i e^{\frac{m_i M}{MRR}} \tag{5.10}$$

Where, Mm_i is a constant for each pass, and within each setup. This is the final form of the solution relating VTW with MRR, showing the exponential correlation between these parameters. The next step involves validating this model against another volumetric tool wear data set in milling and in turning.

5.2.1.7 Results/Analyses: Comparison with Traditional Wear Parameters

This section serves to validate the VTW methodology results against traditional flank wear measurements and their corresponding photomicrographs. Figure 10 and 11 plot the average measured flank wear and the corresponding normalized average VTW of each of the four experimental setups against the material volume removed (cutting length) respectively. Note that each data point in both Figure 5-30 and Figure 5-31 depicts the average wear value of all four color-coded indexable inserts on the mill.

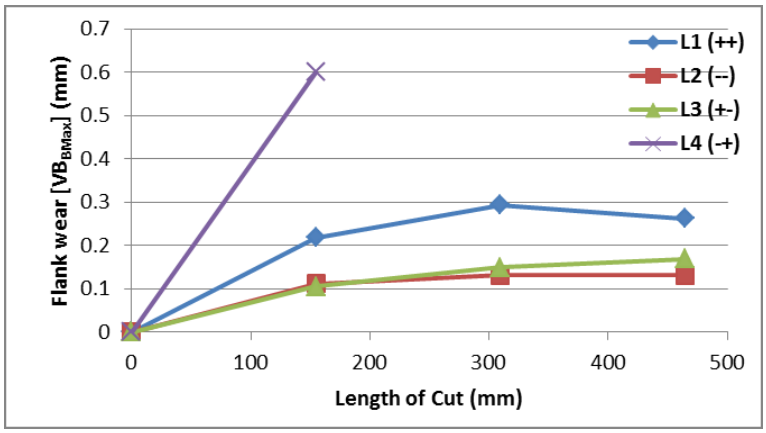

Figure 5-30: Average measured flank wear (4 inserts each)

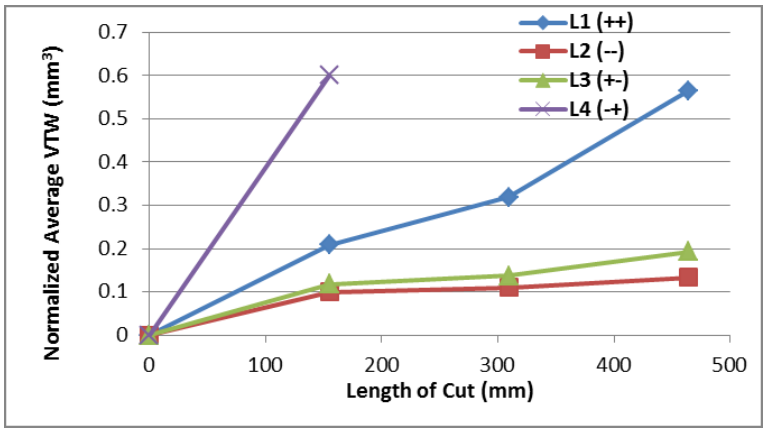

Figure 5-31: Normalized average VTW (4 inserts each)

On comparing the tool wear results from the above two methods, *i.e.,* traditional flank wear measurements and VTW, though generally similar trends are evident, certain marked differences can be observed. For instance, in the case of setup 1 (L1), the flank wear (Figure 5-30) at the end of all 3 steps (cut lengths of 154.8, 316.8, and 464.4 mm) are fairly close to each other (*i.e.,* about 0.2 – 0.3mm), suggesting that the tools have worn to fairly similar extents. However, the VTW plot (Figure 5-31) for setup 1 (L1) shows

significantly varying wear volumes (more than two times increase in absolute wear volume, or three times when normalized). For further examining this variation, a corresponding set of photomicrographs (Figure 5-32, Figure 5-33, and Figure 5-34) of the flank land of one of the four inserts used in L1 were examined at a 40X magnification.

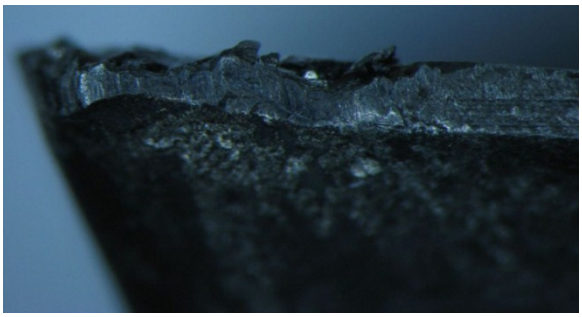

Figure 5-32: Flank land of L1 insert at end of step-1 (154.8 mm)

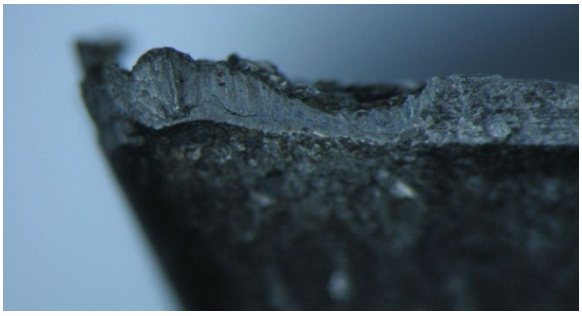

Figure 5-33: Flank land of L1 insert at end of step-2 (316.8 mm)

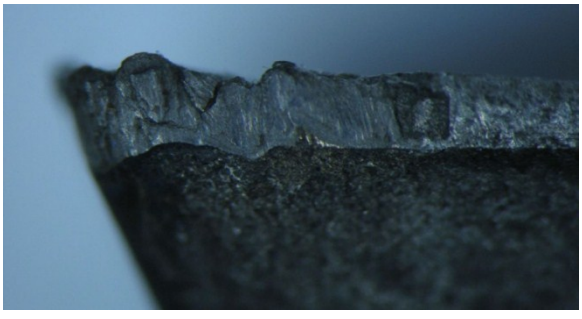

Figure 5-34: Flank land of L1 insert at end of step-3 (464.4 mm)

On examining the above magnified images, it is observed that there are 'considerable' differences in the amounts of wear between each of the wear steps. This difference is especially large (more than twice) in the case of step-3 (~ 0.6 mm^3) compared to step-2 or step 1 (~ 0.2 – 0.3mm^3); this observation has been effectively captured by the volumetric quantification approach while it does not show up in traditional flank wear measurements.

5.2.2 Validation: Turning Experiments

5.2.2.1 Experimental Design/Setup

Two types of turning insert tools with two different grain sizes (0.54 μm 0.61 μm) were acquired. All turning experiments were conducted with cutting inserts from the same box to possibly minimize any batch-to-batch variability if any. The workpiece stock material used was Ti-6Al-4V obtained from American Titanium Works (ATW). Three discrete steps of stock volumes were removed: 10, 20, and 30 cm^3. The final machined workpiece stock for H10A grade and H13A grade inserts are show below

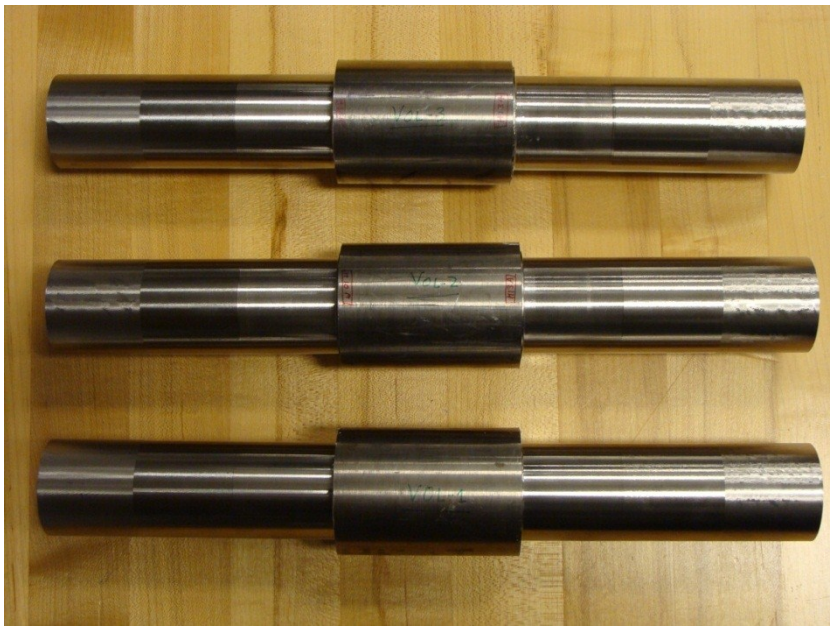

Figure 5-35: Final machined workpieces used for the turning DOE

Following each run, the inserts were removed, cleaned and the wear surfaces measured using an optical microscope, white light interferometer, and SEM and subjected to EDS elemental analysis. The machining experiments were conducted on the OKUMA Space Turn LB4000-EX turning center. No coolant was used.

5.2.2.2 Results/Analyses: Volumetric Tool Wear Data Analysis

The volumetric tool wear characterization procedure developed in the previous section (Task 3-B) was employed to capture the volume of the turning tools worn away for each of the machining DOE runs. As before, at the end of each cut, the point cloud data of the tool and other associated parameters were recorded. After processing it through reverse engineering and CAD software, the actual VTW values were computed by subtracting the retained volume of each of the inserts from the volume of a new

insert. The raw data of volumetric tool wear for H10A and H13A inserts are tabulated in Table 5-7 and Table 5-8, respectively (Note that CF is catastrophic failure).

Table 5-7: Volumetric tool wear data of H10A grade turning inserts

H10A Grade Turning Inserts (0.54 μm)							
Insert Info		Process Parameters			VTW		
Insert	Corner	DoC	f	V	Vol-1	Vol-2	Vol-3
(#)	(#)	(mm)	(mm/rev)	(m/min)	(mm^3)	(mm^3)	(mm^3)
T4-1	4	2	0.05	30	0.00056	0.001813	0.003164
T4-2	1	2	0.05	60	0.00151	0.003605	0.004142
T4-2	2	2	0.05	120	0.00339	0.005130	0.008560
T4-2	3	2	0.15	30	0.00437	0.004586	0.004213
T4-2	4	2	0.15	60	0.00448	0.005719	0.006698
T4-3	1	2	0.15	120	0.00678	0.009009	0.009281
T4-3	2	2	0.30	30	0.00690	0.006910	0.008291
T4-3	3	2	0.30	60	0.01064	0.010879	0.016026
T4-3	4	2	0.30	120	CF	CF	CF

Table 5-8: Volumetric tool wear data of H13A grade turning inserts.

H13A Grade Turning Inserts (0.61 μm)							
Insert Info		Process Parameters			VTW		
Insert	Corner	DoC	f	V	Vol-1	Vol-2	Vol-3
(#)	(#)	(mm)	(mm/rev)	(m/min)	(mm^3)	(mm^3)	(mm^3)
T3-3	2	2	0.05	30	0.00278	0.003954	0.004291
T3-3	3	2	0.05	60	0.00249	0.005102	0.005338
T3-3	4	2	0.05	120	0.00398	0.005649	0.007563
T3-4	1	2	0.15	30	0.00370	0.004675	0.005125
T3-4	2	2	0.15	60	0.00468	0.005396	0.006502
T3-4	3	2	0.15	120	0.00585	0.007467	0.008385
T3-4	4	2	0.30	30	0.00633	0.007857	0.008169
T3-5	1	2	0.30	60	0.01365	0.014490	0.014362
T3-5	2	2	0.30	120	CF	CF	CF

H10A Grade Inserts

The plots of VTW against the process parameters (feed and speed) are given below:

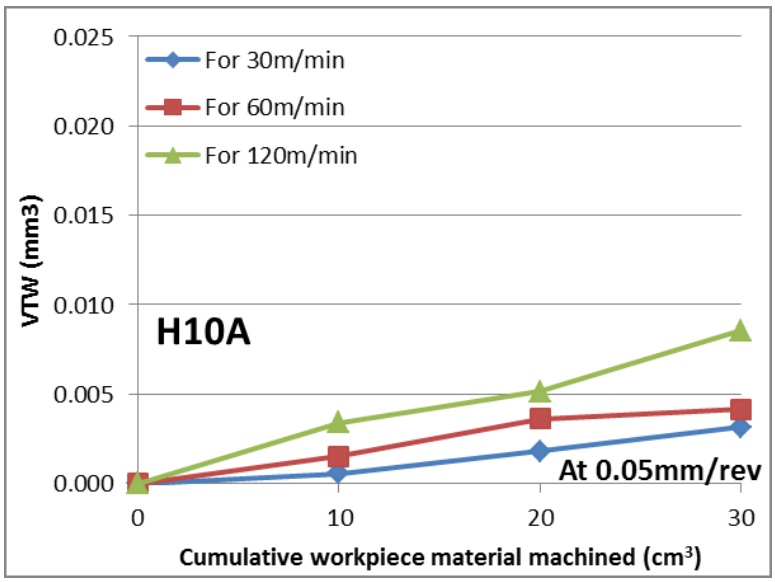

Figure 5-36: Volumetric tool wear of the H10A grade insert at a feed rate of 0.05 mm/rev for different cutting speeds.

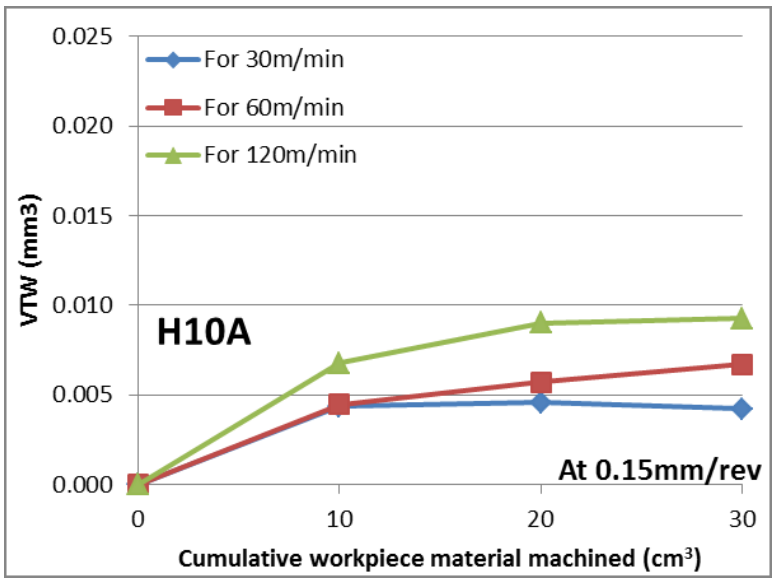

Figure 5-37: Volumetric tool wear of the H10A grade insert at a feed rate of 0.15 mm/rev for different cutting speeds.

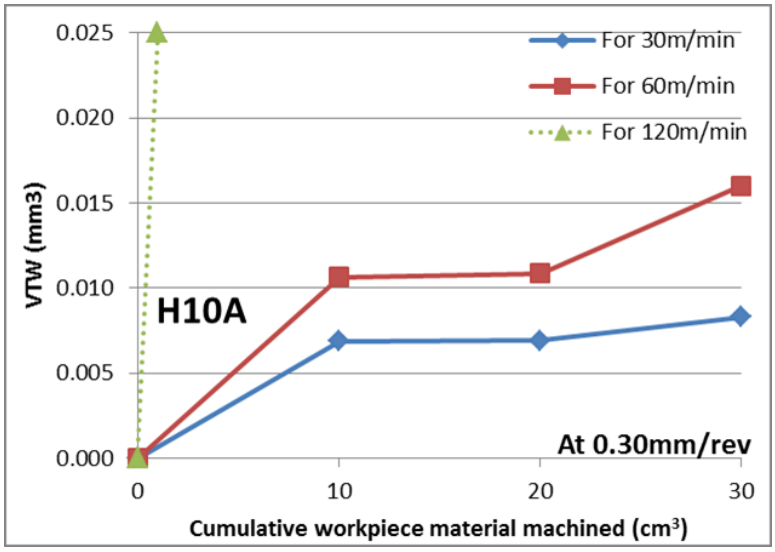

Figure 5-38: Volumetric tool wear of the H10A grade insert at a feed rate of 0.30 mm/rev for different cutting speeds. Note that the data point for a cutting speed of 120 m/min, though shown as 0.025 mm³, is actually catastrophically failed.

In general, as with milling, the volumetric wear of all the inserts increased monotonically with cutting length, *i.e.,* stock material volume removed. Further, the volumes increased in general with increasing cutting speeds and in many cases with feeds as well. This was expected since they are both constituents of MRR, to which VTW was found to be proportional to in the case of milling insert wear.

H13A Grade Inserts

The plots of VTW against the process parameters for H13A grade inserts follow:

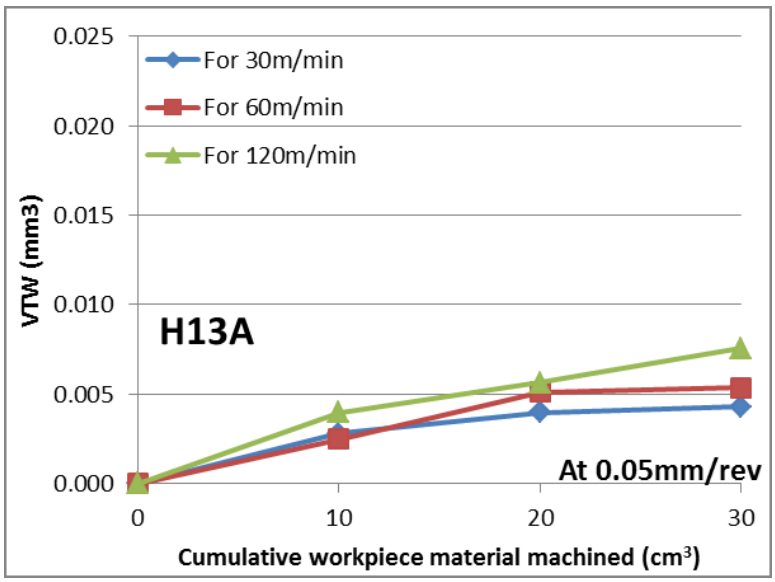

Figure 5-39: Volumetric tool wear of the H13A grade insert at a feed rate of 0.05 mm/rev for different cutting speeds.

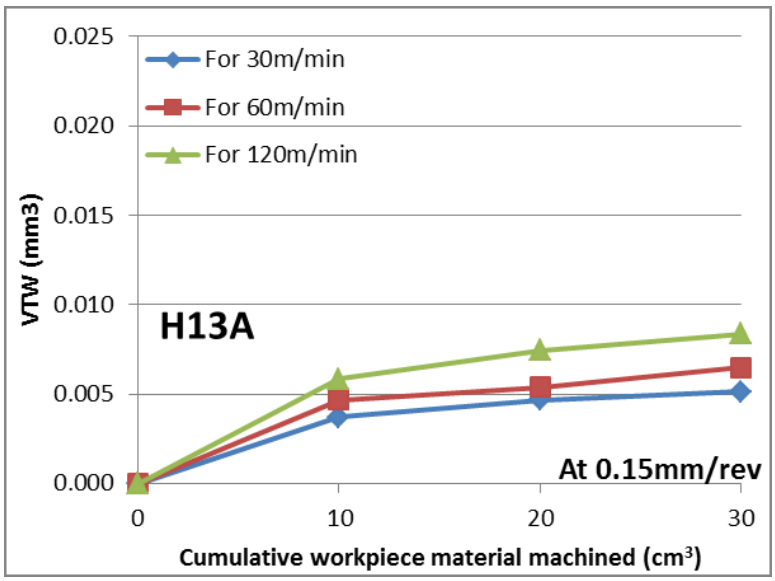

Figure 5-40: Volumetric tool wear of the H13A grade insert at a feed rate of 0.15 mm/rev for different cutting speeds.

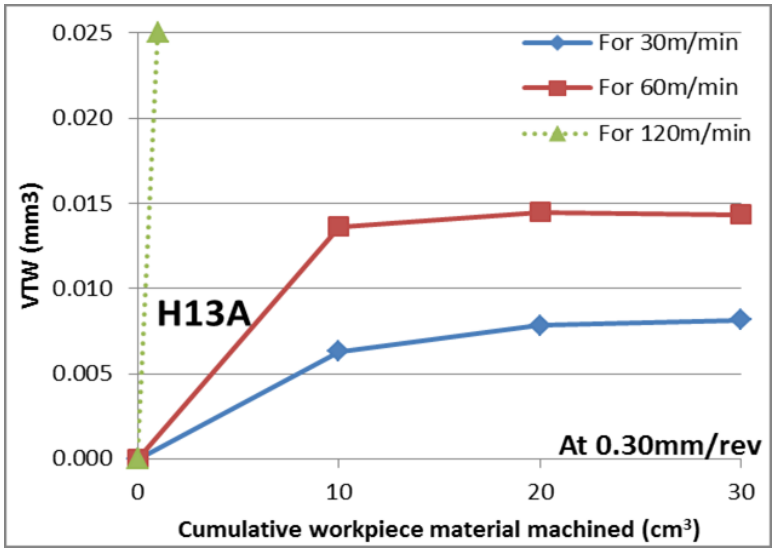

Figure 5-41: Volumetric tool wear of the H13A grade insert at a feed rate of 0.30 mm/rev for different cutting speeds. Note that the data point for a cutting speed of 120 m/min, though shown as 0.025 mm³, was actually catastrophically failed.

Again, as with the H10A grade inserts, the volumetric wear of all the inserts increased monotonically with stock material volume removed. Further, the volumes increased with increasing cutting speeds as well.

5.2.3 Comparison with Model-Predicted Tool Wear

The next step was to compare the model-predicted tool wear from RQ1 with the actual tool material volumes worn away. Note that the model predictions of tool wear are in the form of a wear depth in mm. However, these wear depths were computed by multiplying the cutting time with the wear rate. This wear rate was originally defined as the local volume loss rate on a tool face per unit area per unit time. Hence, the wear depth predicted by the comprehensive model is in fact a representation of the volume

loss of the tool. This is the reason why this wear depth can be compared with the actual volumetric tool wear of the turning inserts. The plots follow:

5.2.3.1 H10A Inserts

The comparative plots of the actual VTW against the model-predicted tool wear values for H10A grade inserts are given below in Figure 5-42(A) through Figure 5-44(A). Figure 5-42(B) through Figure 5-44(B) show additional curves on the same plot for different weighting factors of microstructural wear mechanisms – this serves as a mini-sensitivity analysis of the weighting factor percentages to the actual volume of the tool worn away. The fit of each of these curves will be quantified in the next section.

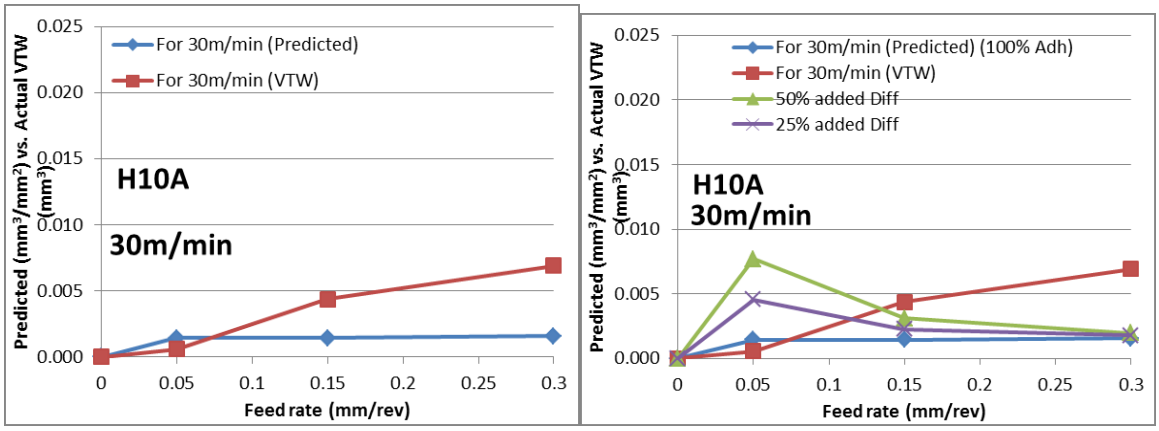

Figure 5-42: Comparison of the (A) actual VTW against the model-predicted tool wear at 30 m/min cutting speed for H10A grade inserts, (B) For different weighting factors.

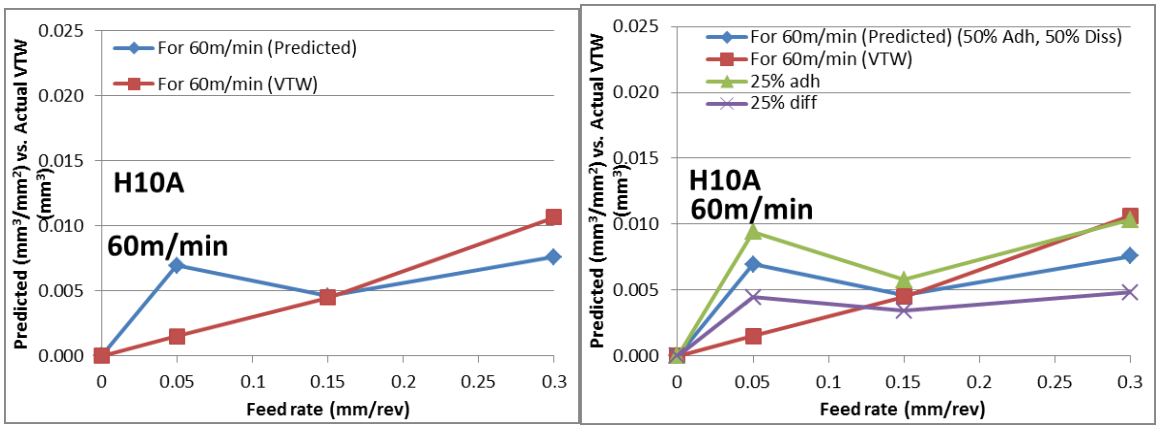

Figure 5-43: Comparison of the (A) actual VTW against the model-predicted tool wear at 60 m/min cutting speed for H10A grade inserts, (B) For different weighting factors.

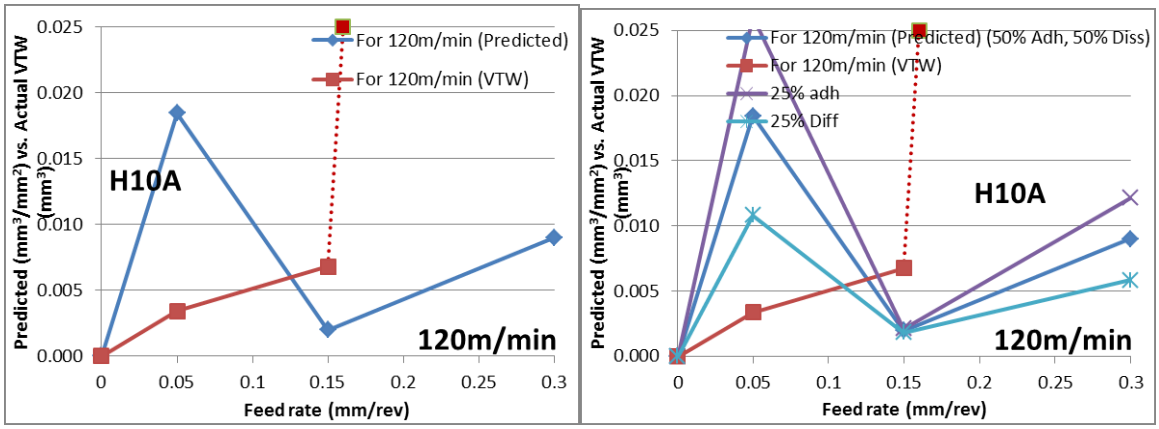

Figure 5-44: Comparison of the (A) actual VTW against the model-predicted tool wear at 120 m/min cutting speed for H10A grade inserts, (B) For different weighting factors.

From the plots it is seen that the model predictions are in the same order of the actual tool volume worn away. Further, the predicted wear curve fits well at low and medium surface speeds. The fit is quantified in the next section.

5.2.3.2 H13A Inserts

Similar plots of the actual VTW against the predicted wear for H13A inserts follow:

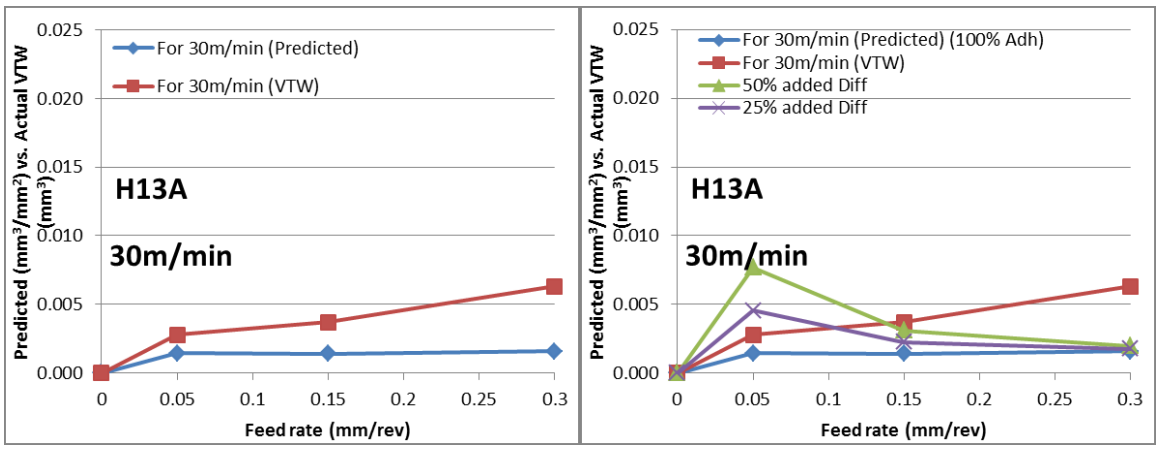

Figure 5-45: Comparison of the (A) actual VTW against the model-predicted tool wear at 30 m/min cutting speed for H13A grade inserts, (B) For different weighting factors.

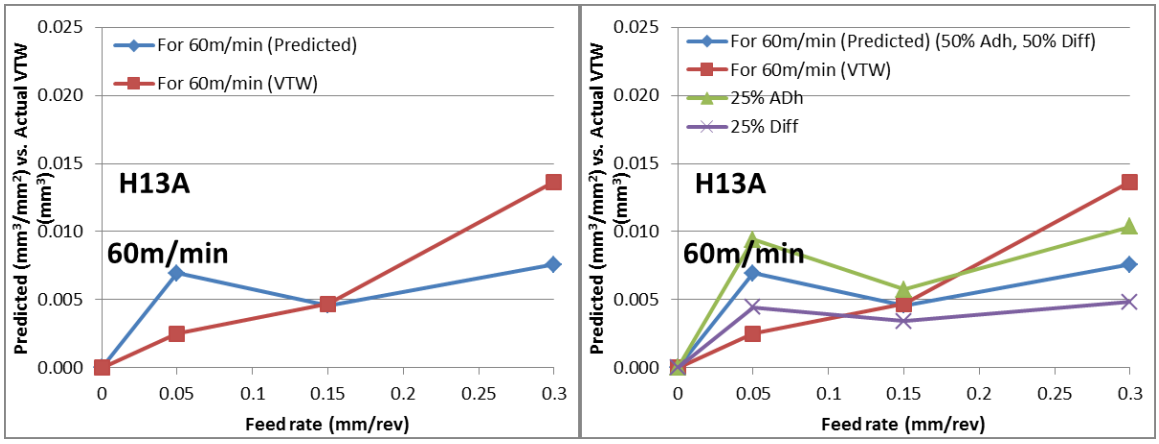

Figure 5-46: Comparison of the (A) actual VTW against the model-predicted tool wear at 60 m/min cutting speed for H13A grade inserts, (B) For different weighting factors.

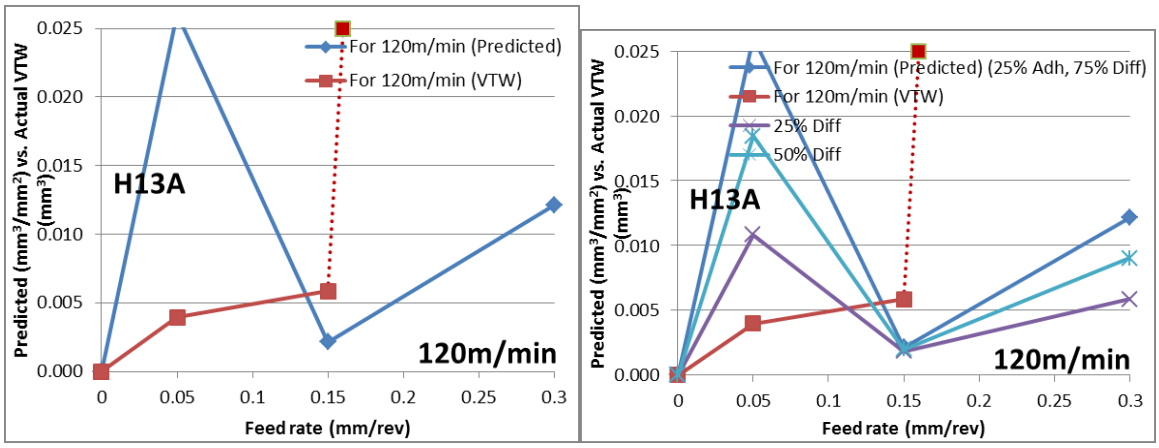

Figure 5-47: Comparison of the (A) actual VTW against the model-predicted tool wear at 120 m/min cutting speed for H13A grade inserts, (B) For different weighting factors.

For both H10A and H13A grade inserts, it can be seen than the model predictions are in the same order of the actual tool volume worn away. Further, the predicted wear curve fits well at low and medium surface speeds (The fit is quantified in the next section). Also, though the VTW values increased consistently with cutting feed and cutting speed, the predicted values sometimes dipped for the case of mid-level feeds for 60 and 120m/min cutting speed. Note that this could be because the transitions happening in the wear maps are around these values, requiring the weighting factors at these cutting conditions to be refined. Further, since the whole design space was sectioned into three discrete regions of feed and speed, there could be wear mechanism dominance changes in between each of these largely spaced data points.

5.2.4 Goodness of Fit

A simple approach to measure the goodness of fit of the model predictions to the actual volumetric tool wear values can be accomplished by doing a sum-of-squares (SS). This is essentially the sum of the squares of the vertical distances of each predicted point from the data point of actual wear. Non-linear regression can be done after this by simply varying the variables to minimize the SS, or in other words, doing least squares.

Table 5-9 tabulates the sum-of-squares for H10A grade inserts in all three speed regimes. The first column under each speed (*) denotes the weighting factor determined from SEM/EDS analysis. The remaining two columns are two variations of the weighting factors to quantify prediction sensitivity. The sum-of-squares (SS) in the last row denotes the fit of each data point (Note that the unit of the SS row is $(mm^3)^2 * 10^{-6}$).

Table 5-9: Sum-of-squares for H10A grade inserts for each speed-regime.

	30m/min			60m/min			120m/min		
	100% Adh (*)	75% Adh	50% Adh	50% Adh (*)	25% Adh	75% Adh	50% Adh (*)	25% Adh	75% Adh
0.05	0.0000008	0.0000508	0.0000160	0.0000295	0.0000627	0.0000086	0.0002263	0.0005127	0.0000554
0.15	0.0000087	0.0000016	0.0000044	0.0000000	0.0000017	0.0000011	0.0000229	0.0000214	0.0000244
0.3	0.0000284	0.0000243	0.0000263	0.0000093	0.0000001	0.0000338	0.0002560	0.0001652	0.0003667
S-S	3.8	7.7	4.7	3.9	6.4	4.4	50.5	69.9	44.7

From the above table it can be seen that at low and medium surface speeds, the fit of the predicted values to the actual volumetric tool wear is much better than that at high surface speeds. Further, the weighting factors that were deduced from SEM/EDS analysis (first column) had the lowest sum-of-squares for low and medium speeds providing a confirmation that they were selected right.

5.3 CONCEPT OF THE M-RATIO

Having the capability to quantify the volume of work machined with respect to the volume of the tool worn away, a concept similar to G-ratio in grinding can be introduced [18, 156]. It is termed the M-ratio and is defined as:

$$M\text{-}ratio = \frac{Volume\ of\ Material\ Machined}{Volume\ of\ Tool\ Insert\ Worn} \tag{5.11}$$

Previous experimental work with the M-ratio [18] showed a general pattern of an initial sharp decline and then a tendency to level off. As mentioned before, the M-ratio represents the changing efficiency of a cutting tool insert during each milling pass. As wear progresses, the cutting efficiency was typically seen remain fairly steady. Figure 5-48 is a plot of the M-ratio against the cumulative stock material removed (MR) for the 2^2 full factorial DOE setup in Table 5-2, and Table 5-10 tabulates these M-ratio values against the cumulative stock material volume removed by the tool.

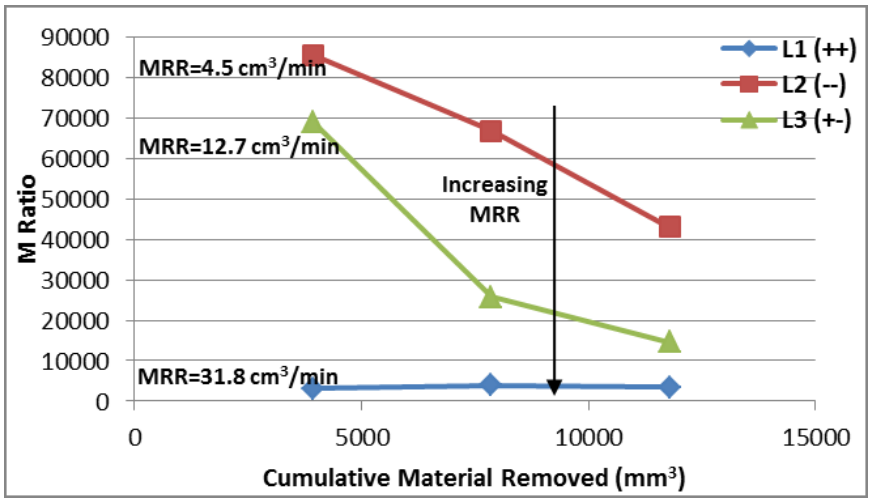

Figure 5-48: The Correlation of the M-ratio with MRR

The trends mentioned before are evident from Figure 5-48 - a decreasing M-ratio with the cutting length, portraying the decreasing efficiency of the tool in removing unit volume of workpiece material, and a tendency to level off as the wear progresses. Note that, each of the three curves in the above plot is a line of constant MRR. The drastic decrease in the M-ratio with an increasing MRR, (intuitively) suggests that it is more beneficial to the tool (not necessarily productivity) to remove work material at lower MRRs – this maintains the tool efficiency, *i.e.,* the wear (accumulation) is lesser.

Table 5-10: M-ratio Against the Cumulative Stock Removed

Pass	Cumulative Stock Volume Removed	M-ratio (Stock removed/Tool worn)			
		Setup 1	Setup 2	Setup 3	Setup 4
		++ (L1)	-- (L2)	+- (L3)	-+ (L4)
1	3931.92	3059.86	85476.52	68981.05	Tool Failure
2	7863.84	4022.42	66642.71	25783.08	
3	11795.76	3397.40	43050.22	14616.80	
MRR (cm^3/min)		31.8	4.5	12.7	11.1

Further, on comparing the volumetric wear values from Table 5-5 with the associated photo-micrographs [18], it was observed that the instances where the M-ratio had 'leveled off' were actually instances when the tool wear status had progressed beyond traditionally specified wear limits (*VB*) – this suggests that the actual usable life of a tool can then be defined to be until the moment the rate of decrease of the M-ratio reduces below a pre-defined cut-off value or till a cut-off M-ratio itself. This makes sense since the actual usable tool life is defined in terms of its efficiency in removing work material, rather than being based on a tool geometry related metric.

5.4 Dominant Profile Evolution Trends

In addition to the absolute volumetric tool wear in mm^3, the evolution of the volumetric wear profile needs to be quantified as well for better assessing the tool wear condition. For this purpose, a set of geometric coefficients are defined for capturing the evolution of the volumetric wear profile. Note that, the choice of these coefficients will depend on the type of cutting insert to be evaluated, and these may or may not be orthogonal to each other. These coefficients are then compared with the primary process factors to determine any dominant profile evolution trends.

For the selected milling insert, two coefficients (*fa, fb*) that lie on the 'flank face plane' are selected as shown in Figure 5-49. The third coefficient (*fc*) is defined as the deepest dimension extending into the tool body, similar to as in Figure 5-51. The basic idea is to track the evolving wear profile using the axes of a half or quarter ellipsoid (Figure 5-50).

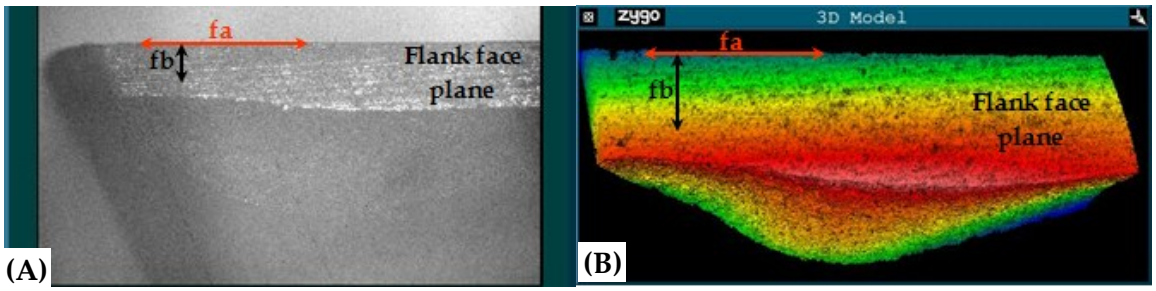

Figure 5-49: Geometric Coefficients Defined on 'Flank Face Plane' for Wear Tracking: (A) Intensity map, (B) 3D model

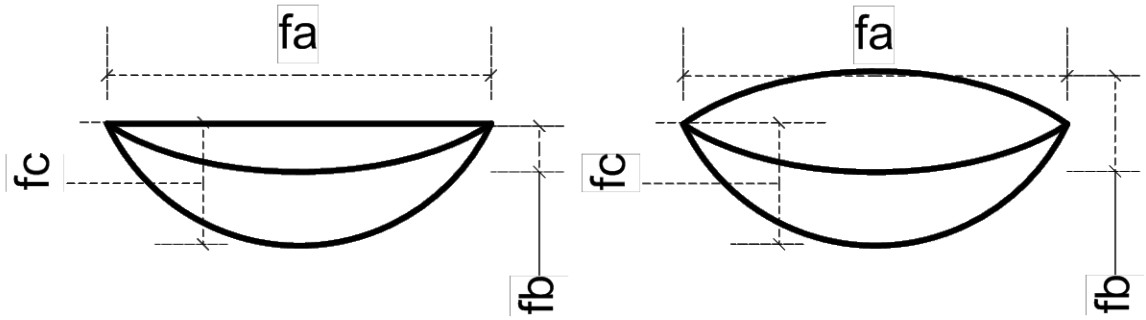

Figure 5-50: Wear profile evolution can be tracked using the axes of a half/quarter ellipsoid.

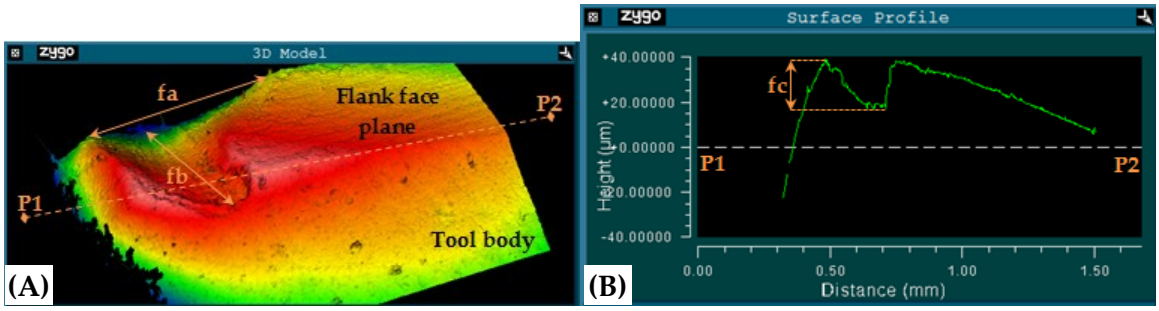

Figure 5-51: Geometric Coefficient Defined into the Tool Body for Wear Tracking: (A) 3D model, (B) Surface profile

These three geometric coefficients were tabulated for each of the four milling inserts at the end of each pass. The averages of all these four inserts were calculated, and the evolution was plotted in Figure 5-52. It is seen that the selected geometric coefficients increase consistently with time and with stock-material volume. It is also observed that the data points of all three coefficients are clustered individually. Further, the *fa* dimension had the maximum values – this is a strong factor of the cutting depth which was 2 mm in this study, and hence cutting depth contributed significantly to wear volume in milling. Another important fact is that the total volume obtained by the

product of these three coefficients will be different from the earlier calculated volumes – this is because, the coefficients serve to approximate the wear volume as half-ellipsoids. A related line of study involves assessing the error induced by approximating the volume with geometric coefficients, and tuning the volume shape and other parameters for better accuracy. Also, note that in some cases, the geometric coefficient *fb* will be equal to the traditional flank wear metric VB_{Bmax}. Thus, VTW and profile evolution capture wear effectively.

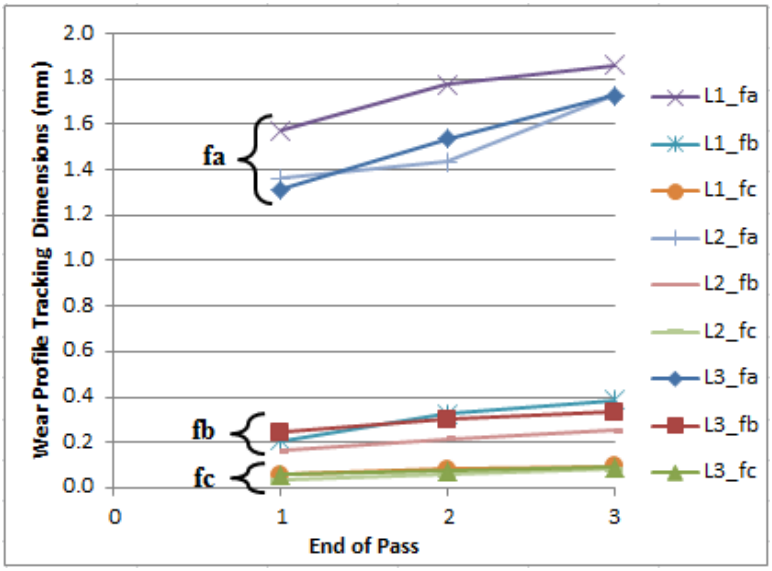

Figure 5-52: Evolution of the Average of the Set of Geometric Coefficients for Each Pass

5.5 Discussion of Results

The main conclusions from this chapter and a discussion of the results follow:

- A qualitative assessment of the inadequacies of the current manner of tool wear representation was conducted thereby highlighting the need for developing a more comprehensive approach of tool wear characterization.

- A methodology for characterizing the volumetric wear of cutting inserts used for machining titanium alloys was developed. The resolution and variability of the measurement system was shown to be good using a gauge R&R study.
- Looking at the variation of VTW from an MRR standpoint, a direct correlation between VTW of WC-Co tools and the MRR of Ti-6Al-4V emerged. This correlation was a of a second order dependence.
- A similar correlation emerged between the VTW rate and the MRR, which was of a second order as well. These dependencies were solved to obtain an exponential dependence of VTW with time or the stock volume removed. Further, the VTW rate was found to have a dependency on the accumulated wear itself. This could possibly explain some of the catastrophic failures of WC tools used for machining Ti-6Al-4V.
- The high feed low speed design space corner in turning as well as in milling was found to be a catastrophic feed-speed condition.
- An inverse dependency of the M-ratio on the MRR was observed which denoted the dropping efficiency of the cutting tool. The actual usable too life could then be defined as a function of a limiting M-ratio or as a function of ta limiting rate of decrease of the M-ratio. The tool life could then be defined on the basis of its efficiency in removing stock material rather than a geometry metric as is traditionally done.

- For both H10A and H13A grade inserts, it was seen than the model predictions of wear were in the same order of the actual tool volume worn away. Further, the predicted wear fits well at low/medium surface speeds.
- The fit of the model to the actual wear data was quantified by a sum-of-squares tabulation. It was observed that at low and medium surface speeds, the fit of the predicted values to the actual volumetric tool wear is much better than that at high surface speeds. Further, the weighting factors that were deduced from SEM/EDS analysis had the lowest sum-of-squares for low and medium speeds providing a confirmation that they were selected right.
- When using geometric coefficient to track the VTW profile evolution, it was observed that the data points of all three coefficients clustered individually.

5.6 SUMMARY & TAKEAWAYS

This chapter served to answer RQ2. The objective of this chapter was to accurately quantify the bulk-3D wear volume and evolution of worn surfaces on complex tool geometries, and validate the model through physical cutting experiments.

A metrology procedure for accurately quantifying the volume of the tool worn away was developed. Using this methodology, the worn volumes of a DOE of machining runs was computed, and then compared with the model-predicted tool wear from the microstructural wear-mechanisms model. Predictions were in the same order of the actual tool volume worn away and fit well at low/medium surface speeds. The model fit

was quantified and wear profile evolution was tracked using a set of geometric coefficients. Thus, the microstructural wear-mechanisms predictive model was validated by developing and measuring the evolution of bul-3D wear.

CHAPTER SIX

6. CONCLUSIONS & FUTURE WORK

The objective of this research work was to create a comprehensive microstructural wear mechanism-based predictive model of tool wear in the tungsten carbide / Ti-6Al-4V machining tribosystem, and to develop a new topology characterization method for worn cutting tools in order to validate the model predictions.

This research work brought together the different microstructural wear mechanisms that significantly affect the WC-Co / Ti-6Al-4V machining tribosystem, and then formulated a weighting scheme to capture the evolving dominance of each mechanism or their combinations. By doing so, the volume of the cutting tool worn away under each operational condition was predicted, with better model fit in the low and medium surface speed regimes. Further, the dominance of adhesion at lower surface speeds and of dissolution wear with increasing surface speeds, as well as their transitions for two different sub-micron grained carbide tools was captured as a predictive aid in the form of wear mechanism maps.

On the macro-scale, an accurate quantification of bulk-3D wear through a topology characterization algorithm elevated tool wear from a 1D to 3D concept. MRR was found to be a more consistent wear-controlling factor over the traditional used cutting speed. Further, a ratio metric of stock volume removed to tool volume lost, termed the M-ratio, helped coin a more universal tool wear definition in terms of stock removal efficiency.

The two major materials science and engineering contributions from this work are:

1. A weighted model of microstructural wear mechanisms to predict 3D wear, and
2. A topology characterization method for quantifying wear in 3D.

Conclusions related to microstructural wear mechanisms include:

- Varying amounts of titanium were found adhered to the crater edges at all speeds. This was more prominent at low speeds, and decreased as the speeds increased. This is in conformance with the lower relative surface speed requirement for micro welds to form and rupture.
- In contrast, dissolution wear dominated with increasing speeds. This high temperature-controlled wear mechanism resulted in crater formation due to tool material being carried away with the chips.
- Thus, straight tungsten carbide wear when machining Ti-6Al-4V is mechanically-driven at low surface speeds and thermally-driven at high surface speeds.
- The smooth surface in the crater showed a dominance of tungsten and cobalt, with sparse distributions of carbon. This suggests that carbon diffuses to the tool surface and gets carried away by the rubbing action of the chips.
- At high surface speeds, carbon from the tool was found diffused into the adhered titanium layer to form a titanium carbide (TiC) boundary layer – this was seen as instances of TiC build-up on the tool edge. This build-up originated from the tool rather than the chip, since it is in the opposite direction to chip flow.

- At low and medium feeds, notch discoloration was observed – this was detected to be carbon from EDS analysis, meaning that it was deposited from the edges of the passing chips.
- No indication of abrasive wear was observed (scratches in chip flow direction).
- A complex wear mechanism interaction was observed, *i.e.*, titanium adhered on top of an earlier worn out crater, additional carbon diffused into this adhered titanium layer to create a more stable boundary layer, and then all were further worn away by dissolution wear as surface speeds (temperatures) increased.
- At the high feed rate, no carbon discoloration was observed, while built-up-edges (BUE) were formed on the tool edges.
- Mapping the dominant wear mechanisms showed the increasing dominance of dissolution wear with increasing grain size – this is because a 13% larger sub-micron grain results in a larger surface area of cobalt exposed to chemical action.
- Weighting factors for H10A grade (finer grain) inserts were: (*i*) In the low-speed regime, adhesion = 100%, (*ii*) In the medium-speed regime, adhesion = 50% and dissolution = 50%, and (*iii*) In the high-speed regime, adhesion = 50% and dissolution = 50%.
- Weighting factors for H13A grade (coarser grain) inserts were: (*i*) In the low-speed regime, adhesion = 100%, (*ii*) In the medium-speed regime, adhesion = 50% and dissolution = 50%, and (*iii*) In the high-speed regime, adhesion = 25% and dissolution = 75%.

- At the low-speed high-feed corner of the design space, chatter was experienced consistently. At the high-feed high-speed corner of the design space, catastrophic tool failures were experienced consistently – both were marked as failure zones.
- From wear mapping, it was seen that the main line demarking the two dominant wear mechanisms essentially represented the line separating high temperature controlled wear from the region of high mechanical load controlled wear. There were some regions of dominant wear mechanism transitions as well.
- In general, predicted diffusive wear depths were the least, followed by adhesive wear depths and then dissolution wear depths. On comparing weighted model-predicted wear to the actual tool volume worn away, predictions on the order of observed wear was achieved, with better prediction at low and medium speeds.

Conclusions related to macro-modeling/validation of volumetric wear include:

- Wear quantification through topology characterization elevated wear from a 1D to 3D concept.
- As expected the volumetric tool wear (VTW) of all inserts, milling or turning, increased consistently with the stock volume removed by the tool.
- A second order dependence of VTW and VTW rate with the material removal rate (MRR) emerged, suggesting that MRR is a more consistent wear-controlling factor instead of the traditionally used cutting speed.

- A predictive model for VTW was developed which showed its exponential dependence with workpiece stock volume removed.
- Both VTW and VTW rate were found to be dependent on the accumulated cumulative wear on the tool.
- The high feed low speed design space corner in turning as well as milling was found to be a catastrophic feed-speed condition.
- The inverse dependency of M-ratio on the MRR denoted the dropping efficiency of the cutting tool. The actual usable too life could then be defined as a function of a limiting M-ratio or as a function of a limiting rate of decrease of the M-ratio - this led to a more comprehensive tool wear definition based on tool efficiency.
- The geometric coefficients used for tracking VTW profile evolution, increased consistently with stock volume removed, besides clustering individually.

The original contributions (intellectual merit) from this work are:

- A weighted model of microstructural wear mechanisms to predict 3D wear,
- A validated topology characterization method for quantifying wear in 3D,
- A first universal quantification of machining tool wear without ambiguity,
- Predictive wear maps of dominant wear mechanisms for this tribosystem,
- Predictive maps of wear profile evolution trends for this tribosystem,
- Identification of MRR as the consistent wear-controlling variable, and
- Concept of the M-ratio as a versatile productivity parameter.

Considering the broader impacts, the commercial automotive industry has been reluctant to adopt titanium alloys in spite of its highly desirable material property combinations such as its high strength-to-weight ratio leading to proven energy/life-cycle savings [157-160]. One of the main reasons is its high processing cost, especially tooling cost. Validated VTW models will improve the understanding of this tribosystem's wear mechanics to facilitate more widespread use of titanium as an automotive material alternative. Such validated 3D wear models, besides providing a first universal tool wear definition, has potential to be incorporated into model-based predictive process-control in industrial applications.

The following future work is suggested so as to further this work:

- For a more quantitative representation of dominant wear mechanisms, software such as *ImageJ* could be used to obtain a better estimate of the wear area.
- Interactions between wear mechanisms could be exclusively studied.
- A data-point dense DOE could narrow the transition zones in the wear maps.
- Besides grain size, the effects of other important microstructural parameters such as cobalt distribution, contiguity, and binder mean free path need to be studied.
- Mass validations could be used in conjunction with VTW for modeling.
- Corner wear, though much lesser than crater wear could be quantified.
- Initial tests with high pressure coolant showed a drastic improvement in surface roughness – this could be explored.

APPENDIX A

A. SOFTWARE & HARDWARE CAPABILITIES PERTAINING TO THIS RESEARCH WORK

This appendix serves to briefly describe the capabilities and features of the special software packages and hardware used for this research work.

A.1 THIRDWAVE SYSTEMS ADVANTEDGE-FEM

AdvantEdge FEM software provides analysis of the machining process by modeling at the tool-workpiece level. The software embodies state-of-the-art finite element technology and material modeling for the accurate representation of cutting mechanics based on machining physics. Third Wave Systems (TWS) began developing AdvantEdge FEM to allow for very detailed modeling of the cutting tool edge effects, contact pressures and temperatures when machining titanium and aluminum stock. Subsequent enhancements have enabled the modeling of brittle workpiece materials such as silicon nitride and silicon carbide [161], along with many other hard metals. Model outputs include tool, workpiece, and chip temperatures, cutting forces, torque, power and workpiece quality characteristics such as residual stress, surface and sub-surface damage, and burr formation.

AdvantEdge FEM is an explicit dynamic, thermo-mechanically coupled finite element model specifically designed to analyze the machining processes. Features necessary to model machining accurately include the resolution of multiple length scales

(cutting edge radius, secondary shear zone and chip load), multiple body deformable contact for tool-workpiece interaction, and transient thermal analysis. Due to large deformations inherent with machining processes, it is crucial that computationally accurate finite element configurations are maintained; therefore, adaptive re-meshing techniques are employed within the analysis. For a comprehensive discussion on numerical techniques, see [162].

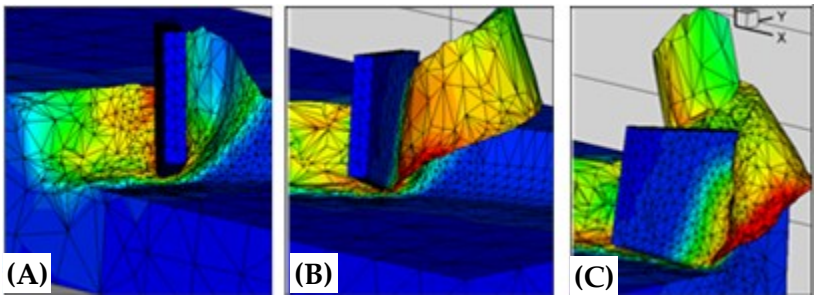

Figure 1: AdvantEdge FEM Machining Model of an Indexable End Milling Process with Temperature Contours Overlaid on the Workpiece: (A) Initial Chip Formation, (B) Complete Chip Formation, (C) Indexable Tool Exiting the Workpiece

A.2 HPC CLUSTER

The Palmetto Cluster is a supercomputer community resource, jointly funded by Clemson University and research grants secured by participating faculty. With over 14000 cores (1627 nodes) and a performance of more than 100+ trillion floating-point operations per second (teraFLOPS), the Palmetto Cluster is ranked number 6 among academic institutions in the country and number 96 worldwide on the June 2011 list of Top 500 Supercomputing Sites.

Clemson's high performance computing (HPC) resources includes a "condominium" style cluster, known as Palmetto, developed to serve the university's wide-ranging research needs. Developed by Clemson Computing and Information Technology (CCIT) in collaboration with faculty researchers across the university, the Palmetto Cluster provides a shared platform that optimizes resources for the benefit of all users. Named for South Carolina's state tree, the Palmetto Cluster is designed to suit different research applications, with a large number of powerful multi-core nodes, each with a significant amount of memory. The Palmetto Cluster is a Linux based system running Scientific Linux 6.1, which is a distribution of Linux maintained by FermiLab and Cern, http://www.scientificlinux.org/.

Figure 2: Clemson Palmetto High-Performance Computing (HPC) Cluster; This Top Global HPC Cluster is Available for Machining Simulation Studies to Generate Data for Input to the Developed Models

APPENDIX B

B. DOE STUDY FOR CHARACTERIZING FEED/SPEED DEPENDENCE (SIMULATIONS)

For characterizing the dependence of feed and speed, a parameter matrix of 12-runs was set up that was centered on the recommended range of cutting parameters for turning Ti-6Al-4V. Besides characterizing their behavior, the objective was to check whether they conformed to known machining trends.

Table 1: Parameter Matrix of 12 Runs Bordering the Feed-Speed Design Space

	0.05	0.15	0.25	f (mm/rev)
30	Run 1	Run 5	Run 9	
60	Run 2	Run 6	Run 10	
90	Run 3	Run 7	Run 11	
120	Run 4	Run 8	Run 12	
V (m/min)				

For this study, 12 input file sets were appropriately generated and successfully simulated in AdvantEdge FEM on a standalone machine at CU-ICAR. The temperature contour at the end of cut for run 1 (f = 0.05 mm/rev, V = 30 m/min), as well as filtered force, power and temperature plots with cutting length are show in Figure 1. For each feed-speed combination, peak temperatures, forces and power values were compiled. The simulation results for the peak temperatures (Figure 2), as well as the resulting variation of cutting and forces with cutting speed and feed rate are shown in Figure 3 and Figure 4, respectively.

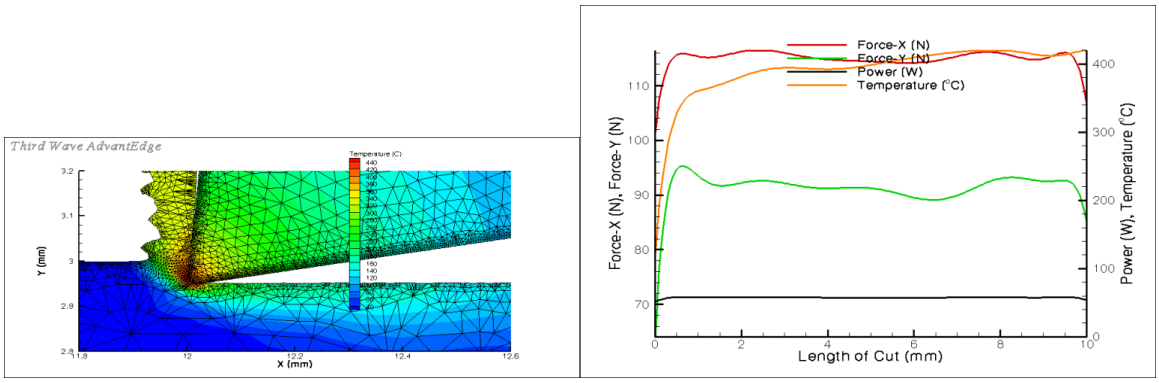

Figure 1: Temperature Contour and Force/Temperature Plots for Run 1

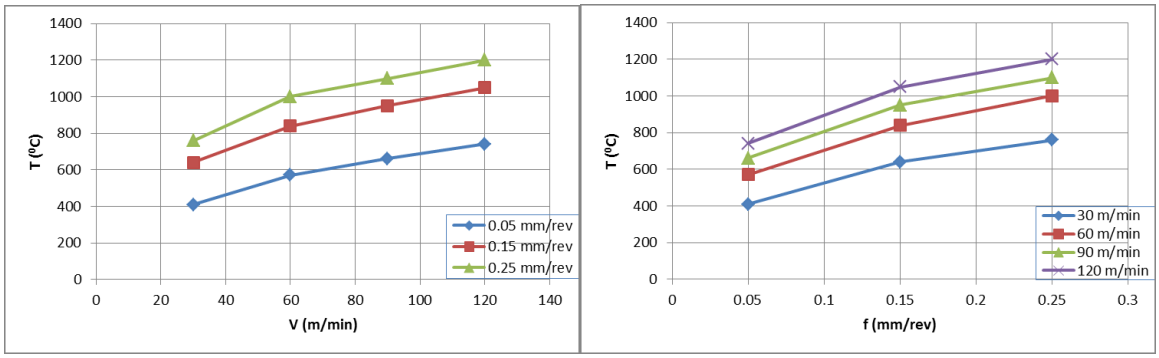

Figure 2: Peak Temperatures for Varying Feeds and Surface Speeds

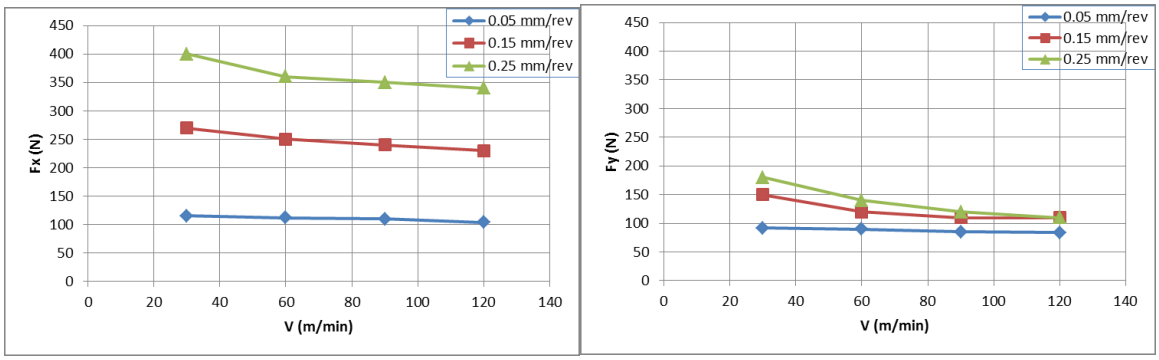

Figure 3: Peak Cutting and Feed Forces Declining with Surface Speed

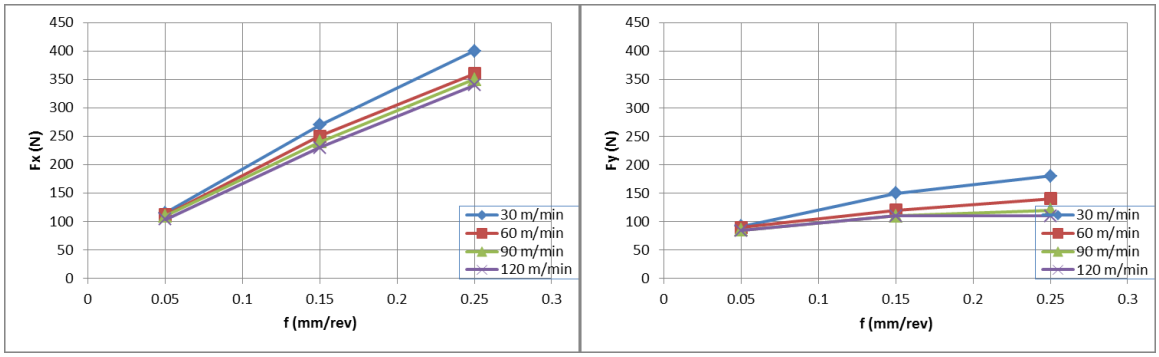

Figure 4: Peak Cutting and Feed Forces Increasing with Feed Rate

From these results, the main observations that can be drawn are:

- A general increase in temperature with increasing feed & cutting speed
- A slight reduction in cutting and feed forces with increasing cutting speed
- A larger increase in cutting and feed forces with increasing feed rate

The tool used for these simulation runs was a standard uncoated carbide (grade-K) tool with generic tool geometry as shown in Figure. For these dry (no coolant) simulation runs, the trends in peak forces and temperature were in conformance to known machining behavior and no anomalies were observed; this serves as a first-step validation of the simulation results.

APPENDIX C

C. DOE STUDY FOR CHARACTERIZING CUTTING DEPTH DEPENDENCE (CUTTING TESTS)

The third constituent of MRR besides cutting speed and feed rate is the depth of cut. Speed and feed rate dependence on the cutting process was characterized in the previous appendix. Depth of cut was found to be a one of the significant factors affecting the cutting forces and feed forces. However, it was found to be not very significant for the temperatures generated in the cut. This is evident from the regression analysis, as well as the corresponding plot of depth of cut against temperature as given below in Figure 1.

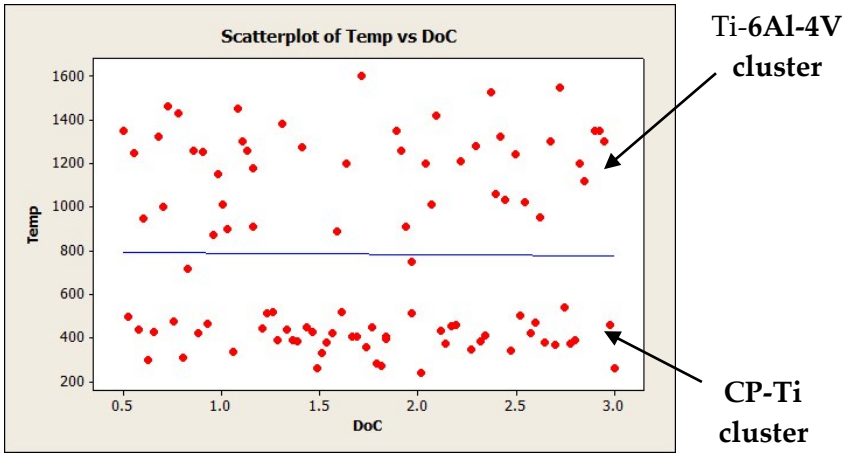

Figure 1: Scatterplot of depth of cut (*DoC*) against temperature from regression analysis. Note the weak correlation between the input cutting depth and output temperature.

Note that even though the data points of both alloys clustered separately, the cutting depth did not seem to have any significant influence on the peak steady-state

temperatures. Since tool failures during titanium machining are more influenced by the higher temperatures at the tool chip interface than the cutting forces, it can be safely assumed that cutting speed and feed rate have more influential on the wear process than depth of cut (Cutting forces/power requirements for machining titanium are lower than that of steel, and their specific cutting energies are comparable [51]). This is of course confirmed by the previous bivariate and regression analyses as well.

Based on the above determined lower significance of cutting depth, it would be beneficial to hold it constant throughout the final DOE of physical cutting experiments, both to reduce its "disturbance" effect on wear as well as to reduce the number of machining runs needed. Thus, for excluding cutting depth, an examination of the total energy expended when removing constant stock material volume at different cutting depths was conducted – the purpose of this was to confirm that there was no significant difference in the total work done in removing material at different cutting depths.

C.1 Cumulative Work vs. Depth of Cut in Turning

A 7-run cutting depth-dependent DOE was formulated for ascertaining the cumulative work done during cutting as a function of the depth of cut, as given below:

Table 1: The 7-run cutting depth-dependent DOE of cumulative work done in turning at the same MRR for removing the same stock material volume (MR) in the same time duration.

Run Info	Process Parameters			Material Removed (MR)			Cut Time
Run	DoC	f	V	MR	Total MR	MRR	Time
(#)	(mm)	(mm/min)	(m/min)	(mm^3)	(mm^3)	(mm^3/min)	(min)
1	0.5	80	60	2819.642	11278.57	2400	0.5
2	0.5	80	60	2819.642		2400	0.5
3	0.5	80	60	2819.642		2400	0.5
4	0.5	80	60	2819.642		2400	0.5
5	1	40	60	5639.284	11278.57	2400	1
6	1	40	60	5639.284		2400	1
7	2	20	60	11278.57	11278.57	2400	2

Based on the above tabulated 7-run DOE, physical cutting experiments were conducted on an OKUMA Space Turn LB4000-EX lathe. Some relevant cutting conditions follow: Workpiece material used was Ti-6Al-4V, Total feed length was 40 mm along the length of the workpiece, The cutting inserts used were Sandvik CNMG 12 04 08-QM (H13A grade) straight uncoated carbide inserts, Cutting condition was dry, and new inserts were used for each machining setup to minimize the effects of wear. The inserts were examined after the cuts and the accumulated wear on each of them was determined to be not significant.

The cutting and feed forces, as well as the power and representative temperature for turning run #7 is shown below in Figure 2.

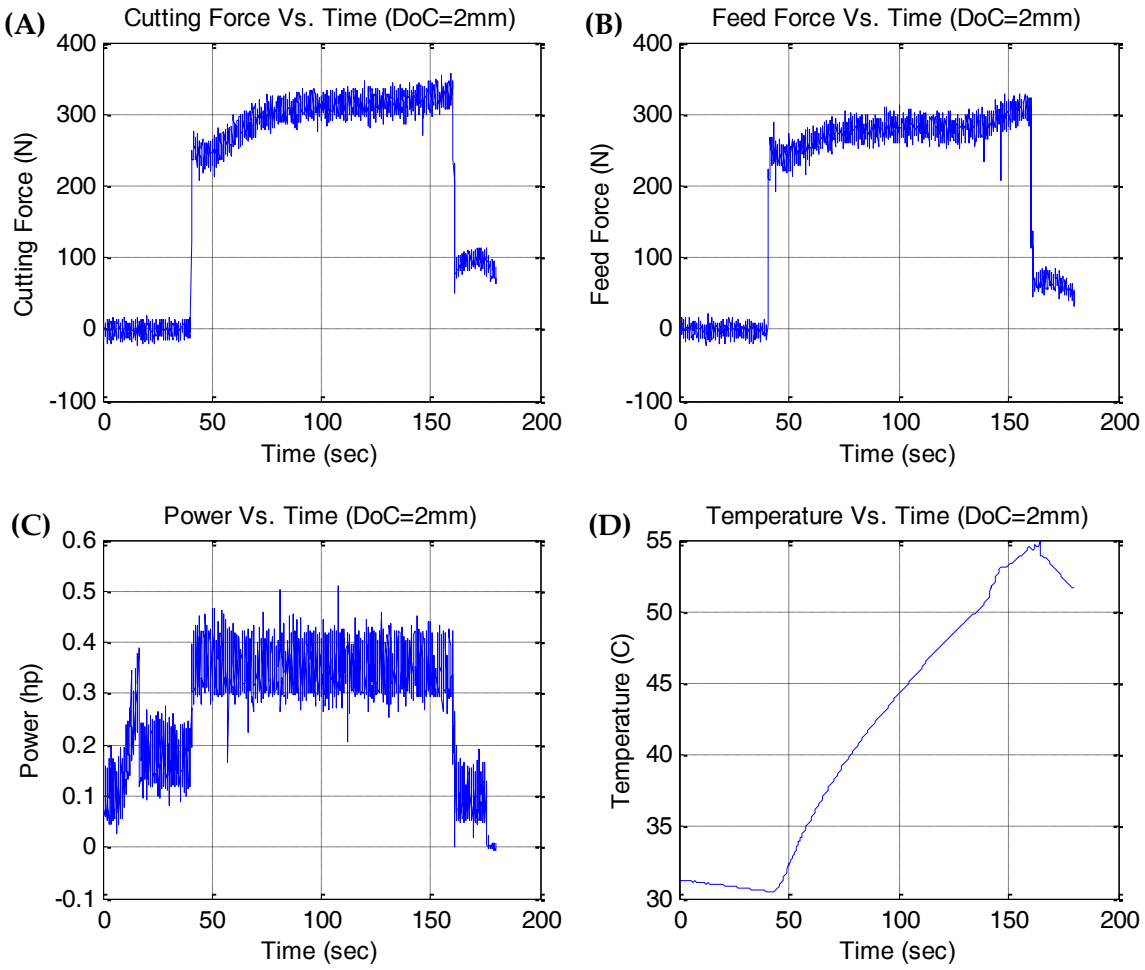

Figure 2: Process variables acquired during run #7 (Cutting depth of 2mm, and the complete stock material volume removed in 1 pass): (A) Cutting force, (B) Feed force, (C) Power, (D) Representative temperature rise

Following the cutting experiments, the power expended by the lathe spindle (Figure 2(C)) was compiled together for each cutting condition, *i.e.*, the power data for runs 1 through 4 were concatenated with each other, power data for runs 5 and 6 were concatenated, and power data for run 7 was maintained as it is. The purpose of this was to integrate the power needed by the spindle over the whole cutting time to obtain the

work done or energy expended in removing the constant volume of the stock material. Then, the cumulative work done for each of the three machining setups were plotted as shown in Figure 3 to compare the energy expended as a function of cutting depth.

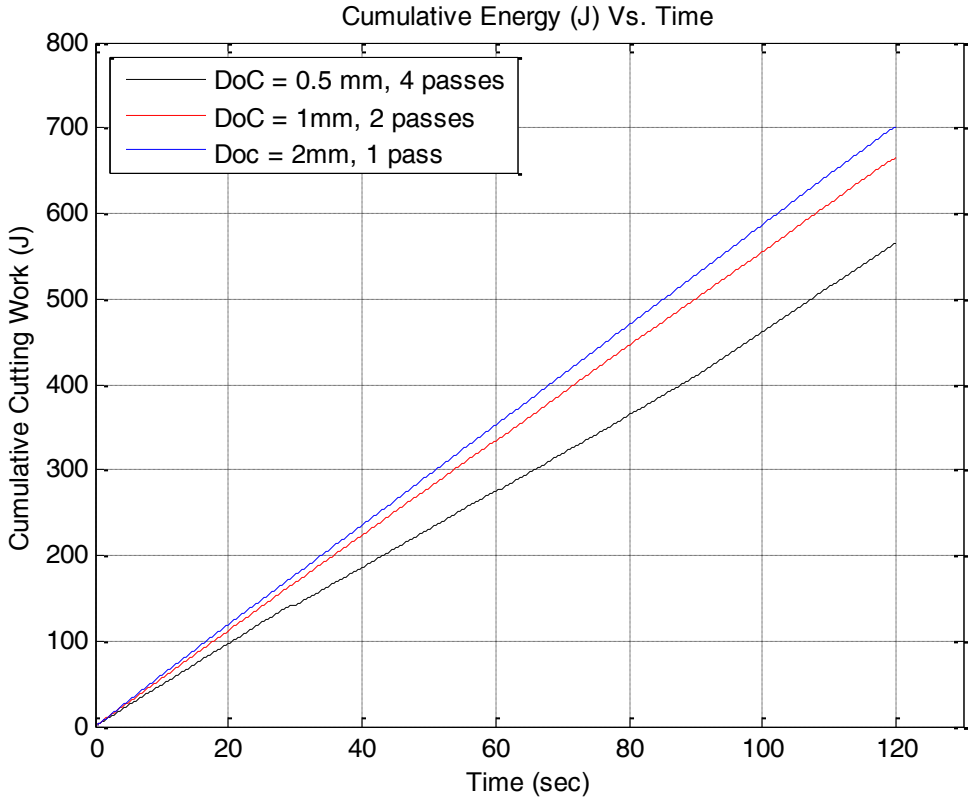

Figure 3: Cumulative work (energy) expended to remove a constant volume of workpiece material as a function of cutting depth. It can be seen that the total energy needed in all three machining setups was comparable, confirming that cutting depth differences do not result in a significant difference in the energy expended for removing constant stock volume.

From the above plot (Figure 3), it is seen that the cumulative work expended or average power required was about the same for removing a constant volume of stock material in the same time and at the same MRR, but at three different cutting depths;

only feed rates were varied accordingly. Based on this, cutting depths were held constant at 2mm for the final DOE of cutting experiments in this work.

C.2 Cumulative Work vs. Depth of Cut in Milling

Even though the modeling and validation runs of this work are for turning experiments, a similar treatment as the above was conducted for milling as well to ascertain the cumulative work done during cutting as a function of the depth of cut. For this, a 14-run cutting depth-dependent DOE of milling runs was set up as given below:

Table 2: The 14-run cutting depth-dependent DOE of cumulative work done in milling at the same MRR for removing the same stock material volume (MR) in the same time duration.

Run Info	Process Parameters			Material Removed (MR)			Cut Time
Run	DoC	f	V	MR	Total MR	MRR	Time
(#)	(mm)	(mm/min)	(m/min)	(mm^3)	(mm^3)	(mm^3/min)	(min)
1	0.5	400	60	737.235	5897.88	12000	0.387
2	0.5	400	60	737.235		12000	0.387
3	0.5	400	60	737.235		12000	0.387
4	0.5	400	60	737.235		12000	0.387
5	0.5	400	60	737.235		12000	0.387
6	0.5	400	60	737.235		12000	0.387
7	0.5	400	60	737.235		12000	0.387
8	0.5	400	60	737.235		12000	0.387
9	1	200	60	1474.47	5897.88	12000	0.774
10	1	200	60	1474.47		12000	0.774
11	1	200	60	1474.47		12000	0.774
12	1	200	60	1474.47		12000	0.774
13	2	100	60	2948.94	5897.88	12000	1.548
14	2	100	60	2948.94		12000	1.548

Based on the above tabulated 14-run DOE, physical cutting experiments were conducted on an OKUMA MB-46VAE 3-Axis Vertical Machining Center (milling machine). Some relevant cutting conditions follow: Workpiece material used was Ti-6Al-4V, Total cutting length was 154.8 mm across the plate, Radial immersion was half at a cutting width of 9.525 mm, spindle speed was 100 rpm (60 m/min constant), Type of milling was conventional (up milling), The cutting inserts used were Iscar HM90 APCR 100304PDFR-P (IC928 grade) coated carbide inserts, 2 inserts were used per cut, Cutting condition was dry, and new inserts were used for each machining setup to minimize the effects of wear. The inserts were examined after the cuts and the accumulated wear on each of them was determined to be not significant.

The cutting torque for milling run #7 is shown below in Figure 4. From the cutting torques, the instantaneous power (Figure 5), and thereby work done in cutting a constant volume of workpiece material away was calculated. This was done by concatenating the torque data (as in the previous section for turning), integrating the torques over the time in cut, and multiplying it with the angular velocity of the milling tool to obtain the total work done; this can be better understood by the following equation:

$$\omega * (Area\ under\ Torque - Time\ plot) = \omega \int Tdt = \int (T\omega)dt = \int Pdt = \Delta W \tag{4.12}$$

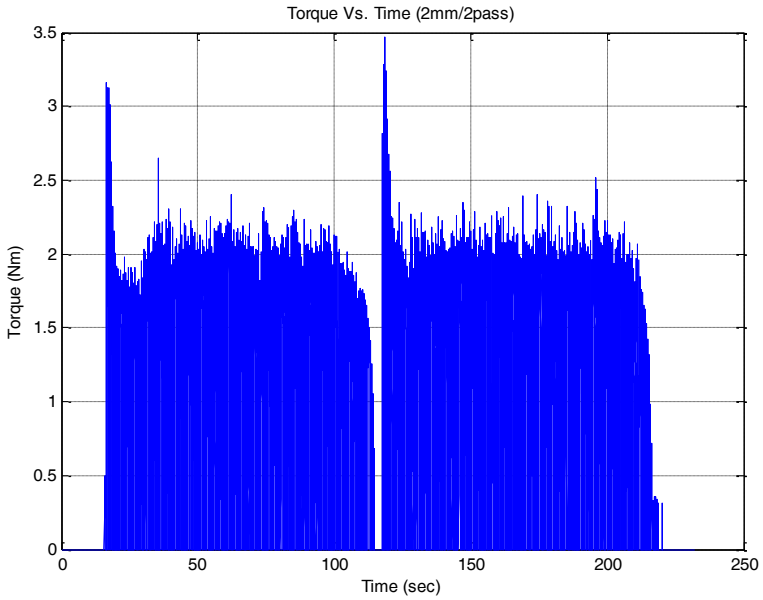

Figure 4: Cutting torque needed by the milling spindle during run #7 (Cutting depth of 2mm and the complete stock material volume removed in 1 pass).

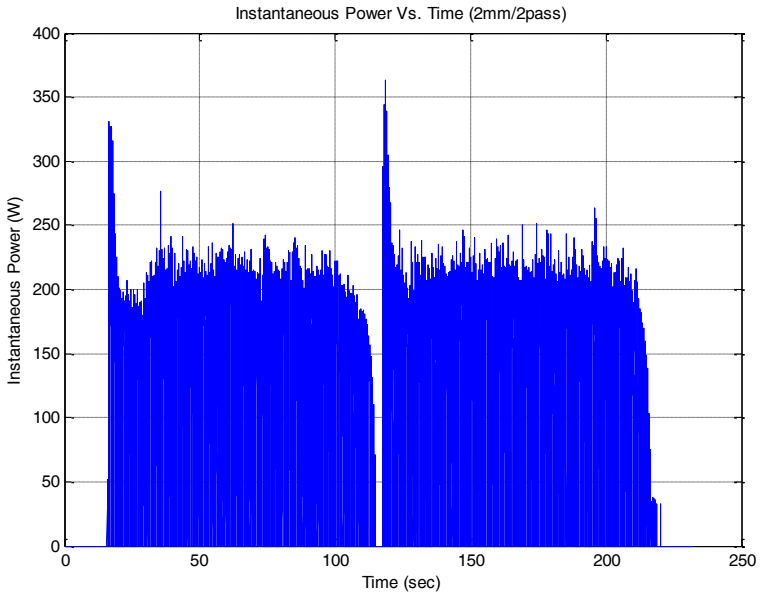

Figure 5: Instantaneous power needed by the spindle for run #7 (calculated from torque) (Cutting depth of 2mm and the complete stock material volume removed in 1 pass).

Then, the cumulative work done for each of the three machining setups were plotted as shown in Figure 6 to compare the energy expended as a function of cutting depth.

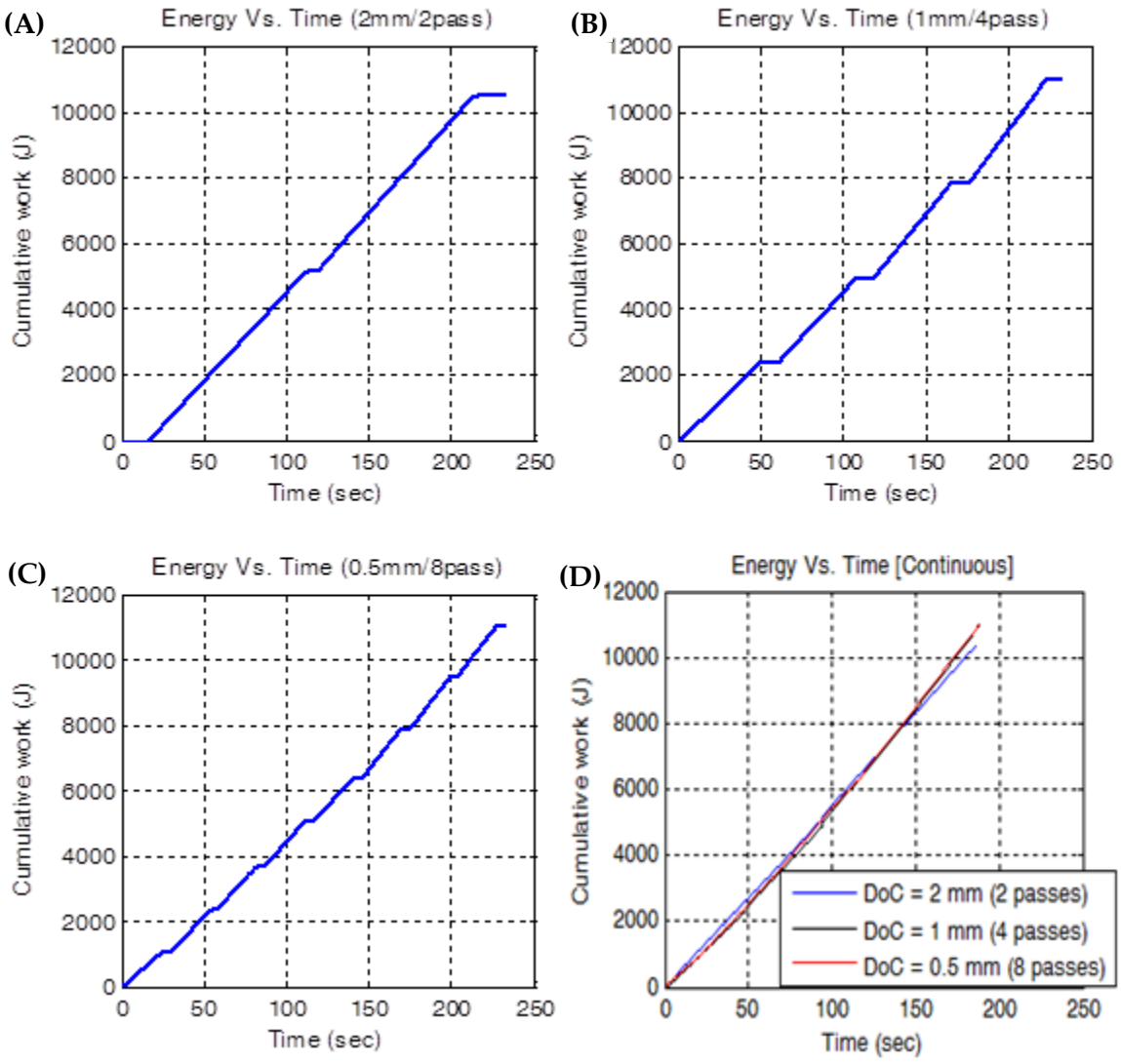

Figure 6: Cumulative work (energy) expended to remove a constant volume of workpiece material in milling as a function of cutting depth. Cumulative work done during: (A) Runs 13 through 14 (2 mm DoC), (B) Runs 9 through 11 (1 mm DoC), (C) Runs 1 through 8 (0.5 mm DoC), and (D) Superimposed cumulative energy plots for each of the 3 milling setups. It can be seen that the total energy needed was comparable in all 3 milling setups.

From the above plot (Figure 6), it is seen that the cumulative work expended or torque required was about the same for removing a constant volume of stock material in the same time and at the same MRR, but at three different cutting depths; only feed rates were varied accordingly. Based on this analysis, cutting depths were held constant.

APPENDIX D

D. TOOL GEOMETRY CHARACTERIZATION

D.1 TOOL GEOMETRY CHARACTERIZATION – ANGLE BETWEEN RAKE & RELIEF FACES

To model the tool in Abaqus, certain unknown tool geometries needed to be determined first. The first one was the angle that the rake face makes with the flank face, *i.e.*, the included angle between the rake and flank faces. For this, a new insert was inspected under a Zygo NewView 7200 3D optical surface profiler. The following figures depict the procedure.

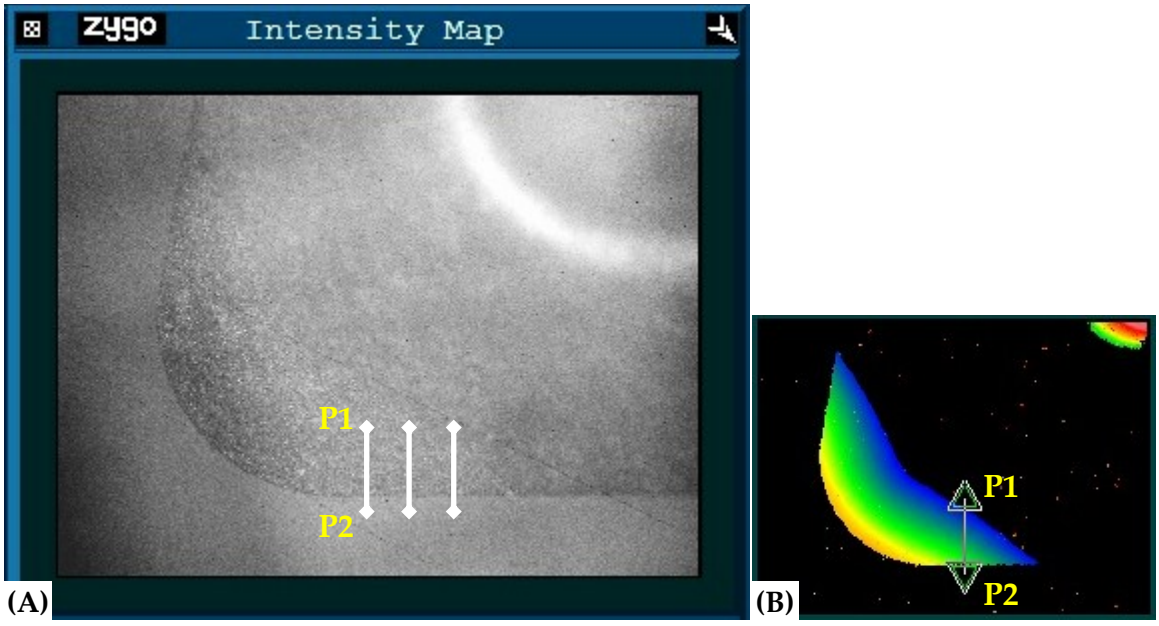

Figure 1: Top view of the rake face of a new turning insert. (A) On an auto-leveled stage (horizontal), three lines were drawn to across the rake face. Note that the flank face (bottom edge in figure) was perpendicular to the stage. (B) The contour plot shows the first drawn line and the next two figures show the measurement procedure.

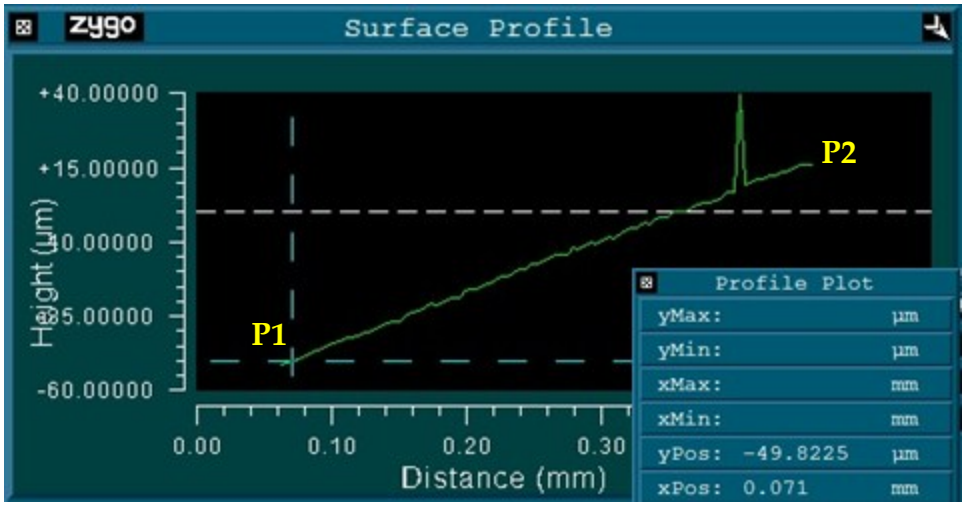

Figure 2: Inspector for measuring the coordinates for P1

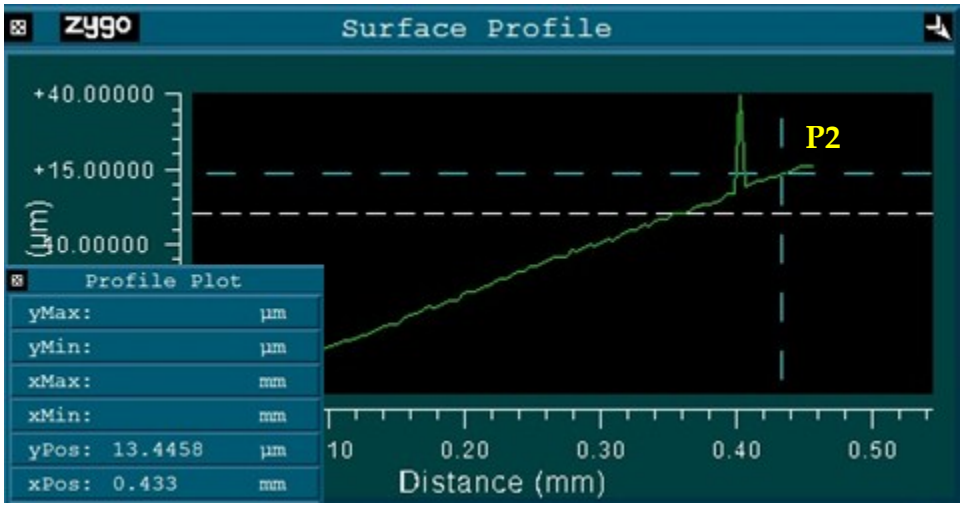

Figure 3: Inspector for measuring the coordinates for P2

Basic calculations were performed for estimating the angle as shown in Table 1. An average of 3 measurements was taken as the value of the included angle between the flank and rake faces; this was calculated to be 80.34^0.

Table 1: Calculation of the included angle between the rake and flank (relief/clearance face) faces for the H10A/H13A grade inserts used in this work.

#	Data File	x_1 (mm)	y_1 (μm)	x_2 (mm)	y_2 (μm)	$\text{Tan}(\theta)=(y_2-y_1)/(x_2-x_1)$	θ
1	Rake_X+1	0.071	-0.0498	0.433	0.0134	0.1748	9.91
2	Rake_X+2	0.075	-0.0528	0.517	0.0174	0.1586	9.01
3	Rake_X+3	0.159	-0.0594	0.729	0.0417	0.1772	10.05
Angle between Rake & Relief Faces = 80.34^0						**Average**	**9.66**

D.2 Tool Geometry Characterization – Tool Edge Radius

The next geometry feature that needed to be estimated was the tool edge radius. Note that this is different from the nose radius which is known. For this, a new insert was again inspected under a Zygo NewView 7200 3D optical surface profiler after orienting it appropriately. The following figures depict the procedure. In this case the cutting edge radius of the H10A/H13A grade inserts used in this work was estimated to be 5.33 μm.

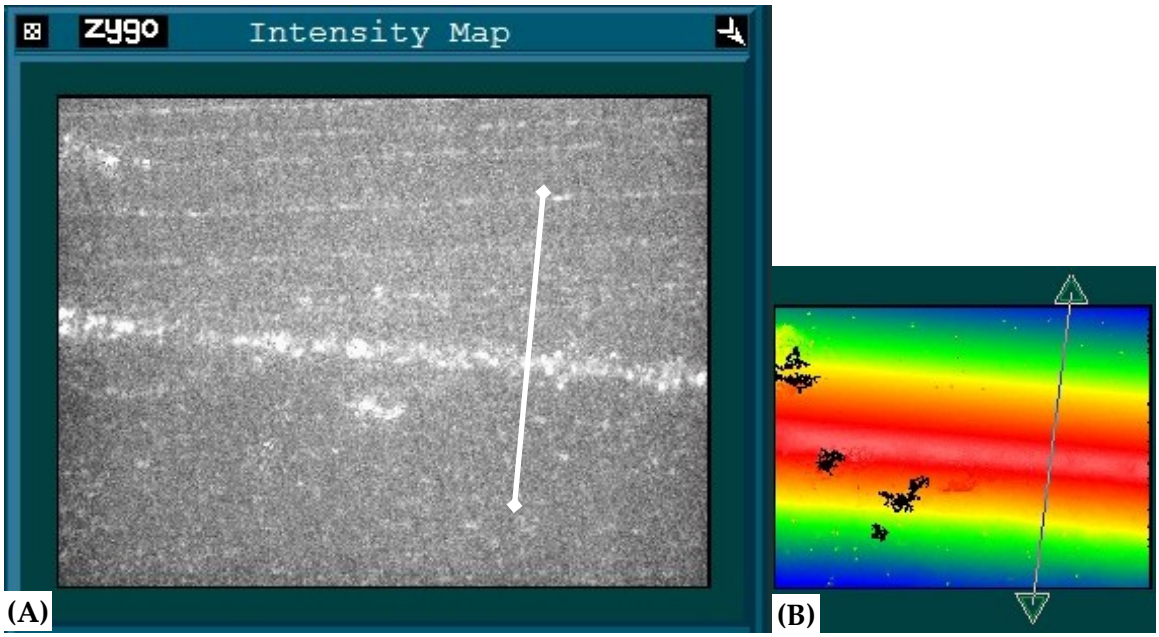

Figure 4: Top view of the cutting edge of a new turning insert. (A) On an auto-leveled stage (horizontal), one line was drawn to across the cutting edge. Note that the rake face was the top portion and flank face was the bottom portion. (B) The contour plot shows the drawn line and the next figure show the measurement procedure.

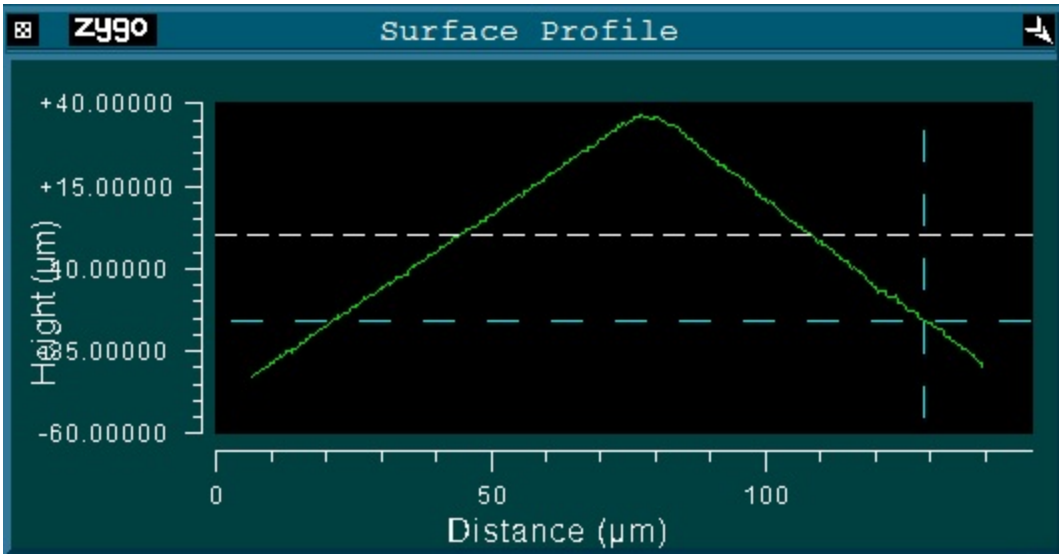

Figure 5: Surface profile of the cutting edge showing the edge radius.

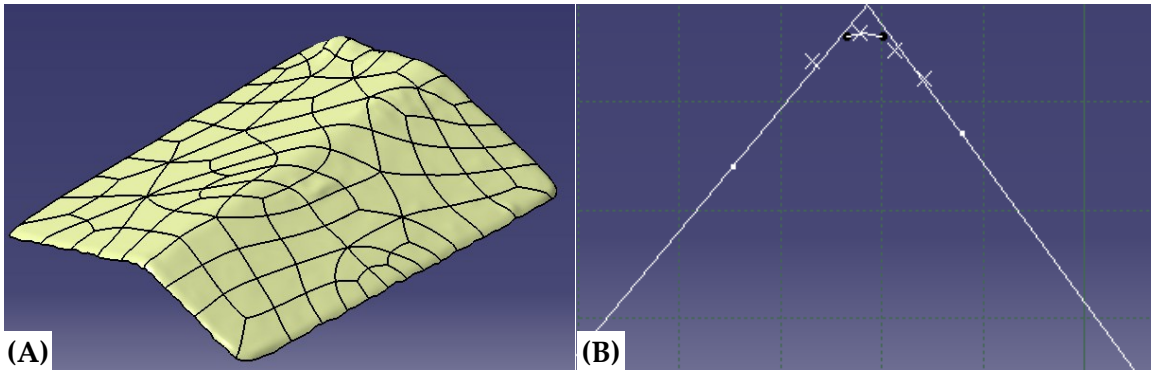

Figure 6: The surface profile was imported into (A) CAD software, and (B) points traced to estimate the cutting edge radius.

Table 2: Calculation of the cutting edge radius of the H10/H13A inserts used in this work.

#	x	y	
1	76.5	36.0722	**CER = 5.33µm = 0.00533mm**
2	77.9	36.3343	
3	80.1	35.9804	

REFERENCES

[1] Leigh, E.P., Tlusty, J., Smith, S., 2000, "Advanced Machining Techniques on Titanium Rotor Parts," American Helicopter Society 56th Annual Forum, Virginia Beach, VA, May 2 - 4, 2000.

[2] Grzesik, W., "An Investigation of the Thermal Effects in Orthogonal Cutting Associated with Multilayer Coatings," Annals of the CIRP (50), pp. 53-56.

[3] Dolinšek, S., Kopač, J., 2006, "Mechanism & Types of Tool Wear Particularities in Advanced Cutting Materials," Journal of Achievements in Materials & Manufacturing Engineering, 19(1), pp. 11-18.

[4] Hill, R., 1950, *Mathematical Theory of Plasticity*, Clarendon Press.

[5] U.S. Dept. of Defense, 1974, *Titanium & Titanium Alloys: Military Handbook (MIL- HDBK697A)*.

[6] Donachie, M.J., 2000, *Titanium: A Technical Guide*, ASM International.

[7] Ezugwu, E.O., Wang, Z.M., 1997, "Titanium Alloys & Their Machinability - A Review," Journal of Materials Processing Technology, 68(3), pp. 262-274.

[8] Upadhyaya, 1998, *Cemented Tungsten Carbides - Production, Properties, & Testing*, William Andrew Publishing.

[9] Travers Tool Co. Inc., < http://www.travers.com/>

[10] Donachie, M.J., 1982, *Titanium and Titanium Alloys (Source Book)*, ASM International.

[11] Leyens, C., Peters, M., 2003, *Titanium and Titanium Alloys: Fundamentals & Applications*, Wiley-VCH, Weinheim, Germany.

[12] ASM, 1994, *ASM Metals Handbook, Vol. 2: Properties and Selection - Non Ferrous Alloys & Special-Purpose Materials*, ASM International.

[13] Boyer, R., Welsch, G., Collings, E.W., 1994, *Materials Properties Handbook: Titanium Alloys*, ASM International, Materials Park, OH.

[14] Taylor, F.W., 1907, "On the Art of Cutting Metals," Trans. ASME, 28, pp. 31-58.

[15] International Standards Organization, 1989, "Tool Life Testing in Milling – Part 1: Face Milling," ISO 8688-1, Geneva, Switzerland.

[16] Davim, J.P., 2008, *Machining: Fundamentals and Recent Advances*, Springer.

[17] International Standards Organization, 1989, "Tool Life Testing in Milling – Part 2: End Milling," ISO 8688-2, Geneva, Switzerland.

[18] Kuttolamadom, M. A., Mears, M. L., 2011, "On the Volumetric Assessment of Tool Wear in Machining Inserts with Complex Geometries: Need, Methodology & Validation (MSEC2011-50278)," Proceedings of the ASME International Manufacturing Science & Engineering Conference (MSEC 2011), Corvallis, OR.

[19] Dieter, G., 1986, *Mechanical Metallurgy*, McGraw-Hill.

[20] Burger, U., Kuttolamadom, M.A., Bryan, A.M., Mears, M.L. Kurfess, T.R., "Volumetric Flank Wear Characterization for Titanium Milling Insert Tools (MSEC2009-84256)," Proceedings of the ASME International Manufacturing Science & Engineering Conference (MSEC 2009), West Lafayette IN.

[21] Dawson, T.G., Kurfess, T.R., 2005, "Quantification of Tool Wear Using White Light Interferometry & Three-Dimensional Computational Metrology," International Journal of Machine Tools and Manufacture, 45(4-5), pp. 591-596.

[22] Astakhov, V. P., 2006, *Tribology and Interface Engineering Series: Tribology of Metal Cutting*, Elsevier.

[23] Zlatin, N., Field, M., 1973, "Procedures & Precautions in Machining Titanium Alloys," Titanium Science & Technology, 1, pp. 489-504.

[24] Sandvik Coromant, 2008, *Application Guide: Titanium Machining*, Sandvik Coromant.

[25] Isakov, E., Ohlund, D., *Tackling Titanium*, *Sandvik Coromant Co.,* Cutting Tool Engineering, Volume 61, Issue 6, June 2009.

[26] Fregly, B.J., Sawyer, W.G., Harman, M.K., Banks, S.A., 2005, "Computational Wear Prediction of a Total Knee Replacement from in Vivo Kinematics," Journal of Biomechanics, 38(3), pp. 621-626.

[27] Sawyer, W.G., Diaz, K.I., Hamilton, M.A., Micklos, B., 2003, "Evaluation of a Model for the Evolution of Wear in a Scotch-Yoke Mechanism," Journal of Tribology, 125, pp. 678-68.

[28] Kalpakjian, S., Schmid, S.R., 2003, *Manufacturing Processes for Engineering Materials*, Prentice Hall, Upper Saddle River, NJ.

[29] Jönsson, M., Andersson, C., Ståhl, J., 2008, "A General Economic Model for Manufacturing Cost Simulation," 41st CIRP Conference on Manufacturing Systems, pp. 33-38.

[30] Froes, F.H., Yu, K., Nishimura, T., 2004, "Developing Applications for Titanium," Cost-Affordable Titanium Symposium Dedicated to Professor Harvey Flower, The Minerals, Metals & Materials Society, pp. 19-26.

[31] Froes, F.H., Gungor, M.N., Imam, M.A., 2007, "Cost-Affordable Titanium: The Component Fabrication Perspective," Journal of Minerals, Metals, and Materials Society, pp. 28-31.

[32] Dhavale, D.G., 1990, "A Manufacturing Cost Model for Computer-Integrated Manufacturing Systems," International Journal of Operations & Production Management, 10(8), pp. 5-18.

[33] Latger, F., Harris, T., Björklund, S., 2002, "Drilling Cost Model," SAE Technical Paper 2002-01-2632, doi:10.4271/2002-01-2632.

[34] Tlusty, J., 2000, *Manufacturing Processes and Equipment*, Prentice-Hall, Upper Saddle River, NJ.

[35] Shaw, M., 2004, *Metal Cutting Principles*, MIT Press.

[36] Wright, P.K., Trent, E.M., 2000, *Metal Cutting*, Butterworth-Heinemann.

[37] Sandkik Coromant, 2012, *Metalcutting Technical Guide,* Sandkik Coromant.

[38] Marinov, V., *Manufacturing Technology*, Kendall Hunt Pub Co.

[39] ASM, 1995, *ASM Specialty Handbook: Tool Materials*, ASM International.

[40] Kendall, L.A., 1994, *ASM Metals Handbook: Vol. 16 - Machining, Tool Wear and Tool Life*, ASM Handbook.

[41] P.K. Wright, "Physical Models of Tool Wear for Adaptive Control in Flexible Machining Cells," Computer Integrated Manufacturing, 1984, PED- 8, ASME, pp. 19-31.

[42] Kalpakjian, S., Schmid, S.R., 2005, *Manufacturing, Engineering & Technology*, Prentice Hall.

[43] Upadhyaya, G.S., 2001, "Materials Science of Cemented Carbides - A Overview," Materials & Design, 22, pp. 483-489.

[44] Kim, C.S., "Microstructural-Mechanical Property Relationships in WC-Co Composites," Ph.D. Thesis, Carnegie Mellon University, Pittsburgh, PA.

[45] Han, X., 2006, "On the Plastic Deformation Mechanisms of WC-Co Alloys at High Temperature," Ph.D. Thesis, University of the Witwatersrand, Johannesburg.

[46] Henjered, A., Hellsing, M., Andren, H.O., Norden, H., 1984, "The Presence of Cobalt at WC/WC Interfaces," Proceedings of the 2nd International Conference on the Science of Hard Materials, Rhodes, Greece, 75, pp. 303-309.

[47] Web Elements <http://www.webelements.com/cobalt/atom_sizes.html>

[48] *Advances in Hard Material Tool Technology* (1976), Carnegie Press, Pittsburg, PA.

[49] Ezugwu, E.O., Wang, Z.M., 1997, "Titanium Alloys & Their Machinability - A Review," Journal of Materials Processing Technology, 68(3), pp. 262-274.

[50] Titanium Alchemy, <http://web-o-rama.net/titanium/index.html>

[51] Konig, W., 1979, "Applied Research on the Machinability of Titanium & Its Alloys," Proc. AGARD Conf. Advanced Fabrication Processes, CP-256, Florence, Italy.

[52] Lutjering, G., Williams, J.C., 2007, *Titanium*, Springer.

[53] Xu, Y., Bai, Y., Meyers, M.A., 2006, "Deformation, Phase Transformation & Recrystallization in the Shear Bands Induced by High-Strain Rate Loading in Titanium and Its Alloys," J. Mater. Sci. Technol., 22(6).

[54] Timothy, S.P., Hutchings, I.M., 1985, "The Structure of Adiabatic Shear Bands in a Titanium Alloy," Acta metall. Vol. 33. No. 4, pp. 667-676.

[55] Timothy, S.P., 1987, "The Structure of Adiabatic Shear Bands in Metals: A Critical Review," Acta metall. Vol. 35, No. 2, pp. 301-306.

[56] Liao. S., Duffy, J., 1998, "Adiabatic Shear Bands in a Ti-6Al-4V Titanium Alloy," J. Mech. Phys. Solids, Vol. 46, No. 11, pp. 2201-2231.

[57] Recht, R.F., 1964, "Catastrophic Thermoplastic Shear," Trans ASME 86, pp. 189–193.

[58] Bayoumi, A.E., Xie, J.Q., 1995, "Some Metallurgical Aspects of Chip Formation in Cutting Ti-6Al-4V Alloy," Materials Science & Engineering A 190, pp. 173-180.

[59] Chichili, D.R., Ramesh, K.T., Hemker, K.J., 2004, "Adiabatic Shear Localization in α-Titanium: Experiments, Modeling & Microstructural Evolution," Journal of the Mechanics & Physics of Solids, 52, pp. 1889 – 1909.

[60] Meyers, M.A., Subhash, G., Kad, B.K., Prasad, L., 1994, "Evolution of Microstructure & Shear-Band Formation in α-HCP Titanium," Mechanics of Materials 17, pp. 175-193.

[61] Liu, X., Tan, C., Zhang, J., Wang, F., Cai, H., 2009, "Correlation of Adiabatic Shearing Behavior with Fracture in Ti-6Al-4V Alloys with Different Microstructures," International Journal of Impact Engineering 36, pp. 1143-1149.

[62] Gahr, K.Z., 1987, *Tribology Series 10: Microstructure & Wear of Materials*, Elsevier.

[63] Ernstmeyer, D., 2012, Learn to Machine Titanium: A Tough Metal of Choice, <http://www.protekcnc.com/machining_titanium.htm>

[64] Carpenter Technical Datasheet: Titanium Alloy Ti 6Al-4V, <http://cartech.ides.com/datasheet.aspx?i=101&e=269>

[65] Calamaz, M., Coupard, D., Girot, F., 2008, "A New Material Model for 2D Numerical Simulation of Serrated Chip Formation When Machining Titanium Alloy Ti-6Al-4V," International Journal of Machine Tools and Manufacture, 48(3-4), pp. 275-288.

[66] Dieter, G.E., 1976, *Mechanical Metallurgy*, McGraw-Hill.

[67] Lim, S.C., Ashby, M.F., 1987, "Overview No. 55: Wear-Mechanism Maps," Acta Metallurgica, 35(1), pp. 1-24.

[68] Jaffery, S., Mativenga, P., 2009, "Assessment of the Machinability of Ti-6Al-4V Alloy using the Wear Map Approach," The International Journal of Advanced Manufacturing Technology, 40(7), pp. 687-696.

[69] Abdel-Aal, H.A., Nouari, M., El Mansori, M., 2009, "Influence of Thermal Conductivity on Wear When Machining Titanium Alloys," Tribology International, 42, pp. 359-372.

[70] Konig, W., Tondorf, J., Bouzakis, K., 1979, "Possibilities to Avoid Built-Up-Edges in Gear Hobbibg," Annals of the CIRP, 28(1), pp. 77-81.

[71] Rahman, M., Wang, Z.G., Wong, Y.S., 2006, "A Review on High-Speed Machining of Titanium Alloys," JSME International Journal, Series C (Mechanical Systems, Machine Elements and Manufacturing), 49(1), pp. 11-20.

[72] Kertesz, K., Pryor, R.J., Richerson, D.W., Cutler, R.A., 1988, "Machining Titanium Alloys with Ceramic Tools," Journal of Materials Processing Technology, 40(5), pp. 50-51.

[73] Wang, Z.G., Wong, Y.S., Rahman, M., 2005, "High-Speed Milling of Titanium Alloys using Binderless CBN Tools," Int. Journal of Machine Tools & Manufacture, 45, pp. 105-114.

[74] Chen, P., 1992, "Cutting Temperature & Forces in Machining of High-Performance Materials with Self-Propelled Rotary Tool," JSME International Journal, Series C (Mechanical Systems, Machine Elements and Manufacturing), 35(1), pp. 180-185.

[75] Shaffer, W., 2007, Gaining the Edge in CBN Tool Performance, < http://gearsolutions.com/>

[76] Kahles, J.F., Eylon, D., Froes, F.H., Field, M., 1985, "Machining of Titanium Alloys," Journal of Metals, 37, pp. 27-35.

[77] Calamaz, M., Limbo, J., Nouari, M., Espinosa, C., Coupard, D., Salun, M., Girot, F., Chieragatti, R., 2009, "Toward a Better Understanding of Tool Wear Effect through a Comparison between Experiments and SPH Numerical Modeling of Machined Hard Materials," Int. Journal of Refractory Metals & Hard Materials, 27, pp. 595-604.

[78] Su, Y., He, N., Li, L., Li, X.L., 2006, "An Experimental Investigation of Effects of Cooling/ Lubrication Conditions on Tool Wear in High-Speed End Milling of Ti-6Al-4V," Wear, 261, pp. 760-766.

[79] Hong, S.Y., Markus, I., Jeong, W., 2001, "New Cooling Approach and Tool Life Improvement in Cryogenic Machining of Titanium Alloy Ti-6Al-4V," Machine Tool & Manufacture, 41, pp. 2245-2260.

[80] Rahman, M., Wong, Y.S., Zareena, A.R., 2003, "Machinability of Titanium Alloys," JSME International Journal, Series C (Mechanical Systems, Machine Elements and Manufacturing), 46(1), pp. 107-115.

[81] Sandvik Coromant, 2008, *Application Guide: Milling Methods*, Sandvik Coromant.

[82] Partners in THINC, 2010, Live Machining Demonstration, THINC Developers' Forum, May 5, 2010, Charlotte, NC.

[83] Ginting, A., Nouari, M., 2007, "Optimal Cutting Conditions When Dry End Milling the Aeroengine Material Ti-6242s," Journal of Materials Processing Technology, 184(1-3), pp. 319-324.

[84] Komanduri, R., 1982, "Some Clarifications on the Mechanics of Chip Formation when Machining Titanium Alloys," Wear, 76(1), pp. 15-34.

[85] Colding, B.N., Konig, W., 1971, "Validity of the Taylor Equation in Metal Cutting," Ann. CIRP, 19(4), pp. 793.

[86] Obikawa, T., Usui, E., 1996, "Computational Machining of Titanium Alloy-Finite Element Modeling & a few Results," Journal of Manufacturing Science and Engineering, 118.

[87] Umbrello, D., 2008, "Finite Element Simulation of Conventional and High Speed Machining of Ti-6Al-4V Alloy," Journal of Materials Processing Technology, 196(1-3), pp. 79-87.

[88] Wang, Z.G., Rahman, M., Wong, Y.S., and Li, X.P., 2005, "A Hybrid Cutting Force Model for High-Speed Milling of Titanium Alloys," CIRP Annals - Manufacturing Technology, 54(1), pp. 71-74.

[89] Zoya, Z. A., Krishnamurthy, R., 2000, "The Performance of CBN Tools in the Machining of Titanium Alloys," Journal of Materials Processing Technology, 100(1-3), pp. 80-86.

[90] Li, R., Shih, A.J., 2006, "Finite Element Modeling of 3D Turning of Titanium," The International Journal of Advanced Manufacturing Technology, 29(3), pp. 253-261.

[91] Che-Haron, C.H., 2001, "Tool Life & Surface Integrity in Turning Titanium Alloy," Journal of Materials Processing Technology, 118(1-3), pp. 231-237.

[92] Nouari, M., Ginting, A., 2006, "Wear Characteristics & Performance of Multi-Layer CVD-Coated Alloyed Carbide Tool in Dry End Milling of Titanium Alloy," Surface & Coatings Technology, 200(18-19), pp. 5663-5676.

[93] Sun, J., Guo, Y., 2009, "Material Flow Stress and Failure in Multiscale Machining Titanium Alloy Ti-6Al-4V," The International Journal of Advanced Manufacturing Technology, 41(7), pp. 651-659.

[94] Usui, E., Shirakashi, T., Kitagawa, T., 1984, "Analytical Prediction of Cutting Tool Wear," Wear, 100(1-3), pp. 129-151.

[95] Takeyama, H., Murata, T., 1963, "Basic Investigations on Tool Wear," Trans. ASME J. Eng. Ind., 85, pp. 33–38.

[96] Childs, T.H.C., Maekawa, K., Obikawa, T., Yamane, Y., 2000, *Metal Machining: Theory and Applications*, Butterworth-Heinemann.

[97] Mackerle, J., 1998, "Finite-Element Analysis & Simulation of Machining: A Bibliography (1976-1996)," Journal of Materials Processing Technology, 86(1-3), pp. 17-44.

[98] Mackerle, J., 2003, "Finite Element Analysis & Simulation of Machining: An Addendum: A Bibliography (1996-2002)," International Journal of Machine Tools & Manufacture, 43(1), pp. 103-114.

[99] Monaghan, J., Macginley, T., 1999, "Modelling the Orthogonal Machining Process Using Coated Carbide Cutting Tools," Computational Materials Science, 16, pp. 275-284.

[100] Ozel, T., 2009, "Computational Modelling of 3D Turning: Influence of Edge Micro-Geometry on Forces, Stresses, Friction & Tool Wear in PCBN Tooling," Journal of Materials Processing Technology, 209, pp. 5167–5177.

[101] Attanasio, A., Ceretti, E., Rizzuti, S., Umbrello, D., Micari, F., 2008, "3D Finite Element Analysis of Tool Wear in Machining," CIRP Annals - Manufacturing Technology, 57, pp. 61–64.

[102] Attanasio, A., Ceretti, E., Fiorentino, A., Cappellini, C., Giardini, C., 2010, "Investigation & FEM-Based Simulation of Tool Wear in Turning Operations with Uncoated Carbide Tools," Wear, 296, pp. 344–350.

[103] Lei, S., Shin, Y.C., Incropera, F.P., 1999, "Thermo-Mechanical Modeling of Orthogonal Machining Process by Finite Element Analysis," International Journal of Machine Tools & Manufacture, 39(5), pp. 731-750.

[104] Kuttolamadom, M.A., Mears, M.L., 2011, "Modeling & Simulation of Tool Wear in AdvantEdge-FEM When Machining Ti-6Al-4V: Challenges & Advances," Third Wave Systems 2011 International User's Conference (TWS 2011), Jacksonville FL.

[105] Sigl, L.S., Fischmeister, H.F., 1988, "On the Fracture Toughness of Cemented Carbides," Acta Metallurgica, 36(4), pp. 887-897.

[106] Fischmeister, H. F., Schmauder, S., Sigl, L.S., 1988, "Finite Element Modelling of Crack Propagation in WC-Co Hard Metals," Materials Science & Engineering, A 105/106, pp. 305-311.

[107] Park, S., 2007, "Development of a Microstructure-Level Finite Element Model for the Prediction of Tool Failure by Chipping in WC-Co Systems," Ph.D. Thesis, University of Illinois at Urbana-Champaign.

[108] Park, S., Kapoor, S.G., Devor, R.E., 2006, "Microstructure-Level Model for the Prediction of Tool Failure in WC-Co Cutting Tool Materials," Journal of Manufacturing Science & Engineering, 128, pp. 739-748.

[109] Park, S., Kapoor, S.G., Devor, R.E., "Microstructure-Level Model for the Prediction of Tool Failure in Coated WC-Co Cutting Tool Materials During Intermittent Cutting," Journal of Manufacturing Science & Engineering, 129(893-901).

[110] Lim, C.Y.H., Lim, S.C., 2004, Wear Mapping and Wear Characterization Methodology, (Totten, G.E., Liang, H., *Mechanical Tribology: Materials, Characterization, & Applications,* Marcel Dekker.

[111] Astakhov, V.P., Shvets, S.V., 1998, "A System Concept in Metal Cutting," J. Mater. Process. Technol., 79, pp. 189-199.

[112] ThirdWave Systems, 2012, *Thirdwave Systems AdvantEdge-FEM User's Manual*.

[113] Callister, W.D., 2007, *Materials Science & Engineering: An Introduction*, John Wiley & Sons (Asia) Pte Ltd.

[114] Askeland, P., 2003, *Science and Engineering of Materials*, Nelson Thornes.

[115] Hall, E.O., 1951, Proc. Phys. Soc., Ser. B, 64, pp. 747-753.

[116] Petch, N.J., 1953, J. Iron and Steel Institute, pp. 25-28.

[117] Roebuck, B., Gee, M., Bennett, E.G., Morrell, R., 1999, "Measurement Good Practice Guide No. 20 - Mechanical Tests for Hardmetals," Centre for Materials Measurement & Technology, National Physical Laboratory.

[118] International Standards Organization, 1975, ISO 3326: Hardmetals - Determination of (the Magnetization) Coercivity, Geneva, Switzerland.

[119] ASTM, 2008, ASTM B887: Standard Test Method for Determination of Coercivity (Hcs) of Cemented Carbides, ASTM.

[120] Roebuck, B., Bennett, E.G., Byrne, W.P ., Gee, M.G., 1999, "Characterisation of Baseline Hardmetals Using Property Maps, NPL Report CMMT(a)172.

[121] Park, S.J., Cowan, K., Johnson, J.L., German, R.M., 2008, "Grain Size Measurement Methods & Models for Nanograined WC–Co," International Journal of Refractory Metals & Hard Materials, 26, pp. 152-163.

[122] Sandvik, 2005, Cemented Carbide, Sandvik New Developments & Applications, Sandvik Hard Materials.

[123] ASM, 1992, *ASM Handbook Volume 12: Fractography*, ASM International.

[124] Hertzberg, R.W., 1996, *Deformation & Fracture Mechanics of Engineering Materials*, John Wiley & Sons, Inc.

[125] Joshi, V.A., 2006, *Titanium Alloys: An Atlas of Structures and Fracture Features*, CRC Press.

[126] Sandvik Coromant, 2008, *Application Guide: Titanium Machining*, Sandvik Coromant.

[127] Kramer, BM., 1986, "A Comprehensive Tool Wear Model," Ann. CIRP, 35(1), pp. 67-70.

[128] Ramalingam, S., 1981, "Abrasive Wear in Machining Experiments with Materials of Controlled Microstructure," ASME Transactions, Journal of Engineering Materials & Technology, 103, pp. 151.

[129] Larsen-Basse, J., 1978, "Abrasion Mechanism - Delamination to Machining," Proc. of Int. Conf. on the Fundamentals of Tribology, MIT Press, Cambridge, pp. 679.

[130] Olortegui-Yume, J.A., Kwon, P.Y., 2007, "Tool Wear Mechanisms in Machining," Int. J. Machining & Machinability of Materials, 2(3).

[131] Cook, N.H., Nayak, P.N., 1969, "Development of Improved Cutting Tool Materials'," Technical Report of AFML-TR-69-185, US Air Force Materials Laboratory.

[132] Naerheim, Y., Trent, E.M., 1977, "Diffusion Wear of Cemented Carbides Tools When Cutting Steel at High Speeds," Metals Technology, 4, pp. 548-556.

[133] Hartung, P.D., Kramer, B.M, 1982, "Tool Wear in Titanium Machining," Annals of the CIRP, 31(1), pp. 75-80.

[134] King, R., 1986, *Handbook of High Speed Machining Technology*, Springer, Chapman & Hall Advanced Industrial Technology Series.

[135] Ozel, T., Sima, M., Srivastava, A.K., Kaftanoglu, B., 2010, "Investigations on the Effects of Multi-Layered Coated Inserts in Machining Ti-6Al-4V Alloy with Experiments & Finite Element Simulations," CIRP Annals - Manufacturing Technology 59, pp. 77–82.

[136] Yen, Y., Söhner, J., Lilly, B., Altan, T., 2004, "Estimation of Tool Wear in Orthogonal Cutting Using the Finite Element Analysis," Journal of Materials Processing Technology, 146, pp. 82-91.

[137] Lorentzon, J., 2008, "Modelling Tool Wear in Cemented-Carbide Machining Alloy 718," International Journal of Machine Tools & Manufacture, 48, pp. 1072– 1080.

[138] Oosthuizen, G.A., 2010, "Wear Characterisation in Milling of Ti-6Al-4V - A Wear Map Approach," Ph.D. Thesis, University of Stellenbosch.

[139] Astakhov, V.P., 2004, "The Assessment of Cutting Tool Wear," International Journal of Machine Tools & Manufacture, 44(6), pp. 637-647.

[140] Roth, J.T., Mears, M.L., Djurdjanovic, D., Yang, X., Kurfess, T., 2007, "Quality & Inspection of Machining Operations: Review of Condition Monitoring and CMM Inspection Techniques 2000 to Present," Proceedings of the ASME International Manufacturing Science & Engineering Conference 2007, MSEC2007, pp. 861-872.

[141] Huang, Y., Liang, S.Y., 2004, "Modelling of CBN Tool Crater Wear in Finish Hard Turning," The International Journal of Advanced Manufacturing Technology, 24(9), pp. 632-639.

[142] Huang, Y., Liang, S.Y., 2004, "Modeling of CBN Tool Flank Wear Progression in Finish Hard Turning," ASME J. of Manufacturing Sci. and Eng., 126(1), pp. 98-106.

[143] Huang, Y., Dawson, T.G., 2005, "Tool Crater Wear Depth Modeling in CBN Hard Turning," Wear, 258(9), pp. 1455-1461.

[144] Huang, Y., Chou, C., Liang, S.Y., 2007, "CBN Tool Wear in Hard Turning: A Survey on Research Progresses," Int J Adv Manuf Technol, 35, pp. 443–453.

[145] Devillez, A., Lesko, S., Mozer, W., 2004, "Cutting Tool Crater Wear Measurement with White Light Interferometry," Wear, 256(1-2), pp. 56-65.

[146] Lane, B.M., Shi, M., Dow, T.A., Scattergood, R., 2010, "Diamond Tool Wear when Machining Al6061 & 1215 Steel," Wear, 268(11-12), pp. 1434-1441.

[147] Wang, W.H., Wong, Y.S., Hong, G.S., 2006, "3D Measurement of Crater Wear by Phase Shifting Method," Wear, 261(2), pp. 164-171.

[148] Ávila, R.F., Godoy, C., Abrão, A.M., Lima, M.M., 2008, "Topographic Analysis of the Crater Wear on TiN, Ti(C,N) & (Ti,Al)N Coated Carbide Tools," Wear, 265(1-2), pp. 49-56.

[149] Dawson, T.G., Kurfess,T.R, 2002, "Machining Hardened Steel with Polycrystalline Cubic Boron Nitride, Ph.D. Dissertation," Ph.D. Thesis, Georgia Institute of Technology.

[150] Dawson, T.G., Kurfess, T.R., 2006, "Modeling the Progression of Flank Wear on Uncoated and Ceramic-Coated Polycrystalline Cubic Boron Nitride Tools in Hard Turning," Journal of Manufacturing Science & Engineering, 128(1), pp. 104-109.

[151] Chawla, R., Datar, S.B., 1980, "Deduction of Flank & Crater Wear from Measurements of the Total Volumetric Wear Rates of Radioactive Tools," Wear, 58(2), pp. 213-222.

[152] Durazo-Cardenas, I., Shore, P., Luo, X., Jacklin, T., Impey, S.A., Cox, A., 2007, "3D Characterisation of Tool Wear Whilst Diamond Turning Silicon," Wear, 262(3-4), pp. 340-349.

[153] Stephenson, D.A., 2007, *Metal Cutting Theory and Practice*, 101 Productions.

[154] Wang, Z.G., Wong, Y.S., Rahman, M., 2005, "High-Speed Milling of Titanium Alloys using Binderless CBN Tools," International Journal of Machine Tools and Manufacture, 45(1), pp. 105-114.

[155] Iscar Corp., 2009, "Milling Tools Catalog," Iscar.

[156] Khare, J.S., 1983, "Machining Ratio as a Basis for Tool Life Assessment," Wear, 88(2), pp. 145-154.

[157] Kuttolamadom, M.A., Jones, J.J., Mears, M.L., Ziegert, J.C., Kurfess, T.R., 2011, "A Systematic Procedure for Integrating Titanium Alloys as a Lightweight Automotive Material Alternative (2011-01-0429)," SAE 2011 World Congress, Detroit, MI.

[158] Jones, J.J., Kuttolamadom, M.A., Mears, M.L., Kurfess, T.R., Funk, K., 2012, "Life-Cycle Integration of Titanium Alloys into the Automotive Segment for Vehicle Light-Weighting: Part I - Component Redesign, Prototyping, & Validation (2012-01-0784)," SAE 2012 World Congress, Detroit MI.

[159] Kuttolamadom, M.A., Jones, J.J., Mears, M.L., Kurfess, T.R., Funk, K., 2012, "Life-Cycle Integration of Titanium Alloys into the Automotive Segment for Vehicle Light-Weighting: Part Ii - Component Life-Cycle Modeling & Cost Justification (2012-01-0785)," SAE 2012 World Congress, Detroit MI.

[160] Mears, M.L., Kurfess, T.R., Ziegert, J.C., Kuttolamadom, M.A., Joshua, J.J. (2012) "Cutting Performance & Tool Wear Simulation in Titanium Machining through High Performance Computing - Final Report (Part 2)," Department of Energy (DOE) - National Energy Technology Lab (NETL).

[161] Stephenson, D.A., Bandhyopadhyay, P., 1997, "Process-Independent Force Characterization for Metal-Cutting Simulation," Journal of Engineering Materials and Technology, 119(1), pp. 86-94.

[162] Marusich, T.D., Ortiz, M., 1995, "Modeling & Simulation of High-Speed Machining," Int. J. Num. Meth. Eng, 38, pp. 3675-3694.

LIST OF PUBLICATIONS

REFEREED JOURNALS

J06. **Kuttolamadom, M.A.**, Mears, M.L., Kurfess, T.R. (2011) "On the Volumetric Assessment of Tool Wear in Machining Inserts with Complex Geometries - Part 1: Need, Methodology & Standardization," *ASME Journal of Manufacturing Science & Engineering (MANU-11-1280)* (Approved for Publication).

J05. **Kuttolamadom, M.A.**, Mears, M.L., Kurfess, T.R., Bryan, M.A., Burger, U. (2011) "On the Volumetric Assessment of Tool Wear in Machining Inserts with Complex Geometries - Part 2: Experimental Investigation & Validation on Ti-6Al-4V," *ASME Journal of Manufacturing Science & Engineering (MANU-11-1282)* (Approved for Publication).

J04. **Kuttolamadom, M.A.**, Jones, J.J., Mears, M.L., Kurfess, T.R., Funk, K. (2012) "Life-Cycle Integration of Titanium Alloys into the Automotive Segment for Vehicle Light-Weighting: Part II - Component Life-Cycle Modeling & Cost Justification," *SAE International Journal of Materials & Manufacturing 5(1)* (doi:10.4271/2012-01-0785).

J03. Jones, J.J., **Kuttolamadom, M.A.**, Mears, M.L., Kurfess, T.R., Funk, K. (2012) "Life-Cycle Integration of Titanium Alloys into the Automotive Segment for Vehicle Light-Weighting: Part I - Component Redesign, Prototyping, & Validation," *SAE International Journal of Materials & Manufacturing 5(1)* (doi:10.4271/2012-01-0784).

J02. Mears, M.L., Mehta, P., **Kuttolamadom, M.A.**, Montes, C., Jones, J.J., Salandro, W., Werner, A. (2012) "Manufacturing Process Modeling & Application to Intelligent Control," *Journal of the South Carolina Academy of Science (Governor's Special Issue)*, Vol. 10, Iss. 1, pp. 13-18 (ISSN 1553-5975).

J01. **Kuttolamadom, M.A.**, Hamzehlouia, S., Mears, M.L. (2010) "Effect of Machining Feed on Surface Roughness in Cutting 6061 Aluminum," *SAE International Journal of Materials & Manufacturing*, 3(1): pp. 108-119 (Also printed in SAE Special Publications Book (SP-2294): *Advances In Light Weight Materials - Aluminum, Casting Materials, & Magnesium Technologies* (ISBN 978-0-7680-3428-8)).

REFEREED CONFERENCES

C10. **Kuttolamadom, M.A.**, Mehta, P., Mears, M.L., Kurfess, T.R. (2012) "The Correlation of Volumetric Tool Wear & Wear Rate of Machining Tools with the Material Removal Rate of Titanium Alloys (MSEC2012-7338)," *Proceedings of the ASME International Manufacturing Science & Engineering Conference (MSEC 2012),* Notre Dame, IN.

C09. Mehta, P., **Kuttolamadom, M.A.**, Mears, M.L. (2012) "Machining Process Power Monitoring: Bayesian Update of Machining Power Model (MSEC2012-7277)," *Proceedings of the ASME International Manufacturing Science & Engineering Conference (MSEC 2012),* Notre Dame, IN.

C08. **Kuttolamadom, M.A.**, Jones, J.J., Mears, M.L., Kurfess, T.R., Funk, K. (2012) "Life-Cycle Integration of Titanium Alloys into the Automotive Segment for Vehicle Light-Weighting: Part II - Component Life-Cycle Modeling & Cost Justification (2012-01-0785)," *SAE 2012 World Congress*, Detroit, MI.

C07. Jones, J.J., **Kuttolamadom, M.A.**, Mears, M.L., Kurfess, T.R., Funk, K. (2012) "Life-Cycle Integration of Titanium Alloys into the Automotive Segment for Vehicle Light-Weighting: Part I - Component Redesign, Prototyping, & Validation (2012-01-0784)," *SAE 2012 World Congress*, Detroit, MI.

C06. **Kuttolamadom, M.A.**, Mears, M.L. (2011) "On the Volumetric Assessment of Tool Wear in Machining Inserts with Complex Geometries: Need, Methodology & Validation (MSEC2011-50278)," *Proceedings of the ASME International Manufacturing Science & Engineering Conference (MSEC 2011)*, Corvallis, OR (***This paper was the finalist for the outstanding paper award from the Surface Modification Technology, Wear & Tribology Symposium (Track 3-3)***).

C05. **Kuttolamadom, M.A.**, Jones, J.J., Mears, M.L., Ziegert, J.C., Kurfess, T.R. (2011) "A Systematic Procedure for Integrating Titanium Alloys as a Lightweight Automotive Material Alternative (2011-01-0429)," *SAE 2011 World Congress*, Detroit, MI.

C04. **Kuttolamadom, M.A.**, Jones, J.J., Mears, M.L., Ziegert, J.C., Kurfess, T.R. (2010) "Integrating Lightweight Materials - Component Manufacture in Titanium (MSEC2010-34337)," *Proceedings of the ASME International Manufacturing Science & Engineering Conference (MSEC 2010),* Erie, PA.

C03. **Kuttolamadom, M.A.**, Jones, J.J, Mears, M.L., Choragudi, A. (2010) "Investigation of the Machining of Titanium Components for Lightweight Vehicles (2010-01-0022)," *SAE 2010 World Congress*, Detroit, MI.

C02. **Kuttolamadom, M.A.**, Hamzehlouia, S., Mears, M.L. (2010) "Effect of Machining Feed on Surface Roughness in Cutting 6061 Aluminum (2010-01-0218)," *SAE 2010 World Congress*, Detroit, MI (Published also as JSAE Paper: 2010-0550).

C01. Burger, U., **Kuttolamadom, M.A.**, Bryan, A.M., Mears, M.L., Kurfess, T.R. (2009) "Volumetric Flank Wear Characterization for Titanium Milling Insert Tools (MSEC2009-84256)," *Proceedings of the ASME International Manufacturing Science & Engineering Conference (MSEC 2009),* West Lafayette, IN.

TECHNICAL REPORTS

R02. Mears, M.L., Kurfess, T.R., Ziegert, J.C., **Kuttolamadom, M.A.**, Joshua, J.J. (2012) "Cutting Performance & Tool Wear Simulation in Titanium Machining through High Performance Computing - Final Report (Part 2)," *National Center for Manufacturing Sciences (NCMS) / Department of Energy (DOE) - National Energy Technology Lab (NETL)*.

R01. Mears, M.L., Kurfess, T.R., Ziegert, J.C., Joshua, J.J., **Kuttolamadom, M.A.,** (2012) "Automotive Component Manufacture in Titanium - Final Report (Part 1)," *National Center for Manufacturing Sciences (NCMS) / Department of Energy (DOE) - National Energy Technology Lab (NETL)*.

SEMINARS & PRESENTATIONS

P07. **Kuttolamadom, M.A.**, "Integrating AdvantEdge FEM on a HPC Cluster for Simulation of Ti-6Al-4V Machining," *11th Annual Third Wave Systems 2012 International User's Conference (TWS 2012)*, May 17, 2012, Minneapolis, MN.

P06. **Kuttolamadom, M.A.**, "The Correlation of Volumetric Tool Wear & Wear Rate of Machining Tools with the Material Removal Rate (MRR) of Titanium Alloys," *Seminar Series - School of Materials Science & Engineering*, April 19, 2012, Clemson University, Clemson, SC.

P05. **Kuttolamadom, M.A.**, "Volumetric Wear Characterization & Modeling for Cutting Tool Wear Prediction," *Seminar Series - School of Materials Science & Engineering*, December 1, 2011, Clemson University, Clemson SC (***This presentation was awarded the Fall 2011 Best Seminar Presentation Award from the Clemson Chapter of Materials Research Society, & the School of Materials Science & Engineering, Clemson University***).

P04. **Kuttolamadom, M.A.**, Mears, M.L., Kurfess, T.R., Ziegert, J.C., Von Oehsen, B., "Adopting Lightweight Materials," *Defense Manufacturing Conference 2011 (DMC 2011)*, November 28-December 1, 2011, Anaheim, CA.

P03. **Kuttolamadom, M.A.**, Mears, M.L., Kurfess, T.R., Von Oehsen, B., "Integrating Light-Weight Automotive Materials: Simulation of Titanium Machining & Tool Wear," *Super Computing 2011 Conference (SC11)*, November 12-18, 2011, Seattle, WA.

P02. **Kuttolamadom, M.A.**, Mears, M.L., Kurfess, T.R., "Modeling & Simulation of Tool Wear in AdvantEdge FEM when Machining Ti-6Al-4V: Challenges & Advances," *10th Annual Third Wave Systems 2011 International User's Conference (TWS 2011)*, May 25, 2011, Jacksonville, FL.

P01. **Kuttolamadom, M.A.**, Jones, J.J., "Lightweight Engineering Focused Redesign, Manufacture & Validation of an Unsprung Vehicle Component for Total Life-Cycle Cost Savings," *Manufacturing Student Design, ASME International Manufacturing Science & Engineering Conference (MSEC 2011),* Corvallis OR, June 15, 2011.